# MICRO/NANO-STRUCTURAL EVOLUTION IN BLENDED CEMENT PASTE DUE TO PROGRESSIVE DEIONISED WATER LEACHING

By

**Shanshan Jia**

Submitted in accordance with the requirements for the degree of

Doctor of Philosophy

The University of Leeds

School of Civil Engineering

November, 2014

The candidate confirms that the work submitted is her own and appropriate credit has been given where reference has been made to the work of others.

## ACKNOWLEDGEMENTS

Many thanks to my supervisors Prof. Ian Richardson and Dr. Leon Black for their professional guidance and continuous support throughout my PhD study.

I also wish to thank Nuclear Decommissioning Authority (NDA) for providing the PhD studentship and Dr. Steve Willams from its research team for valuable discussions.

I appreciate Miss Emilie L'Hopital from EMPA for providing the synthetic C-A-S-H materials.

Thanks are due to Mr. Leslie Arkless and Miss Rebecca Harrison for their technical assistance in the materials laboratories.

I also would like to thank Mr. John Harrington, Dr. Mike Ward, Mr Stuart Michlethwaite and Dr. Richard Walshaw from Leeds electron microscopy and spectroscopy (LEMAS) centre, and for their technical assistance on using electron microscopies.

Thanks are also due to Dr. Timothy Comyn for training the XRD equipment, Dr. David Apperley (Durham University) for providing the solid state NMR service, and Dr. Shuangxin Li, Dr. Rachel Taylor, Mr. Mien Chen, Dr. Robin Shirley, Elena, James, Mark and Meimei in the materials research group with whom I have enjoyed a very good time over the last three and half years.

Finally sincere thanks go to my husband Dongmin Yang and my parents for their love, support and encouragement.

I would like to dedicate this thesis to my baby *Xibei Yang*.

# ABSTRACT

This study investigates the structural evolution of the blended cement pastes at micro-, nano-, and atomic-scale due to environmental factors, such as, water leaching, ageing and curing temperature, with the aid of the analytical techniques, *i.e.* thermal analysis, XRD, SEM, TEM and SS MAS NMR.

The water leaching experiments are performed on the one year old WPC cement paste blended with 30% PFA, as well as 13 years old WPC cement paste blended with 30% and 50% PFA. It is observed that the water leaching induces the phase dissolution and precipitation, *e.g.* CH, anhydrous cement, AFm and TAH dissolution, C-S-H secondary formation and decalcification, AFt secondary formation and dissolution. The microstructure of the cement paste changes from compact feature to dry cracked land like feature. The Op C-S-H transfers from fine fibrillar or foil-like feature to three dimensional net like feature, and the porosity of Ip C-S-H has increased. The aluminosilicate structure changes from single chain to double chain as the chains have cross-linked across the interlayer. It is also observed with higher replacement of PFA, the leaching speed is slower. Additionally, it is observed the chemical composition, the micro- and nano-scale structure evolve with ageing.

The effects of curing temperature on OPC:BFS blended cement hydration is studied. It is found that as curing temperature increases: the general microstructure of the cement paste becomes more porous; more slag reacts, and more Ip C-S-H with high Al and Mg forms; and the MCL of aluminosilicate anion chain increases.

For comparison, synthetic C-A-S-H is also characterized to better understand the structure of the C-A-S-H in the cement paste, especially the atomic-scale structure.

# TABLE OF CONTENTS

# LIST OF FIGURES

# LIST OF TABLES

# LIST OF ABBREVIATIONS

A=Aluminium oxide ($Al_2O_3$)

$Al^{oct}$ or Al [VI] =Octaherally coordinated aluminium

$Al^{tet}$ or Al [IV] =Tetrahedrally coordinated aluminium

AFt= $Al_2O_3$-$Fe_2O_3$-tri phases

AFm=$Al_2O_3$-$Fe_2O_3$-mono phases

BSE=Backscatter Electron

BFS=Blastfurnace slag

C=Calcium oxide (CaO)

$\overline{C}$=Carbon dioxide ($CO_2$)

$C_3A$=Tricalcium Aluminate (Fss)

$C_4AF$=Tetracalcium aluminoferrite ($Ca_2AlFeO_5$)

CH=Ca $(OH)_2$=Calcium Hydroxide

C/S=Calcium/Silicate ratio (Ca/Si)

$C_3S$=Tricalcium Silicate

$C_2S$=Dicalcium Silicate

C-S-H= Calcium silicate hydrate

DEF=Delayed ettringite formation

F=Iron oxide ($Fe_2O_3$)

GDF= Geological disposal facilities

GPC=Gel permeation chromatograghy

H= $H_2O$

HG=Hydroganet/hydrogrossular

HT=Hydrotalcite

ILW= Intermediate-level radioactive waste

Ip= Inner product

ISH=inner slag hdyrate

K=Potassium oxide ($K_2O$)

LDH=Double layered hydroxide family

LOI=Loss on ignition

LLW=Low-level waste

M=Magnesium oxide (MgO)

MAS SS NMR=Magic Angle Spinning Solid-State Nuclear Magnetic Resonace

MCL=Mean silicate (aluminosilicate) chain length

ml=Millilitre

mm=Millimetre

N=Sodium oxide (NaO)

NDA=National Decommissioning Authority

nm=Nanometer

NMR=Nuclear Magnetic Resonace

NNL=National Nuclear Laboratory

Op= Outer product

OPC=Ordinary Portland cement

P=Phosphorous pentoxide ($P_2O_5$)

PC=Portland cement

PFA=Pulverised fly ash

$Q^0$=Isolated silicate unit

$Q^1$=Disilicate or chain end silicate units

$Q^2$=Chain middle silicate groups

$Q^2$(1Al)=Silicate tetrahedron connected to another silicate tetrahedron and one $AlO_4$ tetrahedron via bridging oxygen

$Q^3$=Chain branching or cross linking silicate groups

$Q^3$(1Al)=Silicate tetrahedron connected to another two silicate tetrahedron and one $AlO_4$ tetrahedron via bridging oxygen

$Q^4$=Three dimensional framework silicate groups

S=Silicate ($SiO_2$)

$\overline{S}$=Sulfur trioxide ($SO_3$)

S/S=Solution/solid ratio

SAD=Selective area diffraction

SCMs=Supplementary cementitious materials

SEM-EDX=Scanning Electron Microscopy combined with Energy Dispersive X-ray Analysis

STA=Simultaneous Thermal Analysis

TAH=Third aluminate hydrates

TGA= Thermogravimetric Analysis

T=Titanium dioxide ($TiO_2$)

T/CH=Tobermorite/Calcium hydroxide point of view

T/J=Tobermorite/jennite point of view

TEM-EDX=Transmission Electron Microscopy combined with Energy Dispersive X-ray Analysi

w/s=Water/solid ratio

WPC=White Portland cement

XRD=X-ray Diffraction

XRF=X-ray Fluorescence

# Chapter 1 Introduction

## 1.1 Research background

Cement, a hydraulic binder, is widely used in today's construction, and its most commonly used type is the ordinary Portland cement (OPC). OPC is a low cost material and can be produced by every industrialised country in the world because the raw materials – limestone, clay and gypsum - are readily available everywhere (Juilland et al., 2010). The general cement is a comparably environmentally friendly material with embodied energy of 4.6 ± 2 MJ/kg and embodied carbon of 0.226 kgC/kg (Hammond and Jones, 2008). Nevertheless, 5-8 % of man-made $CO_2$ is still produced by the calcination of the limestone in the cement manufacturing process and also as a result of burning fossil fuels, as such, it is likely to hit by impending emission legislation (Worrell et al., 2001, Rehan and Nehdi, 2005, Pade and Guimaraes, 2007, Purnell, 2009). Supplementary cementitious materials (SCMs), such as pulverized fly ash (PFA), blast furnace slag (BFS) and silica fume (SF) which are mostly by-products of other industrial processes, are added to cement to become part of the total cementitious system, to reduce the usage of cement, and ultimately to reduce the $CO_2$ emission (Mehta, 1985, Gartner, 2004, Toutanji et al., 2004, Scrivener and Kirkpatrick, 2008, Lothenbach et al., 2011, Snellings et al., 2012, Purnell and Black, 2012).

Cementitious materials are proposed by the UK government to be used in geological disposal facilities (GDF) for radioactive wastes in a wide range of applications, such as waste encapsulation grouts, waste containers and overpacks, buffers and backfills, fracture grouts, tunnel plugs, and tunnel/vault linings, floors and roads, *etc*. (Glasser, 1992, Atkins and Glasser, 1992, Glasser and Atkins, 1994, Serco, 2012). There are great advantages of utilising cementitious materials to disposal of radioactive wastes, *e.g.* inexpensive and already available; ensuring low solubility for most radionuclides

due to alkaline chemistry of hydraulic cements; assisting immobilisation of radionuclides because the structure that may accommodate foreign ions, etc. (Sharp et al., 2003). Therefore, to guarantee the performance of GDF for long term, high pH environment and stability of the structure of hydraulic cement must be maintained (Atkinson et al., 1985).

Figure 1.1 shows the multi barrier disposal concept for intermediate level and low level wastes (ILW/LLW) in higher-strength rocks using disposal vaults backfilled with cementitious materials and is based on a multi barrier, phased and retrievable approach. Once the disposal facility is sealed, the wastes are aimed to be isolated deep inside to ensure that no significant or harmful quantities of radioactivity ever reach the surface environment (NDA, 2010).

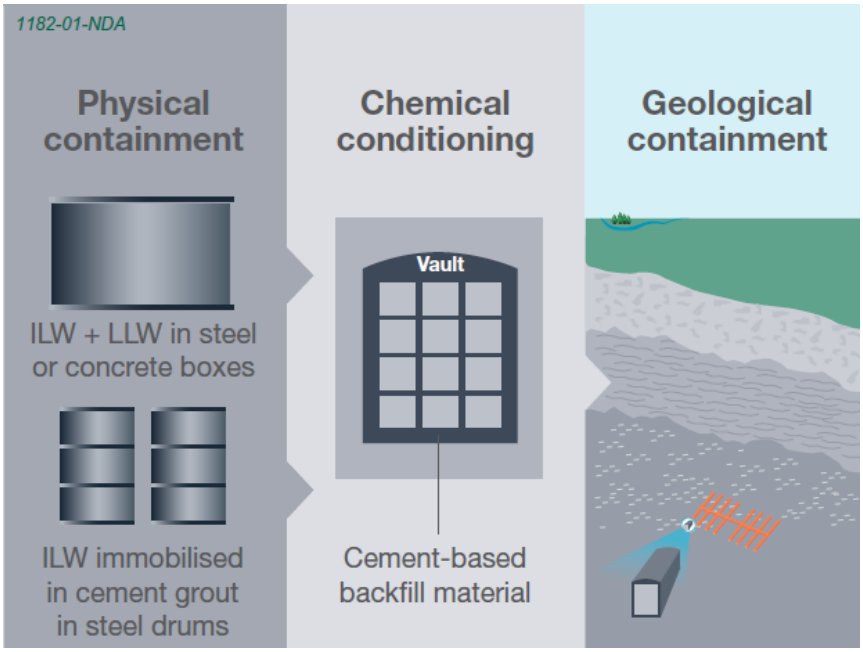


Figure 1.1 illustrations of the UK multi barrier cement-based disposal concept for ILW/LLW (NDA, 2010).

As cementitious materials are expected to have a very long-term service life in the application of GDF, the investigation of ageing on their microstructure is of vital important. It was reported that the micro-, nano-, atomic-scale structural evolution was still occurring in the OPC: BFS blended cement paste after 20 years of hydration

(Taylor et al., 2010).

Water leaching could impair the durability of the cementitious materials when there is groundwater permeation or migration through geologic vaults (Haworth et al., 1989). The cementitious materials are porous materials filled with pore solution, which is approximately pH 13 (Faucon et al., 1998b). When the cementitious materials are attacked by groundwater with a low mineral content and approximately neutral pH, the main cement hydrate phases, *e.g.* first calcium hydroxide (CH) and later also calcium silicate hydrate (C-S-H), ettringite and monosulfate phases will be dissolved or diffused out due to the concentration gradient between the pore solution of cementitious materials and surrounding groundwater, leading to the decrease of the pH of the pore solution and in the long-term the degradation of cement (Adenot and Buil, 1992, Carde et al., 1996).The decrease of the pH of the pore solution may influence the performance of the GDF by increasing the solubility of the radionuclide which is immobilised by the cementitious materials (Sharp et al., 2003). The C-S-H is the most abundant phase in the cementitious systems, therefore, their solubility and leaching behaviour has been the focus of significant efforts (Macphee et al., 1989, Gougar et al., 1996, Sugiyama and Fujita, 2006). The CH is the main phase in buffering the pH of cementitious systems, so the determination of its solubility is also essential. To understand the evolutions of the chemical compositions, the micro-, nano- and atomic-scale structures of the phases, particularly C-S-H, in the cementitious materials are important for developing an effective design and maintenance plan for the GDF.

The planned GDF, after they are sealed, may have an ambient temperature of up to 40°C due to the geothermal gradient in the surrounding rocks. The temperature may be higher because of the heat generated from the waste itself. The maximum temperature is not expected to exceed 80-100°C (Wilding, 1992). It has been reported that the temperature will influence the hydration of the cementious materials and affect their long term performance (Wilding, 1992). Before the cementious materials are utilised in

the GDF, it is important to understand the effects of temperature on the nature of their hydration products, especially their main hydration product, *i.e.* C-S-H gel.

Overall, to enhance the safety of underground storage of radioactive wastes, fundamental effects of ageing, leaching and curing temperature on the structural integrity of cementious materials are the concerns that need to be addressed. As mentioned above, the C-S-H is the main phase in the cementitious materials, and generally, the C-S-H formed in conventional cementitious materials should not be pure C-S-H but C-A-S-H, because there are aluminate phases in Portland-based cementitious materials, and the aluminium substitutes for silicon in 4-fold coordination in the bridging tetrahedra of the "dreierkette" structure (Richardson et al., 1993). However, it is generally difficult to analyse the structures and properties as the C-A-S-H formed in the cementitious materials are generally intermixed with other phases, *e.g.* CH, ettringite and monosulfate, *etc*, therefore it is difficult to analyse the structures and properties. Synthesizing the pure C-A-S-H phase with specific chemical compositions to study the structures and properties of the C-A-S-H (Sun et al., 2006, Pardal et al., 2009), particularly the atomic-scale structure, could help us to better understand the structures of the C-A-S-H formed in the cementitious materials.

## 1.2 Research objectives

The cementitious materials utilised in the study are blended cement paste. Investigating and understanding the structure and chemical compositions of blended cement paste at micro-, nano- and atomic-scale is of vital importance when designing and maintaining the cementitious radioactive waste disposal repositories, because they are associated with the durability. C-S-H, the main phase in the blended cement paste, has great adsorption as it has large surface area and micropore volume, so it plays a crucial role in immobilising the nuclear waste. Therefore special attention is paid in this study to the nature of C-S-H gel in cement paste.

The principle objectives of the study are therefore:

(1) Revealing the leaching mechanism by performing the leaching experiments on one year old white Portland cement paste blended with 30% pulverised fly ash and 13 years old white Portland cement paste blended with 30% and 50% pulverised fly ash, observing the evolution of their micro-, nano- and atomic-scale structure, and assessing their leaching resistance performance;

(2) Investigating the micro-, nano- and atomic-scale structure of the white Portland cement paste blended with different percentage of pulverised fly ash;

(3) Understanding the ageing effects on the micro, nano and atomic-scale structure of the white Portland cement paste blended with pulverised fly ash;

(4) Evaluating the effects of curing temperature on the micro-, nano- and atomic-scale structure of ordinary Portland cement paste blended with blast furnace slag;

(5) Investigating the nano- and atomic-scale structure of synthetic C-A-S-H so as to better understand the atomic-scale structure of the C-A-S-H formed in the cement paste.

The study aims to provide essential data as inputs into thermodynamic models which can promote our understanding of the impact of different factors such as ageing, chemical composition, temperature and water leaching on the hydrated cementitious materials. In addition, it is possible for thermodynamic models to make the investigation in a long time scale.

## 1.3 Thesis outline

Chapter 2 presents a literature review relating to the study, with a focus on the following aspects: the general chemical composition of ordinary Portland cement and white Portland cement and their main hydration products; the use of supplementary

cementing materials in modern construction, particularly the utilisation of pulverized fly ash and blast furnace slag; the main hydration product C-S-H in the cement paste; the characterization techniques which are widely used in the cementitious material research, *e.g.* thermal analysis, X-ray diffraction, scanning electron microscopy, transmission electron microscopy and solid-state MAS NMR; and the effects of leaching and curing temperature on cement properties.

Chapter 3 describes the materials used in the study, *i.e*. one year old white Portland cement paste blended with 30% pulverised fly ash, and 13 years old white Portland cement paste blended with 30% and 50% pulverised fly ash for the leaching experiments. One year old ordinary Portland cement paste is blended with 77% blast furnace slag hydrated at different curing temperatures to investigate the effect of curing temperature on the structure of the cement paste. Synthetic C-A-S-H with bulk Ca/Si=1.31 (or 0.46) and Al/Si=0.17 is prepared to study their structures. This chapter also presents the experimental techniques used in the study.

Chapters 4, 5 and 6 include the leaching results and discussions performed on three sets of blended cement paste as mentioned above. Chapter 7 covers the characterisation results and discussions on three sets of blended cement paste hydrated at different curing temperatures. Chapter 8 presents the characterisation results and discussions on two sets of synthetic C-A-S-H with different Ca/Si atomic ratio. Chapter 9 presents the detailed comparison of the micro-, nano-, atomic-scale structure between the white Portland cement paste blended with 30% pulverised fly ash and 50% pulverised fly ash at different hydration time observed by Love, Girão, Taylor and the author. Comparison of the leaching behaviours of the one year old white Portland cement paste blended with 30% pulverised fly ash, 13 years old white Portland cement paste blended with 30% and 50% pulverised fly ash is also carried out. Finally, the atomic-structure of the synthetic C-A-S-H is compared with the C-A-S-H formed in the cement paste.

Chapter 10 is a summary of the main conclusions in the study and it also includes some suggestions for future works.

# Chapter 2 Literature review

## 2.1 Ordinary Portland cement

Ordinary Portland cement (OPC), as a main ingredient of cement paste, mortar and concrete, is the most commonly used type of cement in the world today. It is produced by grinding Portland cement clinkers which are mainly prepared from calcareous materials such as limestone or chalk, argillaceous materials such as shale or clay, and a limited amount of calcium sulphate and minor constituents depending on cement standards. Classic OPC clinker has four principal mineralogical components, *i.e.* alite ($C_3S$, 60-70% by weight), belite ($C_2S$, 10-20% by weight), tricalcium aluminate ($C_3A$, 5-10% by weight) and calcium aluminate ferrite ($C_4AF$, 3-8% by weight). Alite and belite are essential to the build-up of strength in cement paste. The content of aluminate and ferrite can differ significantly for making special cement. During the OPC production, 2-10 % of gypsum (calcium sulphate dehydrate) is added to control the setting time and influence the rate of strength development (Lerch, 1946).

White Portland cement (WPC) is similar to OPC in all respects except for its high degree of whiteness due to low content of iron. To get better quality of the solid state MAS NMR spectrum, WPC is adopted in this study, because with low content of iron, which is a type of paramagnetic element, the line broadening caused by nuclear-electron dipolar couplings can be largely reduced (Richardson and Groves, 1997).

### 2.1.1 Ordinary Portland cement hydration

OPC is a hydraulic material, which requires the addition of water to form the cement paste and that process is called “hydration”. When OPC is mixed with water its chemical compound constituents undergo a series of chemical reactions that cause it to set. The setting usually takes several hours and the paste hardens in several weeks, resulting in a progressive stiffening, hardening as well as strength development.

Hardening results from hydration reactions between the major phases in the OPC and water. The reactions between major phases and water often occur at the same time but at different rates, and they can influence each other in complex ways. The general principles of the reactions are the same: anhydrous phases dissolve and then precipitate to form colloidal and micro-crystalline hydrates. The kinetics of the cement hydration is influenced by numerous factors, such as the phase composition of the cement and the presence of foreign ions within individual clinker phases; the fineness of the cement; the water-cement ratio used; the curing temperature; the presence of chemical admixtures; the presence of additives, etc. (Odler, 2003).

Alite is the main clinker phase in Portland cement, and the hydration of alite is important for initial set and early strength. It is the impurity form of $C_3S$, modified with foreign ions, *e.g.* $Mg^{2+}$, $Al^{3+}$ and $Fe^{3+}$, in the form of oxides (Maki et al., 1991, Kolovos et al., 2005). The hydration of alite is usually described by the monoclinic phase α-$C_3S$, which is the main polymorph of the tricalcium silicate. As soon as $C_3S$ contacts with water, different ions are immediately dissolved from the $C_3S$ grain surface, *i.e.* $H_2SiO_4^{2-}$, $OH^-$, $Ca^{2+}$, and large amount of heat is released (Angstadt and Hurley, 1963). The pH quickly rises to over 12 due to the largely release of alkaline hydroxide ions, but this initial hydrolysis slows down quickly because of the decrease in heat evolved. Initially, calcium silicate hydrate (C-S-H) gel has started to precipitate around the $C_3S$ grains, however, solid calcium hydroxide (CH) is not precipitated even when its concentration in the liquid phase has reached and exceeded the saturation level, and it is assumed that because of a poisoning of the surface of the CH nuclei by silicate ions (Odler, 2003). The $C_3S$ dissolution and C-S-H gel precipitation slow down and eventually cease because the high concentration of $Ca^{2+}$ and $OH^-$ in the liquid phase, until the concentration of CH in the liquid phase becomes high enough to overcome the poisoning effect and solid CH starts to precipitate (Odler, 2003). The precipitation process accelerates the $C_3S$ to further dissolve and produce $Ca^{2+}$ and $OH^-$ ions, and

then leads to the further precipitation of CH and C-S-H gel (Rodger et al., 1988). Alite is responsible for much of the strength development before 28 days (Harrisson et al., 1985). The following chemical equation illustrates the hydration of $C_3S$ (Odler, 2003).

$$C_3S + (3 + \mathrm{m} - \mathrm{n})H \rightarrow C_nSH_m + (3 - n)CH \qquad \text{Equation 2.1}$$

Belite, which is normally present in a monoclinic β form in Portland cement, is the second abundant clinker in Portland cement. It is the impurity form of $C_2S$, also modified with foreign ions. It reacts with water in a similar manner compared to alite, but hydrates and hardens slowly. It was reported that after 20 years of hydration, there was still a certain amount of anhydrous β-$C_2S$ in the cement paste (Taylor et al., 2010). It usually reacts 30% in the first 28 days and 90% in one year (Bye, 1999), and is largely responsible for strength increases in the first 1-2 years (Jost et al., 1977).

Tricalcium aluminate ($C_3A$) hydrates and hardens the most quickly. It can cause undesirably rapid setting unless a set-controlling agent, usually gypsum, is added (Taylor, 1997). It liberates a large amount of heat almost immediately and contributes somewhat to early strength. However, the strong heat evolution does not last long, typically only a few minutes, and is followed by a period of a few hours of relatively low heat evolution. The early hydration product of aluminate is rod-like AFt and after a period of several hours the early-forming AFt converts to AFm (Black et al., 2006). The following chemical equations illustrate the formation of ettringite and monosulfate, which are the most common type of AFt and AFm, respectively.

$$C_3A + 3C\bar{S}H_2 + 26H \rightarrow C_6A\bar{S}_3H_{32}(ettringite) \qquad \text{Equation 2.2}$$

and

$$C_6A\bar{S}_3H_{32} + 2C_3A + 4H \rightarrow 3C_4A\bar{S}H_{12}(monosulfate) \qquad \text{Equation 2.3}$$

Calcium alumino-ferrite ($C_4AF$) does not have a fixed composition and it is commonly expressed in terms of its ideal composition: $4CaO{\bullet}Al_2O_3{\bullet}Fe_2O_3$ (Brown, 1993). It

hydrates rapidly initially but then slows down later, probably because a layer of iron hydroxide gel forms, coating the $C_4AF$ and acting as barrier which prevents further reaction (Ogbonna et al., 2006). It hydrates in a similar way to $C_3A$ and it contributes very little to strength. The hydration products are also AFt and AFm, with $Al^{3+}$ partially replaced with $Fe^{3+}$ (Chatterji and Jeffery, 1962, Liang and Nanru, 1994).

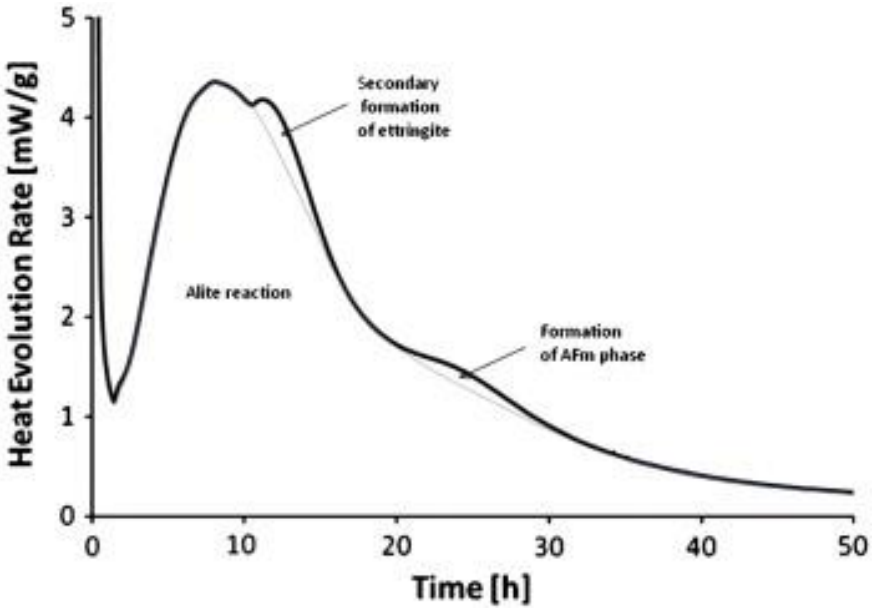


Figure 2.1 Calorimetry curve of modern Portland cement (Bullard et al., 2011).

The calorimetric curve of Portland cement is illustrated in Figure 2.1. It can be seen that there are four peaks over the time. The initial peak is due to the rapid heat release from the initial reaction which can increase the temperature by several degrees. The main reaction during this period is the hydration of aluminate to form an amorphous alumina/silica-rich gel and then short rods like ettringite form as shown in the Figure 2.2 (b). After the initial reaction, a dormant period follows, in which the reaction slows considerably. The main peak corresponds to the heat evolution from the hydration of alite and lesser extent aluminate. Great heat is released due to the rapid reaction of alite. A layer of 'outer' C-S-H form on the rod-like ettringite as illustrated in Figure 2.2 (c). The peak which is on the shoulder of the main peak is due to the heat evolution result from the secondary formation of ettringite. It has a long needle-like structure (see

Figure 2.2 (d)), and it is different from that formed during the initial reaction (Scrivener and Pratt, 1984). Skibsted (1997) observed the formation of monosulfate and a peak rate of formation of ettringite after approximately 12 hours of hydration. A less distinct shoulder has been associated with the formation of AFm and 'inner' C-S-H shown in Figure 2.2 (e) and (f). A flat stable curve is demonstrated because the reactions are continuous and slow.


a) unhydrated b) 10 min→2 hrs c) 10-12 hrs

d) 18 hrs e) 1→3 days f) 14 days

Figure 2.2 Development of microstructure during the hydration of portland cement (Scrivener and Skalny, 1989).

The hydration process may be divided into five stages: initial reaction, induction, acceleratory and deceleratory periods, and the final period of slow reaction (Taylor, 1997), although it is still not possible to make a clear distinction between the induction period and the early age of the acceleratory period (Hewlett, 2003).

### 2.1.2 The main hydration products

The products of the hydration process are termed as “hydration products”. There are typically four main types in hydrated hardened ordinary Portland cement, *i.e.* C-S-H gel, CH, AFt and AFm.

Calcium silicate hydrate (C-S-H) gel, which mainly comes from alite and belite hydration is the main reaction product and is the main source of strength. It is often abbreviated as “C-S-H”, in which the dashes indicate that no strict atomic ratio of Ca/Si is inferred. The Ca/Si atomic ratio of C-S-H is always ≈1.7−1.8 in the hardened $C_3S$, β-$C_2S$ and in ordinary Portland cement pastes (Richardson, 2000), but it is generally lower in the blended cement paste (Rodger and Groves, 1989).

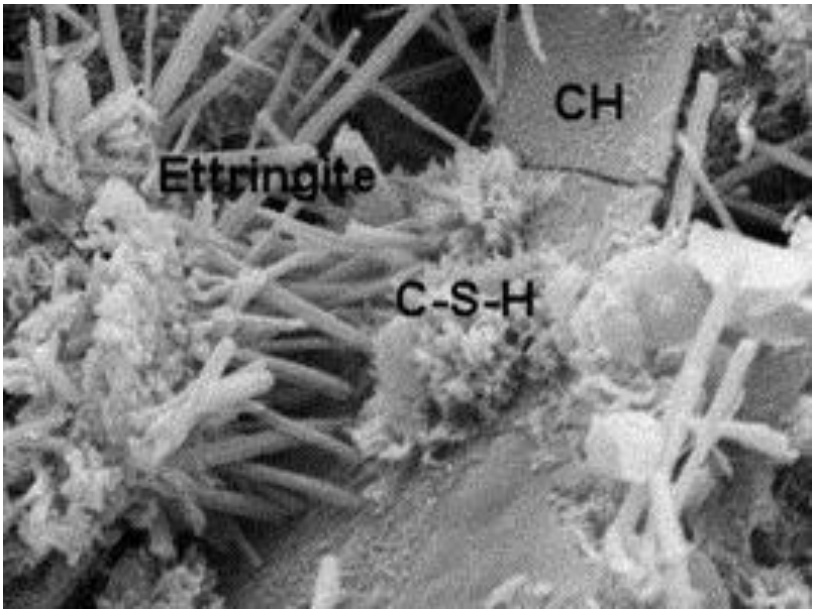


Figure 2.3 SEM pictures of typical hydrated cement paste contains flaky C-S-H, hexagonal CH and needle like ettringite (Margeson).

Calcium hydroxide (CH), also known as its mineral name, portlandite, is one of the main hydration products of alite and belite. CH is a vital component that comprises over 20% of the hydration products in a fully cured pure Portland cement paste, meanwhile estimation of the CH content determines both the hydration characteristics and the degree of hydration of a given cement paste (Bhatty, 1991). The CH often appears to be massive crystal but is also mixed with C-S-H at micro-scale as shown in Figure 2.3. It contributes slightly to the strength and impermeability of the cement paste, because it reduces the total pore volume. However, in this respect, it is much less important than the C-S-H gel. CH with $K_{SP}$ of $4.68\times10^{-6}$ at ambient temperature is the most soluble phase of the hydration products, and thus is a weak link in cement from a durability point of view. When the cement paste is exposed to fresh water, the CH will be leached out, increasing the porosity and thus making the paste more vulnerable to further leaching and chemical attack (Carde and François, 1997).

AFt and AFm phases are two groups of minerals that form from reaction between aluminate/ferrite, gypsum and water. AFt has a higher ratio of S/Ca atomic ratio compared with AFm. One of the most common AFt phases in hydrated cement is ettringite ($C_6A\bar{S}_3H_{32}$) and one of the most common AFm phases is monosulfate ($C_4A\bar{S}H_{12}$). The Al can be partially replaced by Fe in both ettringite and monosulfate. Ettringite is present as rod-like crystals at early stages of hydration as shown in Figure 2.1 or sometimes as massive growth filling pores or cracks in mature concrete or mortar. Mehta (Mehta, 1973) used SEM to study the formation of ettringite, the slender, needle or spherulites of ettringite were observed when sufficient free space is available, which is usually the case in high water-solid ratio solutions, or in large cavities of hydrated cement paste, and the crystals are up to 100 μm long; The short prismatic crystals are formed in low water-solid ratio paste, and under this condition, the crystals are about 0.25 μm thick and 1 μm long. The formation of AFt is believed to be responsible for the expansion phenomena in most expansive cements and for the

formation of cracks in concrete structures which are made out of cements with excessive $SO_3$ contents or those being contacting with ground waters which contain large sulphate contents (Odler and Abdul-Maula, 1984). Monosulfate tends to form in the later stages of hydration, and it forms lamellar structured, hexagonal, or pseudohexagonal plates. Monosulfate is formed from ettringite and additional aluminate or ferrite after depletion of free calcium sulphate in the cement paste. With the presence of sulfates, the monosulfate could resert back into ettringite, whose crystals are 2½ times the size of the monosulfate. The increase of size contributes to the formation of cracks when cement is subject to sulphate attack (Mehta, 1973).

Hydrogarnet ($C_3(A,F)H_6$) phase is the hydration product of tricalcium aluminate or calcium aluminate ferrite, and the most stable hydrogarnet phase is $C_3AH_6$. It is a type of crystalline, and generally intermixing with C-S-H gel in the cement paste (Rodger and Groves, 1989).

## 2.2 Supplementary cementing materials (SCMs)

During the calcination of the cement manufacturing process and also as a result of burning fossil fuels, intensive $CO_2$ is produced. However, reducing $CO_2$ emissions is one of the biggest challenges in the 21$^{st}$ industry. Currently, SCMs, such as pulverized fly ash (PFA), blast furnace slag (BFS) and silica fume (SF) which are mostly by-products of other industrial processes, are added to cement to become part of the total cementitious system, either as an addition or as a partial replacement of OPC to reduce the consumption of cement (Regourd, 1986). Besides the benefit of reducing $CO_2$ emission, SCMs also offer other tremendous benefits, such as waste disposal, cost reduction, energy saving, durability and workability improving. When cement is used for infrastructural constructions, typical replacement levels are up to 60% for BFS and 30% for PFA. To bring dramatic reductions in the reaction rate and amount of heat evolution, and thus improve the long-term integrity, much higher levels of replacement

(can be as high as 90% for BFS and 80% for PFA) are used in the waste encapsulation grouts (Palmer and Fairhall, 1992).

As shown in Figure 2.4(A), the chemistry of SCMs is generally characterized by lower calcium content than OPC. Thus there are differences in the hydration product formed, comparing to OPC in which the main hydration products are C-S-H gel, CH, ettringite and AFm phases. The hydration of OPC blended with SCMs leads to a more complicated system where their hydration occur simultaneously and also influence the reactivity of each other.

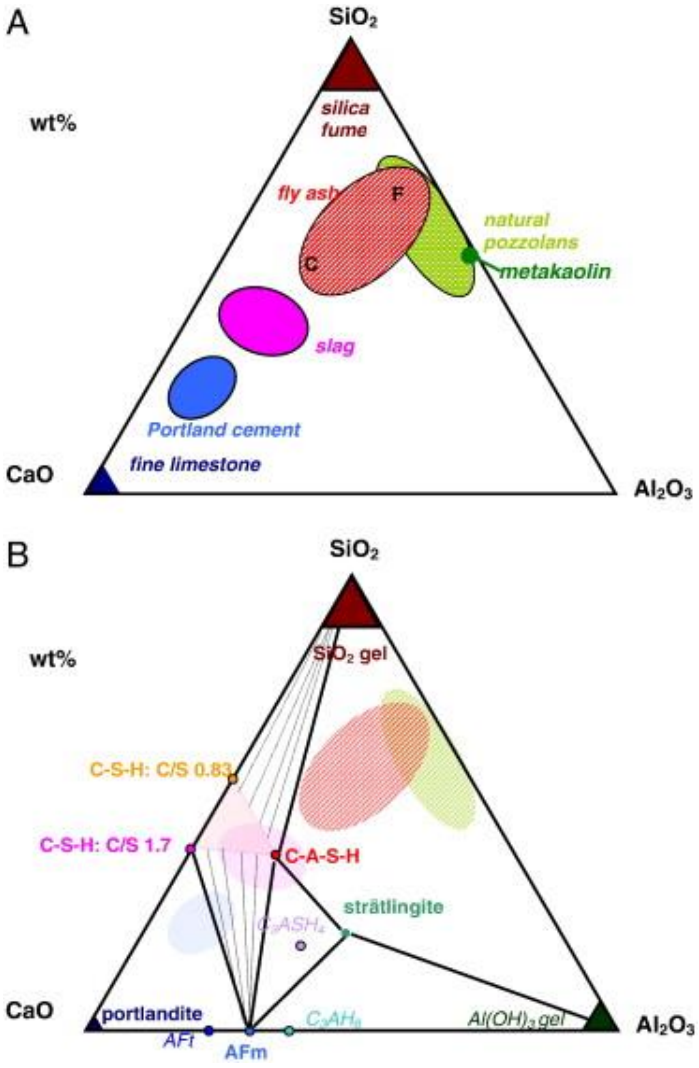


Figure 2.4 (A) $CaO$-$Al_2O_3$-$SiO_2$ ternary diagram of cementitious materials, and (B) hydrate phases in the $CaO$-$Al_2O_3$-$SiO_2$ system (Lothenbach et al., 2011).

Figure 2.4(B) shows that OPC blended with silica fume will lead to a decrease of the content of CH and the increasing formation of C-S-H with lower C/S ratio; OPC blended with fly ash will decrease the amount of CH, while increase the amount of C-S-H with lower C/S ratio and the amount of AFm phases, as fly ash contains high amount of $Al_2O_3$; OPC blended with blast-furnace slag has little effect on the amount of CH with respect to pure OPC, until high level of substitution. However, more C-S-H with a lower C/S ratio is formed due to nature of lower overall C/S ratio of the system (Lothenbach et al., 2011). Al substitutes for Si in 4-fold coordination in the bridging tetrahedra of the "dreier-kette" structure to form the C-A-S-H in the SCMs systems (Richardson et al., 1993).

Generally, there are two groups of SCMs based on their different hydration mechanisms, *i.e*. pozzolanic materials and latent hydraulic materials. The first group, such as PFA, does not have hydraulic property but reacts with CH released by the hydration of OPC to form the C-S-H gel which possesses cementing properties. The second group, such as BFS, has hydraulic characteristic itself, but the reaction is so slow that for practical purposes it needs to be activated, most commonly by blending the slag with OPC (Richardson and Groves, 1992a). Generally, latent hydraulic materials have a higher CaO content than pozzolanic materials, as shown in Figure 2.2 (A).

### 2.2.1 Pulverized fly ash (PFA)

PFA is a by-product resulting from burning of powdered coal at a high temperature. As a pozzolanic material, it is widely used to partially replace OPC due to its economic benefits and engineering impacts.

Generally, there are two types of PFA depending on its calcium content, *i.e.* high-calcium PFA (Class C) and low-calcium PFA (Class F). Class C PFA is generated from burning lignite or sub-bituminous coals and contains 15-40% of analytical CaO. Class F

PFA is produced from burning anthracite or bituminous coal and has less than 10% of analytical CaO. Class F PFA is a common type of pozzolanic material in use throughout the world, and it consists of silicate glass which is modified by aluminium and iron. Kutchko and Kim (2006) characterized class F PFA samples from nine pulverised coal power plants by using SEM-EDS. They observed that the iron oxide and alumio-silicate are mixed throughout the PFA particle from its surfaces and cross-sections. Calcium, which is the fourth abundant element in the PFA, is associated with oxygen, sulphur or phosphorous, not with silicon or aluminium. Both elemental composition and texture of the calcium-rich material are apparently different from the amorphous alumina-silicate spheres. Diamond (2003) pointed out that in PFA, there are compositional variations between different particles within the same PFA, and the effect might be more pronounced in PFA blended cement paste, as there are some particles that behave inertly due to their local chemical and phase composition.

Unlike OPC, Class F PFA requires CH to hydrate (pozzolanic reaction), to form C-S-H gel and gain strength, therefore it only partially replaces OPC cement, and the OPC cement releases CH during its hydration (Papadakis, 1999). He *et al.* (1984) investigated the hydration of fly ash-Portland cements, and they found that the content of CH in the fly ash-Portland cement paste is less than that in the pure Portland cement paste as a result of the pozzolanic reaction. The amount of CH consumed during the pozzalanic reaction can be measured and used to evaluate the reaction degree of the fly ash (Luke and Glasser, 1988).

Rodger (1989) characterized the hydration products formed in OPC-PFA blended paste. Besides general hydration products formed in pure OPC paste, like CH, C-S-H, AFt, and AFm, they observed poorly crystalline iron-containing phase intermixed with C-S-H which is suggested to be the precursor of hydrogarnet phases, and they also identified needles of hydrotalcite-like composition which is high in Mg and Al content, and it generally is intermixed with Ip C-S-H. The general microstructure of the OPC-PFA

blended paste is similar to that in pure OPC paste, except the extra microstructure feature that there is a rim of fibrillar C-S-H gel around un-reactive PFA particles. In addition, the Ca/Si atomic ratio of C-S-H gel produced by OPC-PFA blended cement paste is lower than that in the pure OPC paste. Girão (2007b, 2007, 2010) studied the chemical composition, morphology and nanostructure of water and KOH activated neat WPC and WPC-PFA blended cements. SEM micrographs shows that as hydration proceeds, the microstructure becomes denser since Op C-S-H formed in the originally water occupied spaces and more C-S-H produced from the pozzolanic reaction. The morphology of Ip C-S-H is fine and homogeneous and that of Op C-S-H has fibrillar feature in the water activated systems and foil-like activated by alkali demonstrated by TEM images. The EDX results illustrate that the mean Ca/(Al+Si) atomic ratio is lower in the fly ash blended paste than that in the pure OPC paste due to the pozzolanic reaction which is consistent with Rodger's observation as mentioned above. The mean chain length of the aluminosilicate anion structure of C-S-H increases with age and it is higher in the PFA blended paste observed by $^{29}$Si MASNMR, suggesting the further polymerization. Palomo *et al.* (2004) characterized the hydration products formed in the alkaline activated FA. They pointed out that an aluminium-rich phase formed initially and disappeared at the later reaction stage, and finally a silicon-rich zeolite precursor with a Si/Al ratio around 1.7 formed. Generally, zeolites can form in FA systems if there are sufficient alkali and heating to produce crystalline zeolites.

### 2.2.2 Blast furnace slag (BFS)

BFS is a by-product obtained in the manufacture of pig iron and is formed when iron ore or iron pellets, coke and a flux (either limestone or dolomite) are melted together in the blast furnace. When the molten slag is quickly cooled, it forms into a fine, granular, and almost fully amorphous and glassy form known as granulated slag, having latent hydraulic properties. When such granulated slag is finely ground and mixed with

Portland cement, it exhibits excellent cementitious properties. During the period of cooling and hardening from its molten state, blast furnace slag can be cooled in several ways to form various types of blast furnace slag products. BFS has been widely used as a successful replacement material for Portland cement, producing low hydration heat, having high sulphate and sea water resistance, and bringing environmental and economic benefits. The BFS blended cements are currently used for encapsulation of nuclear waste in the UK, and the BFS replacement percentage could be up to 90% which is much higher than those in the construction industry. However, under ambient curing temperature the strength development of BFS cement paste is considerably slower than that of pure Portland cement paste. Therefore, BFS is not used in applications where high early age strength is required (Wu et al., 1990).

As BFS is a latent hydraulic material, and its hydration reaction rate is very slow, so an activator is usually required, such as alkali, lime and gypsum, and when BFS is activated it dissolves. The most common type of activator in general application is Portland cement which could produce calcium hydroxide during its hydration. The hydroxyls ions $OH^-$ cut the Al-O and Si-O bonds from BFS, and then their combination with $Ca^{2+}$ in solution leads to the formation of C-S-H gel, hydrogarnet, sulphoaluminate hydrate phases like AFt and AFm phases (Murgier et al., 2004). The resulted hydrated cementitious matrix presents good chemical resistance and a more refined pore structure, inducing the improvement of mechanical performance and durability of the slag blended cement paste.

The physical and mechanical properties of the BFS blended cement paste were studied by Kourounis (1995). It was observed that after 90 days of hydration, the compressive strength of the BFS blended cement paste is lower than that of the pure cement paste, and cements containing 15% or 30% slag satisfy the requirements of the strength class 42.5 of EN 197-1, while the cements containing 45% slag satisfy the requirements of the strength class 32.5 of EN 197-1.

Microstructure and microanalysis of the OPC:BFS blended cement paste was investigated by Richardson (1992a) by using TEM together with electron microprobe analysis. The main phases present in OPC:BFS blended cement paste are C-S-H gel, $Ca(OH)_2$, the sulpho-aluminate hydrate phase AFt, and AFm, a Mg, Al-rich hydroxide hydrotalcite phase which is intimately intermixed with Ip C-S-H and a poorly crystalline Fe, Al-rich phase, HG. With more replacement of BFS, in the C-S-H the Ca/Si ratio decreases and the Al/Ca ratio increases. In addition, the morphology of the C-S-H transforms from a strongly linear, fibrillar morphology to fine foil-like morphology in Op C-S-H. The microstructure and microanalysis of the C-S-H gels formed in commercial BFS and synthetic slag glass paste activated with KOH solution were also studied by Richardson (1994). It was found that both composition and morphology of the C-S-H gels observed in the alkaline activated BFS are similar to those observed in the OPC:BFS blended systems, except the C-S-H is more crystalline.

To understand the effects of ageing and replacement of BFS on the microstructure and chemical composition of the C-S-H, Taylor (2010) studied the 20 years old OPC:BFS blends containing different amount of slag. As the slag content increases, both Ca/Si and Ca/(Si+Al) ratios in Op C-S-H decrease, whereas the Al/Si ratio increases. Compared to the specimen at younger ages, the morphology of Op C-S-H in 20 years old cement paste appears to be finer, Ca/Si ratio of C-S-H is lower, the amount of CH decreases and the MCL increases.

## 2.3 C-S-H

The main hydration product of Portland cement is C-S-H gel, which is a generic term used to denote amorphous calcium silicate hydrate gel. It is largely responsible for most of the important properties of cement paste including strength and durability, because it forms a continuous layer that binds together the original cement particles into a cohesive aggregate. Although considerable research have been carried out to

study C-S-H gel, it is still not fully understood, particularly its nanostructure and atomic-structure, due to the facts that its chemical compositions are varying and it is lack of a long range order (Stark, 2011). The manufacturing of every ton of Portland clinker emits approximately 0.8 tons of $CO_2$ into the atmosphere, which comprises 5%-8% of the total human-made $CO_2$ emission, and thus there is a strong motivation to optimize the strength of the concrete and the durability of the C-S-H so that less cement will be needed (Gard and Taylor, 1976, Skinner et al., 2010).

It has been generally agreed that atomic-scale structure of C-S-H has a layered structure close to that of tobermorite particularly in its 1.4-nm form ($C_5S_6H_9$ approximately) which are based on a calcium plan flanked on each side by linear silicate "dreierketten" chains as shown in Figure 2.3, or jennite ($C_9S_6H_{11}$), or both (Taylor, 1993). Richardson (1992b, 2004) proposed a generalized model which could be interpreted from both the Tobermorite/CH (T/CH) and Tobermorite/Jennite (T/J) structural viewpoints.

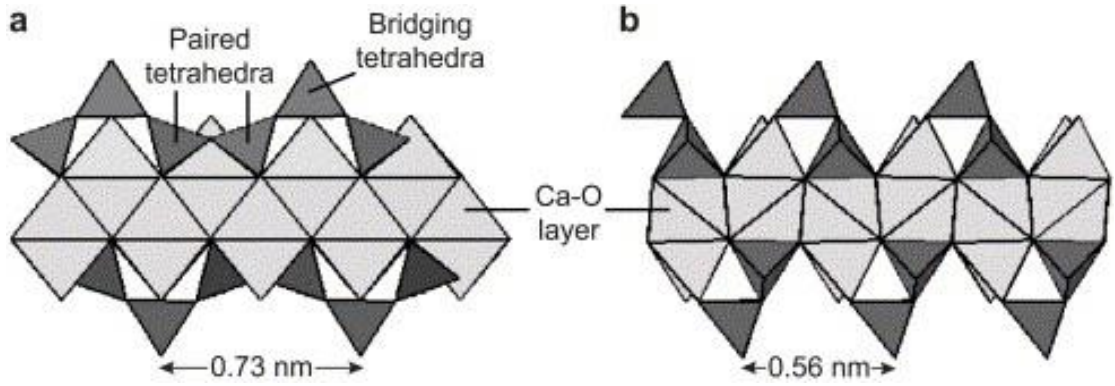


Figure 2.5 A schematic of 1.4-nm tobermorite structure illustrating the Ca-O main layer (light gray) with attached dreierketten (dark gray). Water molecules and Ca atoms present in the interlayer spaces are omitted (Chen et al., 2004).

Synthetic C-S-H, which is prepared from the reaction between CaO and $SiO_2$ or the double decomposition of a Ca salt and an alkali silicate in aqueous solution (Chen et al., 2004), is also being widely investigated nowadays due to its great advantage of

producing C-S-H at specific Ca/Si and Al/Si atomic ratios. The synthetic C-S-H is more easily studied because of the presence of excess water during the reaction, thus eliminating many of the complexities associated with the diffusion controlled reaction kinetics commonly observed in cement paste (Grutzeck, 1999).

### 2.3.1 The nature of C-S-H

Generally, the C-S-H formed in pure PC has a composition of ~1.5-1.9 $CaO \cdot SiO_2 \cdot nH_2O$. The number of n of water molecules depends on relative humidity and temperature. Microanalysis in the TEM which could give compositions for C-S-H free of mixture with other phases has shown that the average Ca/Si atomic ratio of the C-S-H gel present in hardened $C_3S$, $\beta$-$C_2S$, and in OPC paste is always ≈1.7-1.8. Nowadays, the comprehensive application of SCMs leads to the formation of C-S-H with a lower Ca/Si atomic ratio.

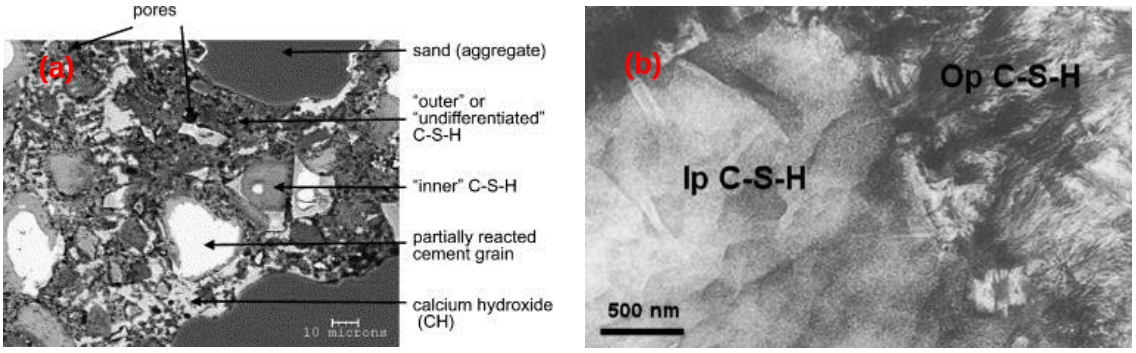


Figure 2.6 (a) A typical BSE image of a Portland cement mortar (200 day old, W/C=0.4), with the microstructural constituents distinguished (Scrivener, 2004); and (b) A typical TEM image showing an Ip C-S-H and Op C-S-H in a paste hydrated for 3 months (20 ºC, W/C=0.4) (Richardson and Groves, 1993).

C-S-H is conventionally classified as inner (Ip) and outer product (Op) C-S-H, defined as those formed in space initially occupied by clinker grains and by water, respectively. They can be distinguished in a backscattered electron (BSE) image in SEM (Scrivener, 2004) or an image in TEM (Richardson and Groves, 1993), however, there is not necessarily an exact correspondence between the positions of the Op and Ip C-S-H in both BSE and TEM images (Groves, 1987).

Richardson (2004) considers that the morphology of Op C-S-H is a function of space constraint. In large pore spaces, Op C-S-H exhibits with a high aspect ratio coarse fibrillar, and in smaller space, it retains a directional aspect but forms in a more space-efficient manner ('fine fibrillar'). Between the fibrillar Op C-S-H there is a three-dimensional interconnected pore network, which is considered to be the capillary porosity and a major concern for durability. Foil-like Op C-S-H is observed in the low Ca/Si atomic ratio Op C-S-H present in slag and pozzolan-containing systems, and it is lack of the linear directional characteristic which is observed in the high Ca/Si atomic ratio C-S-H present in $C_3S$ or OPC paste. Generally, Ip C-S-H formed in larger cement grains (>~5 μm) has a compact, fine-scale and homogeneous morphology, whereas that formed in smaller cement grains (<~5 μm) in a mature Portland cement paste is darker and less dense (see Figure 2.7).

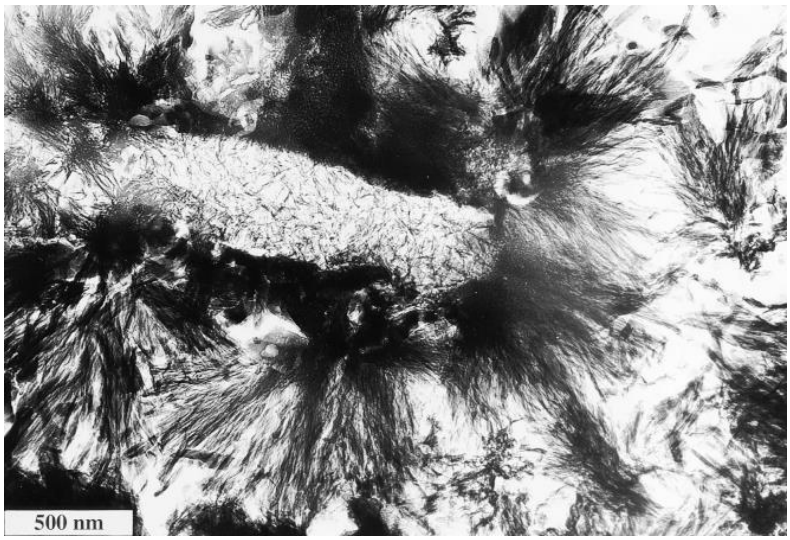


Figure 2.7 TEM image shows low density Ip C-S-H surrounded by a rim of relatively dense C-S-H and fibrillar Op C-S-H in a mature Portland cement paste (Richardson, 1999).

It is difficult to use XRD to determine the amorphous atomic-scale structure of C-S-H, however, it's well known that the atomic-scale structure of C-S-H has been obtained from structural comparisons with crystalline calcium silicate hydrates, 1.4-nm tobermorite with low Ca/Si atomic ratio and jennite with high Ca/Si atomic ratio. An

important characteristic of their structures is their ability of varying in composition, degree of polymerization, and extent of crystallinity while maintaining the essential features of the composite layer structure. The Ca/Si atomic ratio of 1.4-nm tobermorite is 0.83, however, it varies in less crystalline forms. The Ca/Si atomic ratio of jennite is 1.5, which may increase when jennite is in less crystalline forms. There are three other types of less crystalline phases C-S-H, *i.e.* C-S-H (I), C-S-H (II), and C-S-H gel. The C-S-H (I) is an imperfect version of 1.4-nm tobermorite (Taylor, 1950), and it can accommodate a substantial concentration of defects such as the omission of bridging tetrahedra, or variations in the contents of interlayer Ca ions and of protons which attached to $Si\text{-}O^-$, allowing the variations in Ca/Si atomic ratio ranging from 0.67-1.5 (Chen, 2003). It was suggested that the C-S-H (II) is an imperfect version of jennite, although the attempt of synthesizing C-S-H (II) is still unsuccessful (Gard and Taylor, 1976). The C-S-H gel is even less ordered than C-S-H (I) or C-S-H (II), and its XRD patterns show a broad band at 0.26-0.32 nm and a sharper peak at 0.182 nm. The C-S-H gel is generally observed in the $C_3S$ hydrates (Richardson and Groves, 1992b), OPC cement paste, OPC:BFS blended cement paste (Richardson and Groves, 1992a, Wang and Scrivener, 2003, Borges et al., 2010) and WPC:PFA blended cement paste (Girao et al., 2007b, Girao, 2007), *etc*.

### 2.3.2 The nature of Al substituted C-S-H

Because of the environmental impact of cement industry and its consequences on global warming, more and more SCMs are used to partially replace the OPC (Pardal et al., 2012). SCMs are generally alumina-rich and as a consequence some aluminium is incorporated into the C-S-H, forming C-A-S-H gel. The mechanism for the incorporation of Al in the C-S-H suggests that $Al^{3+}$ ions act as a linker for silicate chains that have already been formed (Skibsted and Hall, 2008). The incorporation of Al ions in the C-S-H may have consequences on the cohesion and durability of the C-S-H in the cement

paste, and it is thus of importance to know the amount and the location of aluminium in C-A-S-H and what controls them. The cohesion of the cement paste is believed to be due to the attractive electrostatic forces between charged C-S-H particles, therefore, the substitution by Al could influence these electrostatic cohesion forces (Chen, 2003). The atomic-scale structure of the C-A-S-H is generally studied by the evaluation of different electronically environments of the tetrahedral $SiO_4$, which is an elementary unit of the chain structure, and by the investigation of the Al substituted in the $SiO_4$ chain.

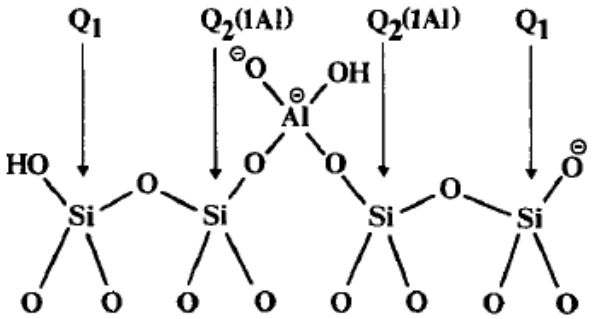


Figure 2.8 Schematic representation of a pentameric silicate chain with Al substituted for Si in the bridging site (Richardson et al., 1993).

Extensive studies have been devoted to the Al substitution in C-S-H (Komarneni et al., 1985, Richardson et al., 1993, Faucon et al., 1999, Garbev et al., 2008, Pena et al., 2008, Manzano et al., 2009, Pardal et al., 2012). Richardson (1993) used $^{27}Al$ and $^{29}Si$ SS MAS NMR, and analytical TEM to study the location of Al in the C-A-S-H gel. It was observed that Al is present in the tetrahedral coordination in the C-A-S-H by $^{27}Al$ SS MAS NMR spectroscopy, indicating the Al coordinating in the C-S-H structure. There is a peak at ≈ -82 ppm which is assigned to $Q^2$ (1Al), and no chain-terminating Al was found from the $^{29}Si$ SS MAS NMR spectrum, suggesting that the Al is absent from the paring of tetrahedra. Meanwhile, the peak areas give an Al/Si ratio for the C-A-S-H is largely consistent with the results from analytical TEM. So, it's concluded that the Al

substituted for Si in 4-fold coordination, and only in the bridging tetrahedra of the "dreierkette" structure (Richardson et al., 1993), as shown in Figure 2.8.

## 2.4 Characterization

Development in the instrumentation of several techniques, *i.e.* thermal analysis, X-ray diffraction (XRD), scanning electron microscopy (SEM), transmission electron microscopy (TEM) and solid-state MAS NMR (SS MAS NMR) enables an improved understanding of the chemical composition, micro-, nano- and atomic-scale structure of the cementitious materials. Especially, the understanding of the nature of the main phase C-S-H gel has been advanced by the technical progresses in analytical TEM and SS MAS NMR spectroscopy.

### 2.4.1 Thermal analysis

Thermal analysis such as simultaneous thermal analysis (STA) and thermogravimetry (TGA) record the thermal changes and weight changes involved in the driving off of the water or gas in the course of the decomposition of cement hydrates, and then it provides analytical information on individual cement hydrates, making it one of the foremost analytical techniques, along with XRD and SEM in the cementitious material study (Taylor et al., 1985a, Bhatty, 1991). Thermal analysis is suitable for studying cement hydration at later stages, especially it is used to determine the degree of hydration of blended cement paste and degree of pozzolanic reaction by estimating CH content (Pane and Hansen, 2005); it is a reliable tool to observe CH dissolution during water leaching (Girao, 2007); it is also applied to measure carbonation profiles in cementitious materials, and it is possible to identify CH and discriminate carbonates from aggregates, from carbonation of CH or from carbonation of C-S-H (Villain et al., 2007).

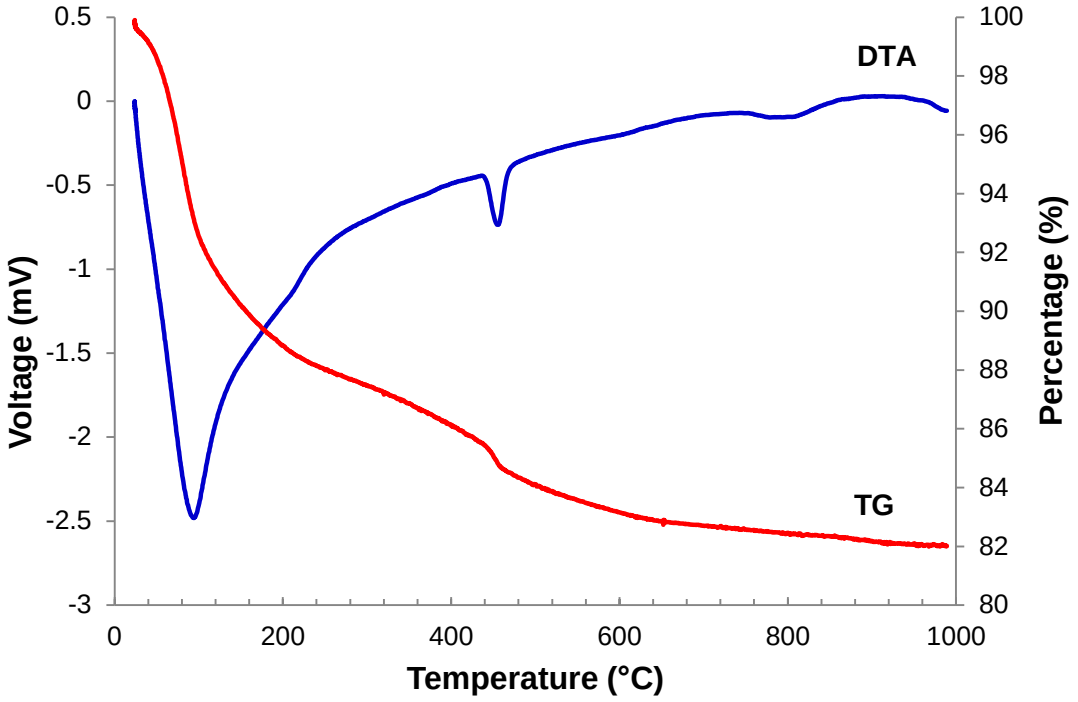


Figure 2.9 Thermal analysis curves of the OPC:BFS blended cement paste.

Table 2.1 Summary of thermal analysis data (Girao, 2007).

| Component | Peak Position [1] (°C) |
|---|---|
| Tobermorite [2] | 120-130 |
| Ettringite | 120-130 |
| Monosulfate | 150-200 |
| C-S-H Gel | <150 |
| Amorphous Hydrates | 200-300 |
| Portlandite (CH) | 450-550 |
| Carbonated Samples (Vaterite) | 450-600 (Endothermic) |
| Carbonated Samples (Calcite) | 600-650 |
| $CaCO_3$ | 750-850 |

[1] At 10°C per minute by DTA specific instrumentation

[2] Peak appears at about 120 and 130 °C, or as a shoulder on the leading edge of an ettringite peak

From the STA curves in Figure 2.9, it is possible to identify the exotherm peaks corresponding to the dehydration of C-S-H and CH at around 130 ºC and 450-550 ºC, respectively, and to estimate the amount of CH present in the cement paste (Midgley, 1979). The loss below the CH step is due to decomposition of C-S-H and the hydrated aluminate phases, but in this zone cement paste show only slight indications of steps. The absence of steps is probably due to a combination of low crystallinity, the presence of other phases and the presence of AFm phases of different compositions in mixture and/or solid solution. Calcium carbonate shows decomposition peaks at the temperature range of 625-875 ºC (Alarcon-Ruiz et al., 2005). Table 2.1 shows the rough decomposition temperature range of each phase in cement paste. The position and nature of the peaks can be affected by many factors such as the type and size of sample holder, furnace, rate of heating, sensitivity of the recording system, temperature calibration, degree of dryness of the sample, particle size, degree of crystallinity, impurities and/or solid solutions, and thus the peaks should be interpreted carefully (Ramachandran et al., 2002). Considerable overlap of some phases, such as ettringite and C-S-H peaks would also make the interpretation difficult (Dweck et al., 2000, Scrivener et al., 2004).

### 2.4.2 X-ray diffraction

X-ray diffraction (XRD) analysis is one of the dominant analytical techniques in cementitious materials study, for instance, to identify and quantify the phases in cement clinkers, ground cements and cement hydration products.

XRD works by bombarding a crystal with X-rays of a fixed wavelength (similar to spacing of the atomic scale crystal lattice planes) at certain incident angles, and the general relationship between the fixed wavelengths of the incident X-rays, angle of incidence and spacing between the crystal lattice planes of atoms is known as Bragg's law, expressed as:

$$n\lambda = 2d\sin\theta$$ Equation 2. 4

where *n* is an integer, *λ* is the wavelength of the radiation used, *d* the spacing of the crystal plane, and *θ* the angle of the diffraction peak.

When Bragg's law is satisfied, X-ray beams scattered from successive planes in the crystal (as shown in Figure 2.10) will travel distances differing by exactly one wavelength (for the case of *n*=1), then a 'Bragg reflection' will be picked up by a detector scanning at this angle. The peak positions of Bragg reflections provide information of the inter-layer spacing of atoms in the crystal structure which can be determined and the different compounds present in a sample identified, and the peak intensity gives information about how much X-ray scattering is contributing to that reflection, so as to identify and provide quantity information of the compounds in a sample.

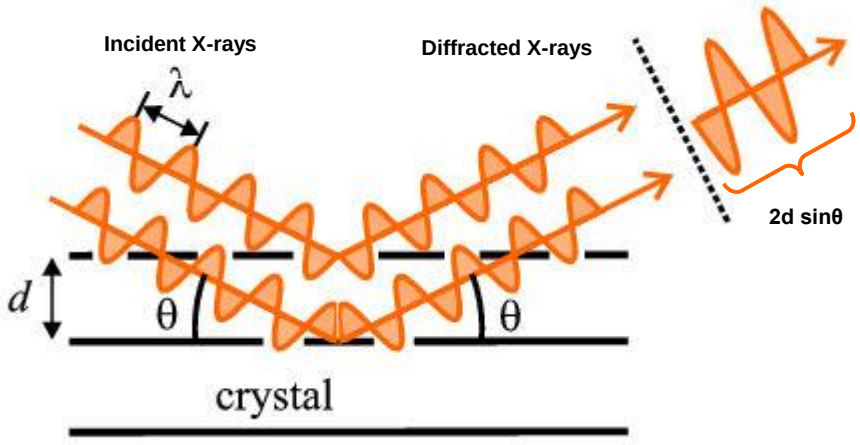


Figure 2.10 Bragg's law reflection

The main application of XRD in cementitious material study is to qualitatively identify phases. Furthermore, the areas under the reflected peaks are related to the amount of each phase present in the sample, which could provide quantitative information of each phase, however, amorphous components such as the C-S-H gel produce a broad amorphous peak, commonly called 'amorphous humps' that cannot be used to give

useful quantitative analysis. A factor could bring broad peak is the crystal size of the crystalline. If a crystal size is less than 100 nm, the x-ray cannot undergo complete destructive interference in scattering and the peak appears broad on the spectrum. On the other hand, it could beneficially provide rough information on the crystal size of the phases in the cementitious materials (Ramachandran and Beaudoin, 2001). Preferentially orientation may occur when the powder sample is compacted in the sample holder due to cleavage or growth mechanisms of some crystals, leading to the modification of the intensities of the diffracted peaks, and it particularly occur in alite, gypsum, anhydrite, hemihydrate, calcite, and portlandite (Le Saout et al., 2011).

Taylor (1985b) used XRD to study blended Portland cement paste, where XRD patterns show sharp peaks from $Ca(OH)_2$, unreacted clinker phases, hydrated aluminate phases (AFt or AFm), broad peaks corresponding to C-S-H gel and unreacted fly ash or slag glasses. Generally, the two peaks definitely attributed to C-S-H gel are a diffuse peak at 0.26-0.32 nm (28.8-33.1 2θ) and a sharper one near 0.182 nm (49.5 2θ) (Chatterji, 1997). The broad peak suggests the presence of wide distribution of Bragg reflection, indicating the lack of development of a single unique structural order parameter but rather a structure that could be highly variably local, and the periodicity in this diffuse peak relates to the Ca-Ca distance in CaO planes. The periodicity in the sharper peak near 0.182 nm is observed in any material containing silicate dreierketten but also may include contributions from the CaO parts of the C-S-H structure. The synthetic C-S-H with high Ca/Si atomic ratio also yield strong peak at around 6.0 2θ, and this peak is generally absent in the C-S-H with low Ca/Si atomic ratio (Black et al., 2005, Garbev et al., 2008). The AFm phase have reflective peaks of 0.89 nm (9.9 2θ) and sometimes also of 0.73-0.82 nm (10.8-12.2 2θ). The 0.89 nm peak could be corresponding to monosulfoaluminate, monosilicoaluminate, or various more complex compositions (Taylor et al., 1985a). The position of the basal reflection for AFm phase is highly variable, depending on the composition as well as the amount

of interlayer water (Richardson et al., 1994). PFA basically has a broad reflected peak between 20-35 2θ and some sharper peaks corresponding to some crystalline phases, *e.g*. quartz and mullite (Fernandez-Jimenez and Palomo, 2003). A broad and diffuse peak from BFS around 30-31 2θ reflects the short range order of the $CaO$-$Al_2O_3$-$MgO$-$SiO_2$ (gehlenite) glass structure (Wang and Scrivener, 1995).

### 2.4.3 Electron microscopy

Electron microscope is a type of microscope that uses an electron beam to illuminate a specimen and produce a magnified image. Two types of electron microscope are commonly used in cementitious materials, *i.e.* scanning electron microscopy (SEM) and transmission electron microscopy (TEM), and each of them has its own advantages and limitations.

#### 2.4.3.1 Scanning electron microscopy

The combination of SEM and energy dispersive X-ray microanalysis (EDX) is widely used to study clinker and cements, because it permits measuring bulk phase abundance and surface areas of the phases, as well as bulk chemistry analysis of constituent phases. Generally, three SEM modes are used in the study of cementitious materials, *i.e.* secondary electrons (SE), backscattered electrons (BSE) and energy dispersive X-ray analysis (EDX). As shown in Figure 2.11, SE are detected from the location close to the surface; BSE are backscattered from a somewhat greater depth; and characteristic X-rays are generated throughout the interaction volume of the electrons with the specimen (Scrivener, 2004).

BSE imaging has great advantages of: observing flat polished sections, which can be prepared to be representative; having a wide range of magnifications from about 20× to 10,000× so that features can be seen in detail and in context at different scales, *e.g.* studying the arrangement of aggregates, paste and any defects in concrete at low magnification and studying the morphology of the hydrate phases, such as C-S-H and

ettringite, down to about 100 nm at the highest magnification; enabling quantification by image analysis of the different microstructural constituents; and combing BSE imaging with information from local chemical microanalyses (Scrivener, 2004). The main limitations of the technique are spatial resolution, only observing two-dimensional sections of a three-dimensional microstructure, and large interaction volume.

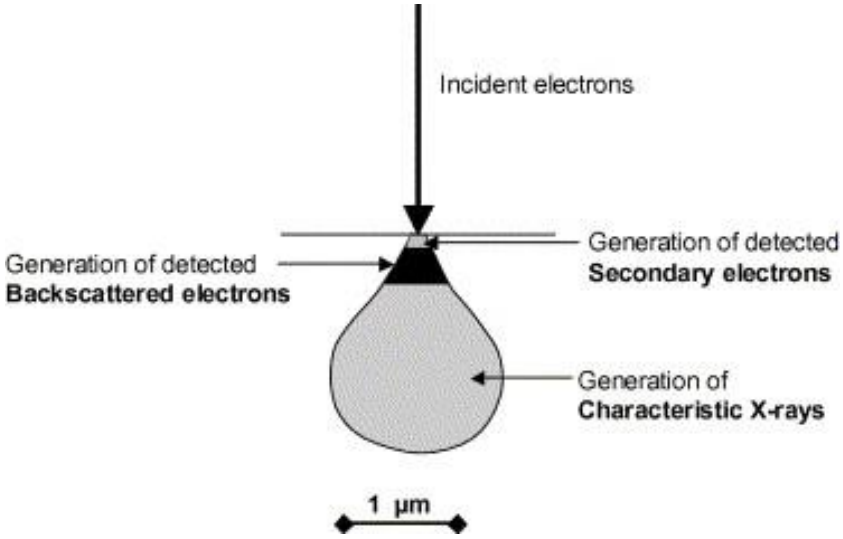


Figure 2.11 Signal generation in the SEM (Scrivener, 2004).

The number of backscattered electrons reaching a BSE detector is proportional to the mean atomic number of the sample. A “brighter” BSE intensity correlates with greater atomic number in the sample, and “dark” areas have lower average atomic number. Thus, different phases with different chemical composition show different grey-scales. The image on the left hand side in Figure 2.12 shows the BSE image of the neat Portland cement paste in which the brightest phase is anhydrous cement grains, less bright phase is CH, the darkest regions usually correspond to pores filled with resin which is from the sample preparation, and the transitional greyscale represents Ip C-S-H and Op C-S-H. The image on right hand side in Figure 2.12 is a BSE image of the OPC:BFS blended cement paste, in which the distinctive microstructure feature is large amount of unreacted slag.

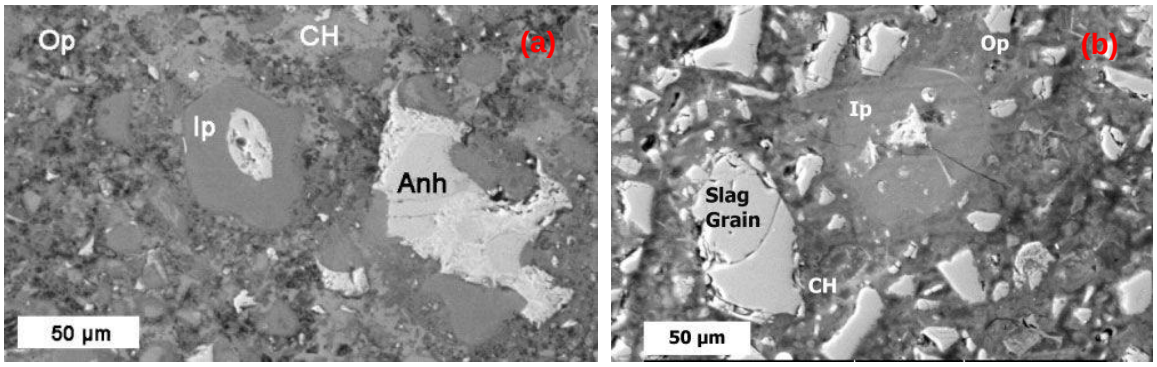


Figure 2.12 BSE images of region in (a) neat cement paste and (b) blended cement paste (Taylor et al., 2007). Regions of anhydrous cement grain (Anh), calcium hydroxide (CH), inner product C-S-H (Ip), outer product C-S-H (Op) and BFS slag grain (Slag Grain) are labelled.

The characteristic X-rays give the chemical composition of the local area. As shown in Figure 2.11, typical X-rays interaction volume for cementitious materials is around 1-2 µm across, which is larger than the size of many hydrate phases, so chemical composition information will come from mixtures of phases, thus care must be taken when analysing data.

X-ray mapping is becoming important in understanding the elemental distributions in materials, as it provides a high magnification image related to the distribution and relative abundance of elements within a given sample (Stutzman, 2004).

#### 2.4.3.2 Transmission electron microscopy

TEM is a powerful tool for characterizing the nano-scale structure and chemical composition of the cementitious materials, thus it enables the understanding of finely intermixed hydration products that are often either amorphous or poorly crystalline and are difficult to be analysed by other techniques, like XRD. A great advantage of TEM technique is that it could provide more accurate local chemical composition information because the TEM specimen is very thin, almost transparent, allowing observation of local analysis of phases nearly free of admixture. As shown in Figure 2.13, the interaction volume between the electron beam and the TEM specimen is much smaller

than SEM specimen. However, great care should be taken when analysing ion-thinned cement specimens in the TEM because it is quite possible for an operator to be unaware that beam damage had occurred (Richardson and Groves, 1993).

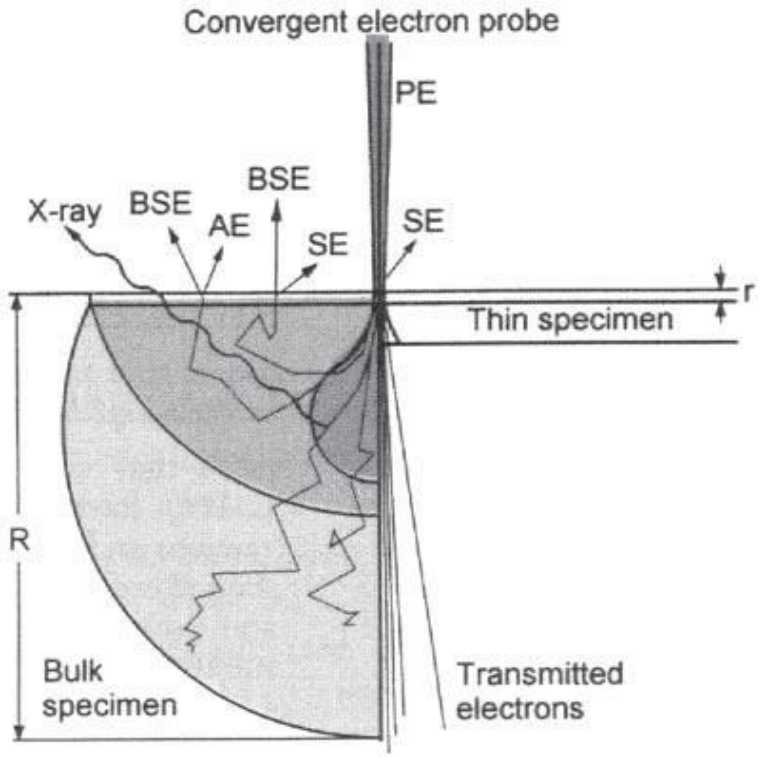


Figure 2.13 The depth of useful signals generated by the interaction of the primary electron beam and a bulk or thin specimen in an electron microscope (Bensted and Barnes, 2008).

Richardson applied analytical TEM to study the nanostructure of $C_3S$, β-$C_2S$, OPC and blended cement paste (1992a, 1992b, 1993). The left image in Figure 2.14 shows that in hardened $C_3S$ paste Op C-S-H has a fibrillar and directional morphology which is a function of space constraint. In contrast, Ip C-S-H has a compact, fine-scale and homogeneous morphology. The morphology of C-S-H in hardened OPC paste is similar to that in hardened $C_3S$ paste, as shown in the right image Figure 2.14, except that relict of AFt was observed in OPC paste. It was observed from EDX analysis that there is a small amount of Aluminium in the C-S-H in OPC paste, but not in $C_3S$ paste.

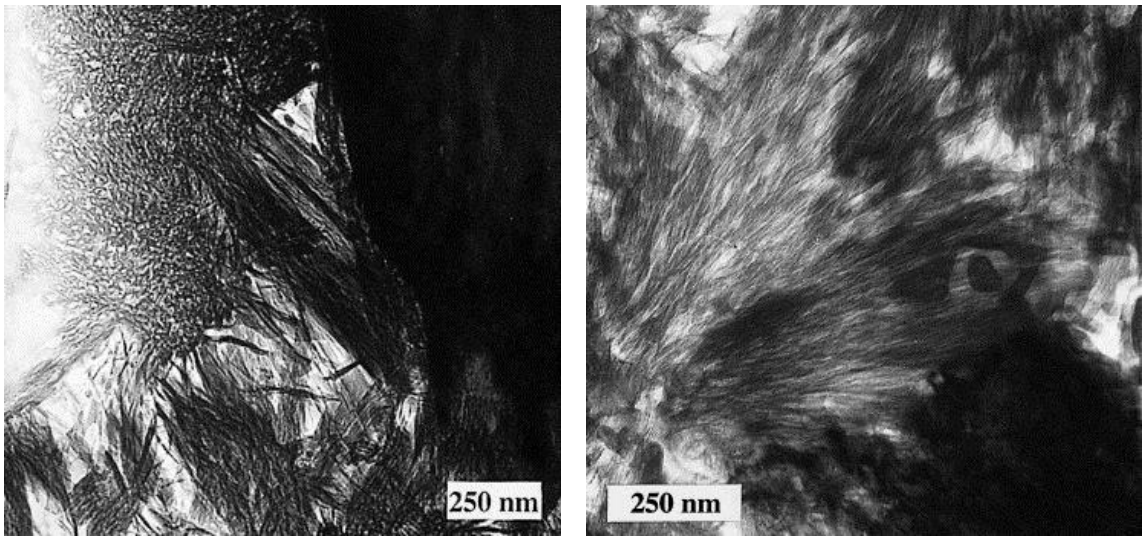


Figure 2.14 The left TEM image showing a region in a mature $C_3S$ paste which contains part of a crystal of CH and examples of Ip C-S-H and 'fine fibrillar' Op C-S-H (Richardson, 2004), and the right image showing a region in a mature ordinary Portland cement which contains 'fine fibrillar' C-S-H, CH (bottom right), and a relict of AFt (top of CH) (Richardson, 2000).

Richardson (1992a) and Taylor (2010) investigated the nano-scale structure and chemical composition of the OPC:BFS blended cement paste with different amount of slag after 14 months and 20 years of hydration. The left TEM image in Figure 2.15 shows the fine fibrillar morphology in the paste containing 75% slag and the right TEM image shows the foil-like feature in the neat slag paste, demonstrating that the morphology of Op C-S-H changes from a strong linear and fibrillar feature at lower level replacement of slag to a fine foil-like feature at a higher level. The EDX analysis showed that the Ca/Si atomic ratio decreases and the Al/Ca atomic ratio increases in the Op C-S-H as the slag replacement percentage increases. It was also observed that the morphology of Op C-S-H appears to be finer in the aged blended cement paste than that in the younger blended cement paste.

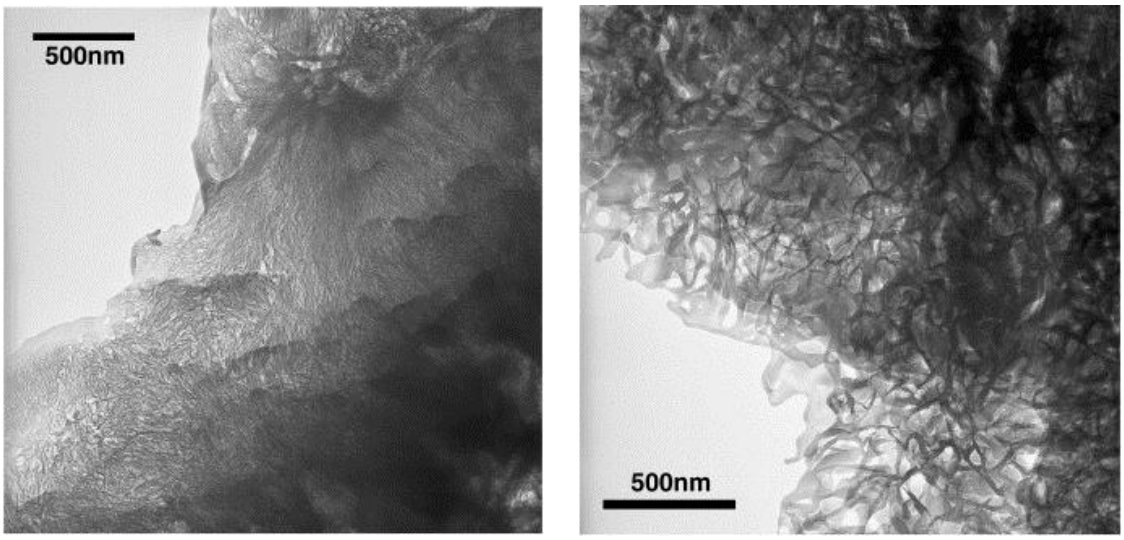


Figure 2.15 The left TEM image illustrating fine, dense Op C-S-H in the OPC paste blended with 75% slag; the right TEM image showing foil-like Op C-S-H in the neat slag paste (Taylor et al., 2010).

The general nano-scale structure of the OPC:PFA blended cement paste is similar to that in pure OPC paste, but the C-S-H gel has a lower C/S ratio (Rodger and Groves, 1989). The nano-scale structure of the WPC:PFA blended cement paste is demonstrated in Figure 2.16, which shows less dense Ip C-S-H formed in the partially reacted PFA grain with a glassy feature and short fibrillar Op C-S-H in the top right .

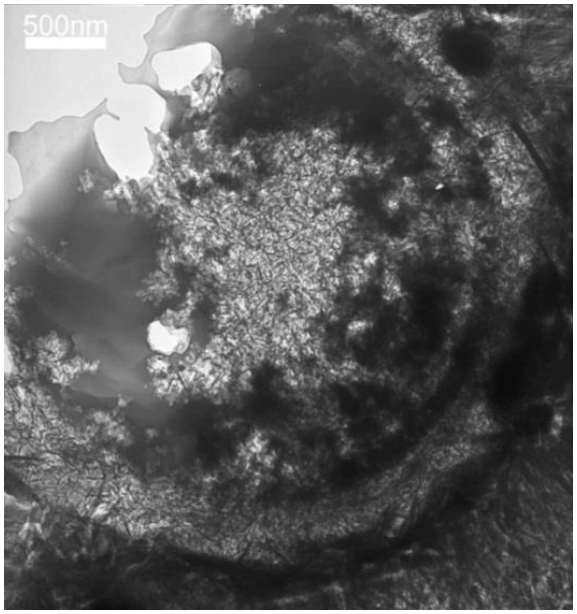


Figure 2.16 A TEM micrograph of water activated WPC cement paste blended with 50% PFA showing a partially reacted fly ash grain (Taylor, 2010).

### 2.4.4 Solid-state MAS NMR

Solid-state MAS NMR spectroscopy is a powerful tool for investigating the structural aspects of both crystalline and amorphous materials at the atomic level due to its non-invasiveness and sensitivity to local environment, especially nearest neighbour and next-nearest neighbour atomic environments, making the technique particularly suitable for amorphous materials, such as C-S-H gel which is the main phase in the cement paste. Recently, it has been proved that this technique can be used to characterize the details of cementitious materials (Barnes et al., 1985, Hjorth et al., 1988, Cong and Kirkpatrick, 1993, Richardson et al., 1993, Wang and Scrivener, 2003, Murgier et al., 2004, Skibsted et al., 2007, Skibsted and Hall, 2008, Brunet et al., 2010).

In a NMR experiment, the quantum nuclei (e.g. $^{29}$Si and $^{27}$Al) are subjected to a strong external magnetic field, thereby causing a splitting of the energy levels for the various spin state in nuclei. When the nuclei are excited by pulses of electromagnetic radiation, energy is absorbed at specific resonance frequencies. The electron density around each nucleus in a molecule varies according to the types of nuclei and bonds in the molecule, therefore the effective field at each nucleus will also vary. This is termed as chemical shift (δ), which is defined by the frequency of the resonance expressed with reference to a standard compound which is defined to 0 ppm.

In cementitious materials research, $^{29}$Si and $^{27}$Al SS MAS NMR spectroscopy are commonly adopted to quantify the fractions of silicon present in different tetrahedral environments in silicates and localize the aluminium atoms which are present in the cementitious materials. In spite of the low natural abundance for $^{29}$Si (4.7%) and its generally long relaxation times, $^{29}$Si SS MAS NMR spectroscopy is still one of the most popular NMR tools for cement research. $^{27}$Al MAS NMR spectroscopy is applied to complement $^{29}$Si MAS NMR spectroscopy, and the spectra generally have good signal/noise ratio due to the 100% natural abundance of $^{27}$Al, however, the spectra are

quite broad due to the second-order quadrupolar interaction which is characteristic of nuclei with spin>1/2. Recently, the 3Q-MAS NMR technique, as a two dimensional technique, is popularly used to remove the second-order quadrupolar contribution to the quadrupolar broadening (Houston et al., 2009). It can be used to identify the different aluminium sites in the aluminium hydrates formed in a cement paste, and to obtain the NMR parameters that characterize these different sites.

#### 2.4.4.1 $^{29}$Si SS MAS NMR

In the $^{29}$Si SS MAS NMR spectrum, the value of δ in the tetrahedral coordination is between -60 and 120 ppm, mainly depending on the degree of condensation of the ($SiO_4$) units, *i.e*. isolated monomers $Q^0$, $Q^1$ dimers, $Q^2$ groups, $Q^3$ branching sites and $Q^4$ fully cross-linking sites, where Q represents the silica tetrahedra (Lippmaa et al., 1980). The Q units are used to calculate the mean chain lengths of C-S-H gel from the following equation, assuming $Q^3$ is absent:

$$MCL\ (mean\ silicate\ chain\ length) = \frac{2 \times (Q^1 + Q^2)}{Q^1} \qquad \text{Equation 2. 5}$$

Generally, in a pure Portland cement paste, there is a mixture of monomer $Q^0$, dimer $Q^1$ and shorter chains ($Q^1$ end units and $Q^2$ middle units). $Q^0$ sites can be largely attributed to anhydrous Portland cement which is present entirely as orthosilicate units, and it is still detectable even after years of hydration (Taylor, 2010). There are up to nine resolvable $Q^0$ peaks in the range -67 to -74 ppm attributed to $Ca_3SiO_5$, but only one for β-$Ca_2SiO_4$ at -71 ppm (Hjorth et al., 1988). $Q^3$ and $Q^4$ units are not found in C-S-H produced at ambient temperatures and pressures. However, $Q^3$ sites are widely found in leached cement paste (Porteneuve et al., 2001a), carbonated cement paste (Groves et al., 1991), and synthetic C-S-H (Cong and Kirkpatrick, 1996a, Cong and Kirkpatrick, 1996b) etc. $Q^4$ sites are present in silica gel or silica fume, and they are not

observed in C-S-H. Table 2.2 shows the characteristic NMR shift of silicate species in the cement paste and synthetic C-S-H.

Table 2.2 Characteritic NMR shifts of silicate species in cement paste and synthetic C-S-H (Wieker et al., 1982, Kwan et al., 1995, Sun et al., 2006).

| Type of silicates | Designation | Tetrahedral structure | Range/ppm |
|---|---|---|---|
| **Ortho(mono)silicates** | $Q^0$ | $O^-$<br>$O^-Si^*O^-$<br>$O^-$ | -66 to -74 |
| **Chain end groups** | $Q^1$ | $O^-$<br>$O^-Si^*OSi$<br>$O^-$ | -75 to -82 |
| **Chain middle groups** | $Q^2$ | $O^-$<br>$SiOSi^*OSi$<br>$O^-$ | -85 to -89 |
| **Chain middle groups** | $Q^2$(1Al) | $O^-$<br>$AlOSi^*OSi$<br>$O^-$ | -80 to -82 |
| **Chain branching sites** | $Q^3$ | Si<br>O<br>$SiOSi^*OSi$<br>$O^-$ | -95 to -100 |
| **Chain branching sites** | $Q^3$(1Al) | Si<br>O<br>$AlOSi^*OSi$<br>$O^-$ | -91 to -94 |
| **Three dimensional framework** | $Q^4$ | Si<br>O<br>$SiOSi^*OSi$<br>O<br>Si | -103 to -115 |

Chen (2003) observed that the chemical shift of the $Q^1$ and $Q^2$ site increase positive values with increasing Ca/Si atomic ratio, suggesting a systematic change with Ca/Si ratio in the local structural environment of the Si sites in C-S-H. The explanation for this transition is still uncertain. The obvious change of the C-S-H is the progressive replacement of Si-O···Ca with Si-O-H with decreasing Ca/Si ratios, however, this substitution would generate a trend in an opposite way. It was proposed that the major contribution to the decrease in chemical shift with decreasing Ca/Si ratio is a decrease in Si-O distance, an increase in Si-O-cation angle, or both, and these changes could conceivably because of changes in the conformation of the Ca-O sheet to which the silicate chains are attached (Xu and Viehland, 1997).

$^{29}$Si SS MAS NMR spectroscopy is widely applied to study the blended cement systems, although with the incorporation of SCMs, quantification is often uncertain, e.g. the overlap of peaks from slag cement and C-S-H in $^{29}$Si SS MAS NMR spectra causing problems with deconvolution (Dyson et al., 2007). Generally, the SCMs are alumina-rich and as a consequence some aluminium is incorporated into the C-S-H, therefore, there is an extra peak formed at around -80~-82 ppm on the shoulder of $Q^2$, assigned to $Q^2$(1Al). Richardson (1993) considers that the formation of $Q^2$(1Al) is due to the Al substitutes for Si in the bridging tetrahedra of the "dreierkette" structure. In the cement blended with BFS, there is a broad peak at around -74 ppm attributing to unreacted BFS, and in the cement blended with PFA, there is a broad peak at around -103 ppm attributing to unreacted PFA. With an extra peak of $Q^2$(1Al), the equations for calculating MCL and Al/Si atomic ratio modified as (Richardson, 2004):

$$MCL\ (mean\ aluminosilicate\ chain\ length) = \frac{2}{\left(\frac{Q^1}{Q^1 + Q^2 + {}^3/_2\, Q^2(1Al)}\right)} \quad \text{Equation 2. 6}$$

and

$$Al/_{Si}\ atomic\ ratio = \frac{1/_2\, Q^2(1Al)}{Q^1 + Q^2 + Q^2(1Al)}$$ Equation 2. 7

### 2.4.4.2 $^{27}$Al SS MAS NMR

$^{27}$Al (I=5/2) is a fairly sensitive nucleus, on which NMR studies are performed, and it can easily be detected. However, $^{27}$Al MAS NMR spectroscopy is difficult to get well resolved spectra at low magnetic field, because the second order quadrupolar interactions are unaverage and consequently the peaks are of differing linewidths and may be asymmetric (Cong and Kirkpatrick, 1993). $^{27}$Al SS MAS NMR has often been used to characterize the material, in which Al nucleus have several chemical environments and can be characterized by different isotropic chemical shifts, for instance, tetrahedral (Al[IV], δ=~50-70 ppm), pentahedral (Al[V], δ=~30-40 ppm) and octahedral (Al[VI], δ=~-10-20 ppm) coordination. Al[IV] substitutes Si in the bridge position of silicate anion chain and it has already been determined by using $^{27}$Al SS MAS spectra and indirectly observed in $^{29}$Si MAS NMR spectra as mentioned above (Richardson et al., 1993). Al[V] site may originate from $Al^{3+}$ substituting for $Ca^{2+}$ ions situated in the interlayer of the C-S-H structure (Sun et al., 2006, Skibsted and Hall, 2008). Al[VI] displays resonances from the sulphoaluminates products (AFt and AFm phases) and a third aluminium hydrate (TAH) phase. The existence of the AFt and AFm aluminate hydrates has already been reported in (Skibsted and Hall, 2008). Skibsted and Andersen (2006, 2008) studied the TAH phase with WPC. Because there are low quantities of paramagnetic ions (e.g. $Fe^{3+}$) in the WPC, the line broadening of the NMR spectra caused by nuclear-electron dipolar couplings between $^{27}$Al, and the unpaired electron of the $Fe^{3+}$ ions could be minimized (Barnes et al., 1985). Skibsted and Andersen (2006, 2008) considered the TAH phase originates from an amorphous or disordered aluminate hydrate, as it has not been observed by other analytical techniques such as XRD. From the NMR spectra, the TAH phase is found to form in C-S-H phases synthesized at ambient temperature with a Ca/Si ratio above 0.83, and it

is assumed to exist as a separate phase or as a nanostructural surface precipitate on the C-S-H phase, however, it is decomposed by thermal treatment at temperature of 70-90 ºC and forms a new phase containing $AlO_4$ tetrahedra.

Solid state $^{29}Si$ and $^{27}Al$ MAS NMR spectroscopy are applied to study synthetic C-S-H (Komarneni et al., 1985, Cong and Kirkpatrick, 1996a, Cong and Kirkpatrick, 1996b, Sun et al., 2006, Pardal et al., 2012). Komarneni *et al*. (1985) studied several types of 1.13 nm tobermorite, most of which were deliberately substituted with aluminium. $^{27}Al$ SS MAS NMR spectra showed the aluminium is tetrahedrally coordinated, and additionally there are two different aluminium environments resonating at ~57 and 64 ppm at that coordination. Sites $Q^2$ and $Q^3$ which are resonated at -85.7 and -95.7 ppm were observed in pure anomalous tobermorite by using $^{29}Si$ SS MAS NMR (Wieker et al., 1982). However, $^{29}Si$ SS MAS NMR spectra for two anomalous Al-substituted tobermorites show four different resonances at ~ -82 ($Q^2$(1Al)), -85 ($Q^2$), -92 ($Q^3$(1Al)) and -96 ($Q^3$) ppm, which indicates that the substitution of aluminium can occur in both $Q^3$ and $Q^2$ units. The spectrum for a normal Al-substituted tobermorite shows the presence of only $Q^2$ and $Q^2$(1Al) sites, due to single-chain silicate anion structure of this type of tobermorite. Sun *et al*. (Sun et al., 2006) investigated in detail the role of Al in synthetic C-S-H by using NMR spectroscopy. It was reported that Al does not enter either the central Ca-O sheet or the pairing tetrahedra of the tobermorite-type layers. There are three possible bridging sites for Al[IV], *i.e.* $Q^3$ sites that bridge across the interlayer (δ≈58 ppm), $Q^2$ sites that are charge balanced by interlayer $Ca^{2+}$, $Na^+$, or $H^+$ (δ≈66 ppm), and $Q^2$ sites that are most likely charge balanced by interlayer or surface Al[V] and Al[VI] through Al[IV]-O-Al[V]/[VI] linkages (δ≈74 ppm).

## 2.5 Leaching

Leaching is the process of extracting minerals from solid by dissolving them into liquid. In the leaching process of a cementitious material, the solid is the cementious material

and the liquid is water. The cementitious material matrix is porous material with different sizes of pores which are generally filled with high basic solution (pH>12.5), therefore any solution (most of the time pure water or at least water with low calcium concentration) with a pH lower than the pH of that basic solution is aggressive to the cementitous material. When water is in contact with the cementitious material, it creates concentration gradients that lead to the diffusion of ions contained in the interstitial pore solution. These transfers modify the chemical balance and induce a total leaching of portlandite and a progressive decalcification of C-S-H. Besides, leaching destroys AFm and AFt phases as well (Faucon et al., 1998b). For practical purposes, the ultimate residue will mainly consist of hydrous forms of silica, alumina and iron oxide, since all the calcium oxides have been lost, inducing the cement paste to be disintegrated (Bi, 2010).

Understanding of how the structures of cementitious materials evolve with the leaching is essential for prediction of their long term engineering performance. The leaching rate is usually very low, and the degradation of cementitious materials due to dissolution rarely affects common cementitious material structures. However, the leaching degradation is particularly crucial for the cementitious materials used as radioactive waste repositories, because long-term stability must be guaranteed for several tens of thousands of years (Berner, 1992). Radioactive waste repositories are normally constructed underground on shorelines, so cementitious materials would remain in contact with groundwater for a long period (Choi and Yang, 2013).

Based on the leaching agents used, there are two common leaching methods, *i.e.* ammonium nitrate solution (Carde et al., 1996, Carde and François, 1997) and water leaching (Adenot and Buil, 1992, Haga et al., 2005). The first method is an accelerated technique which could reduce leaching time from weeks or months to hours, however this technique is unlikely to correspond to the natural leaching. In the second method, the leaching agent is pure water. Although, this type of leaching experiment could take

a long time due to slow kinetics of leaching degradation nature of the cementitious materials, it is still largely adopted because it is more similar with the natural leaching.

In the last three decades, the kinetics of calcium leaching, the effects of decalcification on the mechanical properties of cement paste(Carde et al., 1996, Carde and François, 1997), the behaviour of crystallised phases (Faucon et al., 1997), the evolution of microstructure of C-S-H (Li and Yan, 2010), the change of silicate anion structure in C-S-H gel (Porteneuve et al., 2001a, Porteneuve et al., 2001b, Haga et al., 2002, Girao, 2007) and the solubility of C-S-H phases have been studied and modelled (Kamali et al., 2008, Moranville et al., 2004).

Carde *et al.* (1996) studied the effects of the leaching process on the mechanical properties of cement based materials by performing the leaching experiment in a 50% concentrate solution of ammonium nitrate. They found that the deterioration of the cement paste exposed to the aggressive solution was indicated by a peripheral zone of less resistance, due to the complete dissolution of CH and the progressive decalcification of the C-S-H. In the pure OPC paste sample, the CH dissolution is the essential parameter governing both the decrease in strength and the increase in porosity. The loss of strength due to the C-S-H decalcification is only 6%, which can be neglected compared with the global loss of strength due to the CH dissolution. In the OPC paste blended with silica fume, wherein the CH is consumed by the pozzlanic reaction, the effect of the C-S-H decalcification to the loss of strength is not negligible but the residual strength of the material is important and the material could keep its mechanical functions. Carde *et al.* (1997) performed the leaching experiment on the CEM I cement. The leaching process induced a total loss of CH and a progressive decalcification of C-S-H, however, the compressive resistance and water porosity of the leaching zone are constant regardless the size of the degraded zone and the time of exposure to the chemical attack, suggesting that the dissolution of the CH is the

essential parameter governing the decrease of strength and the increase of porosity of the CEM I cement.

The surface layer of the cement paste attacked by water leaching was studied by Faucon *et al.* (1996). A degraded superficial layer formed when cement paste underwent water leaching, and this layer are characterized by the presence of residual anhydrates, hydrogarnet which was dissolved little by the water leaching, iron-substituted C-S-H and hydrotalcite. Faucon *et al.* (1997) also observed that leaching of cement paste with demineralised water generates a series of dissolution boundaries. Portlandites, then AFm and ettringite dissolve successively, however, hydrogarnets in the surface layer in contact with the aggressive solution only dissolves slightly, or not at all, and hydrotalcites dissolve very slowly at pH values near neutrality, explaining the precipitation of these magnesium-containing phases in the surface layer. It was also found that AFt has greater persistence compared with AFm, in agreement with an observation that AFm is decomposed at or below pH 11.6, whereas for AFt the corresponding value is 10.7. The precipitation of the secondary phases (*e.g.* AFm, ettringite and calcite) was observed in the zones between the core layer and the surface layer due to the local equilibrium and the calcium and hydroxyl concentrations decrease between those two layers. Haga (2005) observed that ettringite precipitation increased as the dissolution of the CH and the C-S-H gel progressed. The CH dissolved as the leaching proceeded, and the larger the pore volume of the samples was, the more rapidly CH dissolved. A clear boundary between the altered and unaltered parts was found on the cross section of the solid phase, which was termed as the CH dissolution front. It was observed that as the leaching proceeded, the CH dissolution front shifted toward the core layer of the sample, and there was a linear relationship between the moved distance of CH fronts and the square root of the leaching time, indicating the dissolution of Ca ions controlled by diffusion.

SS NMR has proven its efficiency in showing the dissolution of the existing species in cement and the precipitation of new species during the leaching process. Porteneuve (2001a, 2001b) studied water leaching of high and ultra-high performance concrete using the SS NMR technique. They were observed that the leaching leads to further hydration of the residual anhydrous cement and hence the precipitation of C-S-H as well as the pozzalanic reaction depending on the amount of remaining silica fume. They also found that after 3 months of leaching, the content of ettringite increases, and then it decreases due to its dissolution nature in the concrete blended with 15% silica fume. The leaching also induces the precipitation of new species, *i.e.* $Q^3$. Haga (2002) applied $^{29}$Si SS MAS NMR to study the silicate anion structural change in C-S-H gel on dissolution of hydrated cement, and it was observed that the CH dissolved first, followed by C-S-H gel, and the mean chain length of silicate anion chain of C-S-H gel increases with the progress of the dissolution.

The effects of decalcification on the microstructure of cement paste were investigated by Thomas (2004). They were observed that the (SANS) intensity across the entire volume fractal regime corresponding to C-S-H gel increases and the nitrogen BSE surface of the WPC paste increases with the decalcification, because the specific surface are of Ip C-S-H increases. Meanwhile, it was found that the 5 nm C-S-H globule building blocks in the unleached cement paste transform into sheet like structures due to the decalcification, which is in agreement with the well-established link between the C-S-H gel with a low Ca/Si atomic ratio and the layered structure mineral tobermorite. Chen (2006) proposed that the change of the morphology resulted from the removal of interlayer Ca could induce the loss of cohesion and subsequent increased mobility of C-S-H, and then induce shrinkage.

SCMs are added in the cement to try to reduce the calcium leaching (Gaitero et al., 2008, Jain and Neithalath, 2009, Li and Yan, 2010). The addition of SCMs (*e.g.* silica nanoparticles) can modify the cement paste in three different ways: (1) reducing the

porosity; (2) transforming CH into C-S-H gel by pozzolanic reaction; (3) modifying the internal structure of the C-S-H gel by increasing the average chain length of the silicate chains, and making the paste more resistant to the water attack (Gaitero et al., 2008). Jain (2009) performed the leaching experiment on the plain and modified cement paste in pure water. They were observed that the modified cement paste with Ca/Si atomic ratio has better water resistance than the plain paste; the glass powder modified paste has the highest leaching resistance; Fly ash and silica fume modified cement paste has leaching resistance in between those of the plain and glass powder modified cement paste. The leaching experiments was performed on the one year old WPC blended with 30% PFA (Girao, 2007). It was found that leaching induced the CH dissolution and C-S-H decalcification; the C-S-H was further polymerised and $Q^3$ was formed; the morphology of the C-S-H changed.

## 2.6 Curing temperature

The curing temperature affects the kinetics of hydration and the nature of the hydration products, especially, the main phase in the cement paste, C-S-H gel. Understanding the effects of high temperatures on cement hydration is important in a number of situations in practice, for example, hot weather climates, accumulated heat evolution, heat curing to accelerate strength gain. When cement is used to dispose the nuclear waste, a repository for the disposal of intermediate level radioactive wastes could – when filled and closed – have an ambient temperature of up to 40 ºC because of the geothermal gradient in the surrounding rocks, and the temperature might be pushed higher by heat generated from the waste up to the region of 80 to 100 ºC (Wilding, 1992). The effect of high curing temperature on the hydration of cement paste can be divided into two parts. On one hand, the microstructure will have more porosity, and on the other hand, the ultimate degree of hydration of anhydrous cement paste is enhanced (Escalante-García and Sharp, 2001).

High curing temperature leads to the formation of brighter rims around the cement grains regarded to constitute the Ip C-S-H structure in the BSE images, and the bright rims associated with the increase in the average atomic number (Kjellsen et al., 1990).

The microstructure of the cement paste hydrated at different temperature was widely studied (Cao and Detwiler, 1995, Escalante-García and Sharp, 2001, Girao, 2007). Cao and Detwiler (1995) investigated the microstructure of cement paste containing 5% SF or 30% BFS hydrated at 23 ºC and 70 ºC. It was observed that the degree of hydration is 30% and 70% at 23 ºC and 70 ºC, respectively, and the elevated curing temperature resulted in a coarse, more continuous pore structure. Escalante-Garcia and Sharp (1998) studied the microstructure of BFS blended cement paste hydrated at 10 ºC, 30 ºC and 60 ºC over a period of 1 year by using SEM, XRD and TG. As curing temperature increases, the hydration degree of slag is enhanced. The SEM image presented that, at 10 ºC, many anhydrous or only slightly hydrated slag grains remain, whereas at 30 ºC, some partially and fully hydrated slag grains are present in the microstructure. In addition, at 60 ºC, the slag hydration further proceeds, as thicker rims have developed around the slag grains. Relatively little CH was observed by SEM in any of the slag blend paste, which is probably due to the few CH crystals remaining which were finely distributed throughout the matrix. The XRD patterns showed that there were monosulfate, a hydrotalcite-like phase, and portlandite in the slag cement paste hydrated at 10 ºC and 60 ºC. Ettringite was observed in the paste hydrated at 10 ºC; however its peaks become very weak indeed in the paste hydrated at 60 ºC. TGA data showed that after 1 year of hydration, as curing temperature increases, the amount of CH present in the paste slightly decreases. Giao and Richardson (2007) also studied the micro/nano/atomic-scale structure of the cement paste cured at different temperatures, and it was observed by SEM that increasing the curing temperature leads to coarsen of the hydration product, increases porosity and decreases the general uniformity of the microstructure . The nanostructure were

studied by using TEM, and it was observed that Ip C-S-H has a fine, homogeneous morphology and it is abundance in the cement paste hydrated at high temperature. Op C-S-H is generally fibrillar, however, it has a coarse fibrillar feature in the paste cured at high temperatures. The MCL of the C-S-H increases as curing temperature increases due to the increasing of hydration degree, which was calculated from the data deconvoluted of NMR spectra. HG phases formed in the cement pates hydrated at 80 ºC observed by XRD, however, it is absent in lower curing temperature paste.

## 2.7 Summary

In the past, focus was given to the study of the phase, mechanical properties and transport properties evolution due to water leaching, and limited attention was paid to microstructural evolution. The combination of different techniques has been neglected and as such leave a clear gap to study the structural evolution of the cement paste at different scales. Although there is one publication concerning the structural evolution of the cement paste at different scales due to water leaching, the leaching experiment was only performed on young cement paste, and there was only limited observation. Therefore this thesis intends to comprehensive study the structural evolution of both the young and aged cement paste at micro-, nano- and atomic-scale due to water leaching by combining different instrumental techniques, and the leaching experiments are performed on different blended cement systems.

There is also limited amount of micro-, nano-, and atomic-scale structural data on the cement paste cured at different temperature, especially there is no study on the influence of curing temperature on the structure of OPC: BFS blended cement paste by combining XRD, SEM, TEM and NMR techniques.

# Chapter 3 Experimental

## 3.1 Materials

### 3.1.1 WPC:PFA blended cement paste

The 13 years old WPC:PFA blended cement paste was cast by Love in the materials group at the University of Leeds (2002). There are two sets of WPC:PFA blended cement paste with different replacement amount of PFA, i.e. 30% and 50% PFA. Before casting, the PFA was demagnetised in the blended cement paste with 30% replacement of PFA. As shown in Table 3.1 that after the demagnetization, the content of iron in the PFA has decrease. The WPC (Aalborg) was blended with either 30% or 50% Class F PFA (West Burton, National Powder) at a water/solid ratio of 0.55 (ml/g). The paste was casted in 5 ml polypropylene vials, sealed and cured at 25 ºC in a water bath for four years, then collected and stored in desiccator. The 13 years old cement paste was characterized and water leached by the author.

A set of one year old WPC:PFA blended cement paste with 70% of WPC (Ribble WPC 8108, Castle cement limited) and 30% of Class F PFA (Drax Power station, Selby) was cast by the author, and the water/solid ratio is 0.50 (ml/g). The casting technique and curing condition is the same as that for the 13 years old samples.

The one year old WPC cement paste blended with 30% PFA, and the 13 years old WPC cement paste blended with 30% and 50% PFA are nomenclature in Table 3.2. XRF is used to identify the bulk oxide compositions of the WPC and PFA, with results shown in Table 3.1.

Table 3.1 Bulk oxide compositions of raw materials.

| | 13Y-WP30 and 13Y-WP50 | | | 1Y-WP30 | |
|---|---|---|---|---|---|
| | **WPC** | **PFA as received** | **PFA demagnetised** | **WPC** | **PFA as received** |
| **$SiO_2$** | 25.00 | 51.05 | 51.80 | 24.81 | 50.41 |
| **$TiO_2$** | 0.08 | 0.98 | 1.00 | - | - |
| **$Al_2O_3$** | 2.14 | 25.97 | 26.14 | 2.35 | 24.10 |
| **$Fe_2O_3$** | 0.36 | 6.78 | 5.93 | 0.49 | 10.63 |
| **$Mn_3O_4$** | 0.02 | 0.06 | 0.06 | - | - |
| **MgO** | 0.78 | 1.59 | 1.59 | 0.80 | 1.60 |
| **CaO** | 71.02 | 1.65 | 1.67 | 70.64 | 3.40 |
| **$Na_2O$** | <0.30 | 1.44 | 1.48 | 0.15 | 0.89 |
| **$K_2O$** | 0.09 | 3.70 | 3.79 | 0.06 | 2.97 |
| **$P_2O_5$** | 0.08 | 0.24 | 0.24 | - | - |
| **$Cr_2O$** | <0.01 | 0.02 | 0.02 | - | - |
| **$SO_3$** | - | - | - | 2.03 | 0.48 |
| **Total** | 99.57 | 93.49 | 93.69 | 101.3 | 94.48 |
| **LOI at 1025 ºC** | 1.06 | 4.16 | 3.40 | <0.01 | |

Table 3.2 Nomenclature of WPC: PFA blended cement paste.

| Sample | Nomenclature |
|---|---|
| 1 year old WPC: 30%PFA | 1Y-WP30 |
| 13 year old WPC: 30%PFA | 13Y-WP30 |
| 13 year old WPC: 50%PFA | 13Y-WP50 |

### 3.1.2 OPC:BFS blended cement paste

The one year old OPC:BFS blended cement paste was cast by the National Nulcear Laboratory (NNL). Three sets of OPC:BFS blended cement paste were made with the OPC:BFS weight ratio of 1:3.44, and they were cured under the condition of water to powder ratio of 0.35 (ml/g), but with different curing temperature, *i.e.* ambient temperature, 35 ºC and 80 ºC. A Hobart mixer was used for the initial mix, and then it was mixed for 15 minutes at 6000 rpm by a Silverson mixer before finally being mixed for 1 hour by the Hobart mixer. The OPC:BFS blended cement paste nomenclature is given in Table 3.3.

Table 3.3 Nomenclature of one year old OPC:BFS blended cement paste cured at different temperature.

| Curing temperature | Nomenclature |
|---|---|
| Ambient temperature | OPC:BFS-AT |
| 35 ºC | OPC:BFS-35 ºC |
| 80 ºC | OPC:BFS-80 ºC |

### 3.1.3 Synthetic C-A-S-H

The synthetic C-A-S-H was provided by EMPA, Switzerland. The materials used to synthesize C-A-S-H are calcium oxide (CaO), silicon oxide ($SiO_2$) and $CaO{\cdot}Al_2O_3$ (CA). CaO was obtained by burning calcium carbonate ($CaCO_3$, Merck, pro analysis) at 1000°C for 12 hours. CA was synthesized from $CaCO_3$ and $Al_2O_3$ (Sigma Aldrich). The homogenized powder mixture was heated for 1 hour at 800°C, 4 hours at 1000°C and 8 hours at 1400°C and cooled with a rate of 600°C/hr. The resulted solid was ground to a powder with Blaine surface area of 3790 $cm^2/g$. The CA contained 99.1% CA and 0.9 % $C_{12}A_7$ as determined by X-ray diffraction and Rietveld refinement analysis with X'Pert HighScore Plus.

C-A-S-H samples were prepared by adding a total of 2 g of CaO, $SiO_2$ (Aerosil 200) and CA to 90 ml of MilliQ water (water/solid = 45). The proportions of CaO, $SiO_2$ and CA were varied to obtain C-A-S-H with bulk Ca/Si ratios of 1.4 and 0.66, and the Al/Si ratio of 0.15. Synthesis and all sample handling were made in a $N_2$ filled glove box to minimize $CO_2$ contamination. The samples were stored in 100 mL PE-HD containers placed on a horizontal shaker moving at 100 rpm and equilibrated at 20 ºC. For each equilibration time a separate sample was prepared. After 6 months of equilibration, the solid and liquid phase were separated by vacuum filtration using 0.45 µm nylon filter and analysed. After filtration, the solid was washed with a 50%-50% water-ethanol solution, afterwards with pure ethanol, dried for seven days by vacuum drying and then stored until analysis in vacuum desiccators.

## 3.2 Leaching experiments

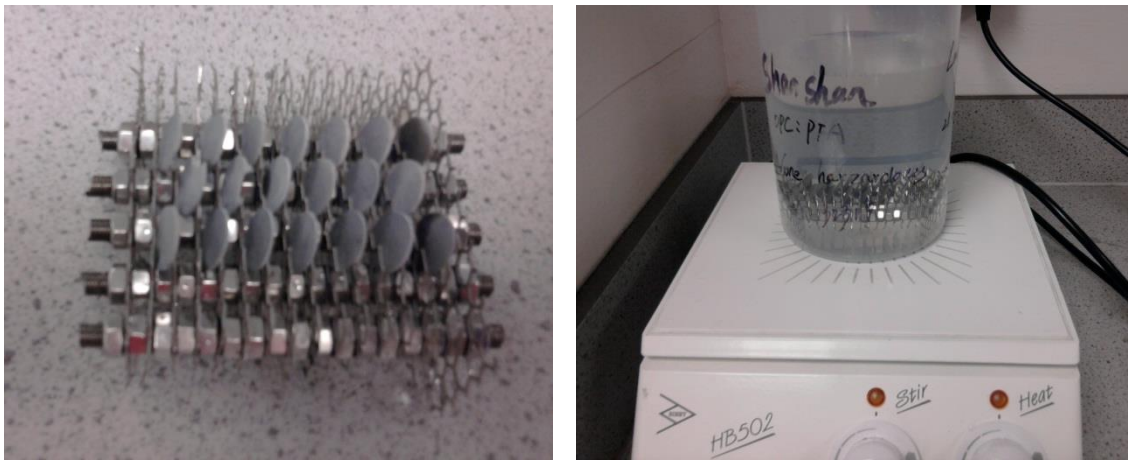


Figure 3.1 The apparatus for leaching experiments.

The 1Y-WP30, 13Y-WP30 and 13Y-WP50 cement paste were used to study the mechanism of the leaching. The paste were cut into 600 μm thick slices with a slow-speed diamond thaw, placed on a stainless steel apparatus as shown in the left image of Figure 3.1, and then submerged into a sealed and continuously stirred (to homogenize the leachate) deionised water bath (liquid/paste mass ratio = 200) as shown in the right image of Figure 3.1, kept at room temperature.

Before leaching, the 1Y-WP30 13Y-WP30 and 13Y-WP50 cement paste were characterized with XRD, thermal analysis, SEM-EDX, TEM-EDX, $^{29}$Si SS MAS NMR and $^{27}$Al SS MAS NMR. The leaching experiments on the 1Y-WP30 13Y-WP30 and 13Y-WP50 took 75 days, 45 days and 55 days, respectively, and the experimental procedure is shown in Figure 3.2. Due to the insufficient amount of 13 years old samples, the leaching experiment performed on those two samples did not take as long as the one year old sample. Every five days, slices were collected to do the characterisation and the leachate was replaced by fresh deionised water each time to force the leaching to carry on. The sample collected was air dried and then characterized with XRD, thermal analysis, SEM-EDX, TEM-EDX, $^{29}$Si SS MAS NMR and $^{27}$Al SS MAS NMR. The results were compared with the results observed in the

cement paste before leaching to study their structure evolutions due to leaching. The superficial degraded layer of the leached sample (in Figure 3.3) was removed before the characterisation, as this layer contacted with the deionized water, and $CaCO_3$ tended to precipitate on this layer observed by XRD.

The alteration in real infrastructure facilities would proceed much more slowly than the alteration in the experiments, but it is assumed that the mechanism involved in the former would be similar to that in the latter (Thomas et al., 2004).

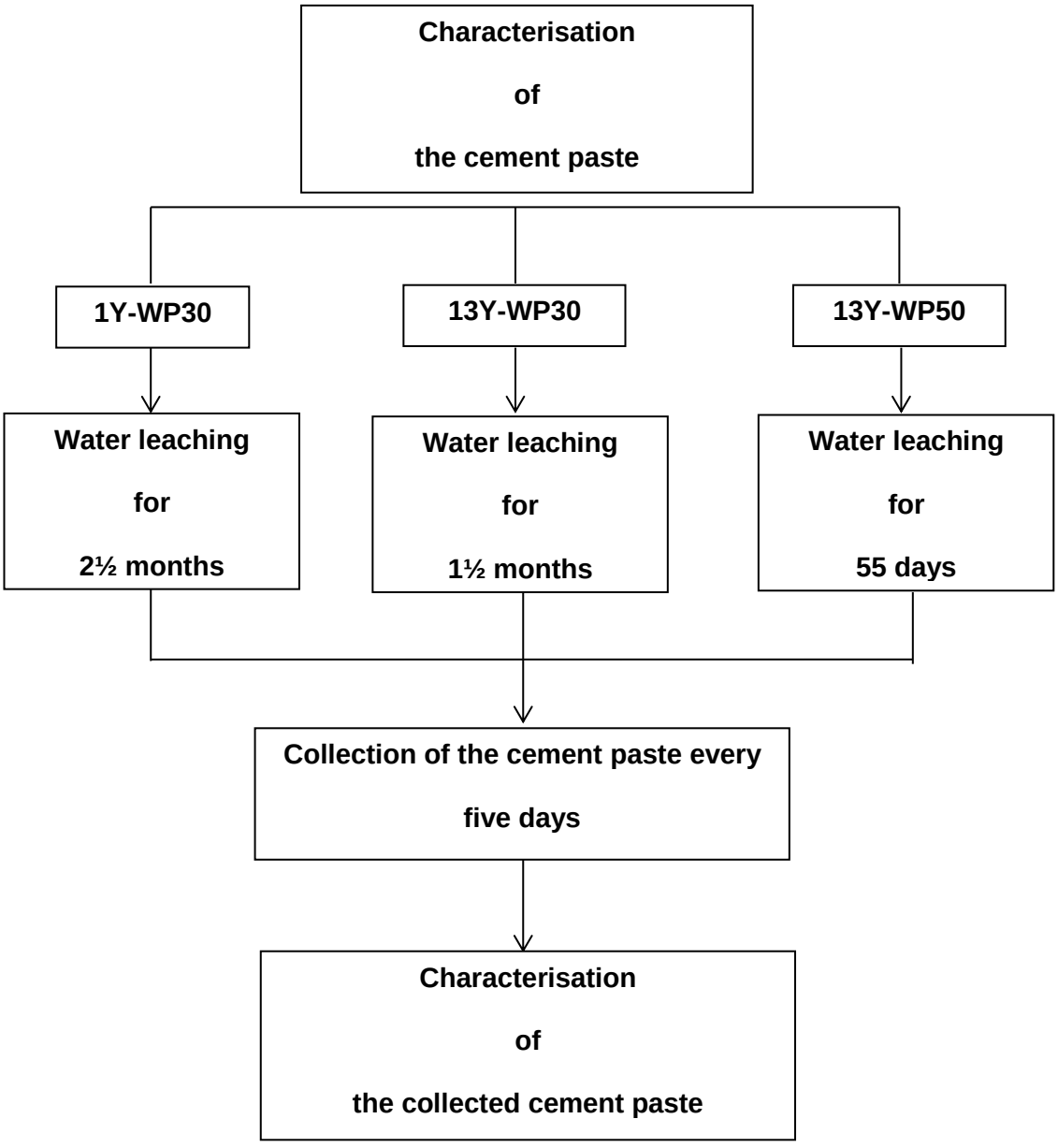


Figure 3.2 Experimental procedures of the leaching process.

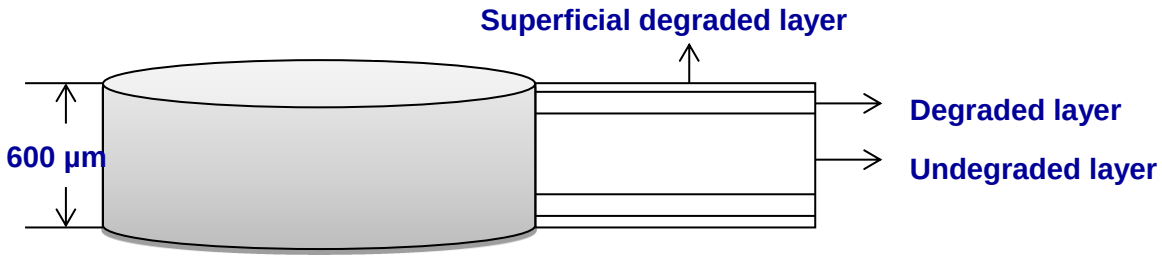


Figure 3.3 The blended cement paste after leaching with a thickness of 600 µm.

## 3.3 Characterization techniques

A range of analytical instruments were used to characterize the WPC:PFA blended cement paste before and after leaching, the OPC:BFS blended cement paste cured at different temperatures, and the synthetic C-A-S-H with different Ca/Si atomic ratio from phase identification and quantification to micro-scale structure and nano-scale structure, and eventually to atomic-scale structure, as shown in Figure 3.4.

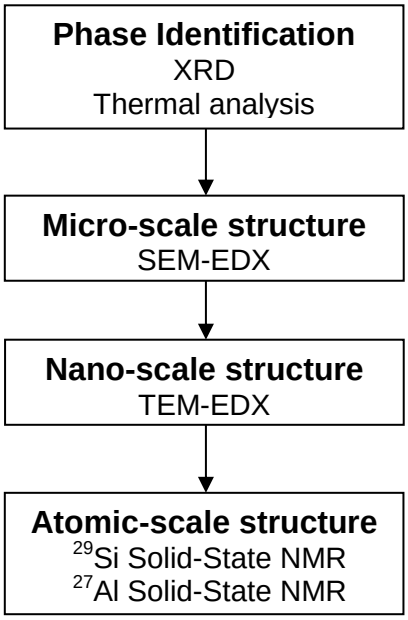


Figure 3.4 Characterisation techniques applied in the study.

### 3.3.1 X-ray diffraction

The XRD measurements were performed on a Panalytical diffractometer system X'PERT-PRO (with X'Celerator real time multiple strip detector), operated with Cu kα

radiation at 40 mA and 45 Kv (W.R.Grace & Co. U.S.A.). Before loading the sample, the paste was cut into slices, crushed and ground into fine powder in an agate mortar/ pestle. The powder sample were mounted on a holder, and then the XRD acquisition was finished on a spinner sample stage running in a continuous scan mode over the range of 5 to 80 º 2θ with a step size of 0.0334 º 2θ and number of steps of 2244, leading the total acquisition time to be 1 hour. The patterns were then analysed with Crystal Diffract software, where the patterns were compared to the reference crystalline patterns.

### 3.3.2 Thermal analysis

Thermal analysis was performance on a Stanton Redcroft STA 1000 (U.K.) equipped with simultaneous thermogravimetric (TG) and differential thermal analysis (DTA). Before loading, the sample was crushed and ground to finer powder in an agate mortar/ pestle. The sample was loaded in a platinum crucible and was heated up to 1000 ºC from 25 ºC with a rate of 20 ºC/min, under a constant flow of nitrogen gas (BOC, U.K.) with a rate of 58 ml/min. The TG curve, where the % weight loss is plotted as a function of a temperature, is used to calculate the amount of CH present in the sample (Girao, 2007).

### 3.3.3 Scanning electron microscopy

The cement paste was cut into thin slices which were then impregnated with Struers epoxy-resin under vacuum. After the resin setting for 1 day, it was demoulded and polished to a flat surface in a Struers mechanical grinding (PdM-Force20 mounted on Rotopol-35) using Struers silicon carbide paper of two different grades, *i.e.* 500 µm and 1200 µm grit. The initial polished samples were finished with diamond paste cloth of 6, 3, 1, and ¼ µm (Struers, U.K.) to obtain a shiny glassy surface. The polished surface was then carbon coated in an EMSCOPE TB500 (U.K.) vacuum coating machine with a thickness of 15 nm to avoid the charging in later SEM examination.

The SEM examination of the WPC:PFA blended cement paste before and after leaching were performed on the Carl Zeiss EVO MA15 variable pressure W SEM with Oxford Instruments INCA EDX system with a 80 mm X-Max SDD detector. The modes used in the study were backscattered imageing, EDX elemental mapping and EDX point analysis. The microscopy was operated at an accelerating voltage of 20 kV, with a working distance of 8 mm and a spot size of 5 nm. The magnification used in the study was ranging from 500 to 2000X. To study the effect of leaching on the micro-scale structure of the 1Y-WP30 cement paste, both the degraded surface and the cross section of the cement paste were characterized by using SEM.

The SEM examination of the OPC:BFS blended cement paste were performed on a Philips XL30 (U.K.) environmental SEM (ESEM). The mode used was backscattering imageing. The microscopy was operated at an accelerating voltage of 20 kV, with 13 mm working distance and a spot size of 5 nm. The magnification used in the study was 500X for taking BSE image.

### 3.3.4 Transmission electron microscopy

The cement paste was cut into thin slices, and then each slice was thinned by hand using the 1200 grit silicon carbide paper to get a flat surface, before being adhered to a glass slide by glue. The sample was continued to be hand polished with the 1200 grit silicon carbide paper as evenly as possible. After a while, it was further polished by using the 2400 grit silicon carbide paper to get an evener and thinner surface until the black ink writing can be read through the sample by naked eyes, and the sample was approximately 30 μm thick. The sample was then soaked to acetone solvent until the glue was dissolved. The next step was to sandwich the thin cement paste with Copper grids using epoxy resin.

Before milling the sample, the sample was checked if there was any hollows and glue in the centre of the sample by using optical microscopy. The checked sample was

milled on a Gatan duomill, with the use of an argon-ion beam. During the milling, the cryocooled stage was used to avoid thermal induced damage. The milling was performed until a visible small hole formed at the centre of the sample, and it took around 10-30 hours depending on the nature of the sample. The sample was taken out until the chamber temperature was warmed up to ambient temperature to reduce the risk of thermal cracking. To reduce the effects of charging on the sample while in the TEM examination, the sample was carbon coated by using an Agar turbo Carbon Coater equipped with an Agar thickness monitor under a high vacuum. The sample was stored in the desiccators to avoid carbonation until the TEM examination.

The powder synthetic C-A-S-H were dispersed in the methanol, and dropped on the shiny side of the carbon film 200 Mesh Cu. Then the specimen was dried on a filter paper. When mounting the specimen to the TEM holder the shiny side was facing down.

The TEM examination of the WPC:PFA blended cement paste and synthetic C-A-S-H sample were performed on FEI Tecnai TF20 TEM equipped with Oxford Instruments INCA EDX system for nano-scale imageing and EDX analysis. To acquire the digital image, different magnifications were used, and the spot size used was 3 nm. Before acquiring each EDX analysis, the area was checked if the C-S-H is mixed with other crystalline phases using selected area diffraction pattern (SAD). The EDX analysis was taken randomly in the thin area of the sample, under the magnification of 17500X and spot size of eight. The analysis area was around 200 nm in diameter.

The TEM examination of the OPC:BFS blended cement paste were performed on a Philips CM200 TEM equipped with Oxford UTW EDX detector (U.K.) and Oxford ISIS software for nano-scale imageing and EDX analysis. The image produced by this equipment was negative film, which was developed and scanned to convert to a digital image. The technique of taking EDX analysis is similar to that in FEI Tecnai TF20 TEM, except the spot size was 6 nm. The EDX data were processed in the ISIS software,

with oxygen calculated by stoichiometry and approximate Cliff Lorimer correction was applied.

### 3.3.5 $^{29}$Si SS MAS NMR

The $^{29}$Si SS MAS NMR measurements of the WPC:PFA blended cement paste and the OPC:BFS blended cement paste were performed on a Varian InfinityPlus 300 MHz, equipped with Chemagnetics style MAS probes (US), and operated at a magnetic field of 7.0 T. Before loading, the paste was ground into fine powder in an agate mortar/ pestle, and then the powder were evenly packed in a 6 mm diameter zirconia rotor sealed with Teflon end caps. The $^{29}$Si SS MAS NMR spectra of the WPC:PFA blended cement paste were acquired using a magic angle spinning speed of 7 kHz, pulse delay of 5 s, pulse width of 5 μs and acquisition time of 2048 ms, with over 10000 scans. The $^{29}$Si SS MAS NMR spectra of the OPC:BFS blended sample were acquired using a magic angle spinning speed of 6 kHz, pulse delay of 9 s, pulse width of 5 μs and acquisition time of 2048 ms, with over 10000 scans.

The $^{29}$Si SS MAS NMR measurements of the synthetic C-A-S-H were performed on a Varian VNMRS spectrometer with a 9.4 T magnet, equipped with 6.0 mm pencil MAS probes, in Durham University. The spectra were acquired using a frequency of 79.435 MHz, magic angle spinning speed of 6800 Hz, spectra width of 40322.6 Hz, pulse duration of 6.2 us, acquisition time of 30.0 ms, recycling time of 120.0 s, with over 1000 scans.

The $^{29}$Si MAS NMR spectra were iteratively fitted using software Wavemetrics Igor Pro 5.0 (US) with additional macros written by Brough (1993) which was modified by the author based on the sample studied.

### 3.3.6 $^{27}$Al SS MAS NMR

The $^{27}$Al SS MAS NMR measurements were performed on a Varian VNMRS spectrometer with a 9.4 T magnet, equipped with 4.0 mm pencil MAS probes, in Durham University. The spectra were acquired using a frequency of 104.198 MHz, magic angle spinning speed of 14,000 Hz, spectra width of 416.7 kHz, pulse duration of 1.0 µs, acquisition time of 10.0 ms, recycling time of 0.2 s, with over 7,000 scans.

# Chapter 4 Characterisation and water leaching on one year old white Portland cement paste blended with 30% pulverised fly ash

## 4.1 Introduction

This chapter presents and discusses the experimental results of the characterisation and leaching on the 1Y-WP30 cement paste. The chapter consists of three sections, each of which is focused on a different aspect of observation:

- Phase identification and quantification studied by XRD and thermal analysis;
- Evolution of structure and chemical composition at micro-scale studied by SEM-EDX;
- Evolution of structure at atomic-scale studied by Solid-state MAS NMR

## 4.2 Bulk analysis-phase identification and quantification studied by XRD and thermal analysis

Figure 4.1 exhibits XRD patterns of the 1Y-WP30 cement paste before and after leaching. Relevant phases are included, and all data are plotted with same intensity scale. In the 1Y-WP30 cement paste before leaching, the main phases identified are C-S-H gel, CH, residual β-belite, ettringite, quartz and mullite. The C-S-H gel, which is generally amorphous, has an abroad reflected peak around 29.5 2θ and a sharper reflected peak around 49.5 2θ (Chatterji, 1997, Xu and Viehland, 1997). Large amount of residual β-belite, which is from anhydrous WPC (Girao et al., 2007a, Girao et al., 2007b), is observed, because the hydration of β-belite is slow and retarded by fly ash (Sakai et al., 2005). Ettringite which is general an early hydration product of aluminates and gypsum (Taylor et al., 1985a), has weak reflected peaks in the patterns. Quartz and mullite, which are the phases from PFA (Gomes and François, 2000, Fernandez-Jimenez and Palomo, 2003), is observed. There is no reflected peak for AFm, however

it is observed from SEM, probably due to the opposite charging between AFm phases and C-S-H, which may produce strong mutual attractions that can physically destroy the AFm crystals, resulting in a poorly crystalline phase which cannot be detected by XRD (Gollop and Taylor, 1994).

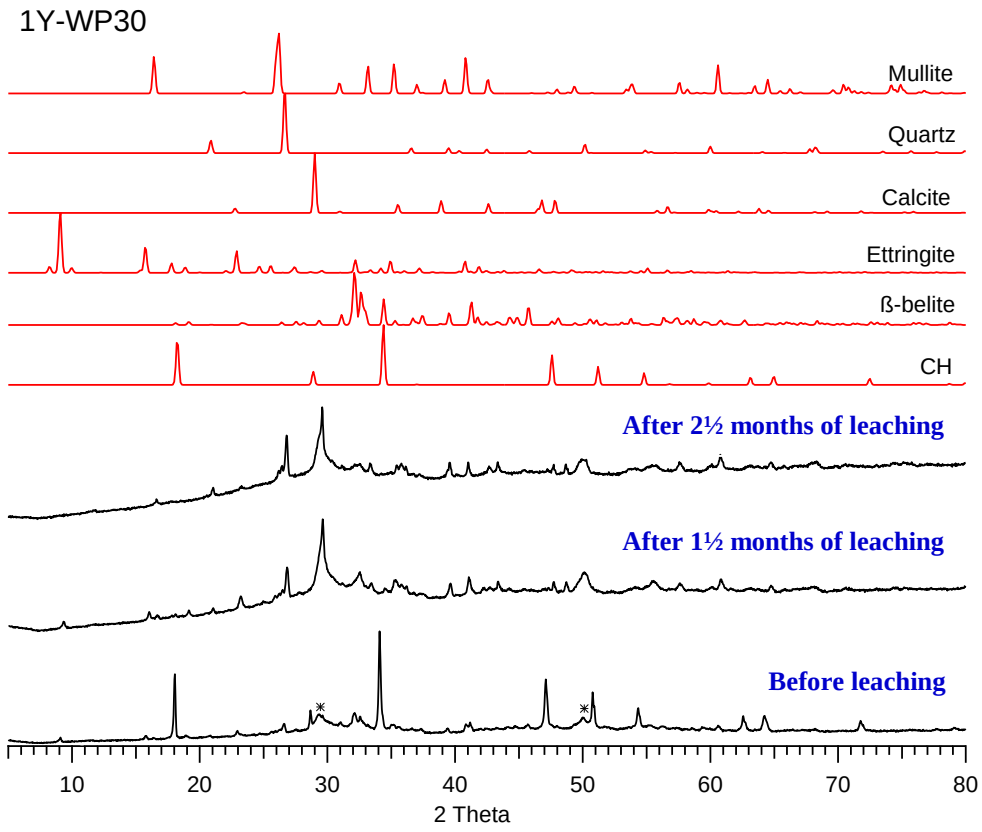


Figure 4.1 XRD patterns of 1Y-WP30 cement paste before leaching, after 1½ months and 2½ months of leaching. (All set to the same intensity scale; the relevant standard phase traces are included and the asterisk labelled peaks are corresponding to the C-S-H gel phase.)

After 1½ months of leaching, the CH has been absolutely dissolved and the content of β-belite has also decreased. CH, as a soluble crystalline, is easily leached from the cement paste. The decrease of β-belite content is due to the increase of water content, inducing the secondary hydration (Haga et al., 2005). On the contrary, the content of ettringite readable increases, which is considered to have been generated near the surface layer of the paste after 1½ months of leaching and is considered to be a secondary mineral (Faucon et al., 1998b), and its formation is confirmed by the NMR.

However, after 2½ months of leaching, the amount of ettringite decreases due to its dissolution nature. Strong reflected peak at 29 2θ is observed in the cement paste after leaching, suggesting that the presence of calcite, and this peak overlaps with the reflected peak from C-S-H gel. It is assumed that calcium ions derived from dissolution of CH is combined with $CO_2$ in the water to form calcite which precipitated on the surface of the paste, although the leaching experiment was performed in a closed environment (Faucon et al., 1998b).

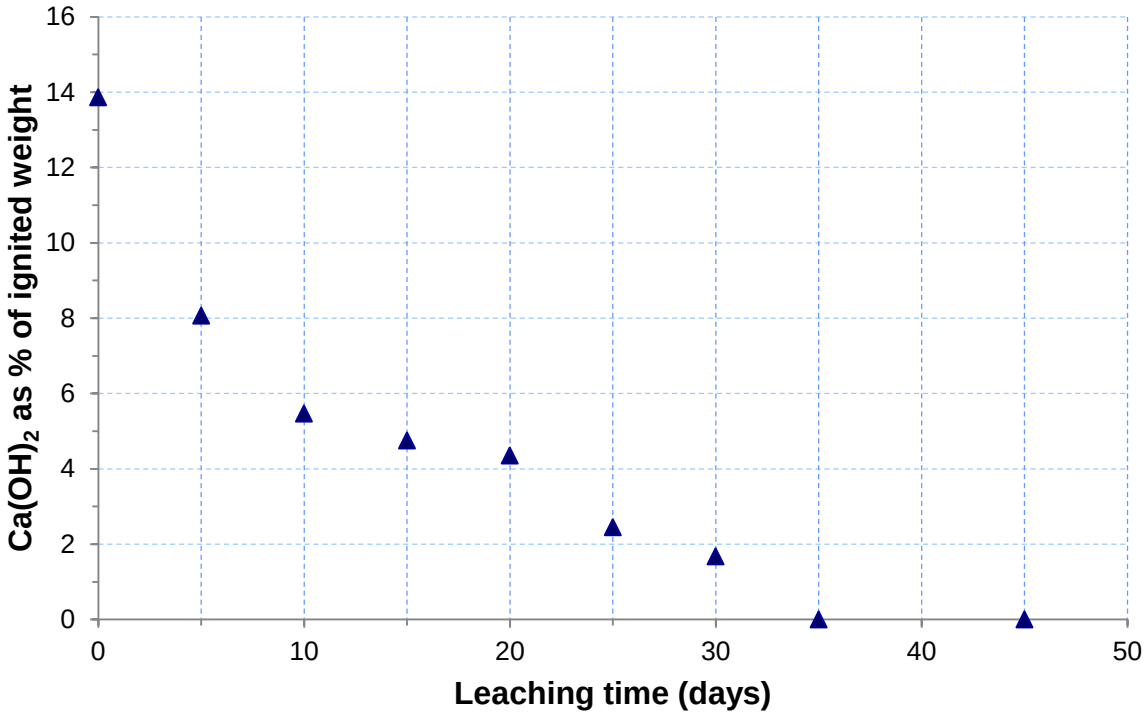


Figure 4.2 $Ca(OH)_2$ evolution during 45 days ( 1½ months) of water leaching in the 1Y-WP30 cement paste.

To characterize the evolution of CH which is the main dissolution phase in the 1Y-WP30 cement paste during the water leaching process, thermal analysis is used to complement the XRD technique. The plot of CH content calculated from the thermal analysis result as a function of leaching time is shown in Figure 4.2, which illustrates that during 45 days of leaching, the content of CH in the 1Y-WP30 cement paste decreased from 14% as percentage of ignited weight to 0. During the first 5 days of

leaching, it dramatically drops 6% due to its easy dissolution nature, and in the next 1 month of water leaching, the CH content gradually decreased, by 35 days, no CH is left, indicating that the CH has already thoroughly been dissolved, which is in agreement with the XRD observation. It is worth noting that during the dissolution of CH due to leaching, the CH may also be consumed by the further pozzolanic reaction, making the accurate interpret of CH dissolution extremely difficult (Girao, 2007).

## 4.3 Evolution of structure and chemical composition at micro-scale studied by SEM-EDX

Two surfaces are investigated by SEM in this study, *i.e.* the degraded surface and the cross section of the cement paste. By investigating the degraded surface, which is the most deteriorated layer in the leached sample as shown in Figure 3.3, the evolutions of the micro-scale structure and chemical compositions at the leaching front can be identified. On the other hand, on the cross section of the leached cement paste, the phase dissolution and precipitation at different fronts can be investigated. Three SEM modes have been used in this study, *i.e.* BSE image, EDX analysis and X-ray element mapping.

### 4.3.1 SEM-EDX analysis of the degraded surface

The BSE image in Figure 4.4 taken at 500 times magnification shows that there are WPC grains, PFA, CH, C-S-H gel and pores in the 1Y-WP30 cement paste before leaching, which is in agreement with Love and Girão's observations (Love, 2002, Girao, 2007). The CH is abundant, which is consistent with the XRD and thermal analysis observations, and anhydrous WPC grains are observed, which are β-belite in the one year old cement paste. The BSE image with 1500 times magnification shows clearer areas of interest, *i.e.* AFm phase, Ip and Op C-S-H. It demonstrates that the Ip C-S-H formed from a fully reacted WPC grain surround with Op C-S-H and large region of CH.

Hexagonal platelets phases are detected, and EDX analysis of these phases are in the direction of AFm phase as shown in the plots in Figure 4.4, although they are not observed by XRD, probably due to their small content or lack of crystallinity. The C-S-H and AFm phases are analysed by EDX, and the data are plotted as $CaO$-$Al_2O_3$-$SiO_2$ ternary diagram, as shown in Figure 4.3. As large volume interaction inherent to this analytical technique, caution should be taken when interpreting the results. Ip and Op C-S-H are not differentiated from the EDX and the corresponding points of analysis are all referenced as C-S-H. Figure 4.3 shows that, in the 1Y-WP30 cement paste before leaching, the points of C-S-H are centred, suggesting the C-S-H is homogeneous. There is no clear trend line in the direction of CH, indicating the CH crystalline is not intermixed with the C-S-H at a micro scale. However, a clear trend line in the direction of AFm phase is observed, suggesting the presence of the AFm phase.

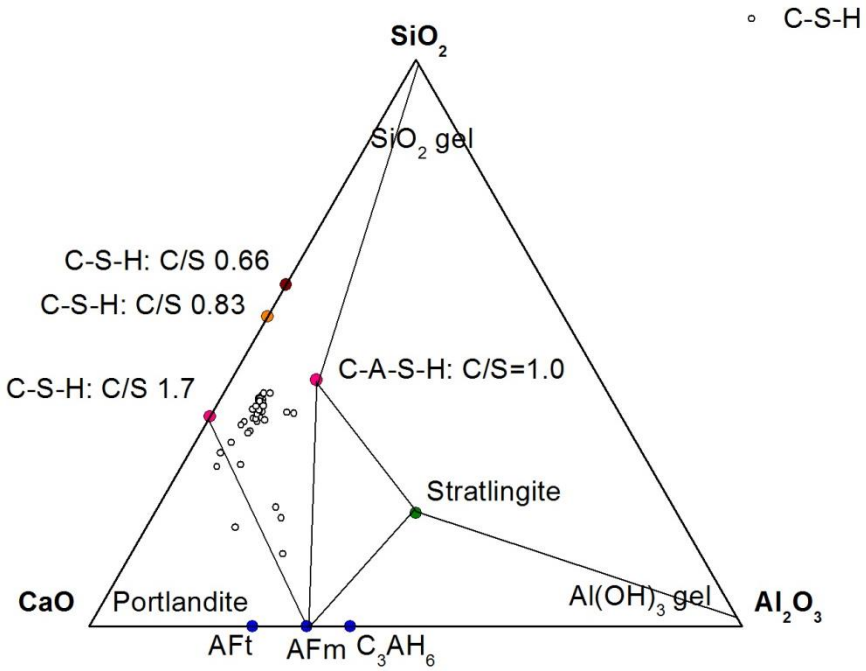


Figure 4.3 $CaO$-$Al_2O_3$-$SiO_2$ ternary diagram for SEM-EDX phase analysis of the 1Y-WP30 cement paste before leaching.

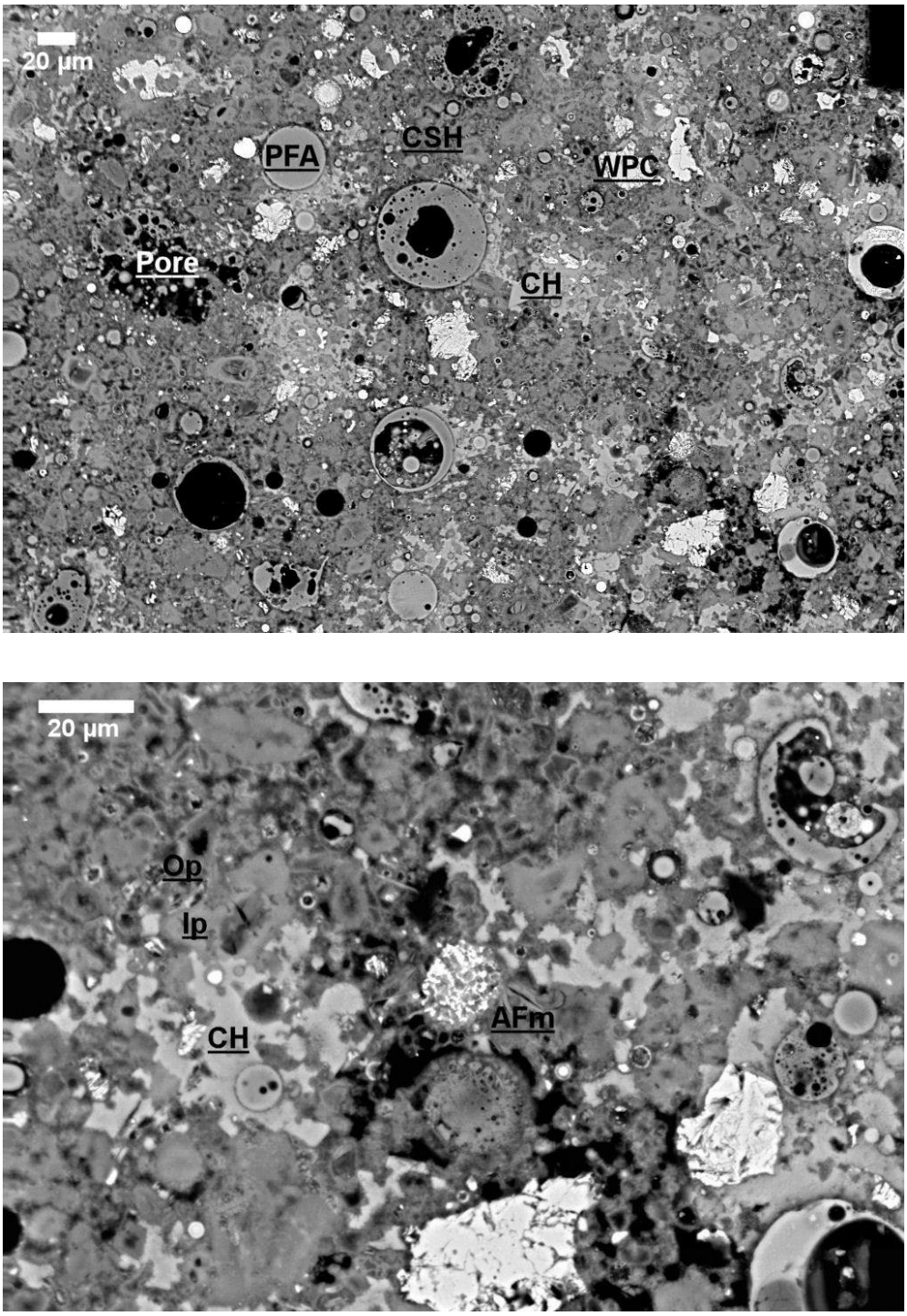


Figure 4.4 BSE images illustrating the microstructure of the 1Y-WP30 cement paste before leaching with 500X (top) and 1500X (bottom) magnification. Regions of pulverised fly ash (PFA), white Portland cement (WPC), calcium hydroxide (CH), C-S-H gel (CSH), inner product C-S-H (Ip), outer product C-S-H (Op), AFm phase (AFm) and pores (Pore) are labelled.

The top BSE image in Figure 4.5 presents the microstructure of the degraded layer of the cement paste after 5 days of leaching. There is visibly less CH comparing to that in the cement paste before leaching, suggesting the CH has been significantly dissolved in the leaching front of the cement paste. There is still abundant anhydrous cement in the cement paste, although more water was added in to induce the further hydration. After 10 days of leaching, there is negligible CH left on the degraded layer of the cement paste, and the microstructure is generally more porous, however, the analysis should be cautiously taken because removed material from the samples whilst polishing, can be easily mistaken for porosity.

Figure 4.6 shows the microstructure of degraded surface of the 1Y-WP30 cement paste after 1½ months of leaching with two magnifications (500 and 1000 times). It illustrates that the CH has been thoroughly dissolved and the WPC has been fully hydrated. The BSE image at higher magnification shows abundant fully hydrated WPC with bright rim as indicated by the black arrows, confirming the further hydration of the cement. The grey-scale contrast between iron rich PFA and C-S-H becomes more obvious, indicating their atomic weight difference becomes larger under the observation of BSE, due to the loss of heavy element Ca from the C-S-H, *i.e.* C-S-H decalcification.

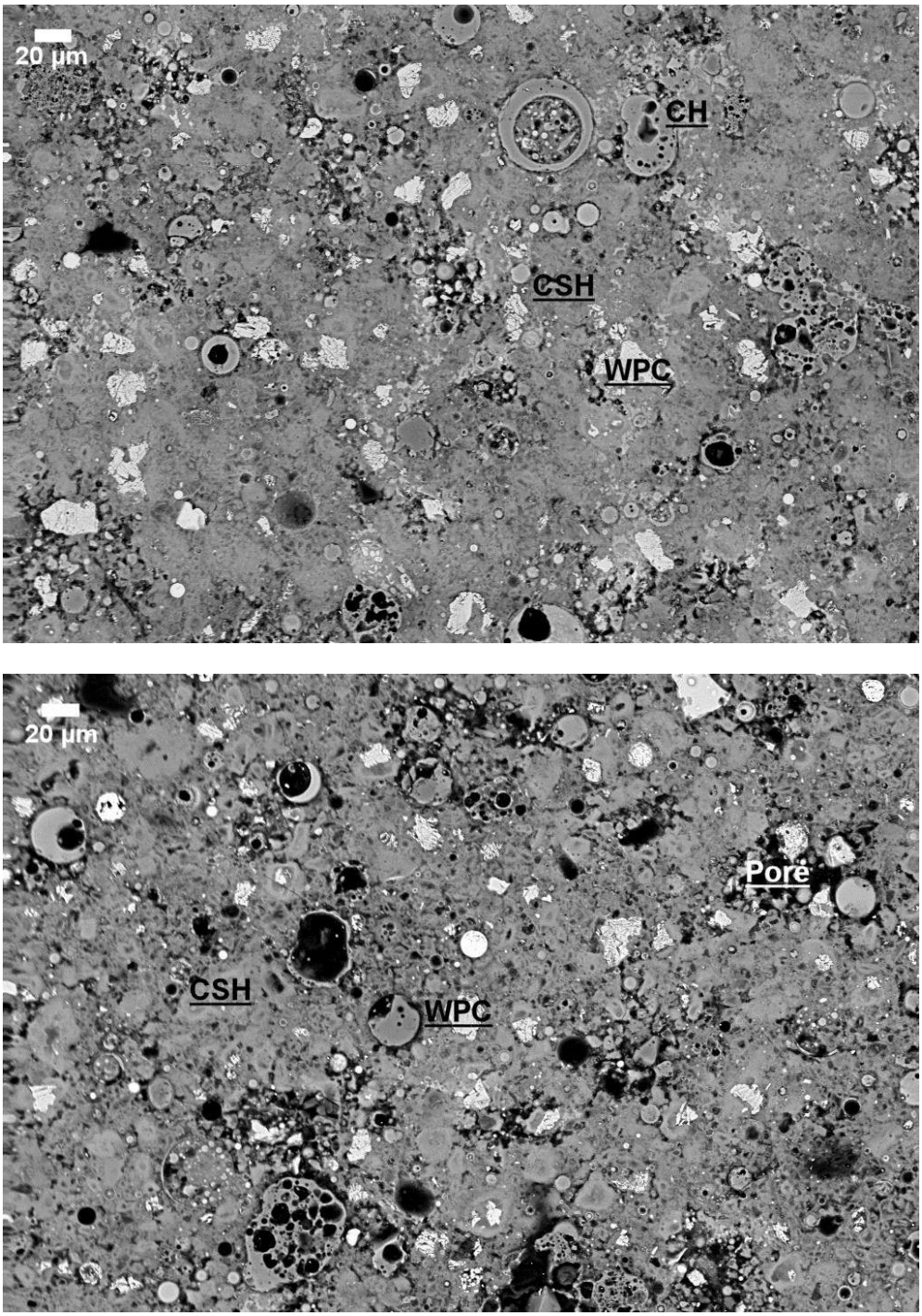


Figure 4.5 Backscattered images illustrate the microstructure of the degraded layer of the 1Y-WP30 cement paste after 5 days (top) and 10 days (bottom) of leaching with 500X magnification. Regions of white Portland cement (WPC), calcium hydroxide (CH) and C-S-H gel (CSH) are labelled.

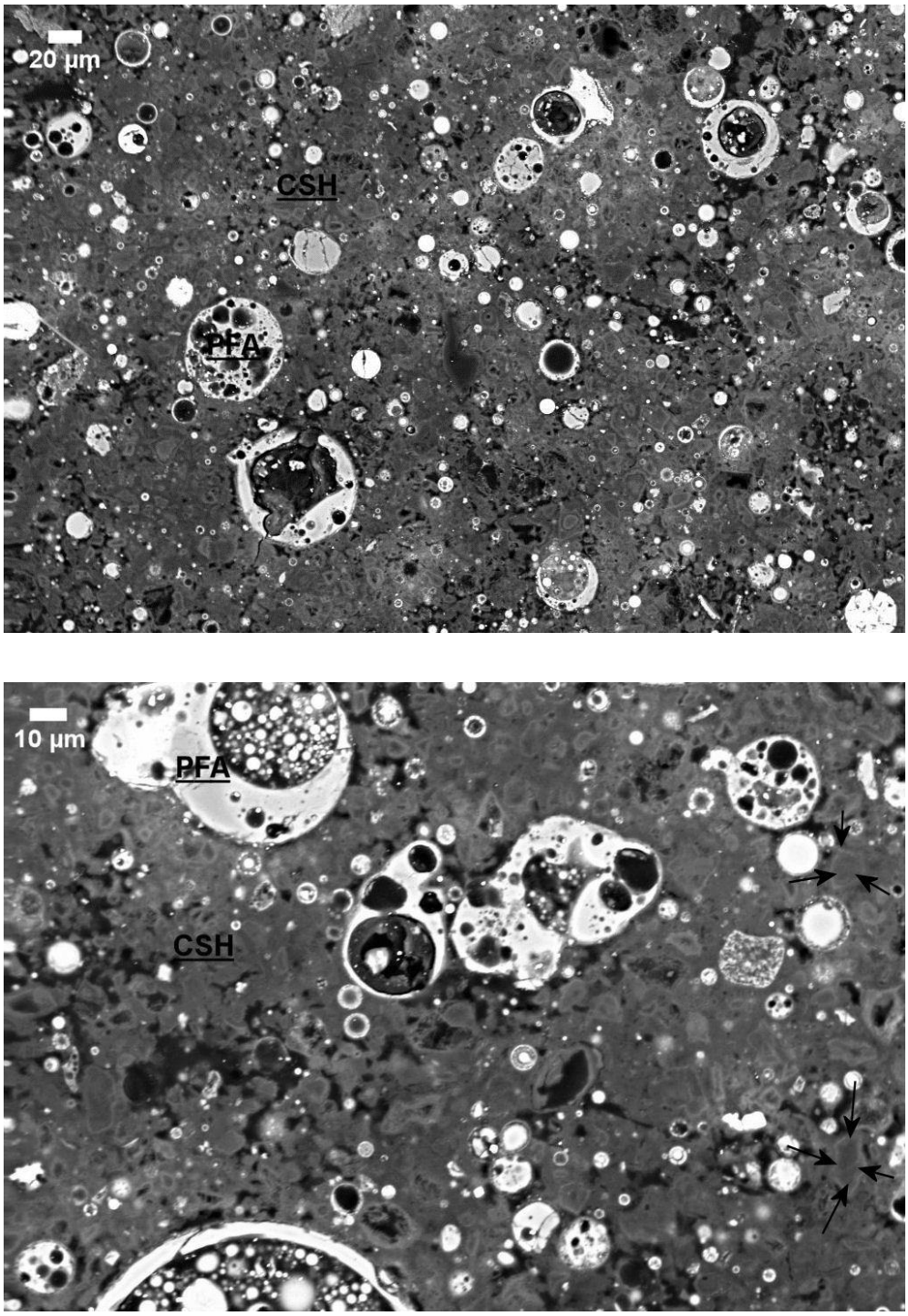


Figure 4.6 Backscattered images illustrate the microstructure of the degraded layer of the 1Y-WP30 cement paste after 1½ months of leaching with 500X (top) and 1000X (bottom) magnification. Regions of pulverised fly ash (PFA) and C-S-H gel (CSH) are labelled. The black arrows indicate the fully reacted WPC that has bright rim.

Figure 4.7 shows the BSE images of the degraded layer of the 1Y-WP30 cement paste after 2½ months of leaching with different magnification. The top BSE image with magnification of 500X demonstrates the general dry cracked land like microstructure of the 1Y-WP30 cement paste after 2½ months of leaching, and large cracks filled with resin are broadly observed. Cracks would largely influence the engineering performance of the cement paste, especially in the application of nuclear waste disposal systems, where the hazards could potentially come out through the large cracks. The bright PFA with higher atomic number are still largely observed, indicating that there are still a large amount of the PFA left in the cement paste, especially the latent iron-rich PFA. The bottom image with magnification of 1000X shows more detail of the microstructure, which presents that the C-S-H is compact and binds the PFA together, although there are cracks all around. It is difficult to distinguish Ip C-S-H and Op C-S-H in the BSE image.

Figure 4.8 shows the $CaO$-$Al_2O_3$-$SiO_2$ ternary diagram for SEM-EDX phase analysis to determine the chemical compositions of C-S-H in the cement paste after 2½ months of leaching. The points become more scatter, indicating the chemical compositions of the C-S-H become less homogeneous after leaching, probably due to the different leaching speeds of the C-S-H with different morphology, and the simultaneous occurrence of decalcification and secondary hydration. The average Ca/Si atomic ratio decreases dramatically comparing to that in the cement paste before leaching, indicating the C-S-H has already been largely decalcified. The decrease of Ca/Si atomic ratio is due to the loss of Ca ions in the interlayer of the C-S-H chain, and the Si ions is considered to be maintained in the cement paste (Chen et al., 2004).

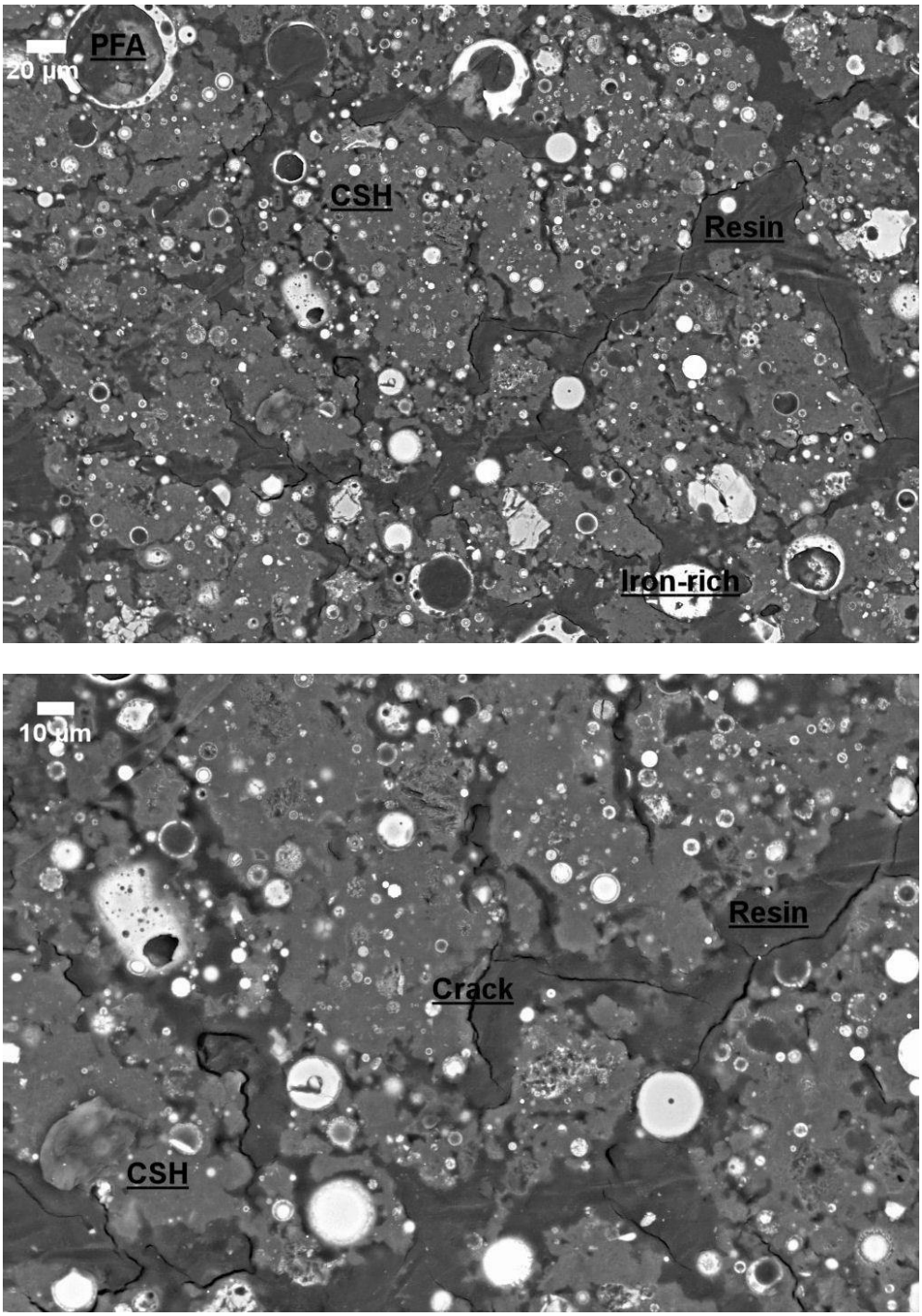


Figure 4.7 Backscattered images illustrate the microstructure of the degraded layer of the 1Y-WP30 cement paste after 2½ months of leaching with 500X (top) and 1000X (bottom) magnification. Regions of pulverised fly ash (PFA), C-S-H gel (CSH), Cracks and Resins are labelled.

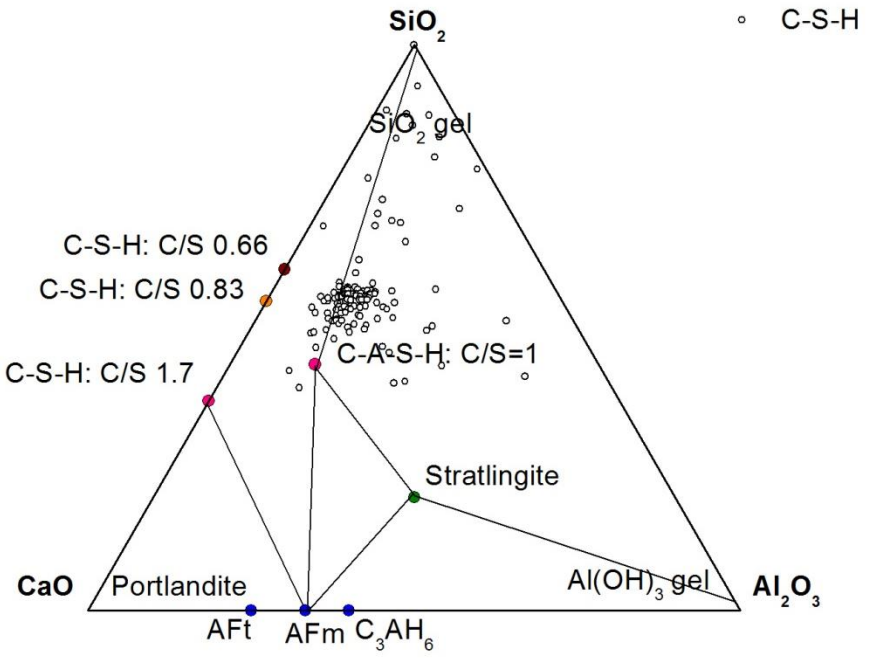


Figure 4.8 $CaO\text{-}Al_2O_3\text{-}SiO_2$ ternary diagram for SEM-EDX phase analysis of the 1Y-WP30 cement paste after 2½ months of leaching.

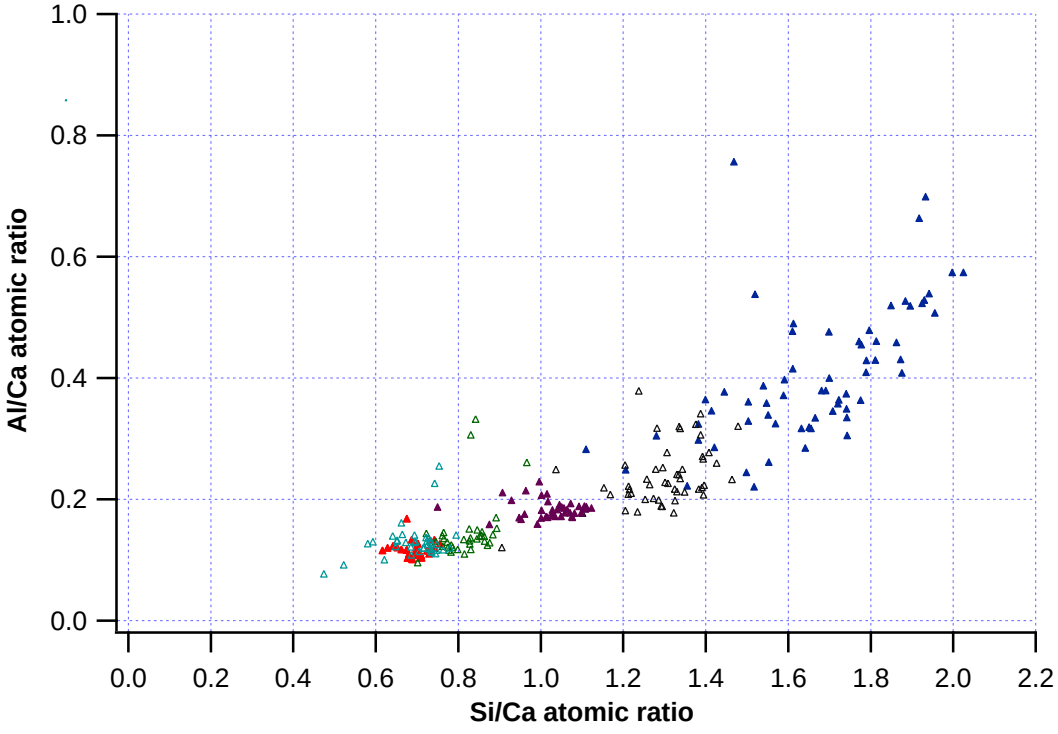


Figure 4.9 Al/Ca against Si/Ca atomic ratio plot for SEM-EDX phase analysis of the C-S-H of 1Y-WP30 before leaching (Δ), after 5 days (▲), 15 days (Δ), 35 days (▲), 45 days (Δ) and 75 days (▲) of leaching.

Figure 4.9 shows the Al/Ca against Si/Ca atomic ratio plot for SEM-EDX phase analysis of the C-S-H of 1Y-WP30 before leaching and at different leaching times. It shows that, as leaching proceeds, the Si/Ca atomic ratio of C-S-H gradually increases and the analysis points becomes more scattered, indicating that the Ca/Si atomic ratio gradually decreases and the chemical composition becomes more inhomogeneous.

Figure 4.10 presents the Ca/Si and Al/Si atomic ratio of the C-S-H from the degraded layer of 1Y-WP30 cement paste during 2½ months of leaching. It shows that, in the cement paste before leaching, the average Ca/Si atomic ratio is 1.42 ± 0.07 (n=32) and the average Al/Si atomic ratio is 0.18 ± 0.04 (n=32). During the first 10 days of leaching, the Ca/Si ratio is not statistically different, whilst the CH content in the cement paste decreases dramatically as observed by thermal analysis, indicating that the CH dissolution occurs before the C-S-H decalcification. After ½ month of leaching, the Ca/Si atomic ratio gradually decreases, and after 55 days of leaching, it has already decreased to 0.65 ± 0.06 (n=41). Afterwards the Ca/Si atomic ratio does not change significantly any more, and after 2½ months of leaching, then it becomes 0.62 ± 0.07 (n=64), suggesting that the C-S-H decalcification has approached equilibrium. The Ca/Si atomic ratio of the C-S-H after 2½ months of leaching is near that of the 1.4 nm tobermorite with all the Si-O•••Ca protonated (Cong and Kirkpatrick, 1996b). Unlike the dissolution of CH, which dissolves to $Ca^{2+}$ ions and $OH^-$ ions, the C-S-H decalcification is much more complicated, because the Ca ions are dissolved from the interlayer of the C-S-H chain, and after a long term of decalcification, there is still a certain amount of Ca ions left in the CaO sub-layer in the C-S-H. The Al/Si atomic ratio is not statistically different during the first 45 days of leaching. However, it gradually increases after 45 days of leaching, and it goes up to 0.23 after 65 days of leaching and becomes constant afterwards. The increase of the Al/Si atomic ratio suggests that more Al substituting Si in the C-S-H chain.

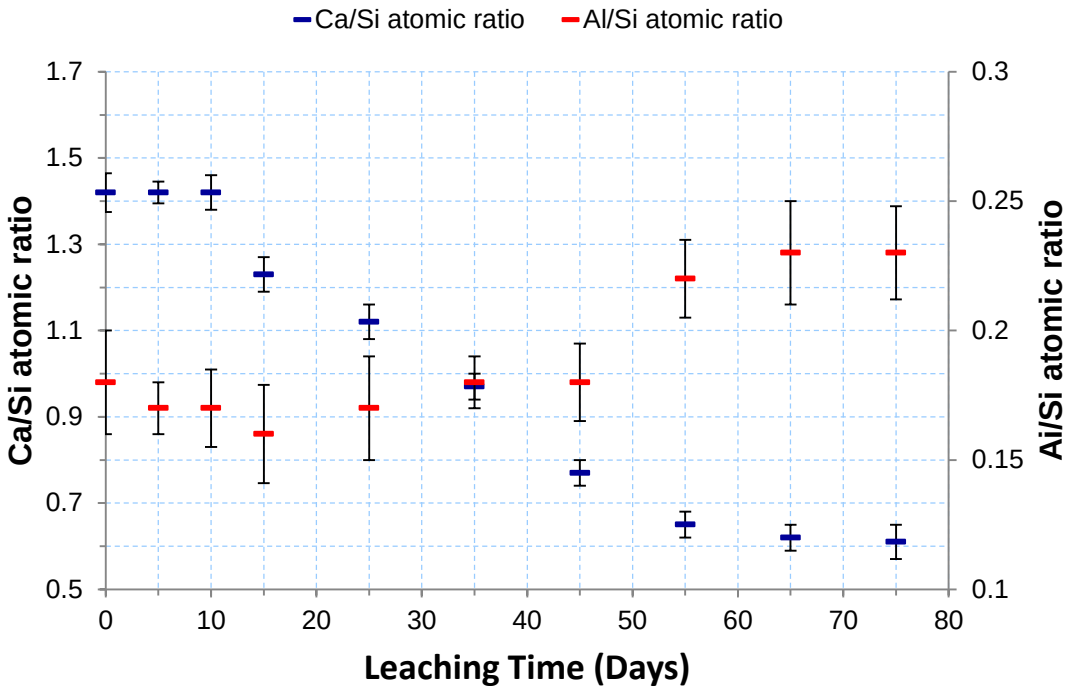


Figure 4.10 Average Ca/Si and Al/Si atomic ratio (with error bar, the C-S-H phase intermixed with other phases are excluded when calculating error bar) observed by SEM-EDX phase analysis of C-S-H as a function of leaching time during 2½ months of leaching.

### 4.3.2 SEM-EDX analysis of the cross section

The cross section specimen is prepared by cutting perpendicular to the degraded surface and then it is analysed by SEM-EDX to study the phases dissolution and precipitation at different leaching fronts (Scrivener, 2004). Three SEM modes are used, *i.e.* BSE image, EDX point analysis and X-ray mapping. The BSE image presents the phase distribution, the EDX data are plotted as Ca/Si atomic ratio against leaching depth, and finally the X-ray mapping is used to show the main ions, *i.e.* Ca, Si and Al ions distribution along the cross section of the cement paste before leaching and after various leaching periods. The CH profile along the cross section is obtained by using image software to pick up the grey-scale belong to CH in the BSE image.

Figure 4.11 shows the BSE image, the profile of CH dissolution, the profile of C-S-H decalcification and main elements mapping (Ca, Si and Al) along the cross section of

1Y-WP30 cement paste before leaching. The BSE image exhibits the phase distribution and the main phases observed are CH, C-S-H, WPC and pores which are all evenly distributed along the cross section, and they are exact the same as the phases observed on the surface layer in the cement paste before leaching as mentioned in section 4.3.1. A processed BSE image is shown in Figure 4.11(b) in which the CH is found evenly distributed along the cross section. Figure 4.11(c) presents the Ca/Si atomic ratio of C-S-H against the leaching depth in the cement paste before leaching. It is shown that the C-S-H is homogeneous and the Ca/Si atomic ratio is around 1.4 along the cross section. The X-ray element mapping crossing the cement paste isshown in Figure 4.11(d) to get the information of the distribution of main ions along the cross section of the blended cement paste, especially, the distribution of Ca ions which mainly exist in the phases of WPC, CH and C-S-H. It is difficult to distinguish CH and anhydrous cements solely from the mapping images, thus they are analysed in conjunction with the BSE images.

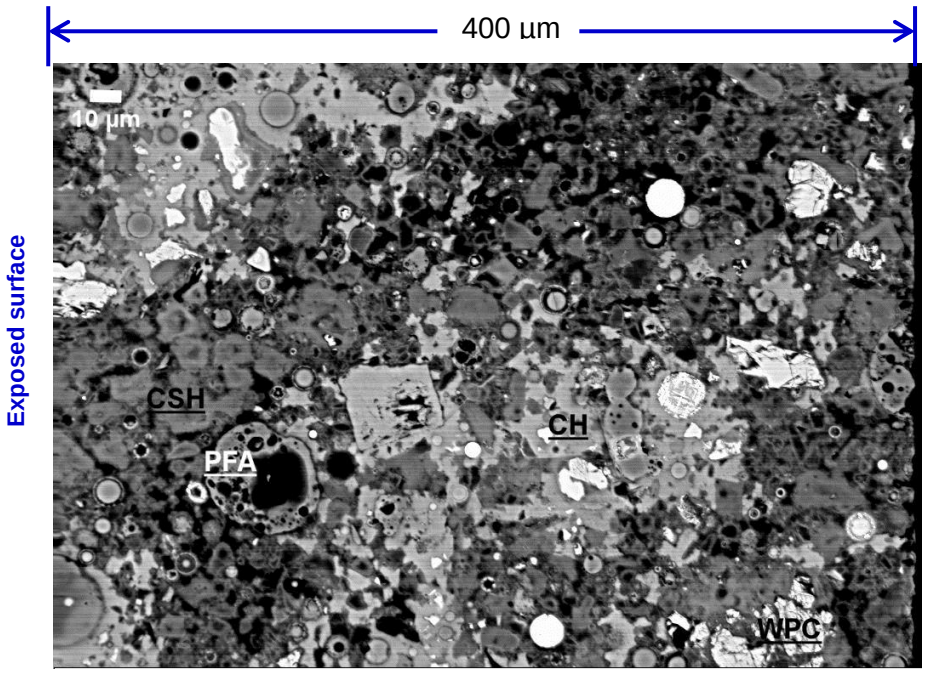


(a) BSE image

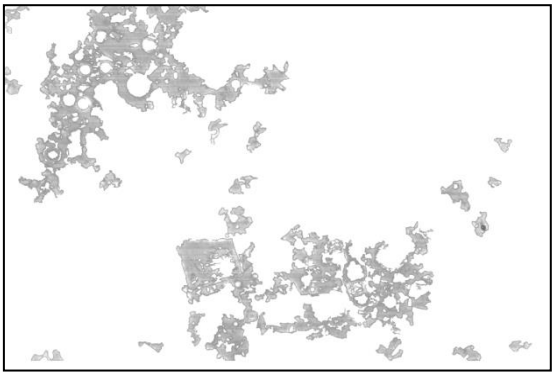

(b) CH dissolution profile

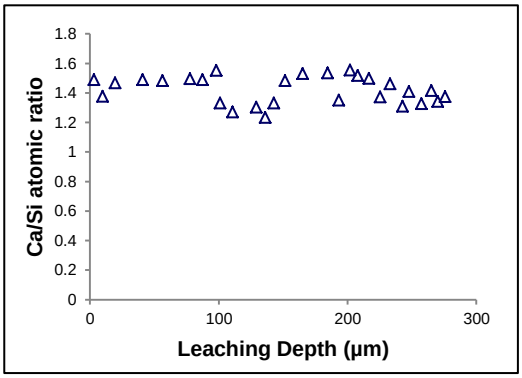


(c) C-S-H decalcification profile

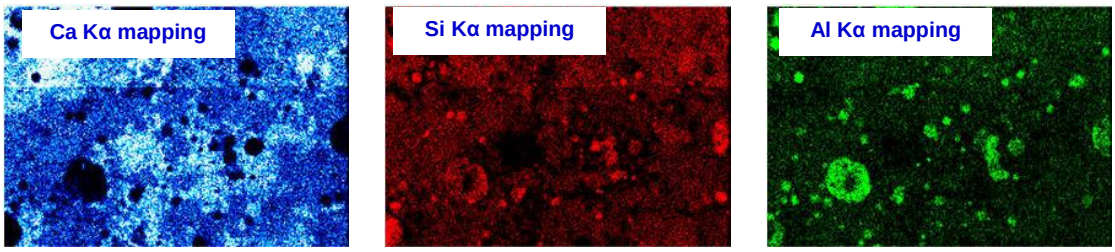


(d) Element X-ray mapping

Figure 4.11 SEM-EDX analysis results of cross-section of 1Y-WP30 cement paste before leaching: (a) BSE image with 1000X magnification; (b) CH dissolution profile analysed with BSE image; (c) C-S-H decalcification profile plotted with SEM-EDX analysis of C-S-H; and (d) X-ray element mappings (including element Ca, Si and Al). Regions of pulverised fly ash (PFA), white Portland cement (WPC), pulverised fly ash (PFA) and C-S-H gel (CSH) are labelled.

Figure 4.12 presents the cross section of the cement paste after ½ month of water leaching. It shows that near the degraded surface, the CH has already disappeared due to its easily dissolving nature, and abundant of fully hydrated cement grains are observed because of the secondary hydration. The porosity near the degraded surface increases significantly. However, the microstructure of the inner core of the cross section maintains the same as that in the cement paste before leaching, suggesting that the degradation initiates from the surface layer towards the inner core. Since it is difficult to identify the CH from the BSE image, image software Photoshop is employed to pick up the specific grey-scale for CH from the BSE image and to produce the profile of CH dissolution, as shown in Figure 4.12 (b). It demonstrates that the CH dissolution depth is roughly about 200 μm. The thickness of the cement paste is 600 μm, and the CH dissolution occurs from both sides of exposed surface spontaneously, so the total CH dissolution depth is approximately 400 μm, which means 66.7% of CH has already been dissolved. This is in consistence with the thermal analysis observation that 66.1% of CH is dissolved after ½ month of leaching as mentioned in section 4.2. From the EDX analysis of C-S-H phase along the cross section of ½ month leached cement paste, the Ca/Si atomic ratio in the C-S-H near the exposed surface decrease to 1.0. The decalcification depth is 150 μm which is shallower than the CH dissolution depth, indicating that the C-S-H decalcification takes place after the CH dissolution. The Ca/Si atomic ratio in the C-S-H in the inner core of the leached cement paste remains 1.4. The element mappings in Figure 4.12 (d) present the distribution of the main elements Ca, Si and Al along the cross section. It shows that near the exposed surface the Ca ions, which are mainly from CH and C-S-H, are dissolved significantly due to CH dissolution and C-S-H decalcification. However, the Al and Si ions, which are mainly from the PFA and C-S-H, are still evenly distributed along the cross section of the leached cement paste, suggesting the Al and Si ions are not dissolved like Ca ions.

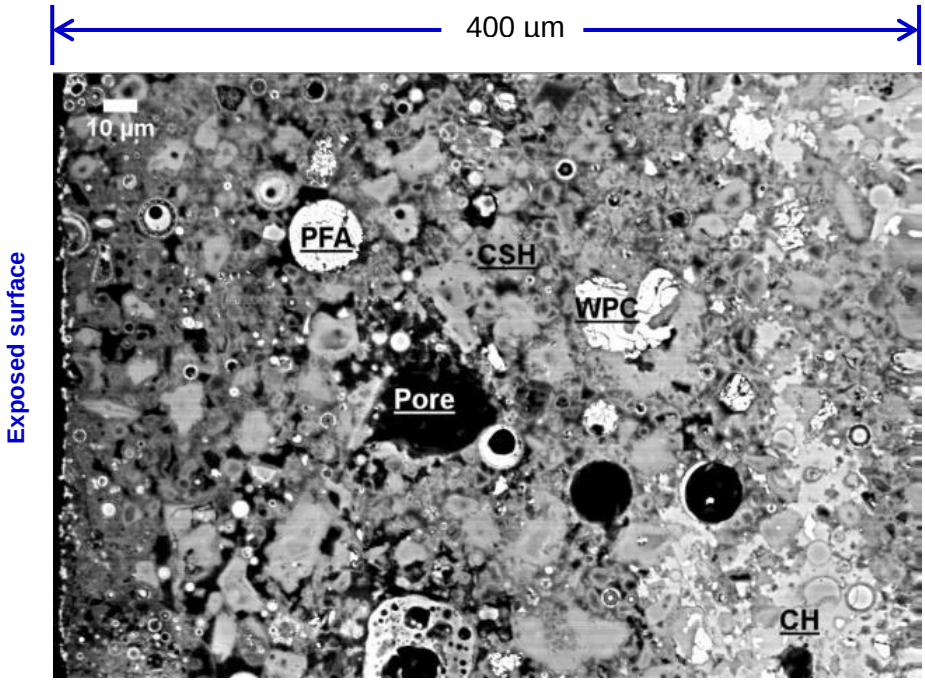


(a) BSE image

(b) CH dissolution profile

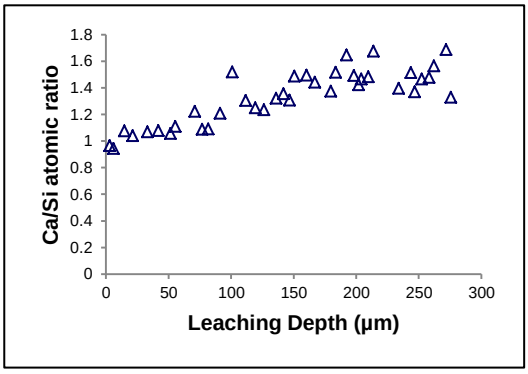


(c) C-S-H decalcification profile

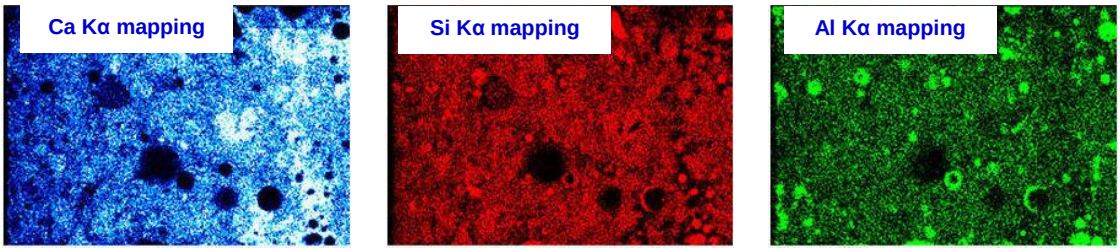


(d) Element X-ray mapping

Figure 4.12 SEM-EDX analysis results of cross-section of 1Y-WP30 cement paste after ½ month of leaching: (a) BSE image with 1000X magnification; (b) CH dissolution profile analysed with BSE image; (c) C-S-H decalcification profile plotted with SEM-EDX analysis of C-S-H; and (d) X-ray element mappings (including element Ca, Si and Al). Regions of pulverised fly ash (PFA), white Portland cement (WPC), pulverised fly ash (PFA) and C-S-H gel (CSH) are labelled.

As shown in Figure 4.13 (a) and (b), after 1½ months of leaching, CH is no longer detected, which agrees with the thermal analysis and XRD observations. On the other hand, from Figure 4.13 (a) abundant of fully hydrated cement grains are observed along the cross section of the cement paste due to the secondary hydration. In addition, the BSE image shows that the C-S-H near the degraded surface has a darker grey scale than that near the centre, indicating the loss of heavy element Ca ions near the degraded surface due to the decalcification of C-S-H. From the EDX analysis of C-S-H along the cross section (see Figure 4.13 (c)), it's found that the Ca/Si atomic ratio in the C-S-H near the degraded surface has further decreased to 0.8 and decalcification depth has increased to 240.5 μm, suggesting that as leaching proceeds, the C-S-H is gradually decalcified toward inner core. However, the Ca/Si atomic ratio of the C-S-H at the inner core of the cement paste still maintains 1.4 after 1½ months of leaching. From the analysis of the X-ray element mapping in Figure 4.13 (d), it is obvious that CH is completely removed and WPC is thoroughly secondary hydrated as no abundance Ca clots are identified. Meanwhile, the Ca ions near the inner core of the cross section are more abundant than they are on the degraded surface, confirming that the C-S-H decalcification occurred from the surface to the inner core.

Figure 4.14 shows that, after 2½ months of intensive water leaching, the overall microstructure along the cross section becomes even again, although the paste near the degraded surface is still slightly more porous than the inner core. The BSE image shows that the anhydrous cements have thoroughly hydrated. The Ca/Si atomic ratio in the C-S-H has ultimately decreased to 0.6, and it is evenly distributed along the cross section of the cement paste, suggesting the cement paste is chemical homogeneous. The X-ray element mappings show that the Ca ions are evenly distributed along the cross section of the cement paste indicating that all the C-S-H has similar Ca/Si atomic ratios. During the leaching process, other elements, i.e. Al and Si, do not have distinct transformation.

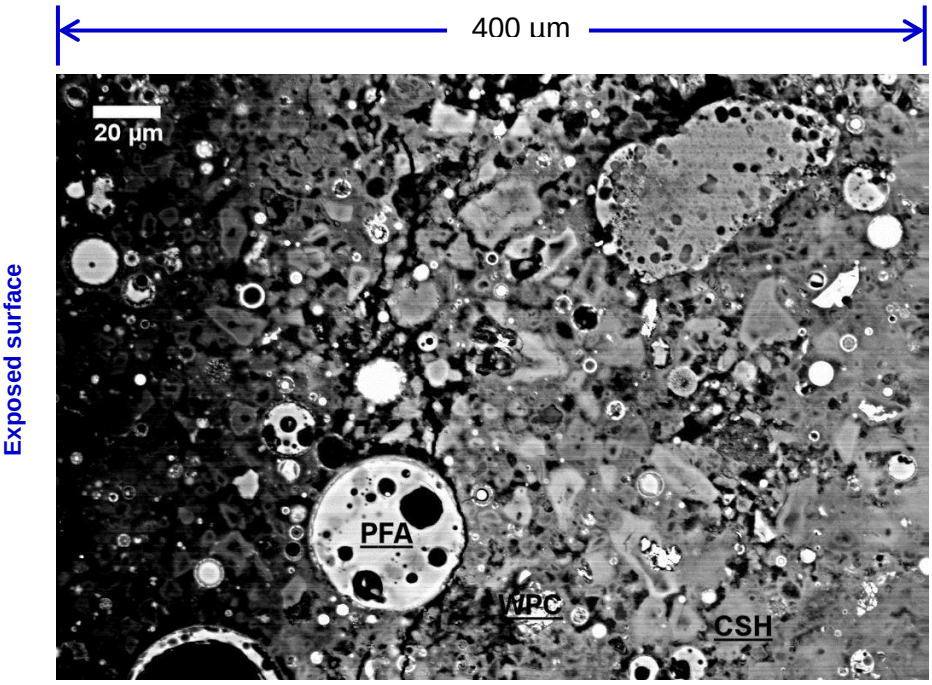


(a) BSE image

No CH phase left after 1½ months of leaching

(b) CH dissolution profile

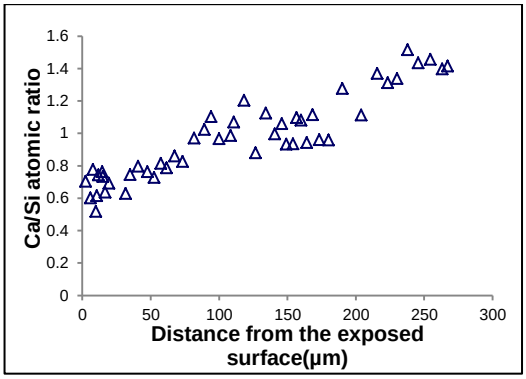


(c) C-S-H decalcification profile

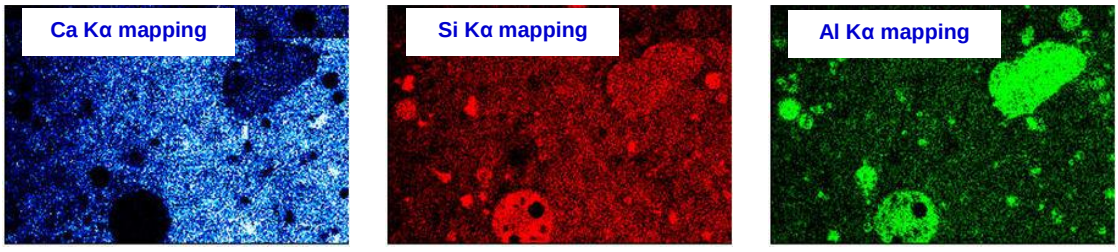


(d) Element X-ray mapping

Figure 4.13 SEM-EDX analysis results of cross-section of 1Y-WP30 cement paste after 1½ month of leaching: (a) BSE image with 1000X magnification; (b) CH dissolution profile analysed with BSE image; (c) C-S-H decalcification profile plotted with SEM-EDX analysis of C-S-H; and (d) X-ray element mappings (including element Ca, Si and Al). Regions of pulverised fly ash (PFA), white Portland cement (WPC), pulverised fly ash (PFA) and C-S-H gel (CSH) are labelled.

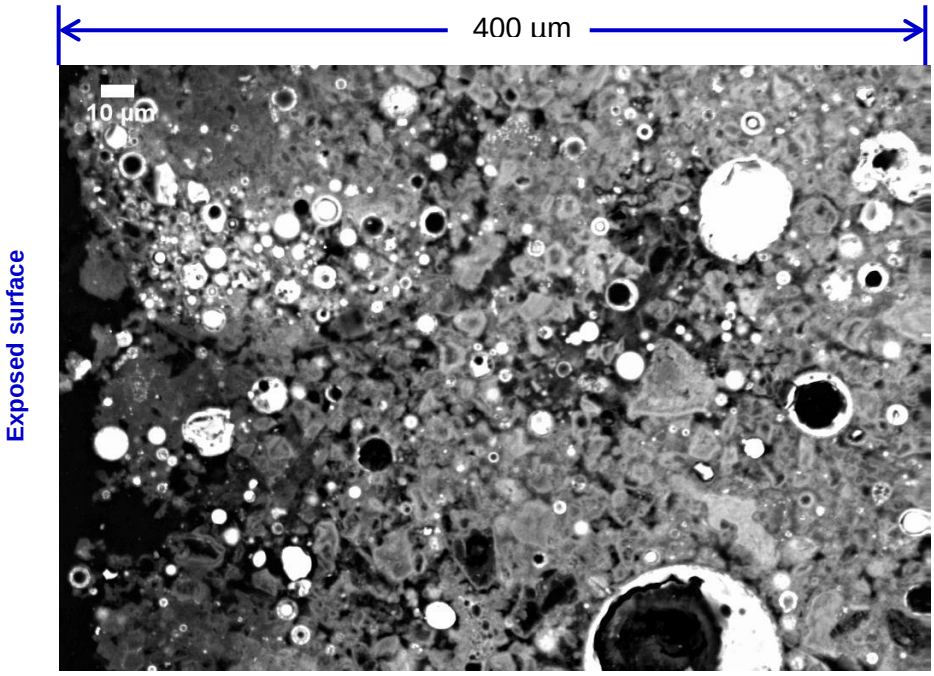


**(a) BSE image**

No CH phase left after 2½ months of leaching

**(b) CH dissolution profile**

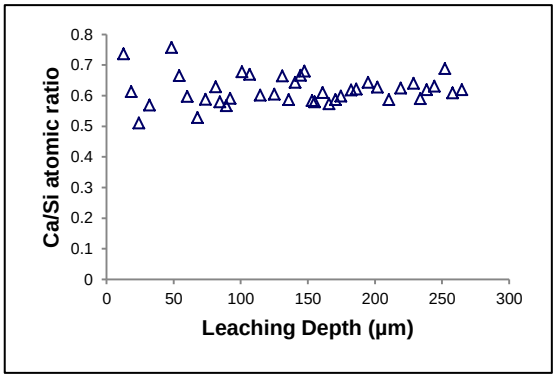


**(c) C-S-H decalcification profile**

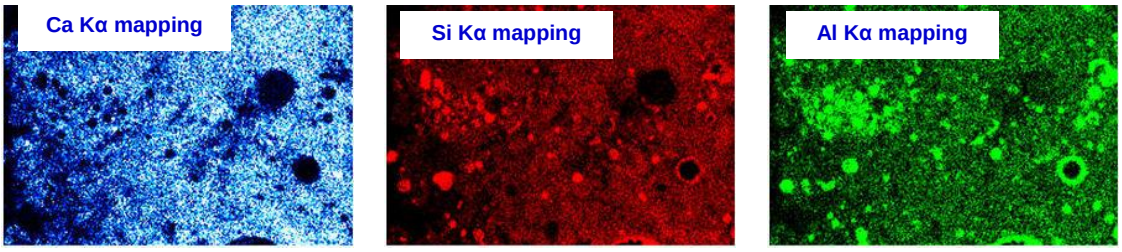


**(d) Element X-ray mapping**

Figure 4.14 SEM-EDX analysis results of cross-section of 1Y-WP30 cement paste after 2½ month of leaching: (a) BSE image with 1000X magnification; (b) CH dissolution profile analysed with BSE image; (c) C-S-H decalcification profile plotted with SEM-EDX analysis of C-S-H; and (d) X-ray element mappings (including element Ca, Si and Al). Regions of pulverised fly ash (PFA), white Portland cement (WPC), pulverised fly ash (PFA) and C-S-H gel (CSH) are labelled.

Investigation of the dissolution of Ca ions before and during leaching requires collective information from the BSE images, X-ray mapping as well as EDX analysis. More specifically, the CH dissolution depth is characterised by the Ca X-ray mapping in conjunction with the BSE image, and the C-S-H decalcification depth is observed by using the EDX analysis. Figure 4.15 shows the depth of the CH dissolution and the C-S-H decalcification in the cement paste at different leaching time. It is illustrated that after ½ month of leaching, the CH dissolution depth is 50 µm deeper than the C-S-H decalcification depth, confirming that the CH dissolution occurs before the C-S-H decalcification. After 1½ months of leaching, the CH has thoroughly dissolved, but some un-decalcified C-S-H still remains in the inner core of the cement paste. After 2½ months of leaching, the decalcification of C-S-H has already reached the inner core of the cement paste.

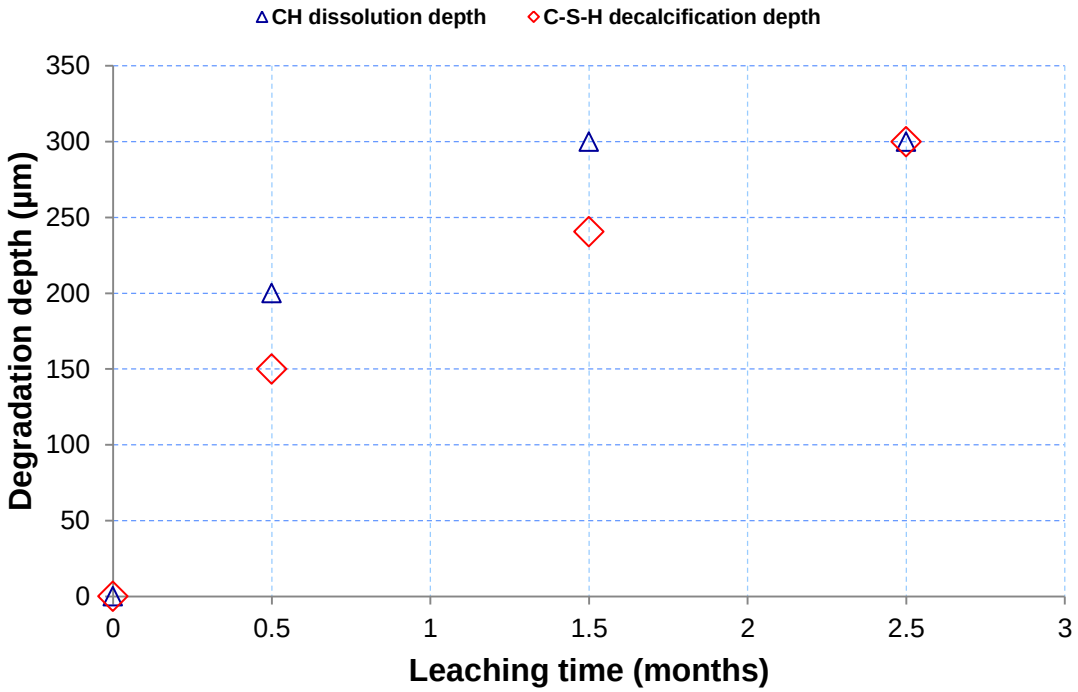


Figure 4.15 CH dissolution depth and C-S-H decalcification depth on cross section of 1Y-WP30 cement paste at different leaching time observed by SEM.

## 4.4 Evolution of structure at atomic-scale studied by Solid-state MAS NMR

Solid-state MAS NMR spectroscopy is used to characterize the evolution of the chemical environment of Al and Si at atomic-scale in the 1Y-WP30 cement paste during the water leaching.

### 4.4.1 $^{29}$Si solid state MAS NMR spectra

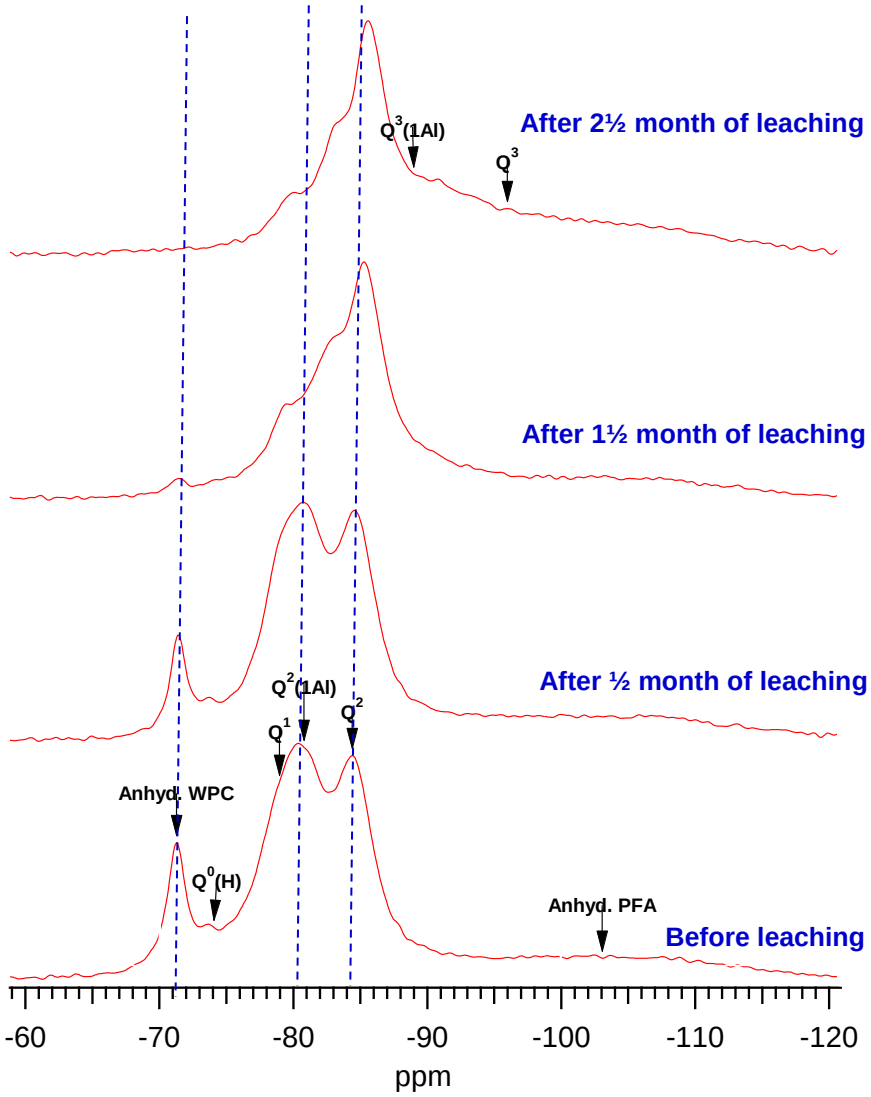


Figure 4.16 $^{29}$Si solid state MAS NMR spectra for the 1Y-WP30 cement paste before leaching and at various leaching time.

$^{29}$Si SS MAS NMR spectroscopy is used to determine the silicate anion structure present in anhydrous WPC, C-S-H and anhydrous PFA. Figure 4.16 presents the original spectra of the 1Y-WP30 cement paste before leaching and at various leaching time. In the spectrum for the cement paste before leaching, there is a sharp peak around -71.3 ppm, which is assigned to the resonance for the anhydrous WPC (Girao et al., 2007b), and a small broad peak at around -73.5 ppm, which is assigned to $Q^0$(H) (Brough et al., 1994). Three main peaks (from -75 to -85 ppm) are assigned to the silicate anion structure present in the C-S-H, *i.e.* $Q^1$ (end chain groups or dimer), $Q^2$ (chain middle groups), and $Q^2$(1Al) (chain middle groups with one neighbouring Si substituted by Al), which are resonated at -79 ppm, -80.7 ppm and -81.5 ppm, respectively. Finally, the broad peak at -103 ppm corresponds to silicon present in the anhydrous PFA.

From the analysis of the 1Y-WP30 cement paste after ½ month of leaching, the spectrum does not change significantly compared to that from the cement paste before leaching, except the intensity of the $Q^0$ decreases as a result of the secondary hydration of the anhydrous WPC cement. This suggests that the aluminosilicate anion of C-S-H has not changed yet. However, after 1½ months of leaching, the spectrum has significantly changed which indicates that the aluminosilicate anion structure has been altered. Meanwhile, two extra peaks, *i.e*. $Q^3$(1Al) and $Q^3$ are observed. Their formation is considered as a result of the loss of Ca ions in the interlayer of the C-S-H chain to form the hydroxyl and then to react across the interlayer (Komarneni et al., 1985, Cong and Kirkpatrick, 1996b). A possible structure of the C-A-S-H with $Q^3$(1Al) and $Q^3$ is illustrated in Figure 4.17. The intensity of $Q^0$ further decreased, indicating the WPC has been further hydrated. After 2½ months of leaching, the peak corresponding to the WPC disappears, suggesting the WPC has already fully hydrated, which is consistent with the XRD and SEM results. In addition, the peaks corresponding to the $Q^3$(1Al) and $Q^3$ become more readable, although it is still difficult to separate them due

to their overlap, indicating that more cross linking has occurred across the interlayer of the C-S-H chain.

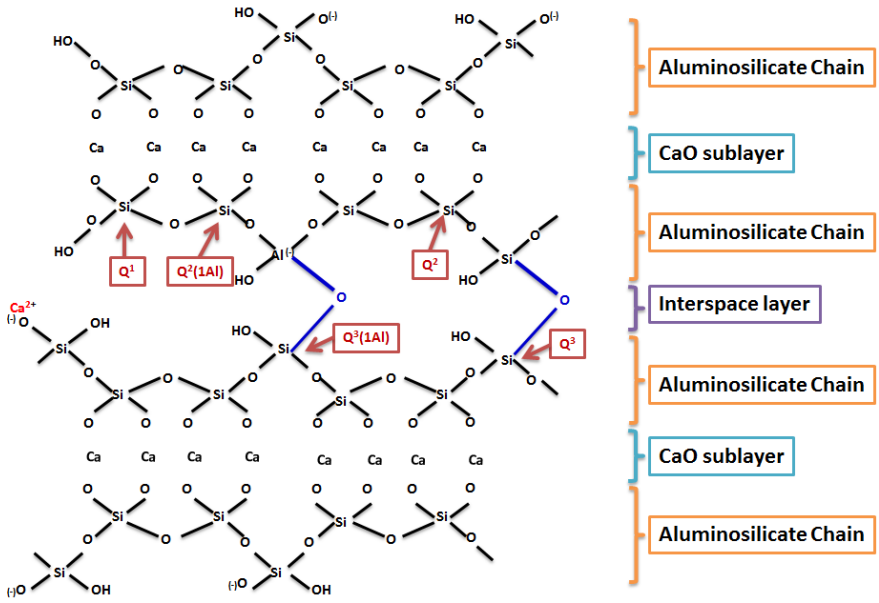


Figure 4.17 Idealised chemical structure of the C-A-S-H with $Q^3$(1Al) and $Q^3$.

When leaching starts, the relative intensity of anhydrous WPC gradually decreases due to the secondary hydration, and thoroughly disappears after 2½ months of leaching. The relative $Q^2$ intensity compared to the $Q^1$ increases gradually, and it is the trend expected with increasing polymerization of the silicate chains. A broad resonance from the range of -90 to -100 ppm due to branching $Q^3$(1Al) and $Q^3$ sites is observed in the spectra for the cement paste after 1½ months and 2½ months of leaching, indicating that a cross-linking occurred in the 1Y-WP30 cement paste after a certain time of leaching (Houston et al., 2009). Figure 4.16 also demonstrates the chemical shifts of both $Q^2$(1Al) and $Q^2$ sites move towards more negative values as leaching proceeds, especially the $Q^2$(1Al) site. The chemical shifts of the $Q^0$ does not move, indicating the change of the chemical shifts of the $Q^2$(1Al) and $Q^2$ is not due to the external factors, *e.g.* the instability of equipment, but due to the change of the their own chemical environment. The chemical shift of the $Q^2$(1Al) and $Q^2$ sites in the cement paste before leaching and at various leaching time are presented in Figure 4.18. During 2½ months

of leaching, the first change of the chemical environments of $Q^2(1Al)$ and $Q^2$ sites is the loss of Ca ions from the interlayer of the C-S-H chain. However, if the loss of Ca ions is the reason for the movement, the chemical shifts should move in the opposite way (Chen et al., 2004). The second change of the chemical environment is the formation of $Q^3(1Al)$ and $Q^3$ sites, which could change the chemical environment of the $Q^2(1Al)$ and $Q^2$ sites, especially the $Q^2(1Al)$ which is directly connected to the $Q^3(1Al)$.

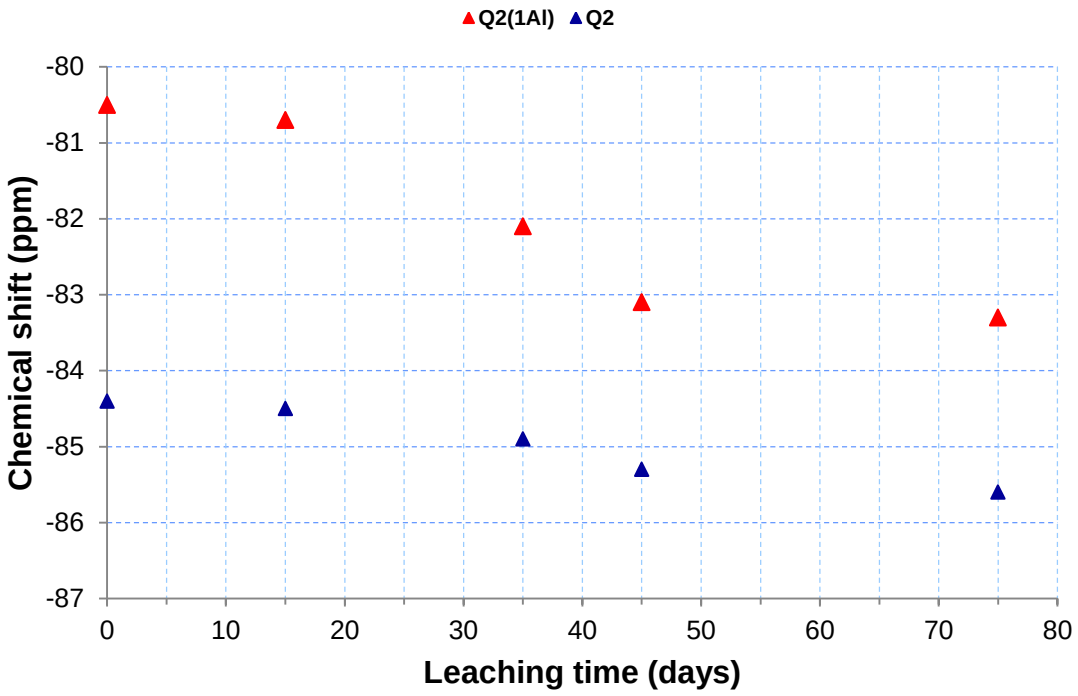


Figure 4.18 Chemical shift of the $Q^2(1Al)$ and $Q^2$ Si sites at various leaching time during 2 ½ months of leaching observed by $^{29}Si$ SS MAS NMR spectroscopy.

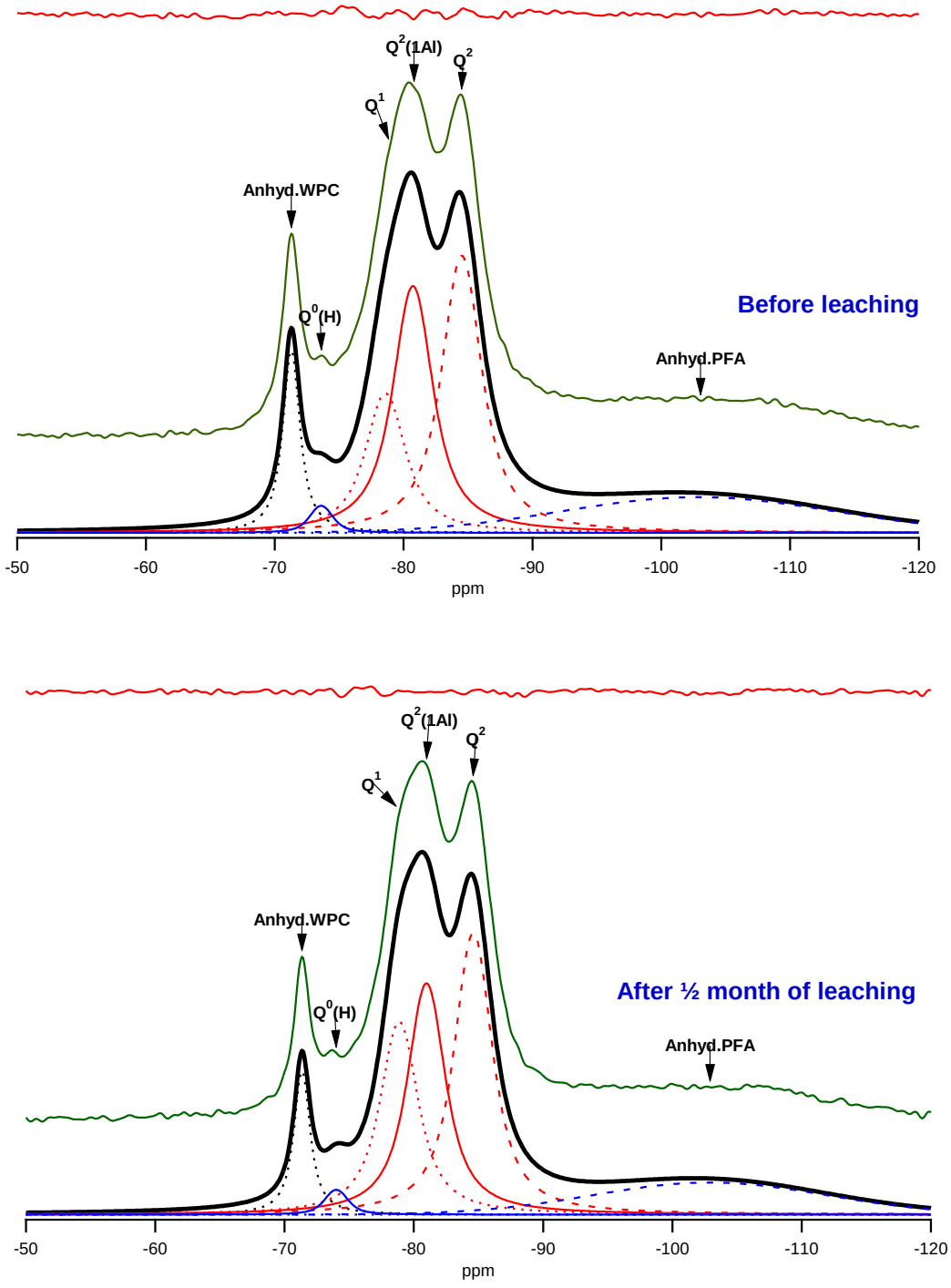


Figure 4.19 $^{29}$Si solid state MAS NMR spectra for 1Y-WP30 cement paste before leaching (top graph) and after ½ month of leaching (bottom graph). Each graph includes the experimental spectrum (middle green line), the fitting peaks (bottom lines), and the residual (top red line: x1).

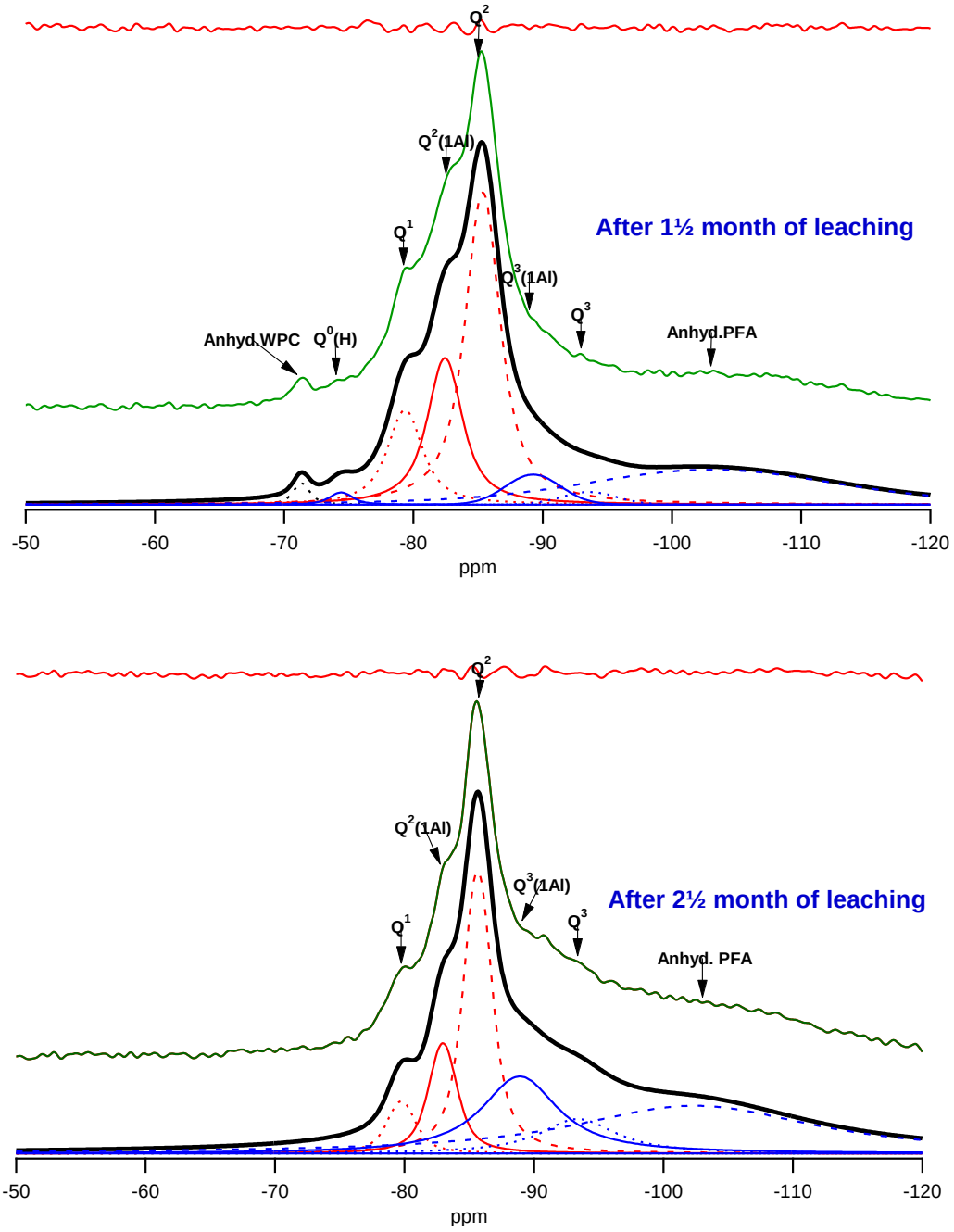


Figure 4.20 $^{29}$Si solid state MAS NMR spectra for 1Y-WP30 cement paste after 1½ month of leaching (top graph) and after 2½ month of leaching (bottom graph). Each graph includes the experimental spectrum (middle green line), the fitting peaks (bottom lines), and the residual (top red line: x1).

Table 4.1 $^{29}$Si chemical shifts and semi-quantitative data for the 1Y-WP30 cement paste before leaching and after 2 ½ months of leaching.

| | | $Q^0$ | $Q^0$(H) | $Q^1$ | $Q^2$(1Al) | $Q^2$ | $Q^3$(1Al) | $Q^3$ | $Q^4$ |
|---|---|---|---|---|---|---|---|---|---|
| **Before leaching** | **Chemical shift** | -71.3 | -73.6 | -78.6 | -80.7 | -84.5 | - | - | -102.8 |
| | **Percentage (%)** | 8.7 | 1.5 | 15.0 | 26.6 | 29.8 | - | - | 18.4 |
| | **Al/Si** | | | | 0.19 | | | | |
| | **MCL** | | | | 11.3 | | | | |
| **½ month** | **Chemical shift** | -71.3 | -74.0 | -78.9 | -81.0 | -84.6 | - | - | -102.8 |
| | **Percentage (%)** | 6.9 | 1.5 | 20.9 | 25.0 | 30.5 | - | - | 15.2 |
| | **Al/Si** | | | | 0.16 | | | | |
| | **MCL** | | | | 8.5 | | | | |
| **1½ months** | **Chemical shift** | -71.3 | -74.9 | -79.4 | -82.4 | -85.4 | -88.9 | -93.9 | -104.1 |
| | **Percentage (%)** | 1.2 | 0.9 | 11.4 | 17.7 | 37.6 | 4.1 | 1.7 | 25.4 |
| | **Al/Si** | | | | - | | | | |
| | **MCL** | | | | - | | | | |
| **2½ months** | **Chemical shift** | - | - | -79.8 | -83.0 | -85.6 | -88.9 | -93.4 | -102.4 |
| | **Percentage (%)** | - | - | 4.3 | 9.0 | 23.1 | 18.8 | 8.4 | 36.4 |
| | **Al/Si** | | | | - | | | | |
| | **MCL** | | | | - | | | | |

The spectra for the 1Y-WP30 cement paste before leaching and after ½ month, 1½ months and 2½ month of leaching fitted with anhydrous WPC, $Q^0$(H), $Q^1$, $Q^2$(1Al), $Q^2$, $Q^3$(1Al), $Q^3$ and anhydrous PFA are shown in Figure 4.19 and Figure 4.20. The percentage of Si attributed to each resonance is determined and used to calculate the average Al/Si atomic ratio and MCL of the C-S-H in the cement paste before leaching and after ½ month of leaching by using the Equations 2.6 and 2.7, with results listed in Table 4.1. The Al/Si atomic ratio in the 1Y-WP30 cement paste before leaching and after ½ month of leaching are 0.19 and 0.16, respectively, which are consistent with the observation from the SEM-EDX analysis, indicating the deconvolution is feasible. The MCL of C-S-H in the cement paste before leaching is 11.3 in this study, which is similar to Girão's observation (2007). The MCL in the cement paste after ½ month of leaching

is shorter than that in the cement paste before leaching, because more $Q^1$ forms during the secondary hydration of anhydrous WPC.

Due to the addition of $Q^3$(1Al) and $Q^3$, the C-S-H structure in the cement paste after 2½ months of leaching becomes so complex that the general model for C-S-H has not been built up yet, then it is difficult to calculate the Al/Si and MCL.

### 4.4.2 $^{27}$Al solid state MAS NMR spectra

The $^{27}$Al SS MAS NMR spectra of 1Y-WP30 cement paste before leaching and after 2½ months of leaching are illustrated in Figure 4.21, from which the evolution of Al coordination in the 1Y-WP30 cement paste during the leaching process can be observed.

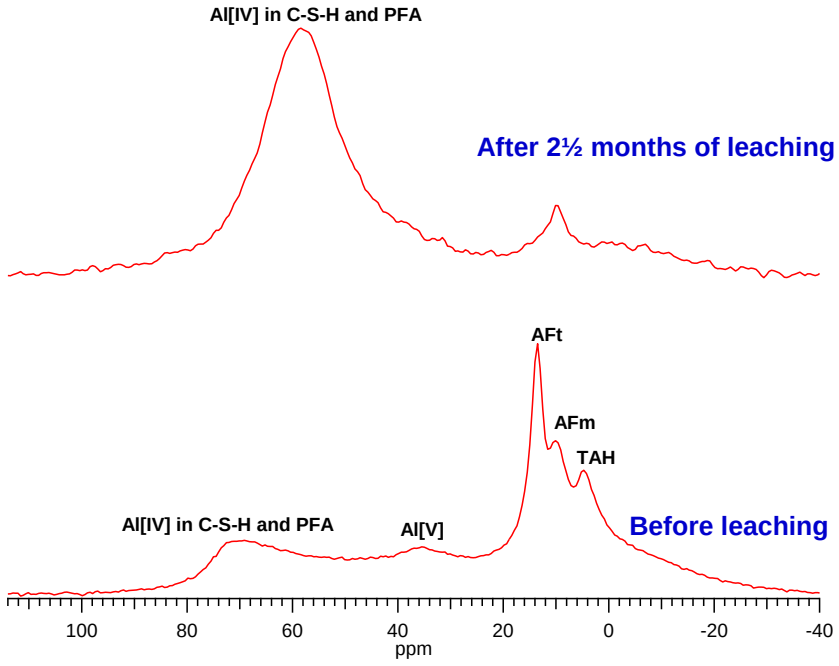


Figure 4.21 $^{27}$Al solid state MAS NMR spectra for the 1Y-WP30 cement paste before leaching (bottom spectrum) and after 2½ months of leaching (top spectrum)

In the spectrum for the 1Y-WP30 cement paste before leaching, there are five Al with centerbands at, *i.e.* 68.9 ppm, 35.2 ppm, 13.2 ppm, 9.8 ppm and 4.5 ppm. The first peak is assigned to Al presented in the unreacted PFA (Puertas and Fernandez-

Jimenez, 2003) and $Q^2$ bridging tetrahedra of silicate chains of the C-A-S-H, and the second peak is generally located in the interlayer of the C-S-H structure for substituting $Ca^{2+}$ ions for balancing (Jansen et al., 1998, Andersen et al., 2006, Skibsted and Hall, 2008). It is easy to assign the high-frequency resonances at 13.27 ppm and 9.85 ppm which are the octahedrally coordinated Al to ettringite and monosulphates, respectively (Skibsted and Hall, 2008). It is still a controversial about the allocation of the resonance at around 4.48 ppm which is also an octahedrally coordinated Al (Andersen et al., 2006, Skibsted and Hall, 2008, Andersen et al., 2003). Andersen *et al*., (2003) tentatively ascribed it to a less crystalline aluminate gel or calcium aluminate hydrate which is called third aluminate hydrate (TAH). In the spectrum for the 1Y-WP30 cement paste after 2½ months of leaching, there are two readily resonances, *i.e*. a Al[IV] coordinated resonance at 58.18 and a Al[VI] coordinated resonance at 9.85. The former resonance is assigned to the Al[IV] in the $Q^3$ branching coordination sites in the C-S-H, and this assignment have also been proposed by Sun et al.,(2006), Komarneni (1985) and Houston (2009).The intensity of the Al[IV] in the C-S-H has clearly increased compared to that in the cement paste before leaching, confirming the further formation of C-S-H during leaching process. The Al[V] coordinated site which originates from $Al^{3+}$ substituting for $Ca^{2+}$ ions situated in the interlayers of the C-S-H structure (Faucon et al., 1999), are not observed. The $Al^{3+}$ ions in the interlayer of the C-S-H structure probably are dissolved due to the leaching, like the dissolution of $Ca^{2+}$ ions (Sun et al., 2006). The disappearance of the resonances from TAH, AFt and AFm is because of their easy dissolution nature, which is also observed by the XRD.

## 4.5 Summary

The effects of water leaching on the evolution of structure at micro-, nano- and atomic-scale of one year old Portland cement blended 30% pulverised fly ash cement paste

have been investigated. It has been found out that the water leaching can affect various aspects of the structures of the cement paste including: CH is removed completely prior to any effect on the C-S-H; initially, secondary ettringite formation occurs on the degraded layer and then it is dissolved due to its dissolution nature; the compact microstructure of the cement paste becomes more porous and eventually it becomes dry cracked land like; the average Ca/Si atomic ratio of the C-S-H decreases from 1.4 to 0.6 due to the dissolution of $Ca^{2+}$ ions from the interlayer; the average Al/Si atomic ratio of the C-S-H increases from 0.18 to 0.23, indicating more Al ions have substituted Si ions in the C-S-H chain; the presence of $Q^3$(1Al) and $Q^3$ suggest that the single silicate chains has been cross-linked to form double chain structure.

# Chapter 5 Characterisation and water leaching on 13 year old white Portland cement paste blended with 30% pulverised fly ash

## 5.1 Introduction

In this chapter the experimental results of 13Y-WP30 cement paste under leaching are presented and discussed. The chapter is organized in four sections which are created according to the focus of the observations:

- Phase identification and quantification studied by XRD and thermal analysis;
- Evolution of structure and chemical composition at micro-scale studied by SEM-EDX;
- Evolution of structure and chemical composition at nano-scale studied by TEM-EDX;
- Evolution of structure at atomic-scale studied by Solid-state MAS NMR.

## 5.2 Bulk analysis-phase identification and quantification studied by XRD and thermal analysis

Figure 5.1 shows XRD patterns of the 13Y-WP30 cement paste before and after leaching. In the cement paste before leaching, the main phases are the same as those are in the 1Y-WP30 cement paste shown in Chapter 4, *i.e*. C-S-H, CH, residual β-belite, ettringite, quartz and mullite. As leaching proceeds, the intensity of the peaks corresponding to CH gradually decreases due to the dissolution nature. After 1½ months of water leaching, the patterns corresponding to CH disappears, suggesting the CH has been dissolved. On the contrary, the content of ettringite increases and it precipitates simultaneously during the dissolution of CH and AFm. The decreasing of calcium concentration in the interstitial solution towards the surface of the paste results in a local increase of concentrations of $Al(OH)_4^-$ and $(SO_4)^{2-}$. These ingredients diffuse

from the dissolution boundary of the ettringite, near the surface, towards the centre of the paste, providing the key ingredients (*i.e.* aluminium and sulphate) required for the secondary ettringite precipitation. The other key ingredient required for the precipitation, Calcium, is provided by the dissolution of CH and AFm phases (Faucon et al., 1998a, Haga et al., 2005). A small amount of calcite is observed in the sample after 1½ months of leaching, because calcium ions derived from dissolution of CH react with the $CO_2$ in water to form calcite which then precipitates on the surface of the cement paste.

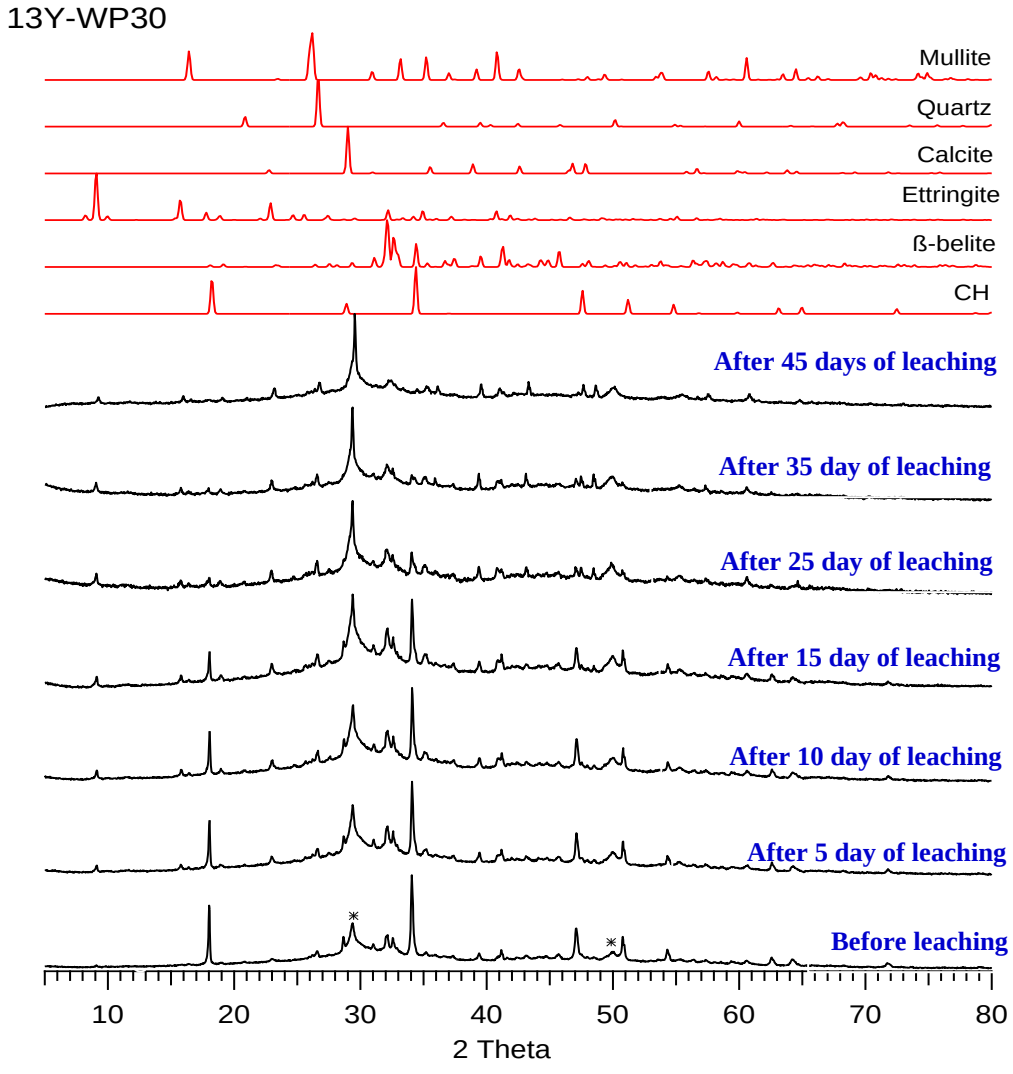


Figure 5.1 XRD patterns of 13Y-WP30 cement paste before and after various leaching time, all set to the same intensity scale. The relevant standard phase traces are included and the asterisk labelled peaks correspond to the C-S-H gel phase.

In order to investigate how water leaching may change the dissolution and precipitation of phases across the thickness, after the surface observation the cement paste is polished to remove 20 μm of material and create a new surface for observation. In a similarly way, the cement paste is polished another four times to enable more observations at depths of 50, 100, 200, 300 μm.

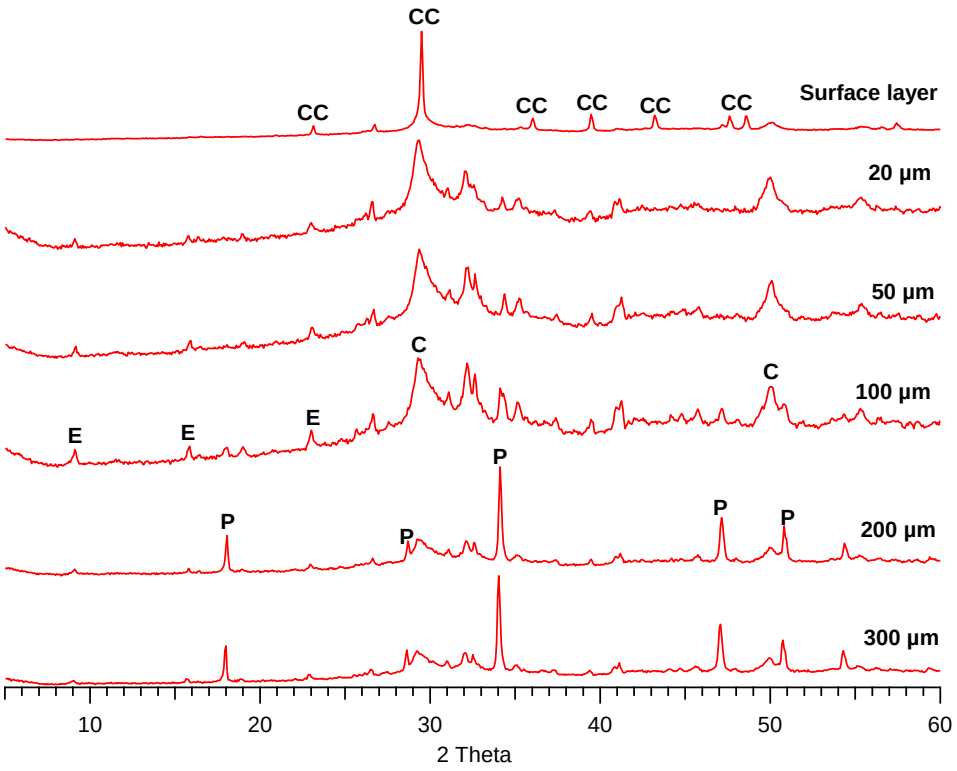


Figure 5.2 X-ray diffraction patterns of six layers at different depth of 13Y-WP30 cement paste after 10 days of leaching at different leaching fronts (CC, E, C and P correspond to calcite, ettringite, C-S-H gel and portlandite, respectively).

Figure 5.2 shows the XRD patterns of different leaching fronts in the 600 μm thick 13Y-WP30 cement paste after 10 days of leaching. It is shown that the surface layer no longer contains CH and ettringite, and this layer is referred to as superficial degraded layer, as already shown in Figure 3.3. At a depth of 100 μm, small amount of CH is left, but at a depth of 200 μm or 300 μm, large amount of CH are retained, indicating the CH is dissolved from the surface layer gradually into the inner core of the cement paste. Ettringite does not exist on the superficial layer due to its dissolution nature, and strong

reflection peak is observed at depths of 20, 50 and 100 µm, where the ettringite tends to precipitate (Faucon et al., 1998b). There is a strong reflection peak at 30 2θ on the superficial degraded layer of the paste, and it is the main reflection peak of the calcite, however, it is not observed at other depths in the paste. The reflection peaks corresponding to C-S-H are observed in all the six layers, suggesting the C-S-H exist in all the layers. The XRD patterns at depths of 200 and 300 µm are similar to those observed in the cement paste before leaching, as shown in Figure 5.1, suggesting the phases in these layers are not dissolved or precipitated.

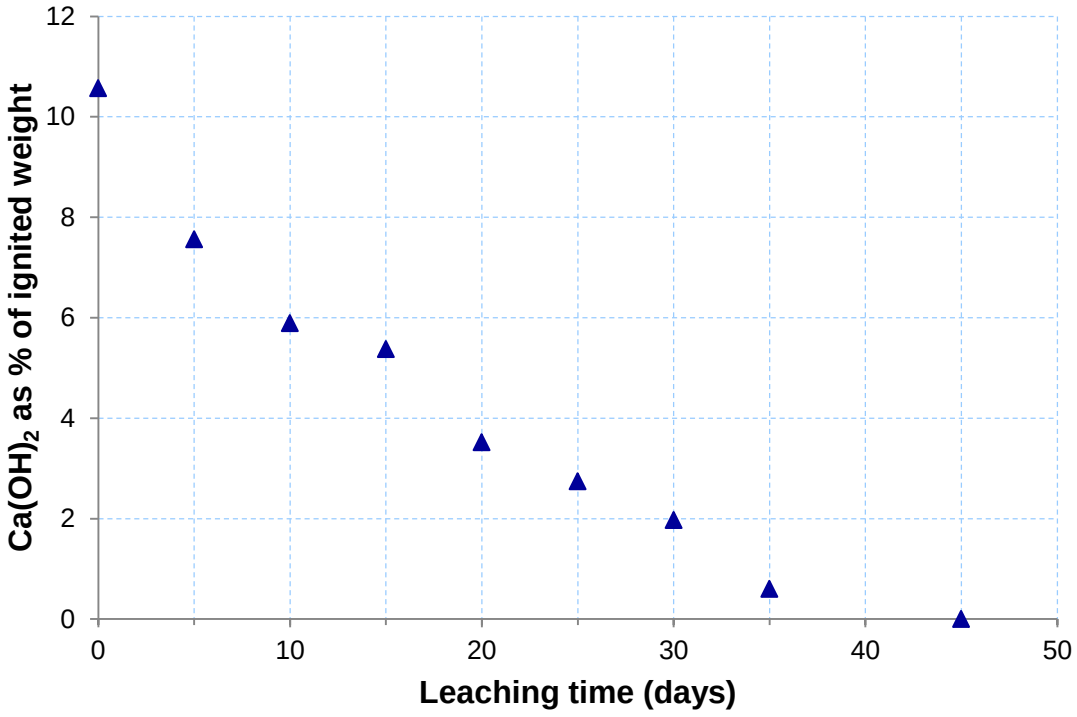


Figure 5.3 $Ca(OH)_2$ evolution during 45 days (1½ months) of water leaching of the 13Y-WP30 cement paste.

Thermal analysis is used to calculate the amount of CH in the cement paste at different leaching times. Figure 5.3 illustrates that before leaching there is 10.57% CH as ignited weight in the 13 years cement paste. A similar result of 11.4% CH was observed in a 9 years old sample by Taylor (2010). After 5 days of leaching, the amount of CH has significantly decreased to 7.6% as ignited weight, due to its easily dissolved nature,

and then the amount of CH decreases gradually in the following one month of leaching. After 40 days of intense water attack, only a very small amount of CH is left in the cement paste, and after 1½ months of leaching, the CH has absolutely been dissolved, which is consistent with the XRD observation. However, during the leaching process, CH is simultaneously formed due to the secondary hydration of anhydrous WPC left in the 13Y-WP30 cement paste, and the CH may also be consumed by the further pozzolanic reaction, making the explanation complicated (Girao, 2007).

## 5.3 Evolution of structure and chemical composition at micro-scale studied by SEM-EDX

The micro-scale structure and the chemical composition of the 13Y-WP30 cement paste before leaching and the degraded layer in the cement paste after different leaching duration are analysed by using SEM-EDX.

Figure 5.4 presents the BSE images of the 13Y-WP30 cement paste before leaching. They show that the main phaes are similar to they are in the 1Y-WP30 cement paste, *i.e*. WPC grains, PFA, CH, C-S-H gel and pores, however, the microstructure is more homogeneous and compact due to further cement hydration (Taylor, 2010). The CH is evenly distributed in the cement paste, and there are still large amounts of CH left after 13 years of hydration, which is observed in aforementioned thermal analysis. There is plerospheres PFA which has hollow spheres with smaller spheres inside shown in the centre of the graph, because it is difficult for water to penetrate the outer shell of the fly ash and to react with the inner spheres. With 2000X magnification, layers of AFm phase around 3 μm sizes are observed. Larger amount of Ip C-S-H are found after 13 years of hydration indicating the cement paste has further hydrated, whereas Ip C-S-H is rare in the one year old cement paste.

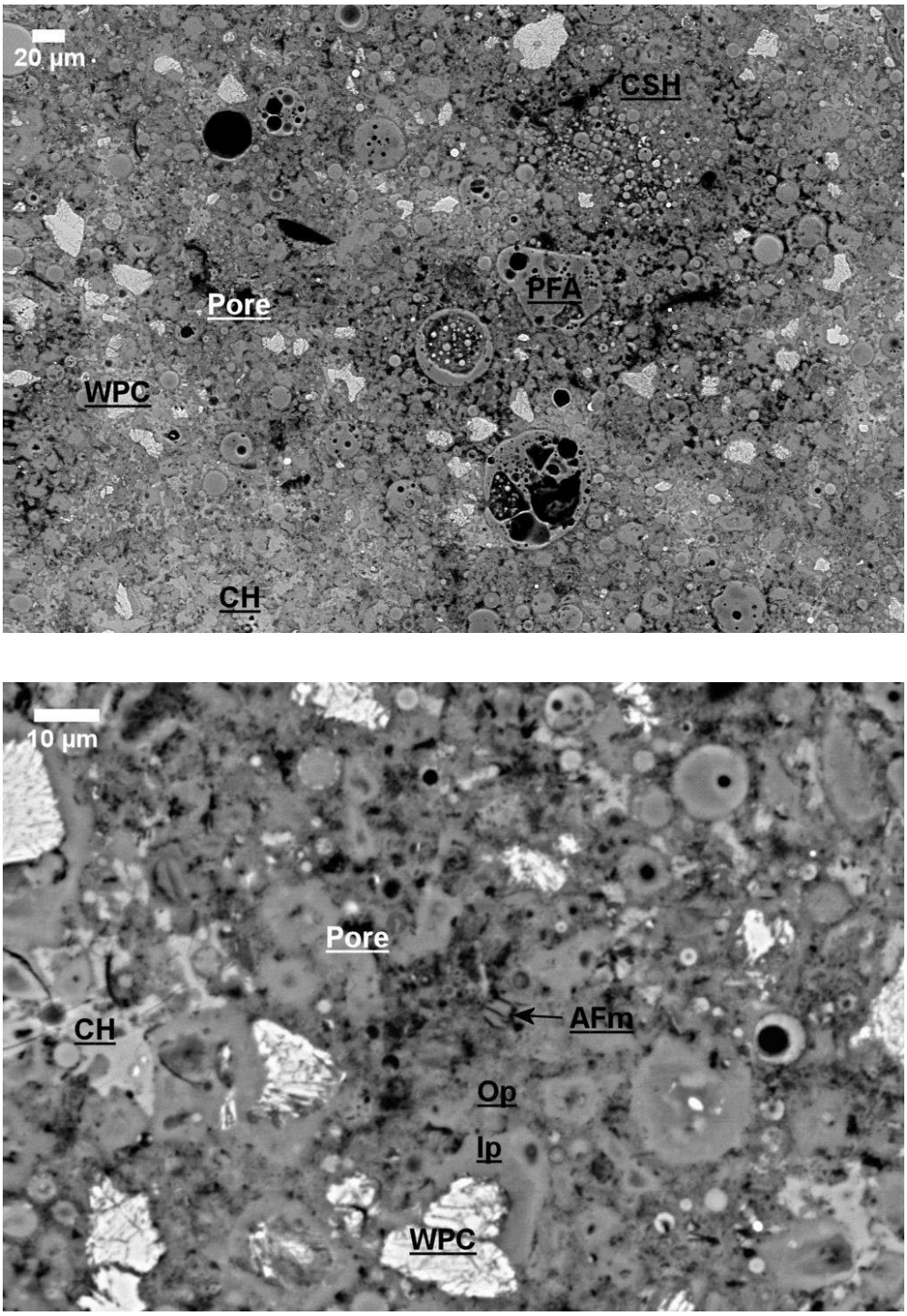


Figure 5.4 Backscattered images illustrating the microstructure of the surface area of the 13Y-WP30 cement paste before leaching with 500X (top) and 2000X (bottom) magnification. Regions of pulverised fly ash (PFA), white Portland cement (WPC), calcium hydroxide (CH), C-S-H gel (CSH), inner product C-S-H (Ip), outer product C-S-H (Op) and pores (Pore) are labelled.

The chemical composition of the C-S-H in the 13 years old cement paste before leaching is analysed by SEM-EDX, and the results are plotted out as $CaO$-$Al_2O_3$-$SiO_2$ ternary diagram, as shown in Figure 5.5. The diagram shows that there is a trend line in the direction of CH, suggesting the CH is intermixing with the C-S-H, suggesting that the CH is intermixing with C-S-H at micro-scale in the aged sample. The average Ca/Si atomic ratio of the C-S-H in the 13Y-WP30 cement paste before leaching is around 1.4.

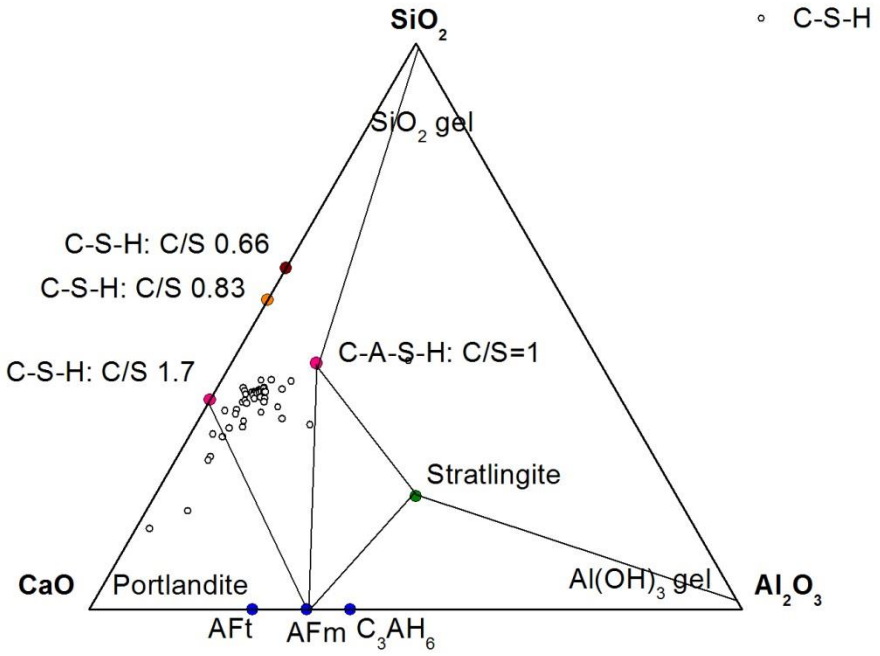


Figure 5.5 $CaO$-$Al_2O_3$-$SiO_2$ ternary diagram for SEM-EDX phase analysis of the 13Y-WP30 cement paste before leaching.

The BSE images in Figure 5.6 shows the microstructure of the degraded surface of 13Y-WP30 cement paste after 5 days and 10 days of leaching. It can be seen that the microstructure has already largely changed after leaching. The CH on the degraded surface has already been dissolved, however, there are still abundant of anhydrous cement grain in the cement paste. Small cracks form on the degraded surface in the 13Y-WP30 cement paste after 5 days of leaching. This is because the leaching process is governed by diffusion, and the degraded surface will inevitably be degraded more than the inner core of the cement paste, producing a gradient in Ca/Si atomic ratio, which results in a differential in stress. If the tensile stress is great enough, the sample will crack at the surface (Chen, 2003). Cracks are not observed in the 1Y-WP30 cement paste after 5 days of leaching, as the C-S-H is not decalcified in the first 10 days of leaching (see Figure 4.9), and larger amount of CH in the 1Y-WP30 cement paste and the C-S-H will only be decalcified after the CH already being dissolved. However, in the 13Y-WP30 cement paste after 5 days of leaching, the C-S-H has already started to be decalcified on the degraded surface, producing the tensile stress and then cracks form.

In the 13Y-WP30 cement paste after 1½ months of leaching, the microstructure has changed significantly with large pores being formed and coarse fibrillar phases being filled in, as shown in the BSE images in Figure 5.7 with magnifications of 500X and 1000X. The coarse fibrillar phases are rich in S content, which are considered to be secondary formatted ettringite, and it is likely to form in the large cavity in the hardened cement paste (Mehta, 1973). The overall porosity of the cement paste has increased, and this may increase its permeability and deteriorate its engineering performance in practice. The anhydrous cement grains shown in the cement paste before leaching have already fully hydrated due to the addition of water.

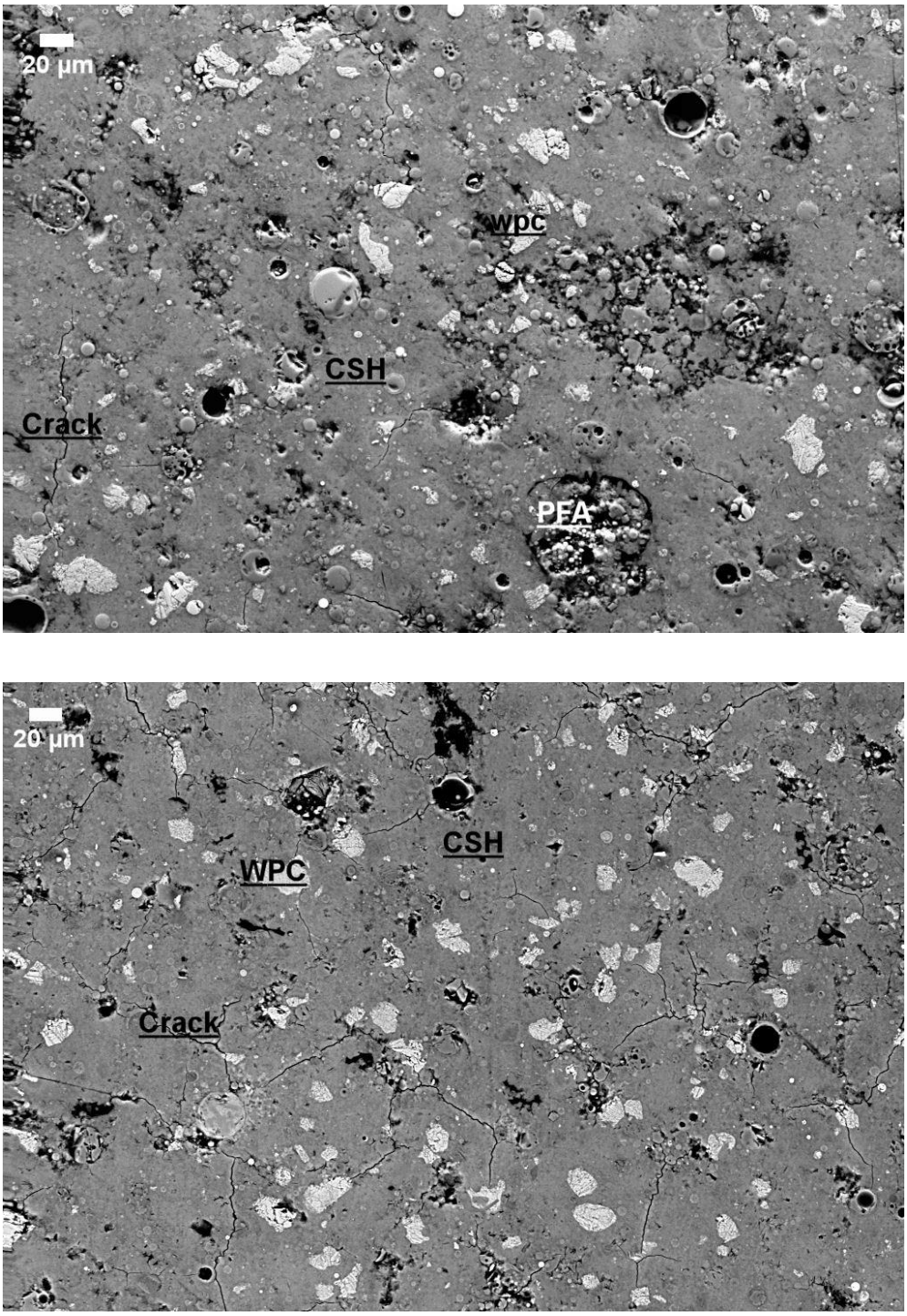


Figure 5.6 Backscattered images illustrating the microstructure of the degraded layer of the 13Y-WP30 cement paste after 5 days (top) and 10 days (bottom) of leaching with 500X magnification. Regions of white Portland cement (WPC) calcium hydroxide (CH), C-S-H gel (CSH) and Cracks (Crack) are labelled.

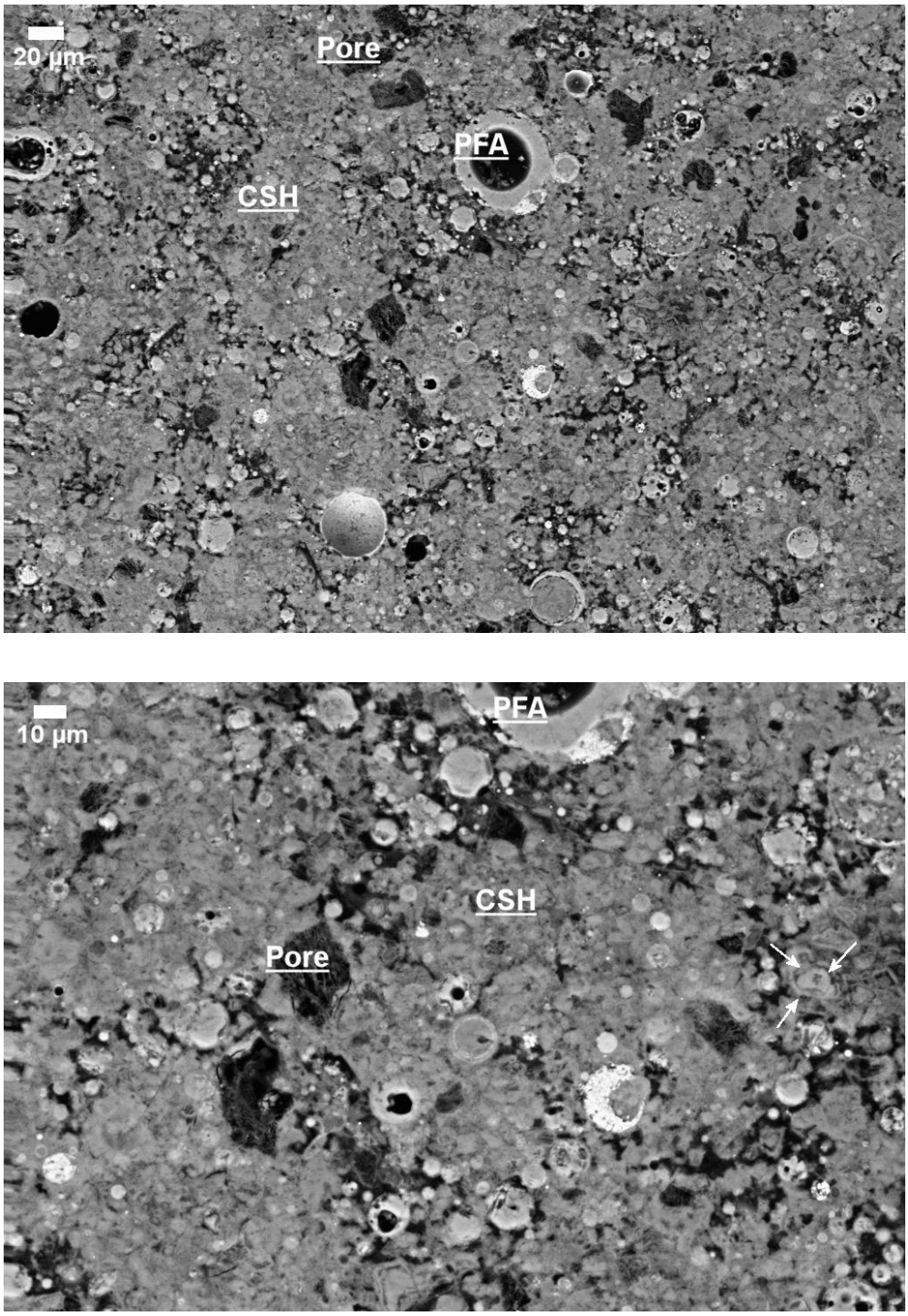


Figure 5.7 Backscattered image illustrating the microstructure of the degraded layer of the 13Y-WP30 cement paste after 1½ months of leaching with 500X (top) and 1000X (bottom) magnification. Regions of pulverised fly ash (PFA) and C-S-H gel (CSH) are labelled. The white arrows indicate the fully reacted WPC that has bright rim.

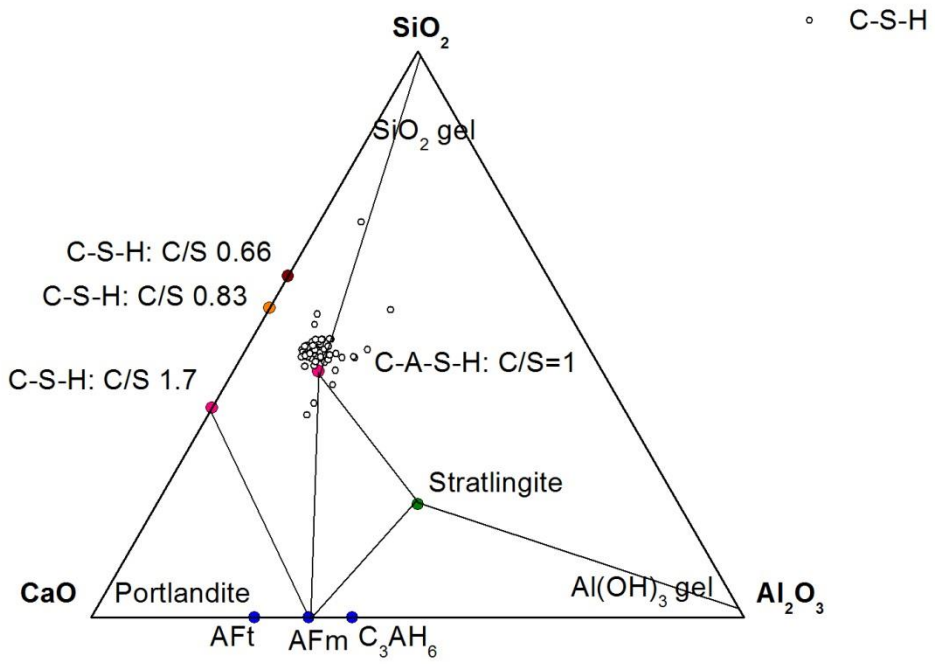


Figure 5.8 $CaO$-$Al_2O_3$-$SiO_2$ ternary diagram for SEM-EDX phase analysis of the 13Y-WP30 cement paste after 1½ months of leaching.

The C-S-H on the degraded surface in the 13Y-WP30 cement paste after 1½ months of leaching is analysed by SEM-EDX, and the data are plotted out as $CaO$-$Al_2O_3$-$SiO_2$ ternary diagram in Figure 5.8. The average Ca/Si atomic ratio has already decreased to around 0.92, suggesting that the C-S-H has been decalcified.

Figure 5.9 presents the average Ca/Si atomic ratio with error bar in the 13Y-WP30 cement paste during 1½ months of leaching. In the first 5 days of leaching, the Ca/Si atomic ratio in the C-S-H slightly decreases. After 1½ months of leaching, the Ca/Si atomic ratio becomes 0.92, which is statistically higher than that in the 1Y-WP30 cement paste at the same leaching time. Because there is larger amount of CH in the 1Y-WP30 cement paste being dissolved, the cement paste becomes more porous with the increasing of permeability, causing the C-S-H to be decalcified faster. The average Al/Si atomic ratio of the C-S-H slightly increases during the 1½ months of leaching.

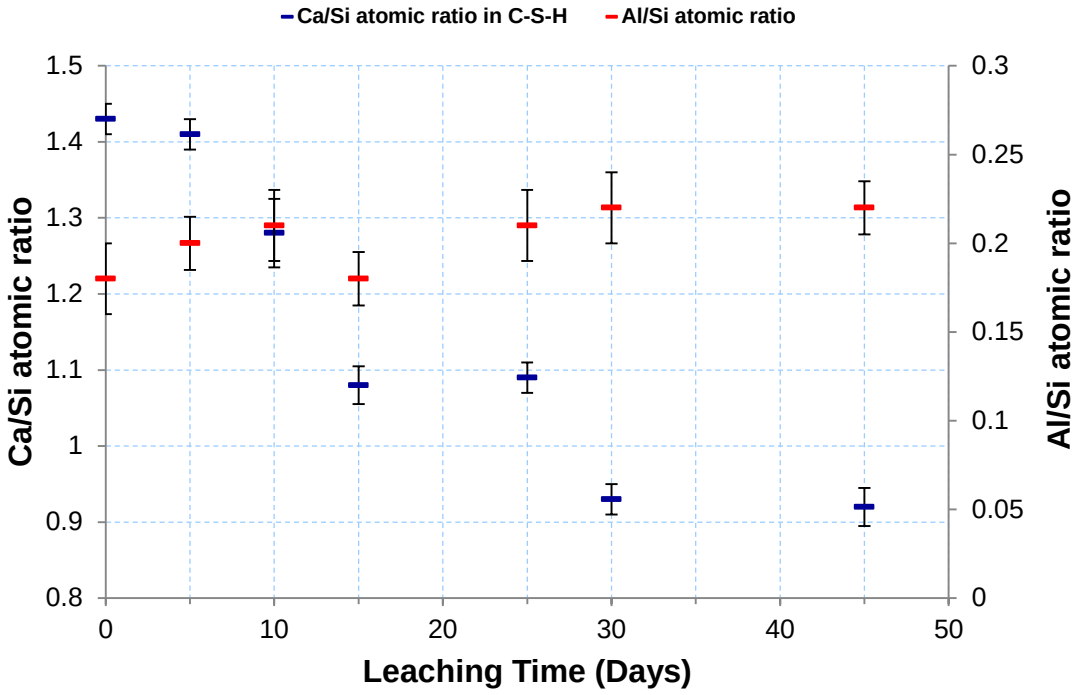


Figure 5.9 Average Ca/Si and Al/Si atomic ratio with error bar from SEM-EDX analysis of the C-S-H in the 13Y-WP30 cement paste at various time during 1½ months of leaching.

## 5.4 Evolution of structure at nano-scale studied by TEM-EDX

The 13Y-WP30 cement paste before leaching and the degraded surface of the cement paste after leaching are analysed by TEM-EDX to study the nano-scale structure and chemical composition evolutions during the leaching.

### 5.4.1 TEM images and EDX analysis of 13Y-WP30 cement paste before leaching

A typical TEM image of partially hydrated PFA is shown in Figure 5.10. Less density foil-like Ip C-S-H is formed in the PFA with a Ca/Si atomic ratio of 1.38 analysed by the EDX and the dark feature in the PFA is most likely unreacted glassy PFA. It is observed that there is a morphology difference in density between the inner core of the PFA particle and the outside rim, as PFA particle reacts with CH from the outside rim gradually towards the inner core. Most of the PFA are still partially reacted after 13

years of hydration. There are gaps between the partially hydrated PFA grain and the fine fibrillar feature Op C-S-H with a Ca/Si atomic ratio of 1.42.

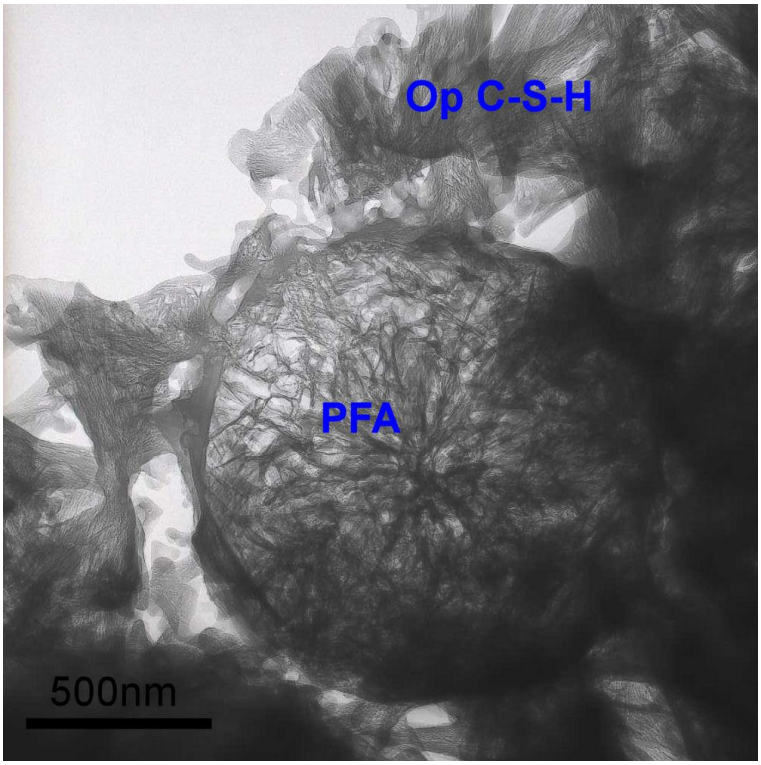


Figure 5.10 TEM image of partially hydrated PFA with less density foil-like Ip C-S-H and fine fibrillar Op C-S-H in the 13Y-WP30 cement paste before leaching.

Figure 5.11 demonstrates compact and homogeneous Ip C-S-H and fibrillar feature Op C-S-H, which is a typical morphology of C-S-H formed in a WPC grain (Girao, 2007, Girao et al., 2007a, Taylor, 2010), and different from that of C-S-H formed in PFA (see Figure 5.10). The left image in Figure 5.12 shows fully hydrated WPC with less dense foil-like Ip C-S-H, which is generally present in small fully hydrated cement grains. Fine fibrillar feature Op C-S-H is observed surrounding the fully hydrated WPC. Foil-like Op C-S-H is also observed in the cement paste, as shown in the right TEM image, which is a typical Op C-S-H morphology with low a Ca/Si ratio in the blended cement paste.

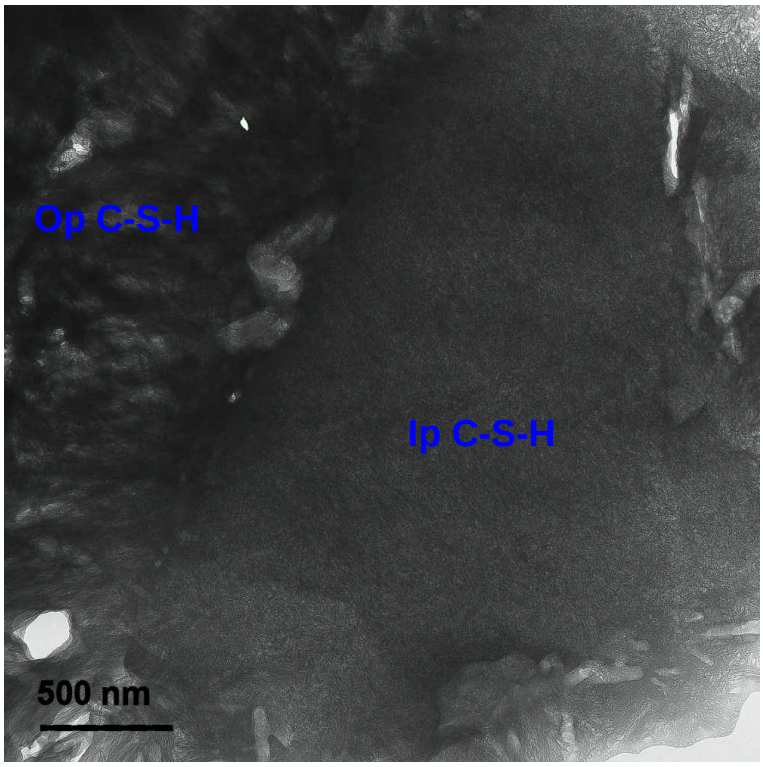


Figure 5.11 A TEM graph showing compact and homogeneous Ip C-S-H and fine fibrillar feature Op C-S-H.

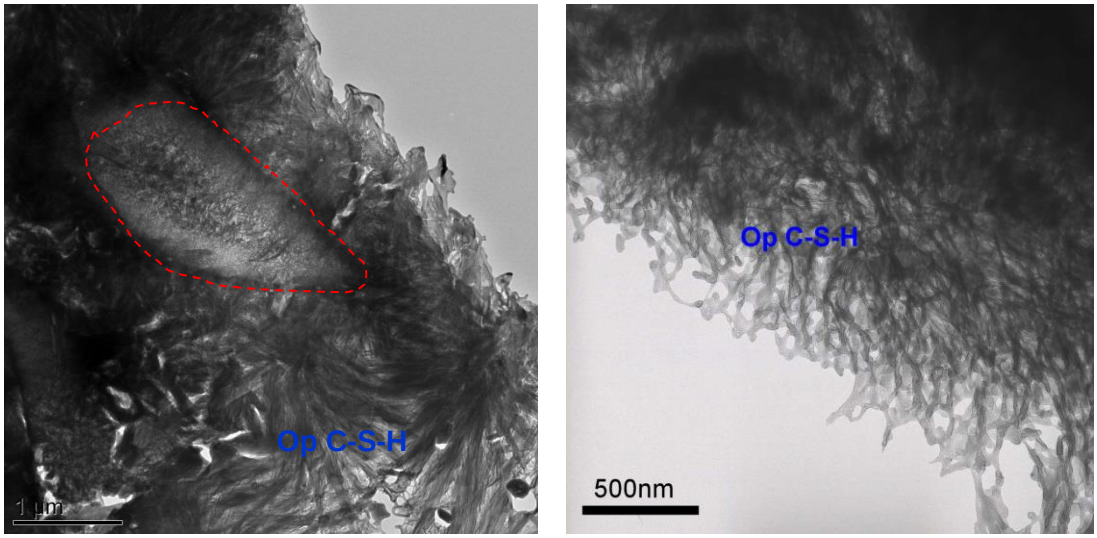


Figure 5.12 TEM images of foil-like Ip C-S-H in the fully hydrated cement grain and short fibrillar Op C-S-H (left image), and foil-like Op C-S-H in the 13Y-WP30 cement paste before leaching (right image).

The Ip and Op C-S-H in the 13Y-WP30 cement paste before leaching are analysed by TEM-EDX with data plotted out as $CaO$-$Al_2O_3$-$SiO_2$ ternary diagram in Figure 5.13. The diagram clearly shows that the Ca/Si atomic ratio in Ip and Op C-S-H is statistically similar, and the value is centred at 1.36 ± 0.08 (n=30), indicating the C-S-H is homogenous. A similar result was obtained by Taylor using a 9 years old cement paste (2010), suggesting that the Ca/Si atomic ratio does not change significantly after 4 years more hydration. The Ca/Si atomic ratio observed by TEM-EDX is slightly lower than that observed by SEM-EDX, because the SEM-EDX has a larger interaction volume of incident beam, causing the CH mistakenly analysed with the C-S-H.

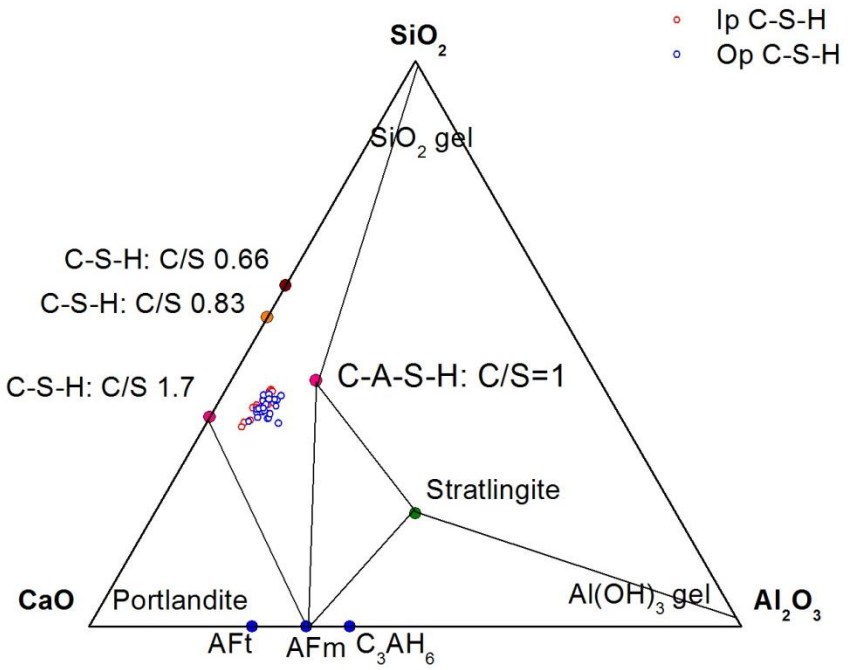


Figure 5.13 $CaO$-$Al_2O_3$-$SiO_2$ ternary diagram for TEM-EDX phase analysis of the 13Y-WP30 cement paste before leaching.

### 5.4.2 TEM images and EDX analysis of 13Y-WP30 cement paste after leaching

The left TEM image in Figure 5.14 is a typical TEM image of the degraded surface in the 13Y-WP30 cement paste after 1½ months of leaching, and it shows two features of Ip C-S-H, referred to as Ip C-S-H and Ip C-S-H'. The Ip C-S-H is the hydration product of WPC particle, and has a compact and homogeneous morphology. The Ip C-S-H' is the hydration product of the PFA, and it is less dense and has a foil-like feature, as shown in the enlarged image in Figure 5.14. In addition, Ip C-S-H' has high content of Al with an Al/Si atomic ratio of 0.26, as observed by TEM-EDX.

TEM image in Figure 5.15 illustrates a clear boundary between fine fibrillar Op C-S-H and homogeneous Ip C-S-H, both of which are typical hydration products of the WPC grain. Compared to the Ip C-S-H in the unleached cement paste demonstrated in Figure 5.11, the Ip C-S-H in the degraded surface of the leached sample is more porous and has a much lower Ca/Si atomic ratio due to the decalcification. Considering the Op C-S-H in this graph, there is no significantly change of the morphology after leaching, although the chemical composition of C-S-H has largely changed due to the decalcification.

The left TEM image in Figure 5.16 illustrates the three-dimensional net-like Op C-S-H on the degraded surface of the 13Y-WP30 cement paste after 1½ months of leaching. From TEM-EDX observation, it has a Ca/Si atomic ratio of 0.8. The transformation of one dimensional fine fibrillar feature and two dimensional foil-like feature before leaching to a three dimensional net-like feature after leaching, is probably due to the loss of Ca ions in the interlayer of the C-S-H chain and the consequent formation of the double chain of the C-S-H structure. The right TEM image in Figure 5.16 shows the porous Ip C-S-H in the cement paste after leaching.

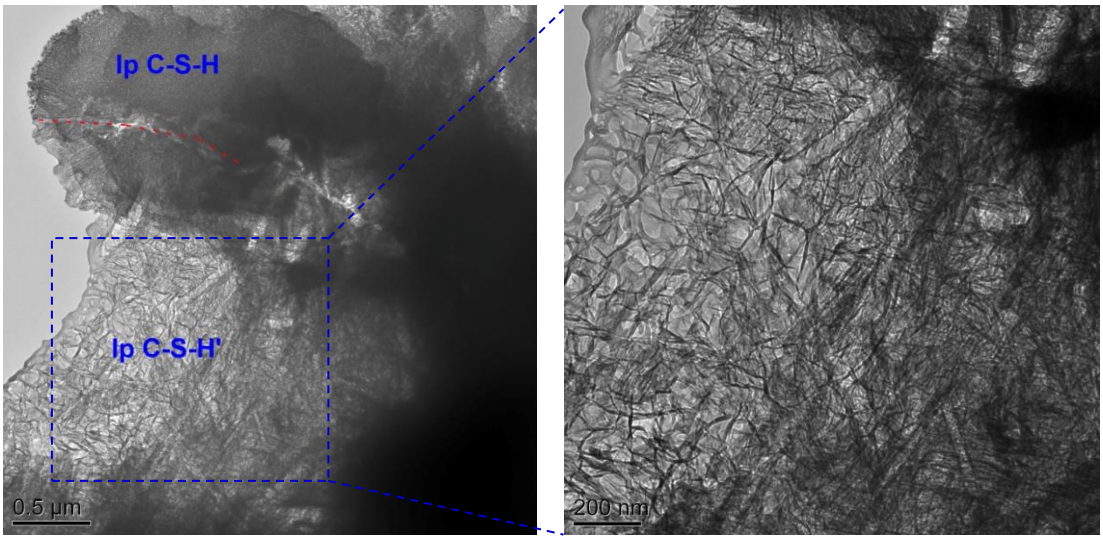


Figure 5.14 TEM image (left) of partially hydrated PFA formed foil-like Ip C-S-H' and compact Ip C-S-H with clear boundary, and the enlarged area (right) of the Ip C-S-H' with Ca/Si=0.75 and Al/Si=0.26. Both images are from the 13Y-WP30 cement paste after 1½ months of leaching.

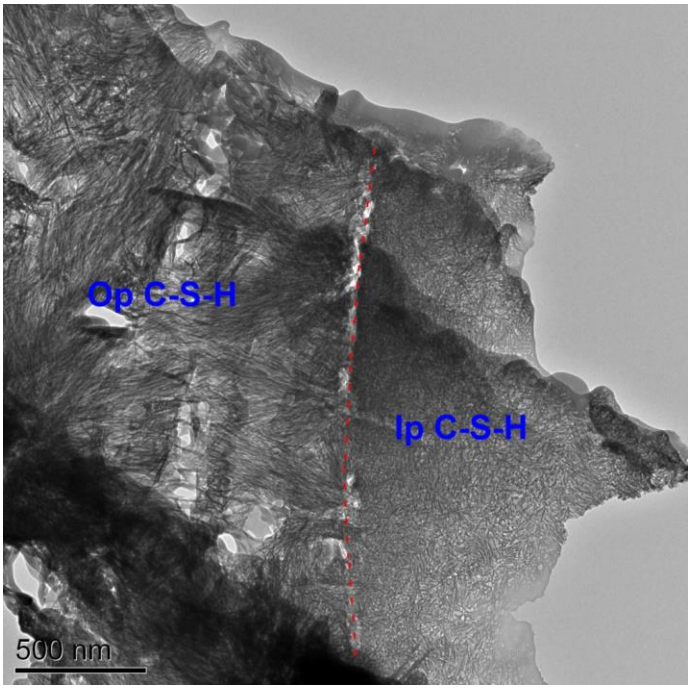


Figure 5.15 TEM image illustrating decalcified short fibrillar Op C-S-H (Ca/Si=0.80, Al/Si=0.21)) and homogeneous Ip C-S-H with clear boundary in the 13Y-WP30 cement paste after 1½ months of leaching.

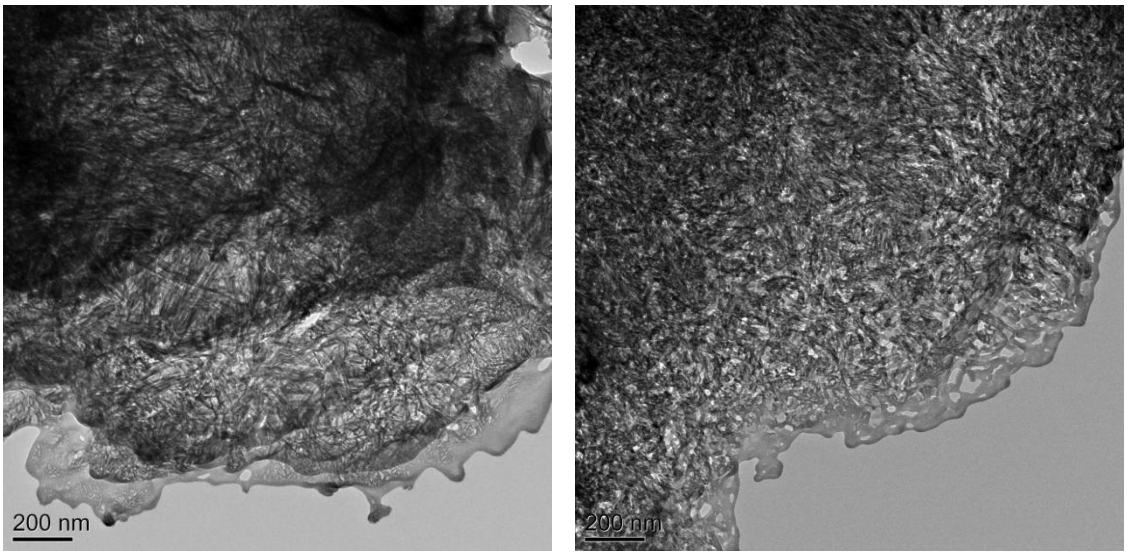


Figure 5.16 Left TEM image illustrating three-dimensional net-like decalcified Op C-S-H; and the right TEM image showing porous Ip C-S-H on the degraded surface of the 13Y-WP30 cement paste after 1½ months of leaching.

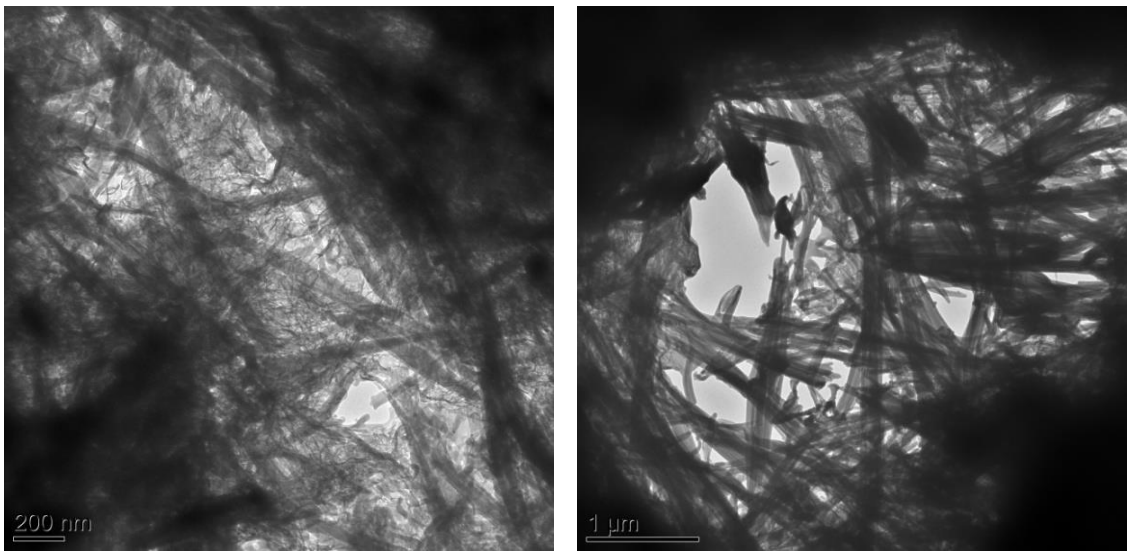


Figure 5.17 Left TEM image illustrating decalcified short C-S-H intermixed with coarse fibrillar Op C-S-H formed from the secondary hydration; and right TEM image illustrating a coarse needle-like ettringite with Ca/Si=2.52, Al/Si=1.10 and S/Ca=0.28 formed in a void in the 13Y-WP30 cement paste after 1½ months of leaching.

The left TEM image in Figure 5.17 shows that decalcified short C-S-H is intermixed with coarse fibrillar featured Op C-S-H which is formed during the secondary hydration. The morphology of Op C-S-H depends on the space that is available for it to form (Love, 2002, Richardson, 1999). The Op C-S-H formed in large pore spaces is produced by the leaching process, and it has a coarse and fibrillar morphology. The right TEM image presents a coarse needle-like phase with Ca/Si=2.52, Al/Si=1.10 and S/Ca=0.28 formed in a void, which is considered to be the secondary ettringite is also observed by the SEM. In this secondary ettringite, Ca ions are deficient due to leaching, and the S/Ca is lower than that in the general ettringite.

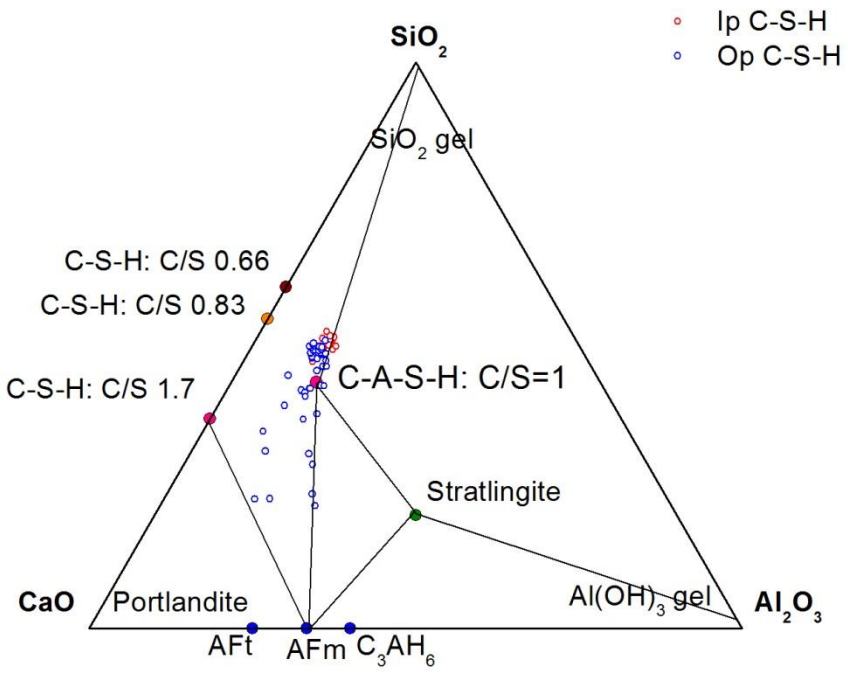


Figure 5.18 CaO-$Al_2O_3$-$SiO_2$ ternary diagram for TEM-EDX phase analysis of the 13Y-WP30 cement paste after 1½ months of leaching.

The Ip C-S-H and Op C-S-H on the degraded surface of the 13Y-WP30 cement paste after 1½ months of leaching are analysed by TEM-EDX with data plotted out as CaO-$Al_2O_3$-$SiO_2$ ternary diagram in Figure 5.18. The diagram clearly shows that the points of C-S-H are more scattered than those from the unleached sample, indicating that the

C-S-H is more inhomogeneous. The average Ca/Si atomic ratio of the Op C-S-H is higher than that in the Ip C-S-H, probably due to the lower content of Ca in the Ip C-S-H in the cement paste before leaching or extra $Ca^{2+}$ ions existing in the Op C-S-H for balancing the $SO_4^{2-}$ ions. The average Ca/Si atomic ratio is around 0.80, confirming the decalcification. Some of the Op C-S-H is roughly in the direction of the AFt and AFm phase, confirming the ettringite secondary formation.

### 5.4.3 Ca/Si and Al/Si atomic ratio in the C-S-H observed by TEM-EDX

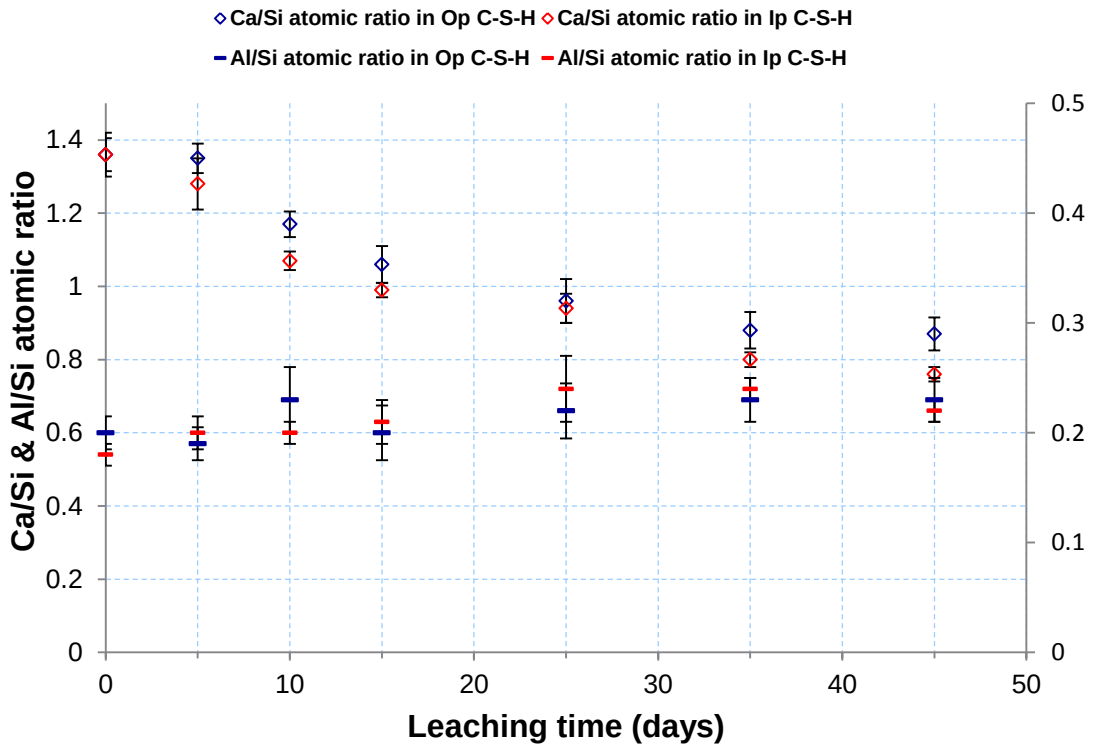


Figure 5.19 Mean Ca/Si and Al/Si atomic ratio with error bar in Op C-S-H and Ip C-S-H in the 13Y-WP30 cement paste at different leaching time.

Figure 5.19 shows the average Ca/Si and Al/Si atomic ratios in the Ip C-S-H and Op C-S-H by TEM-EDX analysis of the 13Y-WP30 cement paste before leaching and its degraded surface at different leaching times. It shows that as leaching proceeds, the Ca/Si atomic ratio in both Ip C-S-H and Op C-S-H decreases. In the first 5 days, the C-S-H is not decalcified significantly, due to that the C-S-H is decalcified after the CH

being dissolved. However, after another five days of leaching, the CH has already been dissolved on the degraded layer, which is confirmed by the BSE image (see Figure 5.6), so the C-S-H is decalcified much more. After 35 days of leaching, the decalcification of C-S-H becomes slowly, as there are not many Ca ions left in the interlayer of the C-S-H chain to be dissolved. It is also observed that the Ca/Si atomic ratio in the Ip C-S-H is statistically lower than that in the Op C-S-H. As leaching proceeds, the average Al/Si atomic ratio slightly increases due to more pozzolanic reaction of the PFA which are rich in Al content. The Ca/Si atomic ratio of the C-S-H in the cement paste before leaching observed by TEM-EDX is lower than that observed by SEM-EDX (see Figure 5.9), because the CH is mistakenly analysed with the C-S-H from SEM-EDX. The Ca/Si atomic ratio of the C-S-H on the degraded surface of the cement paste after leaching observed by TEM-EDX is lower than that observed by SEM-EDX, because SEM-EDX has larger interaction volume of incident beam and thus can measure the atomic ratio in deeper subsurface. As mentioned in section 4.3.2 that the decalcification of C-S-H occurred from the surface to the core of the cement paste, so the deeper the analysis, the higher the Ca/Si.

## 5.5 Evolution of atomic-scale structure studied by Solid-state MAS NMR

### 5.5.1 $^{29}$Si solid state MAS NMR spectra

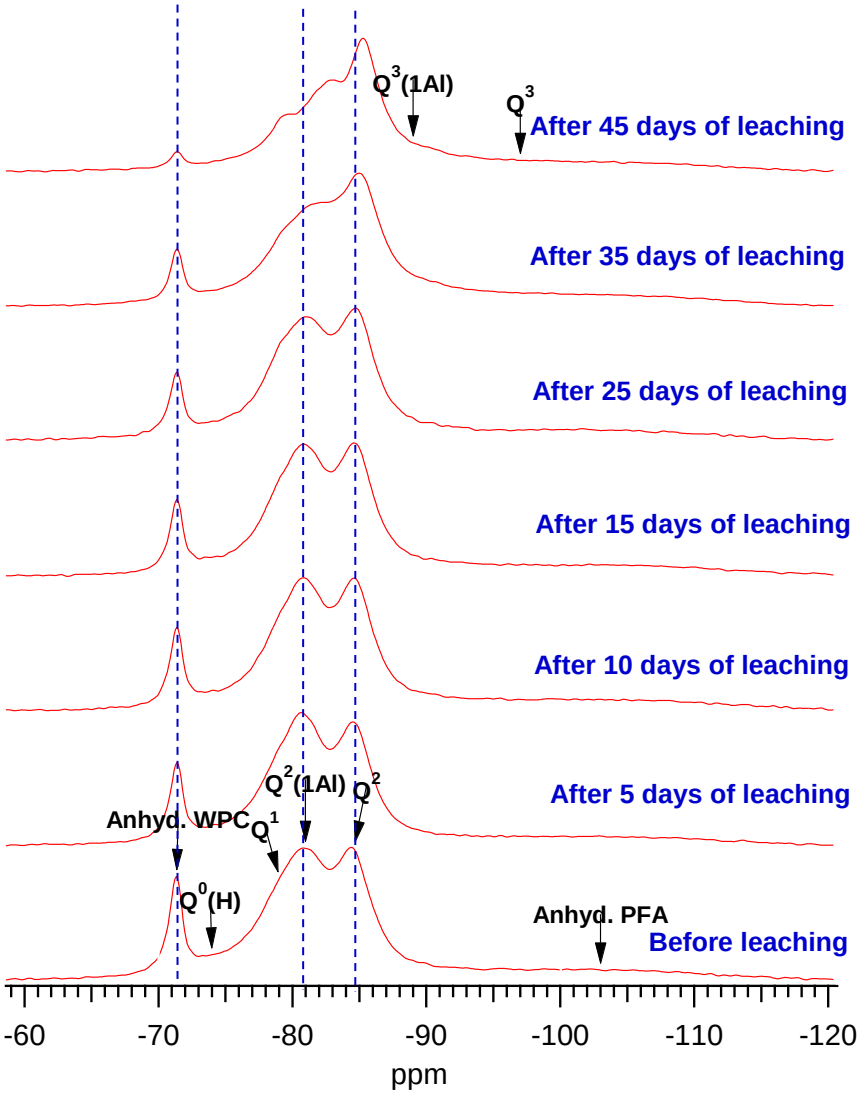


Figure 5.20 $^{29}$Si solid state MAS NMR spectra for the 13Y-WP30 cement paste before leaching and at various leaching time.

Figure 5.20 shows a set of the $^{29}Si$ solid state MAS NMR spectra for the 13Y-WP30 cement paste before leaching and at various leaching time. The spectrum for the 13Y-WP30 cement paste before leaching shows peaks at -71.3 ppm, -74 ppm, -78 ppm, -80.9 ppm, -84.5 ppm, -103 ppm corresponding to $Q^0$, $Q^0$(H), $Q^1$, $Q^2$(1Al), $Q^2$ and $Q^4$, which are the same as observed in 1Y-WP30 cement paste before leaching. The $Q^0$ represents isolated tetrahedron, and in the 13 years old blended cement paste, it is β-belite; the $Q^0$(H) is a hydrated monomeric silicate phase, displaying a broad peak at around -74 ppm; the $Q^1$, $Q^2$(1Al) and $Q^2$ indicate the resonance from the C-A-S-H; the $Q^4$ is the chemical shift of anhydrous PFA which has a structure formed from cross-linked silica tetrahedra. The spectra show that as leaching proceeds: the amount of β-belite gradually decreases due to the addition of water which induces the anhydrous cements secondary hydrate; in terms of intensity, $Q^2$ increases whereas $Q^1$ decreases, indicating the MCL of the C-A-S-H increases; after ½ month of leaching, when the C-S-H has already decalcified as observed by the SEM-EDX and TEM-EDX, a broad peak at around -90 ppm is observed, indicating the formation of $Q^3$(1Al) and $Q^3$ units in the cement paste (Komarneni et al., 1985, Cong and Kirkpatrick, 1996b), but it is very difficult to separate them due to their severe overlap. They become more dominant after 1½ months of leaching as shown in the Figure 5.20. The presence of $Q^3$(1Al) and $Q^3$ units indicates that a considerable degree of silicate cross-linked has occurred during the leaching process, and this is also observed during the leaching of the 1Y-WP30 cement paste.

As shown in the spectra in Figure 5.20, the chemical shifts of the $Q^2$(1Al) and $Q^2$ sites moves to increasingly negative values as leaching proceeds. Same phenomenon is also observed in the 1Y-WP30 cement paste during the leaching (see Figure 4.15). Figure 5.21 illustrates that during the first ½ month of leaching, the chemical shifts for the $Q^2$(1Al) and $Q^2$ Si sites do not change significantly. However, after 1½ months of

leaching, they have largely changed. The reason for the change of chemical shifts has already been explained in Chapter 4.

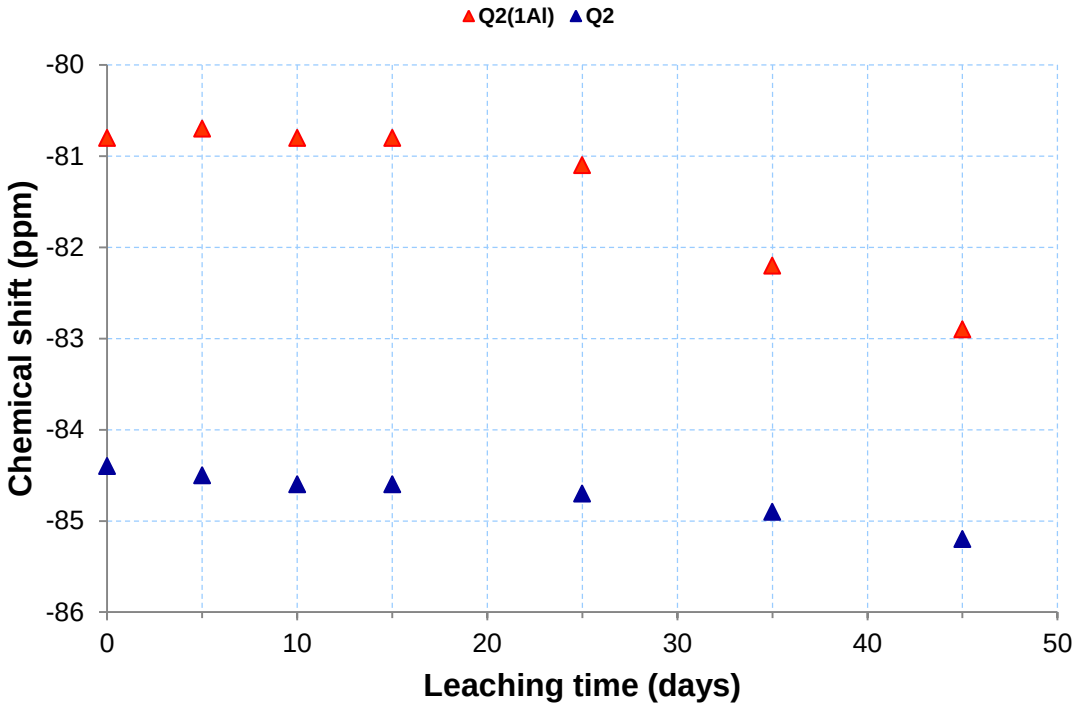


Figure 5.21 Chemical shifts of the $Q^2$(1Al) and $Q^2$ sites at various leaching time.

The spectrum for the 13Y-WP30 cement paste before leaching fitted with the $Q^0$, $Q^0$(H), $Q^1$, $Q^2$(1Al), $Q^2$ and $Q^4$ is shown Figure 5.22. The percentage of Si attributed to each peak is determined by using the software Igor. It is then used to calculate the Al/Si=0.20 and MCL=13.8 using equations 2.6 and 2.7, with results listed in Table 5.1. Compared to the 9 years old sample analysed by Taylor, in which the Al/Si was 0.19 and MCL was 12.4, the Al/Si atomic ratio slightly increases suggesting that more Al substitutes Si probably due to further hydration of PFA which is high in Al content; the MCL increases as a result of more cement being hydrated. The spectrum for the 13Y-WP30 cement paste after 1½ months of leaching has also been fitted by using Igor, and two more peaks are identified, *i.e.* $Q^3$(1Al) and $Q^3$ at -90.1 and -94.5 ppm, respectively. The Ai/Si and MCL of the C-S-H in the leached sample are not calculated due to the complexity of the aluminosilicate anion structure in the paste.

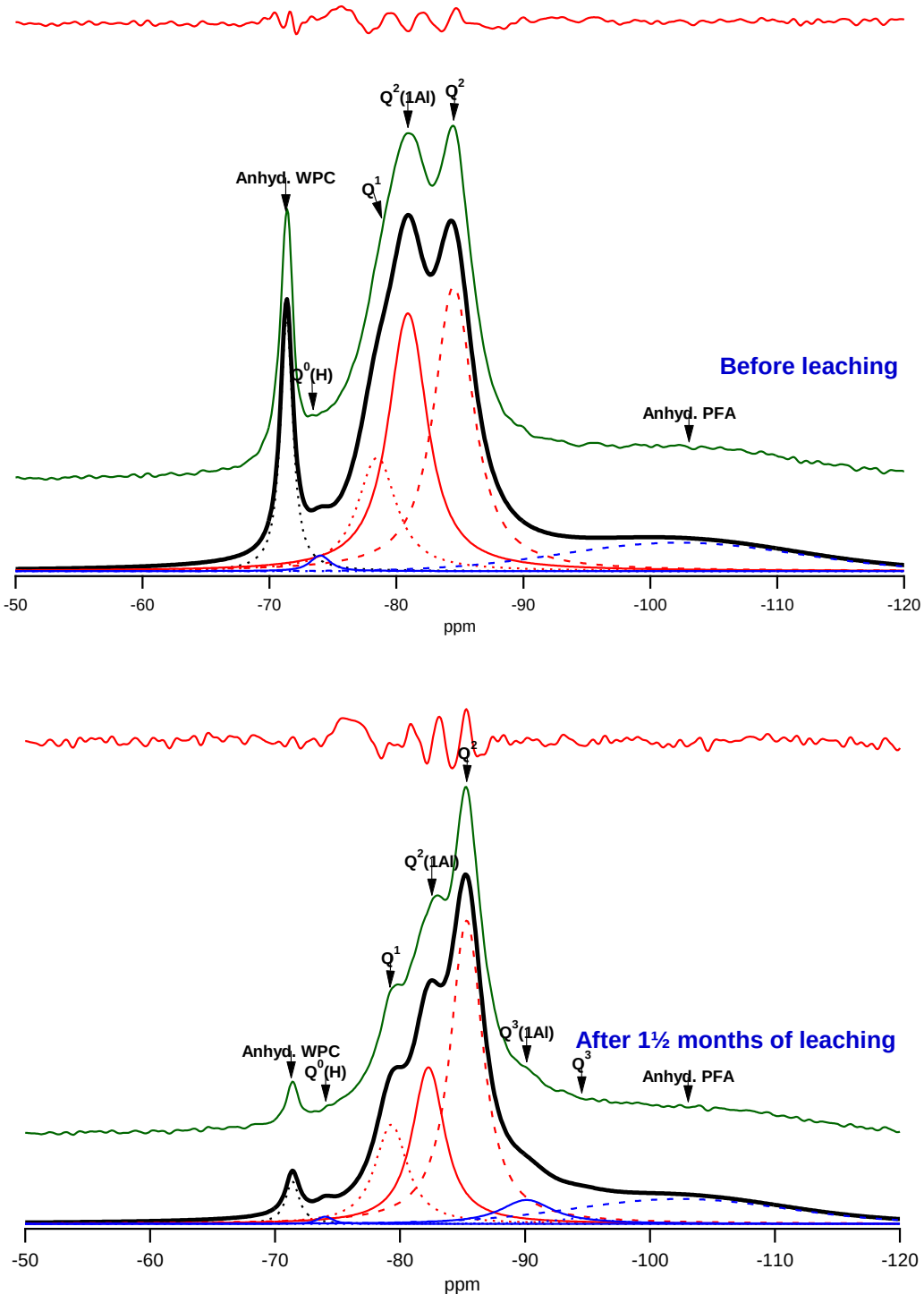


Figure 5.22 $^{29}$Si solid state MAS NMR spectra for 13Y-WP30 before leaching (top graph) and after 1½ months of leaching (bottom graph). Each graph includes the experimental spectrum (middle green line), the fitting peaks (bottom lines), and the residual (top red line: x1).

Table 5.1 $^{29}$Si chemical shifts and semi-quantitative data for the 13Y-WP30 cement paste before and after 1½ months of leaching.

| | | $Q^0$ | $Q^0$(H) | $Q^1$ | $Q^2$(1Al) | $Q^2$ | $Q^3$(1Al) | $Q^3$ | $Q^4$ |
|---|---|---|---|---|---|---|---|---|---|
| Before leaching | Chemical shift | -71.4 | -74 | -78.5 | -80.9 | -84.5 | - | - | -102.3 |
| | Percentage(%) | 9.4 | 0.9 | 13.1 | 29.8 | 32.9 | - | - | 13.8 |
| | Al/Si | 0.20 | | | | | | | |
| | MCL | 13.8 | | | | | | | |
| After leaching | Chemical shift | -71.4 | -74 | -79.3 | -82.3 | -85.3 | -90.1 | -94.5 | -102.4 |
| | Percentage(%) | 2.4 | 0.4 | 13.2 | 20.8 | 40.3 | 5.2 | 1.2 | 16.5 |
| | Al/Si | - | | | | | | | |
| | MCL | - | | | | | | | |

## 5.5.2 $^{27}$Al solid state MAS NMR spectra

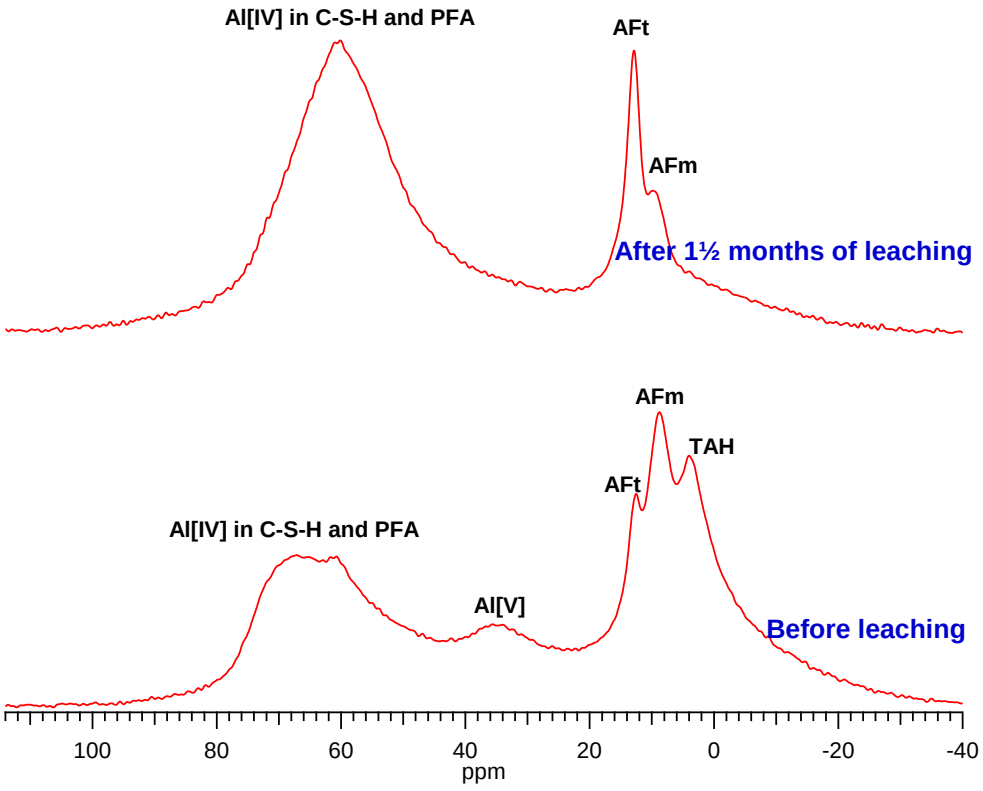


Figure 5.23 $^{27}$Al solid state MAS NMR spectra for 13Y-WP30 cement paste before leaching (bottom spectrum) and after 1½ months of leaching (top spectrum)

The $^{27}$Al SS MAS NMR spectra illustrated in Figure 5.23 for the 13Y-WP30 cement paste before and after 1½ months of leaching are analysed to investigate the evolution of Al coordinated structures in the cement paste during leaching. In the 13Y-WP30 cement paste before leaching, there are six Al resonances, *i.e*. 67.0 ppm, 60.7 ppm 35.5 ppm, 12.5 ppm, 8.7 ppm and 3.9 ppm. The first two peaks are assigned to Al[IV] coordination. More specifically, the first peak is assigned to Al presented in the bridging position and connected to two Si tetrahedral sites in the aluminosilicate (Jansen et al., 1998, Andersen et al., 2006, Skibsted and Hall, 2008), and the second peak is assigned to the Al in the PFA (Puertas and Fernandez-Jimenez, 2003). The third peak is assigned to the Al[V] coordination in the interlayer for balancing. The last three peaks are assigned to Al[VI]. More specifically, the peaks at 12.5 ppm, 8.7 ppm correspond to AFt and AFm, respectively, and the last peak is assigned to the TAH as mentioned in section 4.4.2 (Skibsted and Hall, 2008). The Al resonances in the 13Y-WP30 cement paste are similar to those in the 9 years old sample observed by Taylor (2010), indicating the aluminate structure does not change significantly after four more years of hydration. The Al spectrum for the 13Y-WP30 cement paste after 1½ months of leaching illustrates that the Al[IV] resonance at 60.1 ppm becomes dominant, indicating the cross-linking has already largely occurred due to the leaching, however, it is difficult to identify whether the Al[V] still exists after 1½ months of leaching due to the poor resolution of the spectrum. The peak for TAH has already disappeared after 1½ months leaching, indicating the phase is dissolved during the water leaching. The amount of AFt slightly increases after leaching, which is consistent with the XRD result due to the secondary ettringite formation, The amount of AFm decreases due to its dissolution during the leaching, providing the essential elements of S and Al for forming the secondary ettringite phases (Faucon et al., 1998a, Haga et al., 2005).

## 5.6 Summary

This chapter assesses the effect of ageing and water leaching on the micro-scale，nano-scale and atomic-scale structures as well as the chemical compositions of 13 years old Portland cement paste blended with 30% pulverised fly ash.

Regarding the effects of ageing on the cement paste, it is observed that after four years of hydration, the MCL of the C-S-H chain has increased from 12.4 to 13.8, indicating the cement paste has further hydrated.

It is also found that water leaching influences the structures and chemical compositions of the 13Y-WP30 cement paste: (1) the CH has been absolutely dissolved after 1½ months of leaching; (2) the amount of ettringite has slightly increased due to its secondary formation; (3) the microstructure of the cement paste becomes more porous; (4) the morphology of Ip C-S-H becomes more porous and the Op C-S-H changes from one-dimensional fibrillar feature and two dimensional foil like feature to three dimentional net-like feature, and abundance of coarse fibrillar C-S-H, forms in the pores; (5) the C-S-H has been largely decalcified due to the loss of Ca ions in the interlayer of the C-S-H chain; and the average Ca/Si of Ip C-S-H and Op C-S-H which are both 1.36 before leaching, have decreased to 0.76 and 0.87 after leaching, suggesting the Ip C-S-H is decalcified more than the Op C-S-H; (6) $Q^3$(1Al) and $Q^3$ have formed in the interlayer of the C-S-H chain, suggesting the transformation of single chain to double chain structure of the C-S-H, and they are observed after the Ca ions having been already leached from the interlayer of the C-S-H chain; (7) the aluminosilicate anion is further polymerized.

# Chapter 6 Characterisation and water leaching on 13 year old white Portland cement paste blended with 50% pulverised fly ash

## 6.1 Introduction

This chapter demonstrates and discusses the experimental results obtained from 13Y-WP50 cement paste due to the water leaching. Four sections are created according different aspects of observation:

- Phase identification and quantification studied by XRD and thermal analysis;
- Evolution of structure and chemical composition at micro-scale studied by SEM-EDX;
- Evolution of structure and chemical composition at nano-scale studied by TEM-EDX;
- Evolution of structure at atomic-scale studied by Solid-state MAS NMR.

## 6.2 Bulk analysis-Phase identification and quantification studied by XRD and thermal analysis

Figure 6.1 shows XRD patterns for the 13Y-WP50 cement paste before leaching and after leaching. Before leaching, the main phases are C-S-H gel, CH, residual β-belite, ettringite, quartz and mullite, which are similar to the phases observed in the 13Y-WP30 cement paste. After 1½ months of leaching, the sharp peaks corresponding to CH have already disappeared due to its dissolution nature, and the content of β-belite has decreased significantly due to the secondary hydration. On the contrary, the intensity of the peaks assigned to ettringite has obviously increased, because of the secondary ettringite formation. Sharp peaks at 30 2θ assigned to calcite are present, and their formation mechanism has been explained in Chapter 4. After 55 days of leaching, the patterns do not change largely except that the content of ettringite has

decreased due to its dissolution nature. The C-S-H is present in the cement paste before leaching and after leaching.

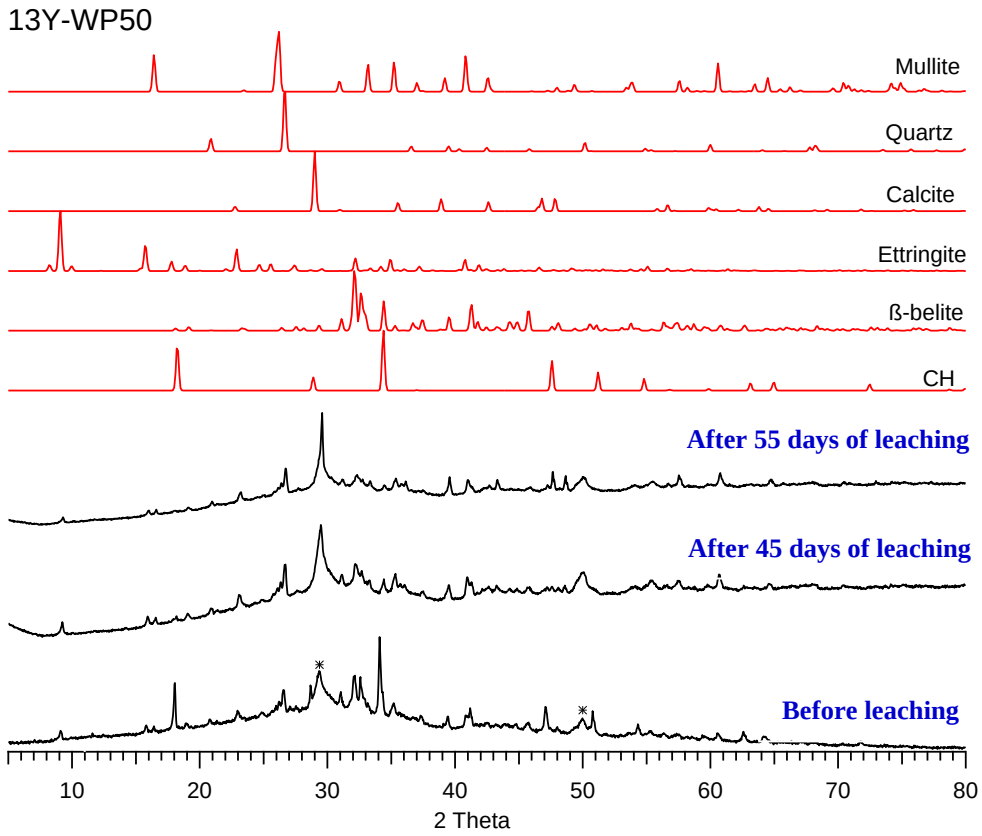


Figure 6.1 XRD patterns of 13Y-WP50 cement paste before leaching, after 45 days and 55 days of leaching. All are set to the same intensity scale. The relevant standard phase traces are included and the asterisk labelled peaks correspond to the C-S-H gel phase.

Figure 6.2 shows the CH content calculated from thermal analysis in the 13Y-WP50 cement paste before leaching and at various leaching time. Before leaching, the CH content is 6.3% as ignited weight in the 13 years aged 50% PFA blended cement paste. Compared to the CH in the 13Y-WP30 which is 10.57% as ignited weight, the CH content in the 13Y-WP50 is much less, due to higher content of PFA leading to more CH consumption during the pozzlanic reaction and lower content of WPC resulting in less formation of CH. The content of CH was 5.9% when the cement paste was 9 years old (Taylor, 2010), and the slightly increase of CH content after four years of hydration is due to the more hydration of cement paste. During the first 5 days of leaching, the

CH has dramatically decreased by 2.3% as ignited weight, because the CH is easily dissolved in water. Since then, it gradually decreases until it is totally dissolved after 45 days of leaching, which is consistent with the XRD observation.

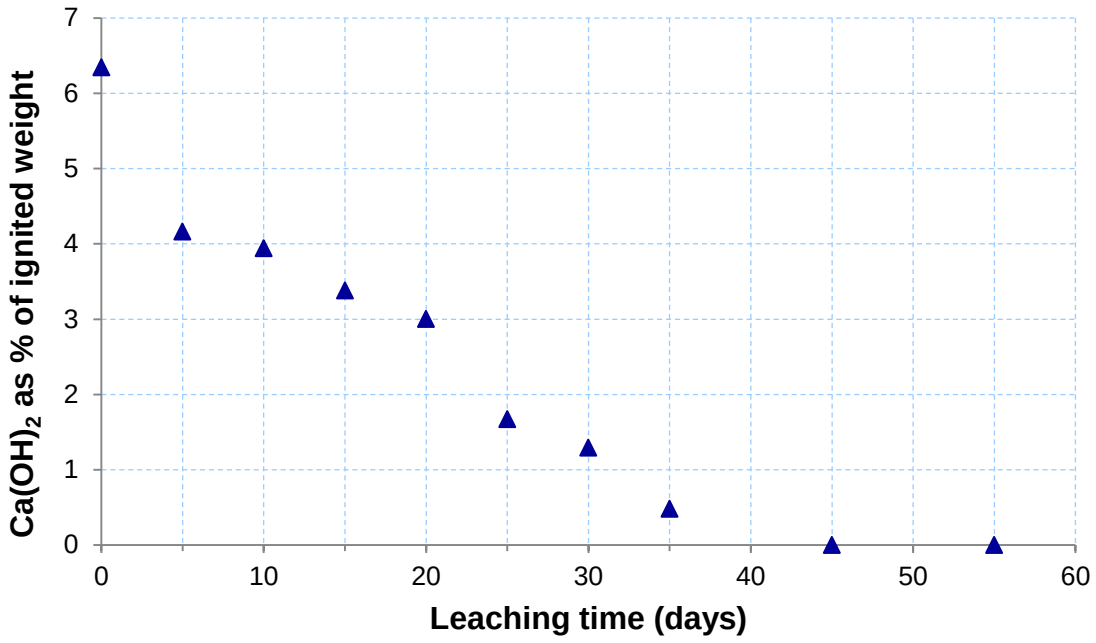


Figure 6.2 $Ca(OH)_2$ evolution in 13Y-WP50 cement paste during 55 days of water leaching

## 6.3 Evolution of structure and chemical compositions at micro-scale studied by SEM-EDX

In the 13Y-WP50 cement paste before leaching, the main phases are similar to those are in the 13Y-WP30 cement paste, however, the microstructure is more porous and more unreacted PFA is left, as shown in the top graph in Figure 6.4. These are due to the higher PFA replacement content which requires more CH to activate, but the formation of CH is limited as the amount of WPC is less, thus less amount of C-S-H is formed and the porosity increases. Detailed microstructure 13Y-WP50 cement paste is shown in the bottom graph with a high magnification in Figure 6.4. There is abundant of Ip C-S-H, and there are some fully hydrated small cement grains which are labelled

with black arrows in the graph. Layers of AFm phases are observed around the anhydrous PFA, as shown in the middle of the graph. The average size of the AFm phases in this graph is approximately 10 μm, however, it is not observed from the XRD, probably due to the lack of the crystalline feature. The C-S-H and AFm are analysed by EDX which is equipped with the SEM, and the data are plotted out in Figure 6.3 in terms of $CaO$-$Al_2O_3$-$SiO_2$ ternary diagram. The diagram illustrates that the Ca/Si atomic ratio is 1.32 ± 0.09 (n=36), which is much lower than that in the 13Y-WP30 cement paste due to the higher replacement of PFA which has lower Ca content, and there are two clear trend lines indicating that the presences of microcrystalline CH and AFm. The average Al/Si atomic ratio is 0.22 ± 0.02 (n=36), and it is slightly higher than that in the 13Y-WP30, due to the higher replacement of PFA which is higher in the Al content.

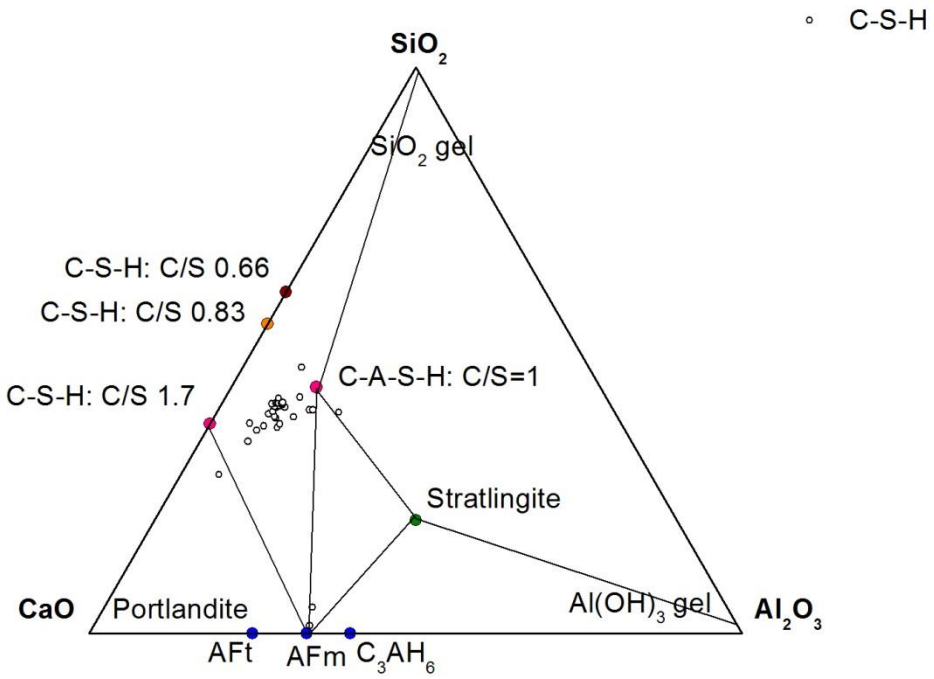


Figure 6.3 $CaO$-$Al_2O_3$-$SiO_2$ ternary diagram for SEM-EDX phase analysis of the 13Y-WP50 cement paste before leaching.

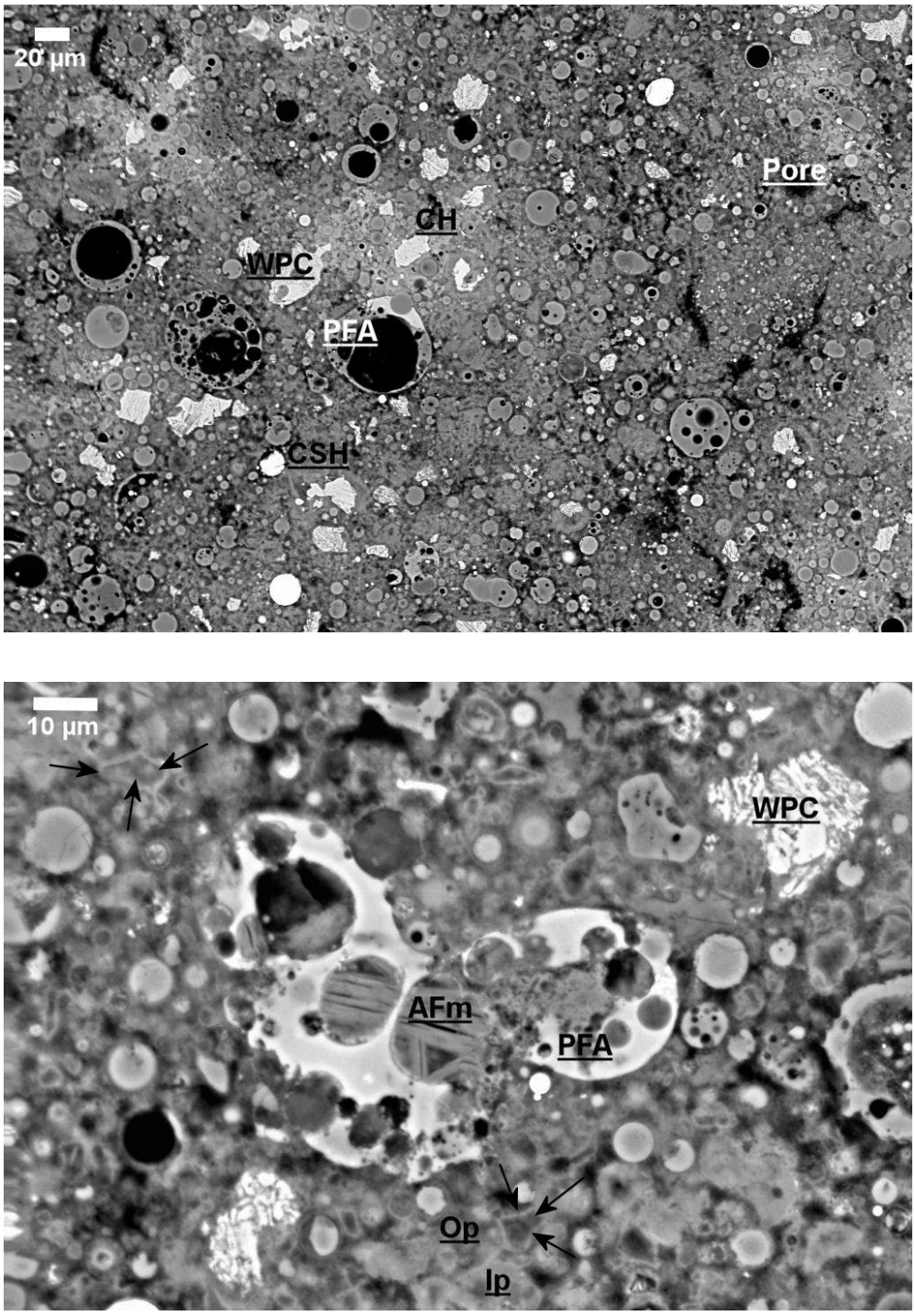


Figure 6.4 Backscattered images of the microstructure of the 13Y-WP50 cement paste before leaching with 500X (top) and 2000X (bottom) magnification. Regions of pulverised fly ash (PFA), white Portland cement (WPC), calcium hydroxide (CH), C-S-H gel (CSH), AFm phase (AFm), inner product C-S-H (Ip), outer product C-S-H (Op) and pores (Pore) are labelled.

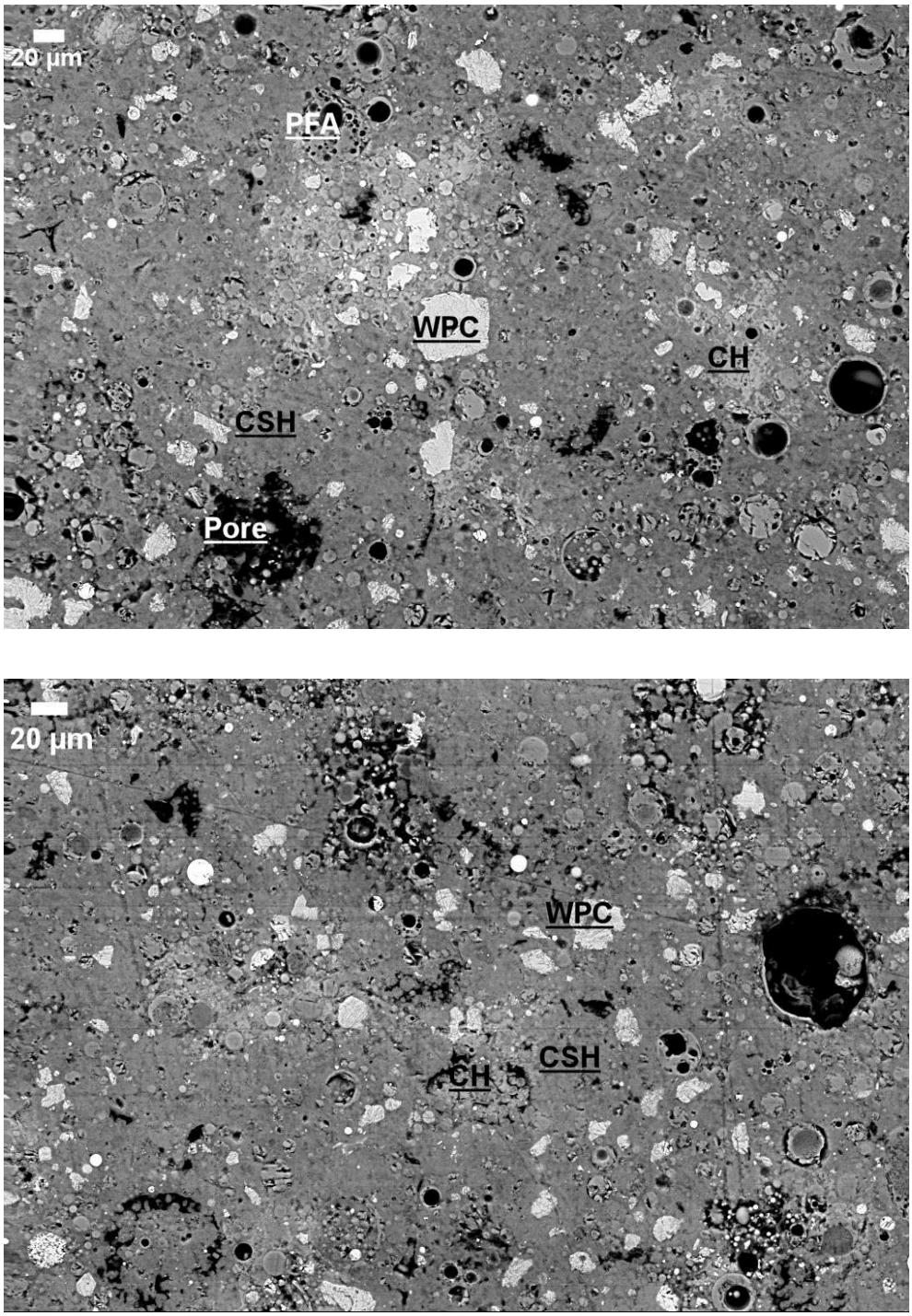


Figure 6.5 Backscattered images illustrating the microstructure of the surface area of the 13Y-WP50 cement paste after 5 days (top) and 10 days (bottom) of leaching with 500X magnification. Regions of white Portland cement (WPC), calcium hydroxide (CH) and C-S-H gel (CSH) are labelled.

Figure 6.5 shows the BSE images of the degraded surface of 13Y-WP50 cement paste after 5 and 10 days of leaching. It can be seen that the quantity of CH has gradually decreased, due to its easy dissolution nature, and that is consistent with the XRD and thermal analysis observations.

Figure 6.6 shows the microstructure of the degraded surface of the 13Y-WP50 cement paste after 55 days of leaching. It can be observed that after 55 days of intense water leaching, the CH and anhydrous cement grains have absolutely disappeared from the degraded surface, and the main phases left on the degraded surface are PFA grains and C-S-H gel. The microstructure of the cement paste has become more porous due to the dissolution of CH and the decalcification of the C-S-H, although some C-S-H is formed simultaneously. Larger quantity of Ip C-S-H and fully hydrated cement grains with bright rims are observed in the BSE image with a higher magnification, indicating the addition of water induces further hydration of the cement paste.

The C-S-H are analysed by using SEM-EDX, and the results are plotted out in terms of $CaO\text{-}Al_2O_3\text{-}SiO_2$ ternary diagram, as shown in Figure 6.7. The diagram shows that the average Ca/Si ratio is 0.68 ± 0.05 (n=45) after 55 days of leaching, which is much lower than that in the cement paste before leaching, suggesting water leaching induces the C-S-H decalcification. The points for the C-S-H are much scatter than those in the cement paste before leaching, suggesting the C-S-H is more inhomogeneous, because the two types of C-S-H have different leaching rates, and the decalcification and secondary formation occurs at the same time making the decalcification even more complicated.

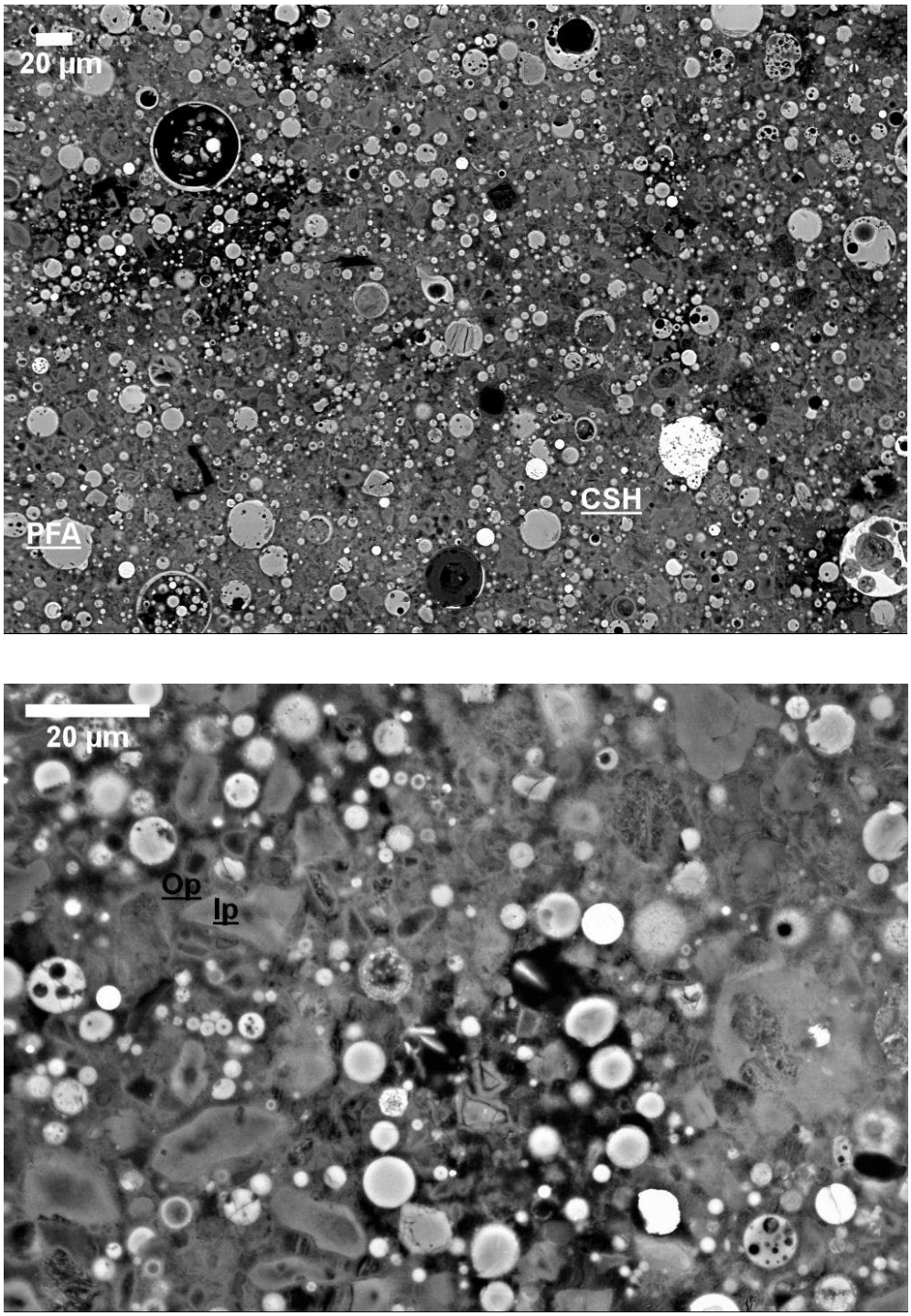


Figure 6.6 Backscattered image illustrating the microstructure of the surface area of the 13Y-WP50 cement paste after 55 days of leaching with 500X (top) and 2000X (bottom) magnification. Regions of pulverised fly ash (PFA), C-S-H gel (CSH), Ip C-S-H (Ip) and Op C-S-H ((Op) are labelled.

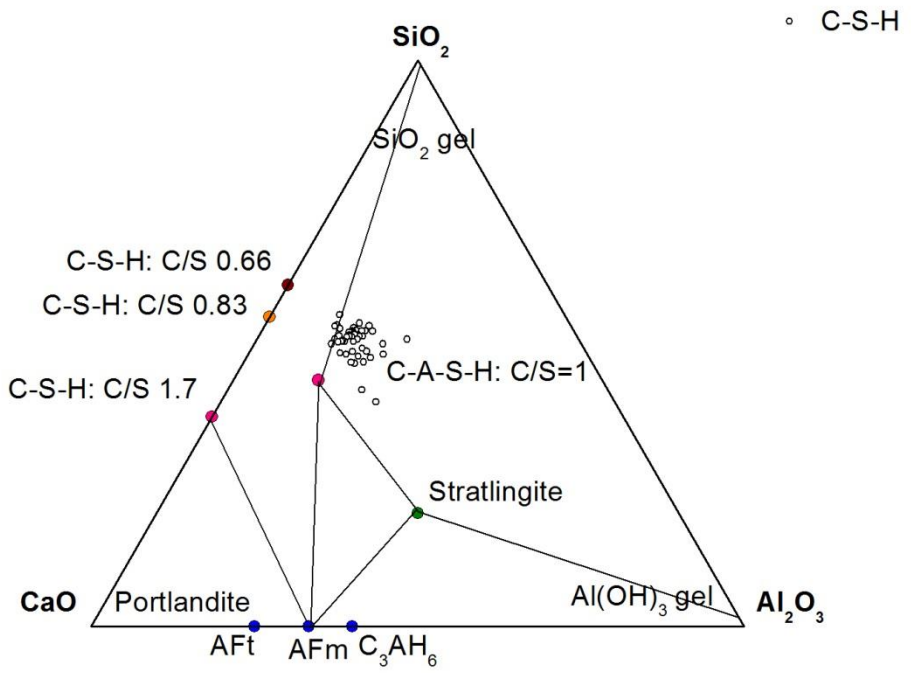


Figure 6.7 CaO-$Al_2O_3$-$SiO_2$ ternary diagram for SEM-EDX phase analysis of the 13Y-WP50 cement paste after 55 days of leaching.

Figure 6.8 shows the average Ca/Si atomic ratio with error bars from the degraded surface of the 13Y-WP50 cement paste during 55 days of leaching. It can be seen that the average Ca/Si atomic ratio decreases as the leaching proceeds. In the first 5 days of leaching, the Ca/Si atomic ratio in the C-S-H slightly decreases from 1.32 to 1.30, and the C-S-H is not decalcified significantly, probably due to fact that the C-S-H is decalcified after the CH being dissolved. However, after another five days of leaching, the CH has already been dissolved on the degraded layer, which can be confirmed by the BSE image (see Figure 6.5). In addition, after 25 days of leaching, the decalcification becomes slowly, as there are not sufficient Ca ions to be leached out from the interlayer of the C-S-H chain. Eventually, the Ca/Si atomic ratio has decreased to 0.68 after 55 days of leaching, which is statistically higher than that in the 1Y-WP30 cement paste after 55 days of leaching. The 1Y-WP30 cement paste has higher CH content before leaching, so more porosity is produced by leaching, and

consequently more C-S-H is decalcified. The average Al/Si atomic ratio of the C-S-H does not change statistically during the first 15 days of leaching, however, after 25 days of leaching, it has increased from 0.22 to 0.28, indicating more Al has substituted Si in the C-S-H chain.

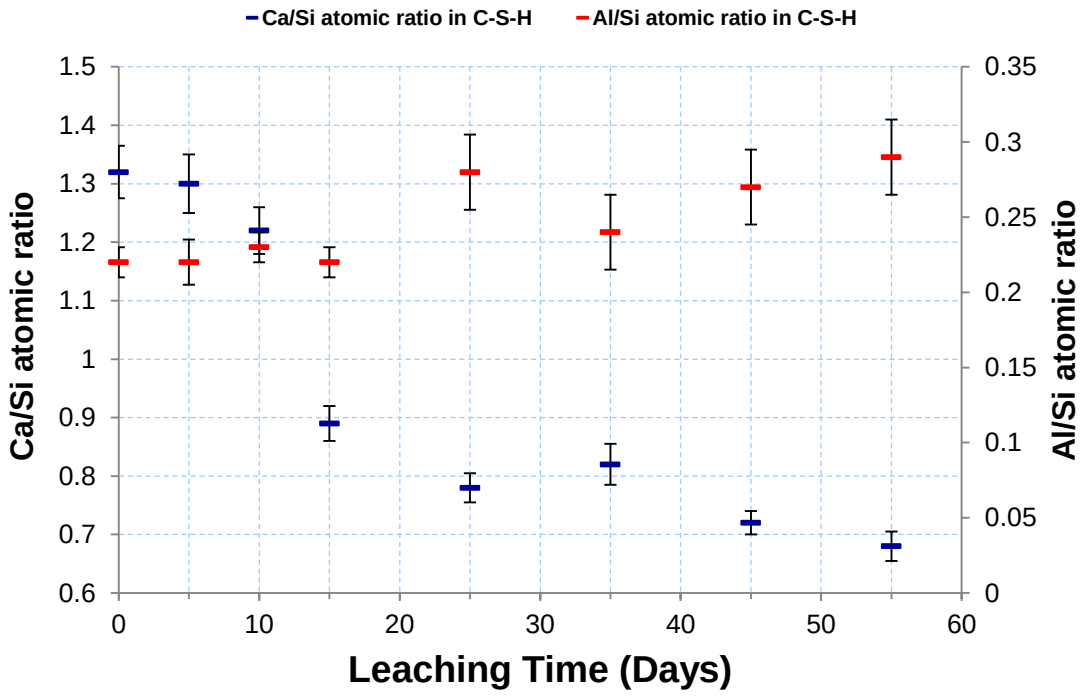


Figure 6.8 Average Ca/Si and Al/Si atomic ratio with error bar from SEM-EDX analysis of the C-S-H in the 13Y-WP50 cement paste at various time during 55 days of leaching.

## 6.4 Evolution of structure at nano-scale studied by TEM-EDX

### 6.4.1 TEM images of 13Y-WP50 cement paste before leaching

Figure 6.9 shows a typical nano-scale structure of the PFA blended cement paste, which exhibits partially unreacted and glassy fly ash, short fibrillar like Op C-S-H around the PFA grain, as well as foil-like Ip C-S-H formed in the PFA. Except that more unhyrated PFA grains are observed, the morphology is similar to that observed in the 13Y-WP30 cement paste in Chapter 5.

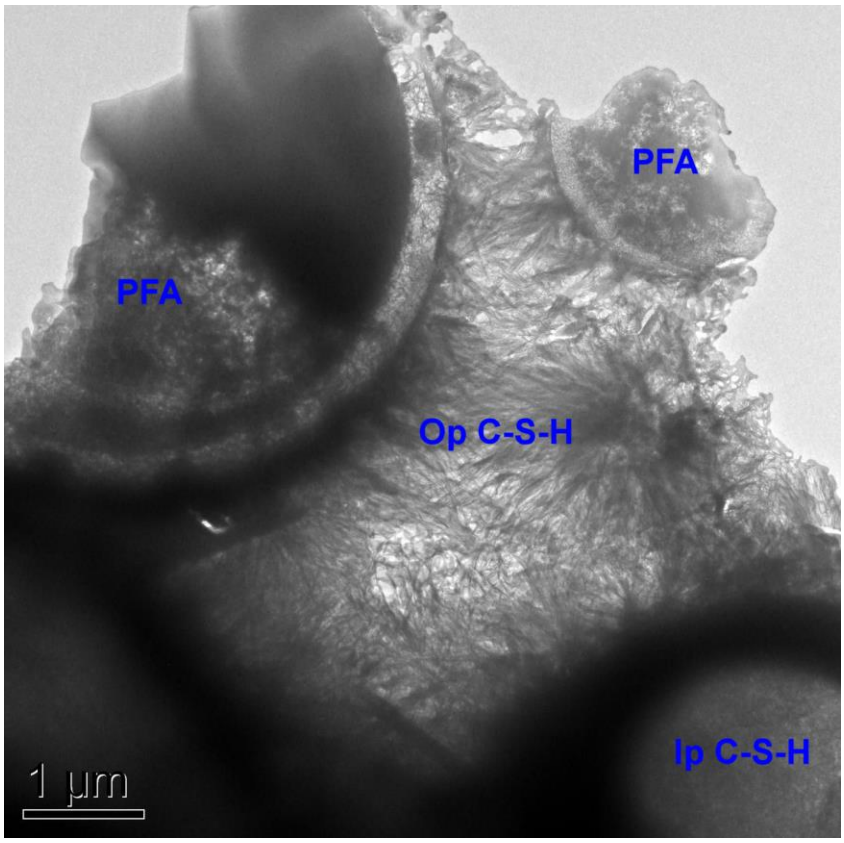


Figure 6.9 A TEM image of the 13Y-WP50 cement paste before leaching shows partially reacted fly ash grains, short fibrillar like Op C-S-H, as well as foil like Ip C-S-H.

The compact and homogeneous Ip C-S-H and fibrillar Op C-S-H with boundary is shown in the left TEM graph in Figure 6.10. It can be seen that the Op C-S-H has a short fibrillar feature with a Ca/Si atomic ratio of 1.01 observed by TEM-EDX, and the Ip C-S-H has a layered compact feature. Therefore, the Op and Ip C-S-H formed in the WPC cement paste are different with those in the PFA. The right TEM image in Figure 6.10 shows that the Op C-S-H has a fine long fibrillar feature, with a Ca/Si ratio of 1.20 observed by the local chemical composition analysis. The ratio is higher than that of the Op C-S-H in the left image, in which Op C-S-H has short fibrillar feature, indicating that Op C-S-H with a long fibrillar feature generally has a higher Ca/Si atomic ratio than that with a short fibrillar feature.

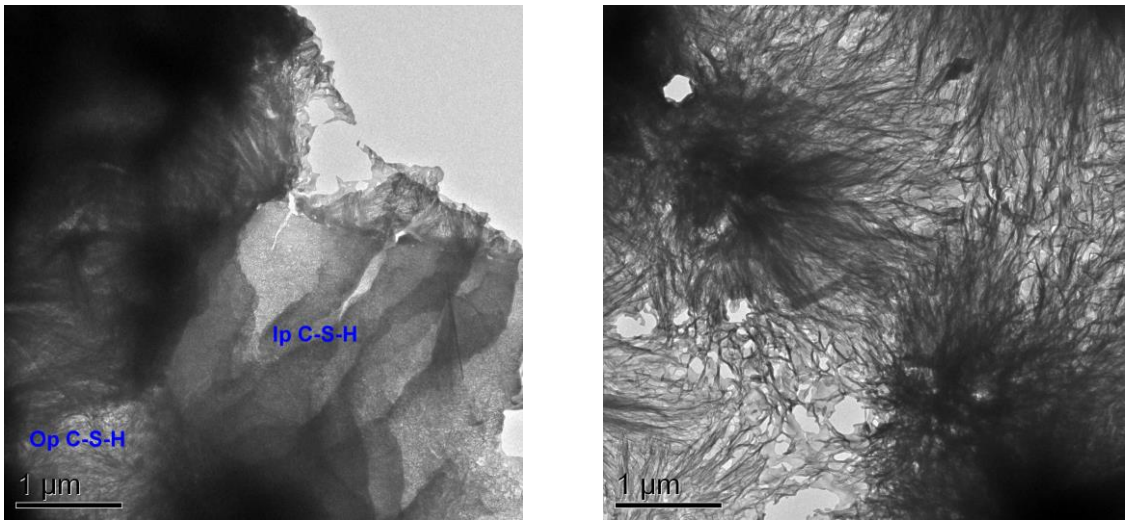


Figure 6.10 TEM images of the 13Y-WP50 cement paste before leaching showing fine and layered compact Ip C-S-H and short fibrillar Op C-S-H (left image), as well as fine long fibrillar Op C-S-H (right image).

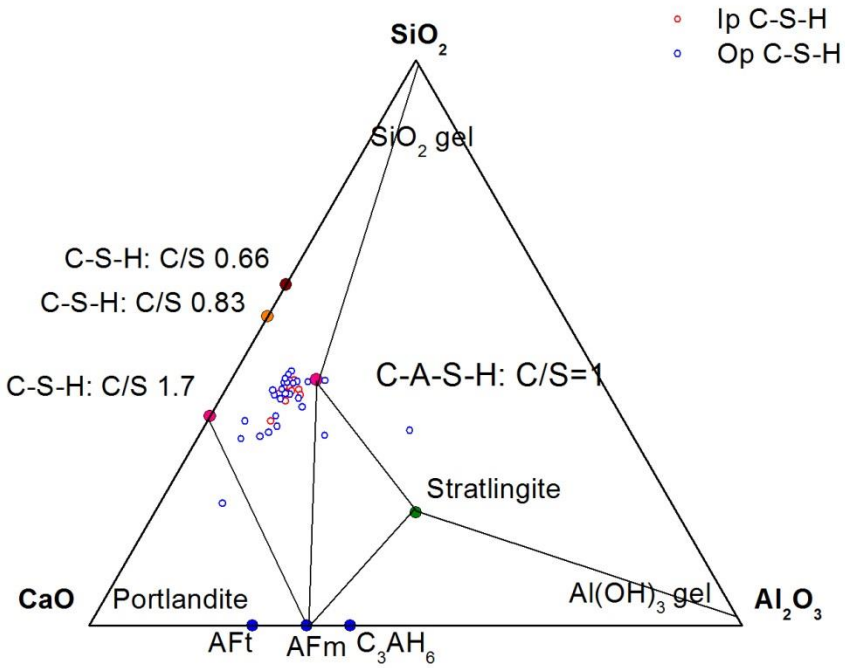


Figure 6.11 CaO-$Al_2O_3$-$SiO_2$ ternary diagram for TEM-EDX phase analysis of the 13Y-WP50 cement paste before leaching.

The EDX atomic plots given in Figure 6.11 indicate the presence of the intermixture of CH with C-S-H, as there is a trend line towards CH in the $CaO$-$Al_2O_3$-$SiO_2$ ternary diagram, however, it is not well intermixed as that formed in the alkalis activated WPC: PFA systems (Taylor, 2010). It's also observed that the average Ca/Si atomic ratio is 1.26 ± 0.12 (n=25), which is lower than that analysed by the SEM-EDX, *i.e.* 1.32 ± 0.09 (n=36). In the SEM-EDX analysis, the CH in the neighbouring site of the C-S-H may be counted as C-S-H, as there is a larger interactive beam volume. As a result, the Ca/Si atomic ratio observed by SEM-EDX is higher than that observed by TEM-EDX.

### 6.4.2 TEM images of 13Y-WP50 cement paste after leaching

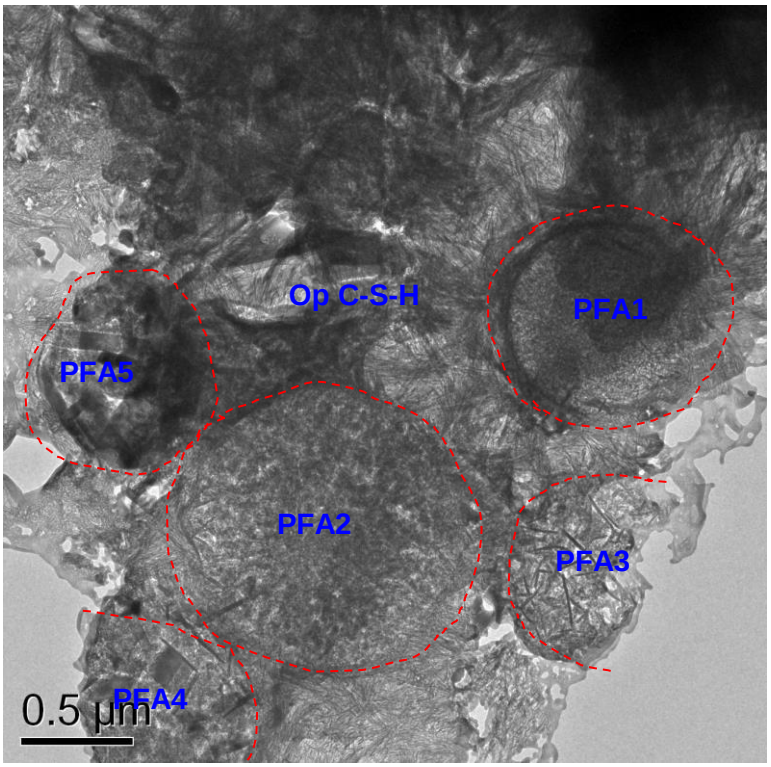


Figure 6.12 A TEM image shows fully hydrated PFA grains labelled with red dashed circles and short fibrillar Op C-S-H on the degraded surface of the 13Y-WP50 cement paste after 55 days of leaching.

A typical TEM image of the 13Y-WP50 cement paste after 55 days of leaching is presented in Figure 6.12. Abundant fully hydrated PFA grains are observed, indicating that water leaching has largely induced further hydration of the PFA. It's also found that the morphology of the Ip C-S-H in the PFA grains are varying, which are not easily

observed in the PFA cement paste hydrated at ambient temperature as they are generally not largely hydrated. The difference of morphology is probably due to the difference of chemical composition, as Diamond (2003) pointed out that there are compositional variations between different particles within the same type of PFA. The Ip C-S-H in PFA1 has a homogeneous and compact feature, which is similar to that formed in the WPC, however, the Ip C-S-H in PFA2, PFA3, PFA4 and PFA5 is less dense. There is needle-like HT phase, which has high Mg and Al content well intermixed with the Ip C-S-H in the PFA3.

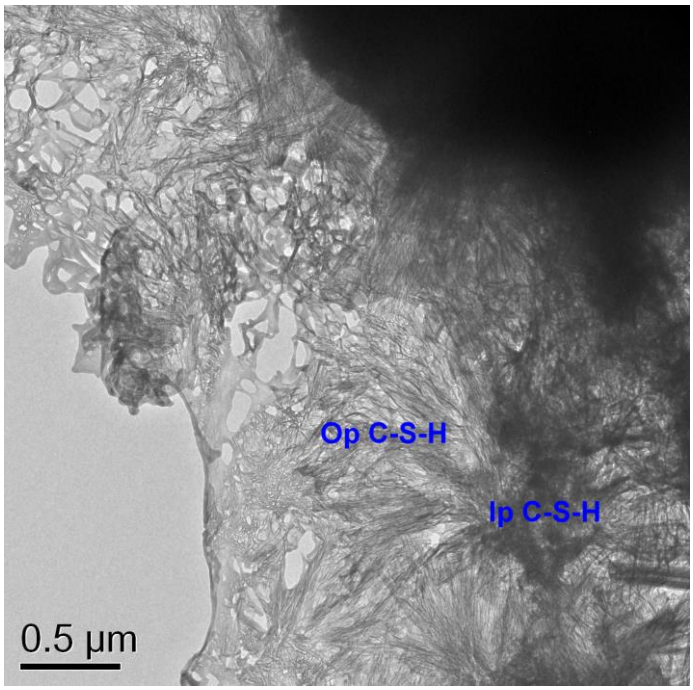


Figure 6.13 A TEM image shows compact Ip C-S-H and fine fibrillar Op C-S-H on the degraded surface of the 13Y-WP50 cement paste after 55 days of leaching.

The chemical compositions of the C-S-H are analysed by TEM-EDX and the EDX data are plotted out in terms of the $CaO$-$Al_2O_3$-$SiO_2$ ternary diagram, as shown in Figure 6.14. The diagram shows that the average Ca/Si ratio has clearly decreased dramatically to 0.68 ± 0.20 (n=30). In addition, the Ca/Si ratio in the Ip C-S-H is statistically lower than that observed in the Op C-S-H, probably due to lower content of

Ca in the Ip C-S-H in the cement paste before leaching or extra $Ca^{2+}$ ions existing in the Op C-S-H for balancing the $SO_4^{2-}$ ions.

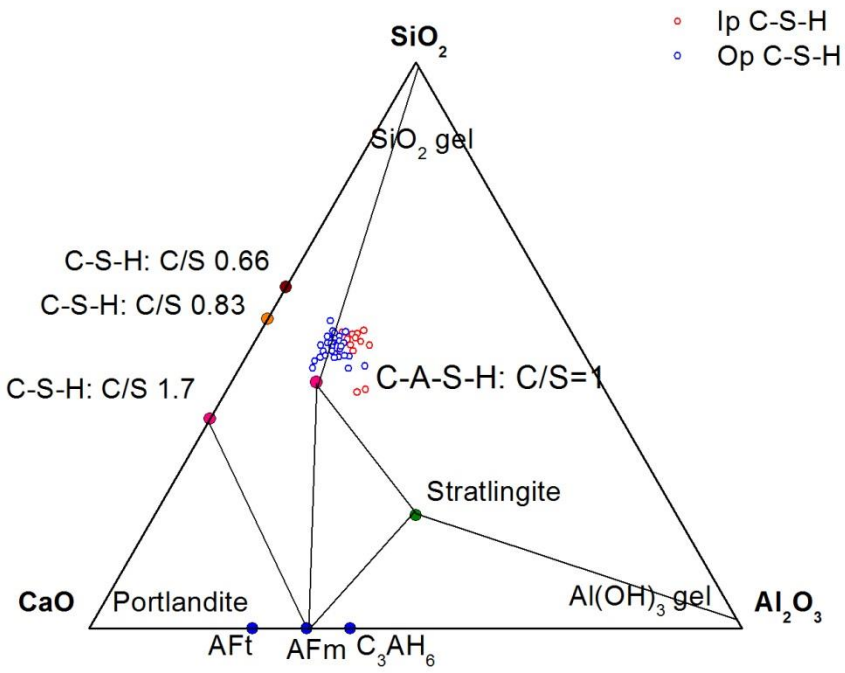


Figure 6.14 $CaO$-$Al_2O_3$-$SiO_2$ ternary diagram for TEM-EDX phase analysis of the 13Y-WP50 cement paste after 55 days of leaching.

## 6.5 Evolution of structure at atomic-scale studied by Solid-state MAS NMR

### 6.5.1 $^{29}$Si solid state MAS NMR spectra

Figure 6.15 shows a set of $^{29}$Si solid state MAS NMR spectra for the 13Y-WP50 cement paste before leaching and at various leaching time. In the 13Y-WP50 cement paste before leaching, the main Si coordinates are similar to those in the 13Y-WP30 cement paste, as shown in Chapter 5, *i.e.* $Q^0$, $Q^0$(H), $Q^1$, $Q^2$(1Al), $Q^2$ and $Q^4$. As leaching proceeds, the intensity of $Q^0$ deceases, indicating that the leaching has induced further hydration of the anhydrous cements. After 15 days of leaching, new

species are observed, *i.e.* $Q^3$(1Al) and $Q^3$, due to the cross-linking is formed across the interlayer of the C-S-H. Meanwhile, the height of the $Q^2$ peak relative to the $Q^1$ peak increases, suggesting the MCL of the C-S-H is elongated, which agrees with the observation in the leaching experiment performed on the 13Y-WP30 cement paste.

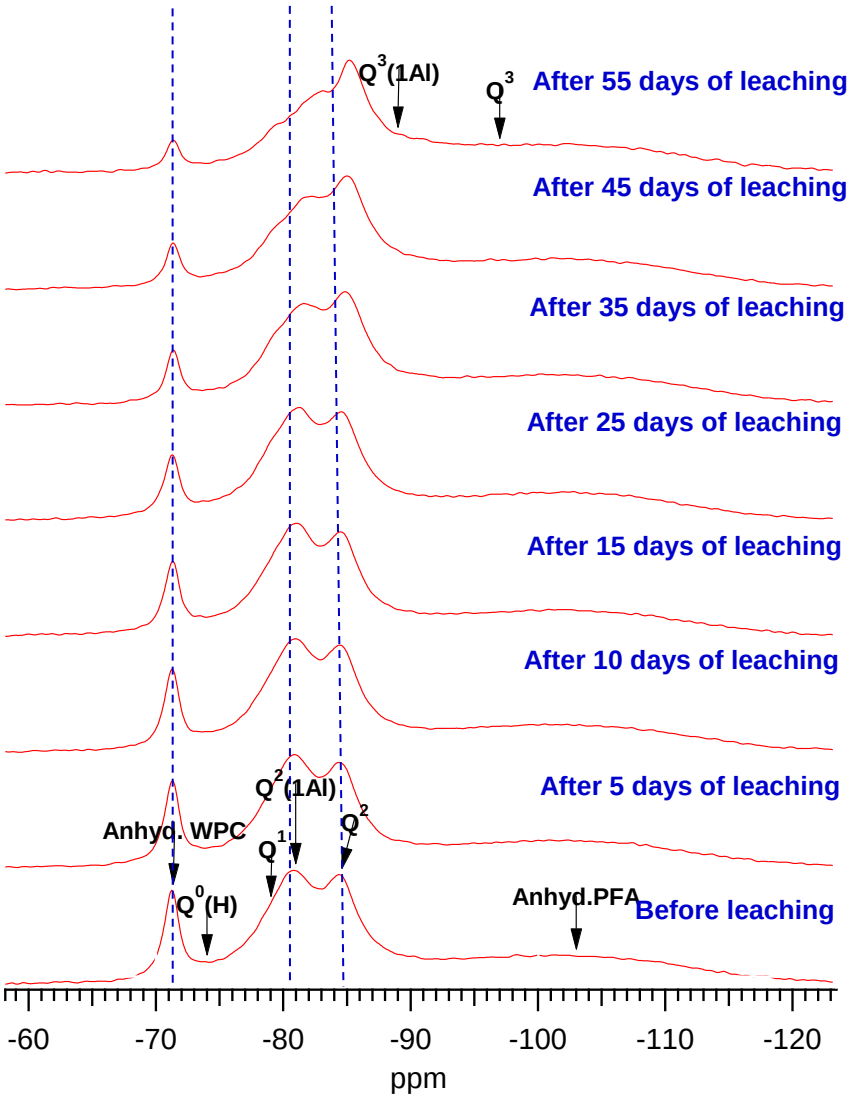


Figure 6.15 $^{29}$Si solid state MAS NMR spectra for the 13Y-WP50 cement paste before leaching and at various leaching time.

It is also shown in Figure 6.15 that the chemical shifts of the $Q^2$(1Al) and $Q^2$ gradually move to the negative side as leaching proceeds, however, the chemical shifts of anhydrous WPC do not change, indicating the change of the chemical shifts of the $Q^2$(1Al) and $Q^2$ is not due to the external factors, but due to the change of the their own chemical environment. Figure 6.16 presents the chemical shifts of the $Q^2$(1Al) and $Q^2$ at different leaching time. During the first ½ month of leaching, the chemical shifts of the $Q^2$(1Al) and $Q^2$ have slightly changed, and after ½ month of leaching, they have started to change significantly. The possible reason for this has already discussed in Chapter 4.

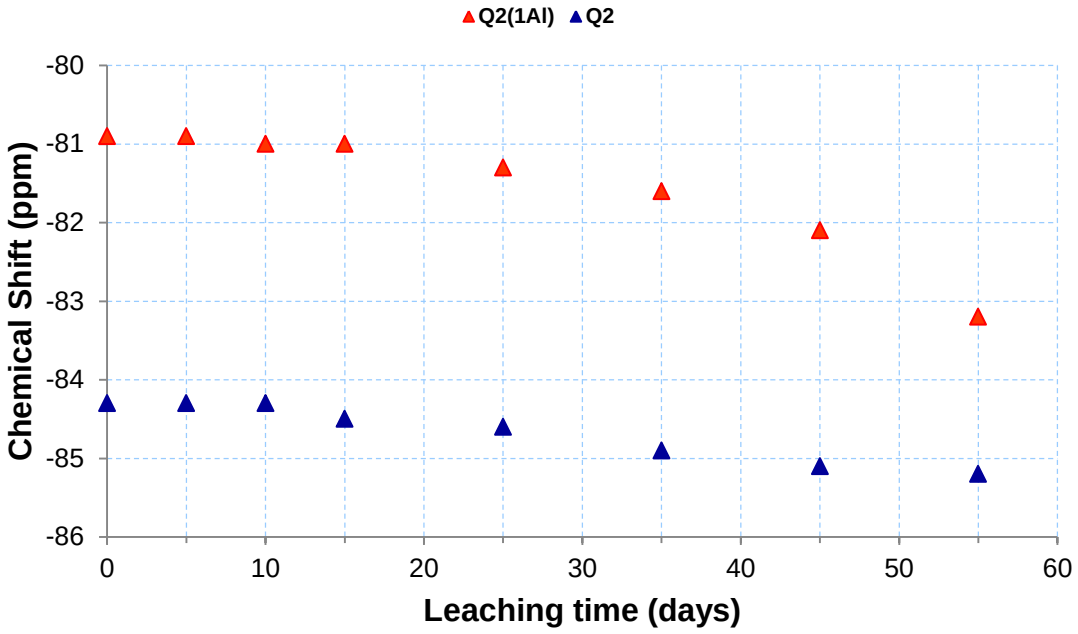


Figure 6.16 Chemical shifts of the $Q^2$(1Al) and $Q^2$ sites as a function of leaching time.

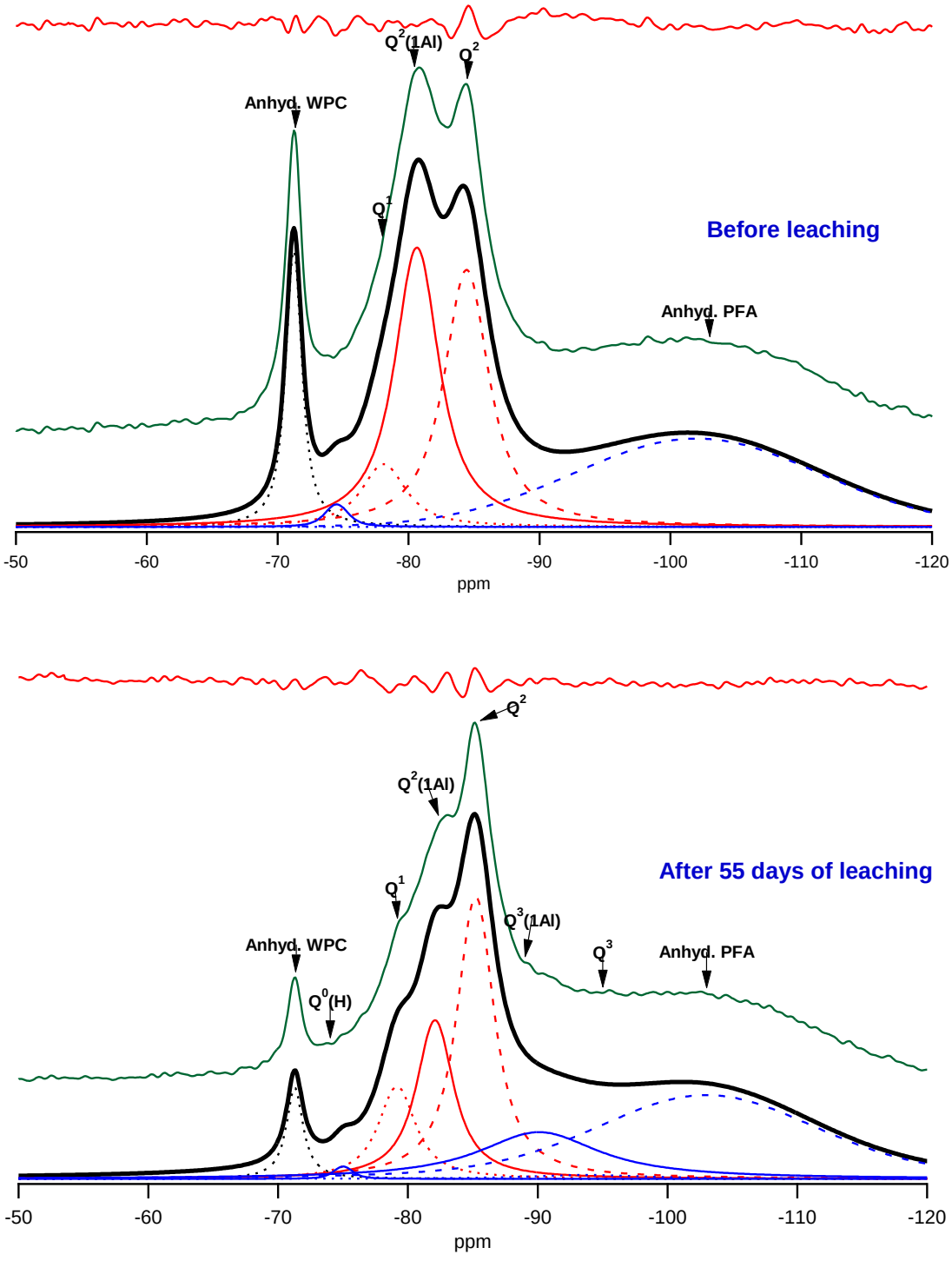


Figure 6.17 $^{29}$Si solid state MAS NMR spectra for 13Y-WP50 cement paste before leaching (top graph) and after 55 days of leaching (bottom graph). Each graph includes the experimental spectrum (middle green line), the fitting peaks (bottom lines), and the residual (top red line: x1).

Table 6.1 $^{29}$Si chemical shifts and semi-quantitative data for the 13Y-WP50 cement paste before leaching and after 55 days of leaching.

| | | $Q^0$ | $Q^0$(H) | $Q^1$ | $Q^2$(1Al) | $Q^2$ | $Q^3$(1Al) | $Q^3$ | $Q^4$ |
|---|---|---|---|---|---|---|---|---|---|
| **Before leaching** | **Chemical shift** | -71.2 | -74.5 | -78.1 | -80.6 | -84.4 | - | - | -102 |
| | **Percentage(%)** | 9.5 | 1.0 | 6.0 | 26.7 | 24.6 | - | - | 32.2 |
| | **Al/Si** | 0.23 | | | | | | | |
| | **MCL** | 23.5 | | | | | | | |
| **After leaching** | **Chemical shift** | -71.3 | -75 | -79.2 | -82.09 | -85.21 | -90.1 | -93.9 | -103 |
| | **Percentage(%)** | 3.7 | 0.5 | 8.1 | 13.9 | 24.8 | 13.5 | 1.1 | 34.4 |
| | **Al/Si** | - | | | | | | | |
| | **MCL** | - | | | | | | | |

The $^{29}$Si SS MAS NMR Spectra for the 13Y-WP50 cement paste before leaching and after leaching are fitted with Anhyd. WPC, $Q^0$(H), $Q^1$, $Q^2$(1Al), $Q^2$, $Q^3$(1Al), $Q^3$ and Anhyd. PFA, as shown in Figure 6.17. The percentage of Si attribute to each peak is determined by Igor software. The data are used in equations 2.6 and 2.7 to calculate the Al/Si and MCL, with results listed in Table 6.1. In the cement paste before leaching, the Al/Si ratio is 0.23 which is consistent with the chemical composition analysis from SEM-EDX and TEM-EDX, confirming the fitting is reasonable. The Al/Si atomic ratio is similar to that calculated by Taylor using the 9 years old cement paste (Taylor, 2010), however, the MCL is much longer after 4 years more hydration, indicating further hydration of the cement paste during that period of time. In the cement paste after leaching, the percentage of the $Q^0$ has decreased due to further hydration, and there is clearly an extra hump observed between the chemical shifts of -85 and -100 ppm, as shown in Figure 6.17. According to the literatures (Komarneni et al., 1985, Cong and Kirkpatrick, 1996b), the hump is assigned to the $Q^3$(1Al) and $Q^3$ at that range of chemical shift. In this case, the chemical shifts of $Q^3$(1Al) and $Q^3$ are at -90.1 and -93.9 ppm, respectively, and the percentage of $Q^3$(1Al) is much higher than $Q^3$, so the crosslinking prefers to occur in the aluminium bridge sites rather than the silicon bridge

sites. The Al/Si and MCL are not calculated due to the complexity of its aluminosilicate anion structure.

### 6.5.2 $^{27}$Al solid state MAS NMR spectra

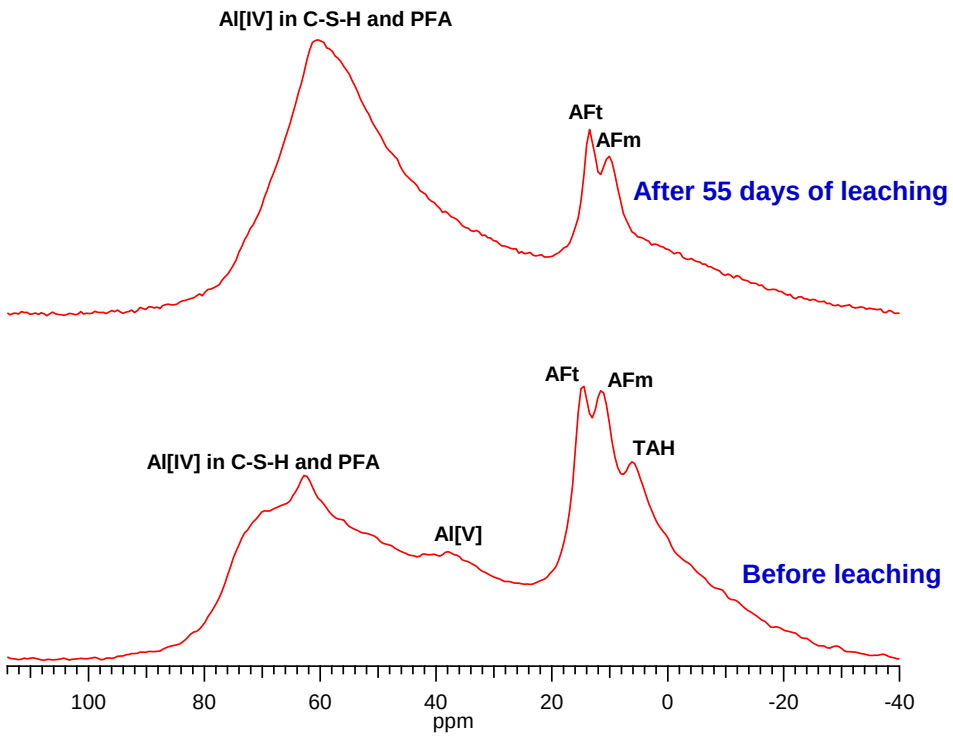


Figure 6.18 $^{27}$Al solid state MAS NMR spectra for 13Y-WP50 cement paste before leaching (bottom spectrum) and after 55 days of leaching (top spectrum)

The $^{27}$Al SS MAS NMR spectra of 13Y-WP50 cement paste before leaching and after leaching illustrate the evolutions of Al coordinated structures during the leaching process (see Figure 6.18). In the cement paste before leaching, there are six peaks, *i.e.* 68.4 ppm, 62.6 ppm, 36.5 ppm, 14.2 ppm, 11.3 ppm and 5.9 ppm. The first broad peak is assigned to the Al present in $Q^2$ bridging tetrahedra of silicate chains of the C-A-S-H; the second sharp peak is assigned to the Al present in PFA, and it is more abundant than it's in the 13Y-WP30 cement paste, because of the increase of PFA replacement in the blended cement paste; the third peak is assigned to the Al in the interlayer substituting for interlayer $Ca^{2+}$ ions; the peaks at 14.2 ppm, 11.3 ppm correspond to

AFt and AFm, respectively; the peak at 5.9 ppm is assigned to the TAH as mentioned in Chapter 4 and 5. In the spectrum for the cement paste after 55 days of leaching, the chemical shift corresponds to Al[IV] is at 60.1 ppm, which is considered to originate from the Al in the bridging position to connect the three Si sites due to the cross-linking occurred in the interlayer of the aluminosilicate anion structure (Sun et al., 2006). The peak corresponding to TAH has disappeared after leaching, indicating this phase has been dissolved.

## 6.6 Summary

This chapter has assessed the effects of PFA replacement amount and water leaching on the microstructure, atomic structure and chemical compositions of 13 years old White Portland cement blended 50% pulverised fly ash cement paste.

Regarding the effects of the PFA replacement amount on the structure of the cement paste, it has been observed that as the amount of PFA replacement becomes 50 percentage instead of 30 percentage, the content of CH has decreased from 10.6 to 6.3 due to further consumption by pozzolanic reaction; the microstructure of the cement paste becomes more porous as the PFA is less reactive; the Ca/Si atomic ratio in the C-S-H is 1.26.

Regarding the effects of the leaching on the structure of the cement paste, it has been found that it influences in the following aspects: the CH has been dissolved after 1½ months of leaching. The morphology of C-S-H becomes more porous and the Ca/Si atomic ratio decreases from 1.26 to 0.68. There are $Q^3$(1Al) and $Q^3$ formed in the cement paste after leaching, indicating the transformation of the single chains to double chains.

# Chapter 7 Effects of curing temperature on the micro-, nano- and atomic-scale structures of OPC cement paste blended with BFS

## 7.1 Introduction

This chapter presents the results and discussions of the OPC cement paste blended with BFS hydrated for 1year at ambient temperature (OPC:BFS-AT ), 35 ºC (OPC:BFS-35 ºC ) and 80 ºC (OPC:BFS-80 ºC). A range of analytical techniques are used to assess the influence of curing temperature on the structure of the OPC: BFS blended cement paste:

- Identification the phases by using XRD;
- CH content studied by using thermal analysis;
- Micro-scale structure studied by SEM;
- Nano-scale structure and chemical composition studied by TEM-EDX;
- Atomic-scale structure studied by $^{29}$Si SS MAS NMR.

## 7.2 The phase identification studied by XRD

Figure 7.1 shows XRD traces from slices of one year old OPC: BFS blended cement paste hydrated at ambient temperature, 35 ºC and 80 ºC, respectively. The main phases in the OPC:BFS-AT are C-S-H gel, CH, AFm, HT, gehlenite and β-$C_2S$. The weak reflections at around 29.5 and 50 2θ correspond to C-S-H gel, which is the main phase in the paste and plays the role to adhere the whole mass. CH has strong reflection peaks, and the main CH reflection peak is around 34 2θ which can be used to calculate the content of CH and to estimate the consumption of CH by the hydration reaction of BFS. Due to complexity of the patterns, it is difficult to obtain the quantitative information of CH in the paste. Nevertheless, it is shown in Figure 7.1 that

as the curing temperature increases, the intensity of CH peaks increases, indicating the CH content increases, as confirmed by the thermal analysis.

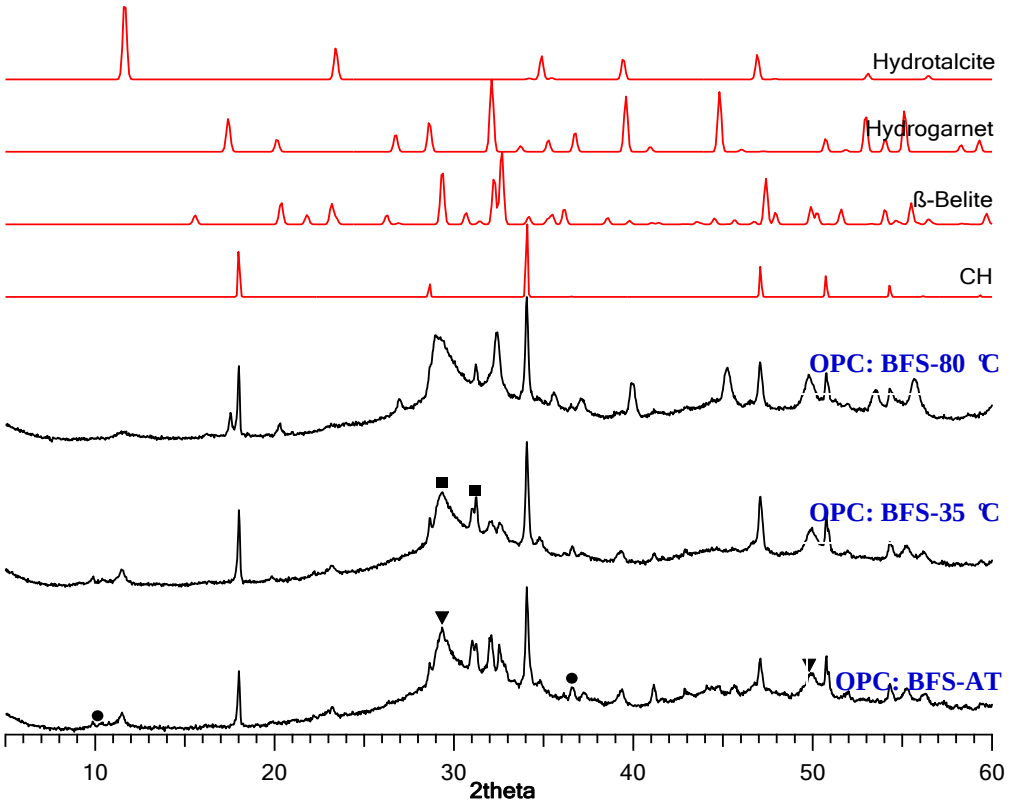


Figure 7.1 XRD patterns of the 1 year old OPC:BFS blended cement paste hydrated at ambient temperature, 35 ºC and 80 ºC. All are set to the same intensity scale. The relevant standard phase traces are included. The triangles labelled peaks (▼), the filled circles (●) labelled peaks and the filled square (■) labelled peaks correspond to the C-S-H gel phase, AFm phase and gehlenite, respectively.

The doublet at around 10 º 2θ suggests the presence of the monosulfate phases in the OPC: BFS-AT and OPC: BFS-35 ºC blended cement paste. However, it is absent in the OPC: BFS-35 ºC blended cement paste, probably due to its poor crystallinity. HT, as a typical hydration product from OPC: BFS blended cement system due to the presence of high content of $Al_2O_3$ and MgO in BFS, is observed in all the paste. As curing temperature increases, the intensity of the peaks corresponding to β-belite decreases, suggesting further hydration of the cement due to the increasing of curing temperature. A significant quantity of a crystalline hydrogarnet phase are formed in the OPC:BFS blended cement paste hydrated at 80 ºC. The crystalline hydrogarnet phase

has a cell parameter α of 1.236 nm, and it intends to form in the blended cement systems at high curing temperature (Girao et al., 2007b). Overall the phases in the OPC:BFS blended cement paste hydrated at different temperature are similar, except the HG phases formed in the 80 ºC curing temperature.

## 7.3 CH content studied by thermal analysis

Thermal analysis in combination with DTA and TG is used to complement the XRD to analyse the amount of CH in the paste at different curing temperature, and then evaluate the reaction degree. From the TG curves, the loss of mass below 400 ºC is mainly due to the evaporation of free water, and the decomposition of C-S-H gel and AFm phase. There is an obvious mass loss step around 450 ºC, which is due to the decomposition of CH. CH quantities calculated from TG curve are given as a percentage of ignited weight with 1.47%, 1.72% and 2.36%, indicating that as curing temperature increases, the hydration degree of the cement enhances, although at the same time, CH could be consumed by the BFS. The absence of the mass loss around 650-750 ºC suggests that the OPC:BFS blended cement paste are not carbonated during the storage, in agreement with the absence from the XRD trace of peaks for any of the polymorphs of $CaCO_3$.

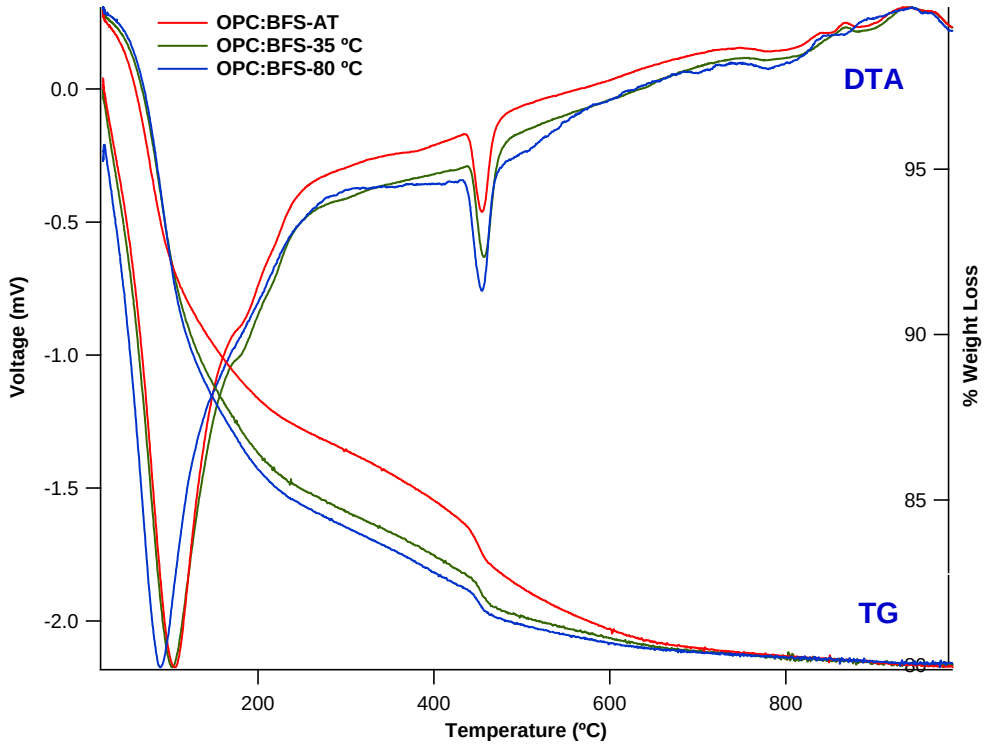


Figure 7.2 Thermal analysis (DTA and TG) results of the OPC:BFS blended cement paste hydrated at ambient temperature, 35 ºC and 80 ºC, respectively.

## 7.4 Micro-scale structure studied by using SEM

Figure 7.3 (a) shows that the microstructure of the OPC:BFS blended cement paste hydrated at ambient temperature is compact and homogeneous. There are a large amount of angular anhydrous BFS grains, small amount of anhydrous cement grains which are β-belite in this case, and small amount of CH due to the consumption by BFS reaction. High content of Op C-S-H is found, and rarely Ip C-S-H is detected.

Figure 7.3 (b) shows the microstructure of the OPC:BFS blended cement paste hydrated at 35 ºC, and it is similar to that of the paste hydrated at ambient temperature, except that there is Ip C-S-H formed surrounding the small BFS particles, indicating that higher curing temperature has induced the further hydration of BFS. In addition less anhydrous cement grains are observed, suggesting the higher curing temperature has also induced the further hydration of OPC.

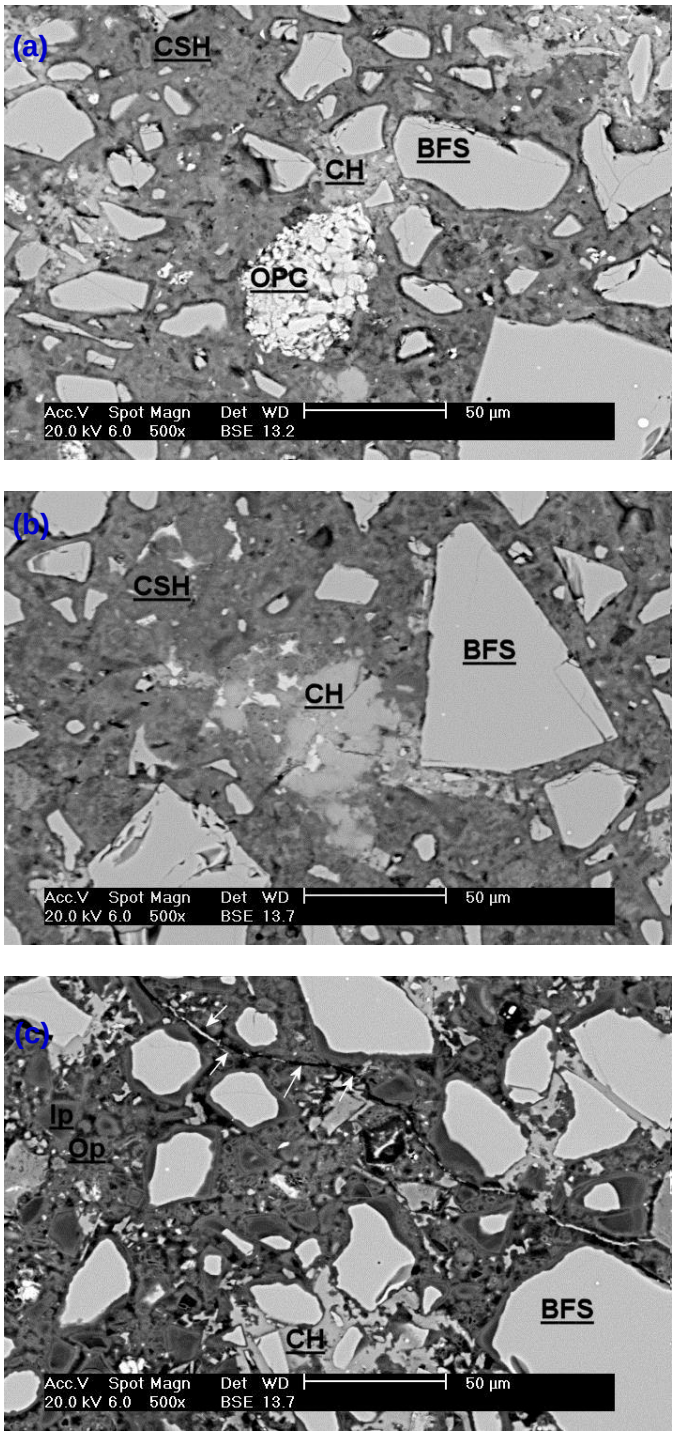


Figure 7.3 Backscattered images illustrating the microstructure of the OPC:BFS blended cement paste hydrated at (a) ambient temperature, (b) 35 ºC, and (c) 80 ºC with 500X magnification. Regions of blast furnace slag (BFS), Ordinary Portland cement (OPC), calcium hydroxide (CH), C-S-H gel (CSH), inner product C-S-H (Ip), outer product C-S-H (Op) are labelled.

Compared to the paste hydrated at lower temperature, the microstructure of the OPC:BFS blended cement paste hydrated at 80 ºC has distinctive features, as shown in Figure 7.3 (c). The microstructure of the paste is more porous. Ip C-S-H produced by partially reacted BFS grains is largely observed. The microstructure of Ip C-S-H is compact and it is darker than other phases in the paste shown in the BSE image, suggesting less presence of Ca content. This type of Ip C-S-H is termed as inner slag hydrate (ISP). In addition, there are large cracks induced by high curing temperature, and they could be a concern for the durability.

## 7.5 Nano-scale structure studied by TEM-EDX

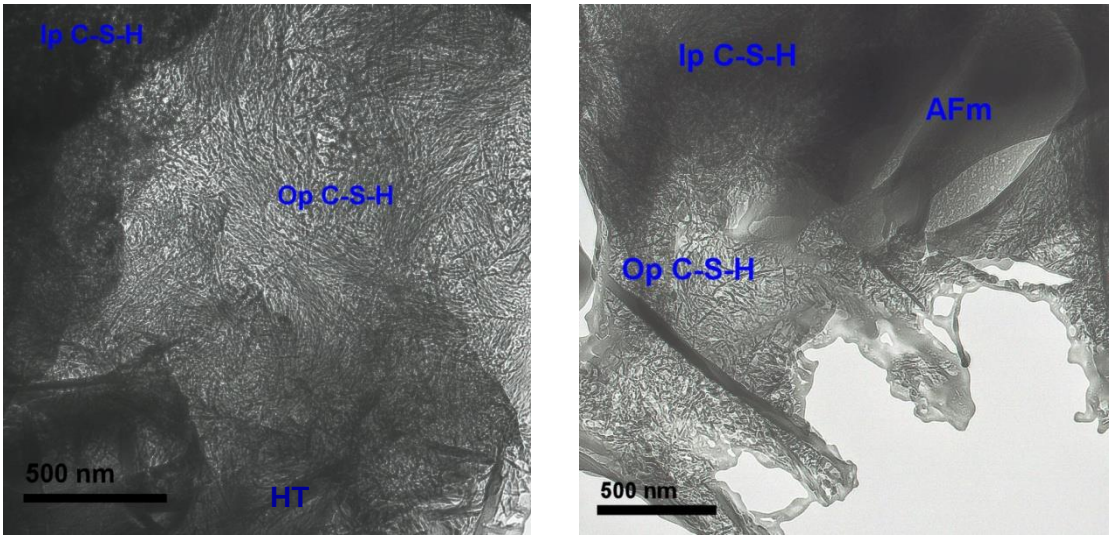


Figure 7.4 The left TEM image shows compact Ip C-S-H and short fibrillar Op C-S-H; the right TEM image shows crystal AFm phases in the OPC: BFS blended cement paste hydrated at ambient temperature.

Phases identified in the OPC: BFS-AT blended systems are Ip C-S-H, Op C-S-H, CH, AFm and HT, and they are in agreement with Richardson and Taylor's observation with similar blended cement systems (1992a, 2010). Figure 7.4 shows that the Ip C-S-H has a compact morphology and Op C-S-H has a foil-like and short fibrillar feature, which are typical features of C-S-H in high replacement of BFS blended cement systems. In addition, Ip C-S-H is finely intermixed with HT phase, which is high in Al and Mg

content observed by TEM-EDX analysis. Laths or plates of AFm phases are shown in the right TEM image of Figure 7.4, and they are intermixed with foil-like Op C-S-H and compact Ip C-S-H.

Areas of AFm, Ip and Op C-S-H formed in the OPC:BFS-AT cement paste are analysed by EDX (~200 nm in diameter). The EDX data are plotted in terms of Al/Ca against Si/Ca, Mg/Si against Al/Si and S/Ca against Al/Ca, as shown in Figure 7.5.

The black arrow in the S/Ca *vs.* Al/Ca plot is the trend of AFm, and the Al in the AFm in this sample is at the high side, probably due to the intermixture with the high aluminium content Ip C-S-H. The average Ca/Si ratio in the C-S-H is around 1.45 ± 0.05, which is similar to the value observed by Taylor with similar slag replacement (2010). The Mg/Al ratio determined by the regression analysis (*i.e*. 2.04) is sitting between the possible value for HT phases (Brindley and Kikkawa, 1979), and the Al/Si ratio was 0.17 ± 0.01 (n=22). The S/Ca *vs.* Al/Ca graph shows that the AFm phase is on the trend of S/Al≈0.3.

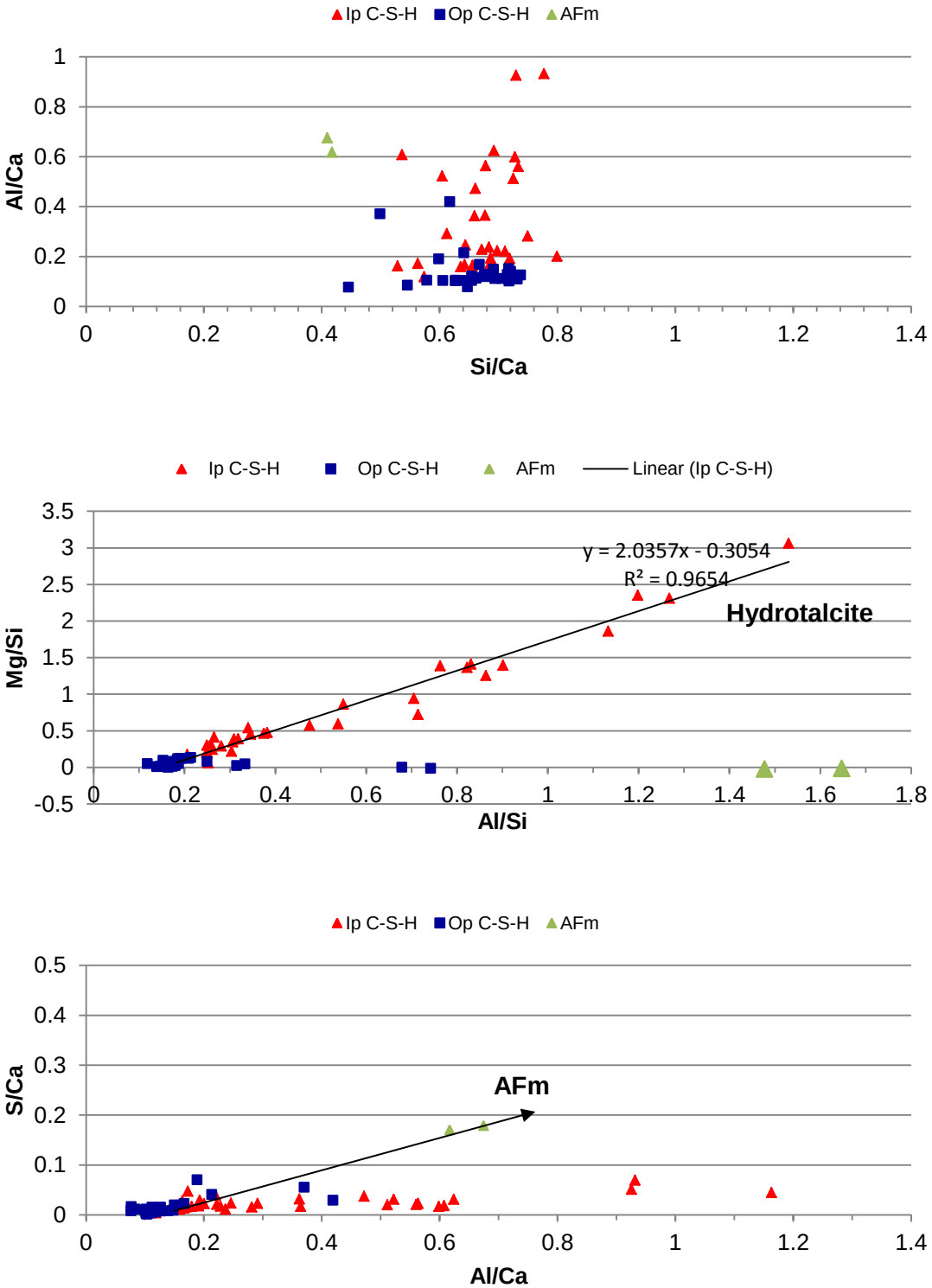


Figure 7.5 Atomic ratios of Al/Ca against Si/Ca (top), Mg/Si against Al/Si (middle) and S/Ca against Al/Ca (bottom) from TEM-EDX analyses with AFm, Op and Ip C-S-H present in the OPC:BFS blended cement paste hydrated at ambient temperature.

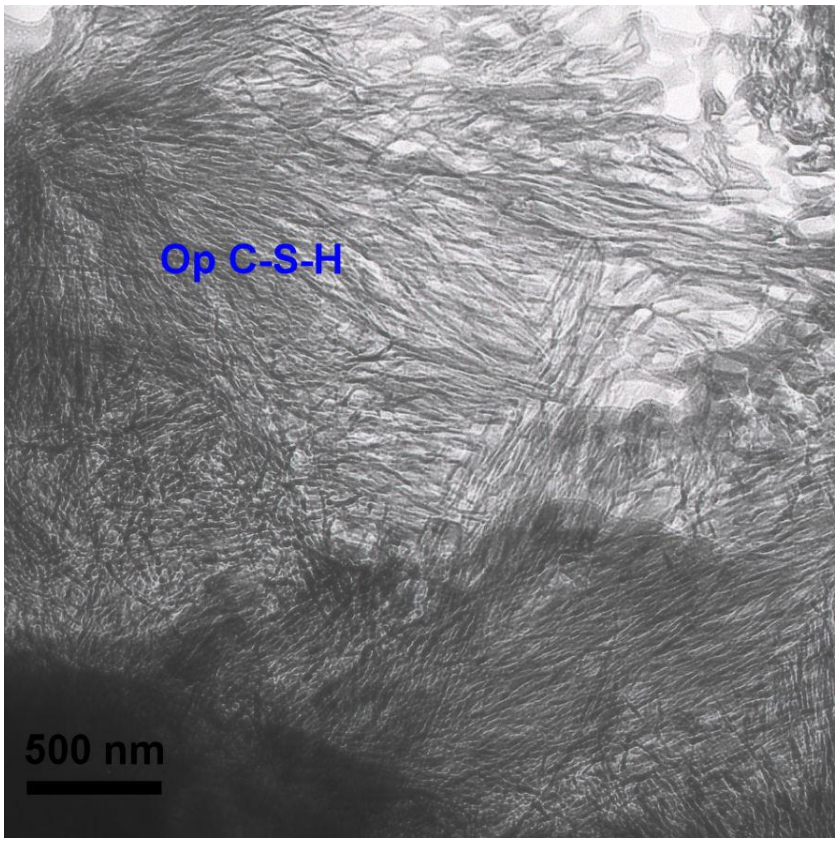


Figure 7.6 TEM image of the long and short fibrillar Op C-S-H in the OPC:BFS blended cement paste hydrated at 35 ºC.

Figure 7.6 shows the interface between the fibrillar Op C-S-H and the dense Ip C-S-H in the OPC: BFS-35 ºC. The Op C-S-H is much coarser than that formed at ambient temperature. The sample is easy to be dehydrated under a high voltage electron beam as damage can be seen at the top right of the image.

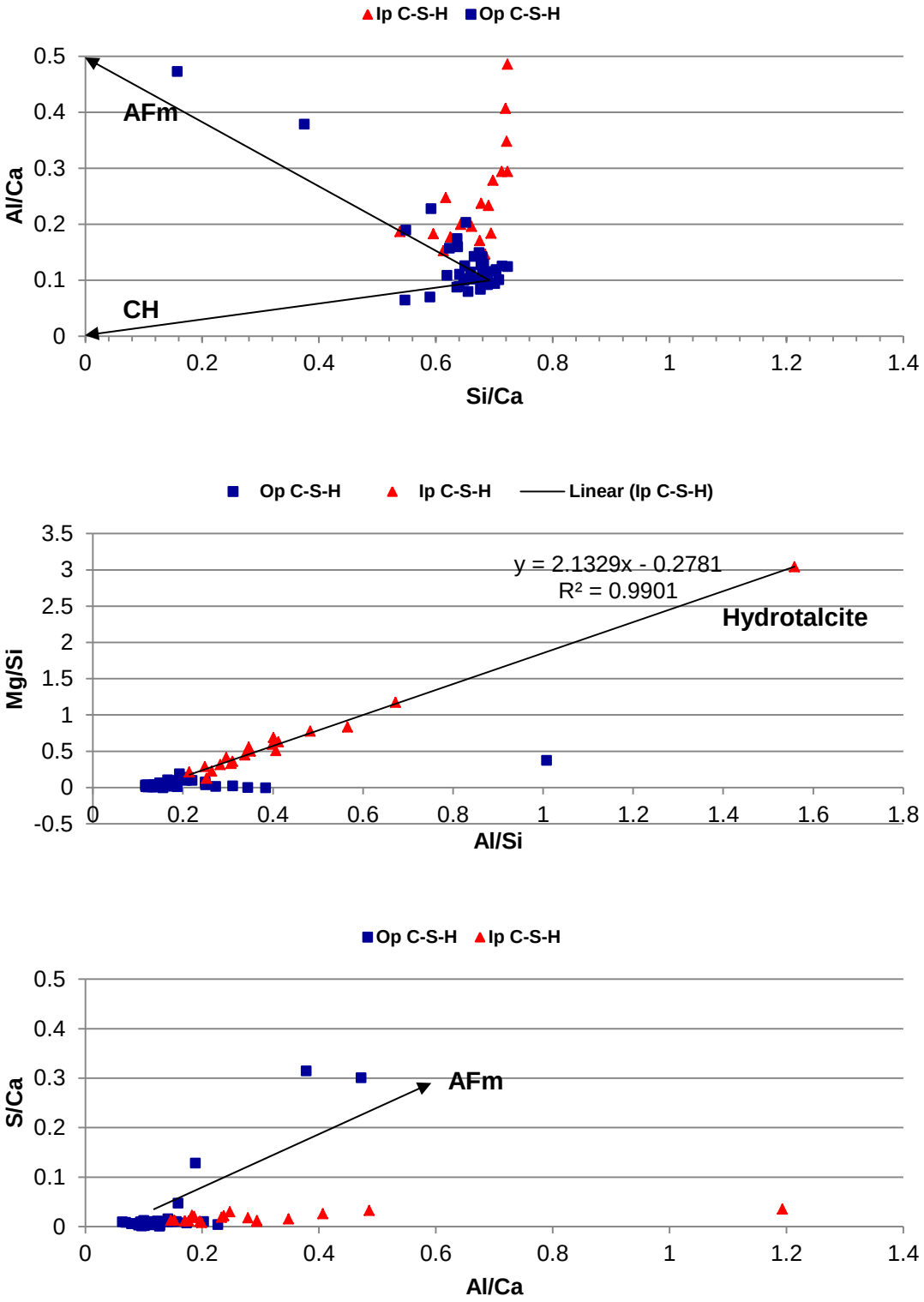


Figure 7.7 Atomic ratios of Al/Ca against Si/Ca (top), Mg/Si against Al/Si (middle) and S/Ca against Al/Ca (bottom) from TEM-EDX analyses of the OPC:BFS blended cement paste hydrated at 35 ºC.

The EDX data of Op and Ip C-S-H present in the OPC:BFS blended cement paste hydrated at 35 ºC, are plotted as Al/Ca against Si/Ca, Mg/Si against Al/Si and S/Ca against Al/Ca, as shown in Figure 7.7. From the plots, it is observed that the Ca/Si and Al/Si atomic ratios of the C-S-H are 1.47 ± 0.05 (n=18) and 0.15 ± 0.02 (n=18), respectively, and the Ca/Si atomic ratio is statistically similar to that in the cement paste hydrated at ambient temperature. However, the Al/Si atomic ratio is lower, indicating less Al are substituted Si in the C-S-H. It is clear that the Op C-S-H are intermixed with the AFm phase and CH, and the Ip C-S-H are finely intermixed with the HT phase.

Figure 7.8 shows the foil-like Op C-S-H intermixed with the crystalline AFm phase. It is a good illustration of the sensitivity of TEM for detecting this phase, which can be poorly ordered and present as very fine crystals (Love et al., 2007).

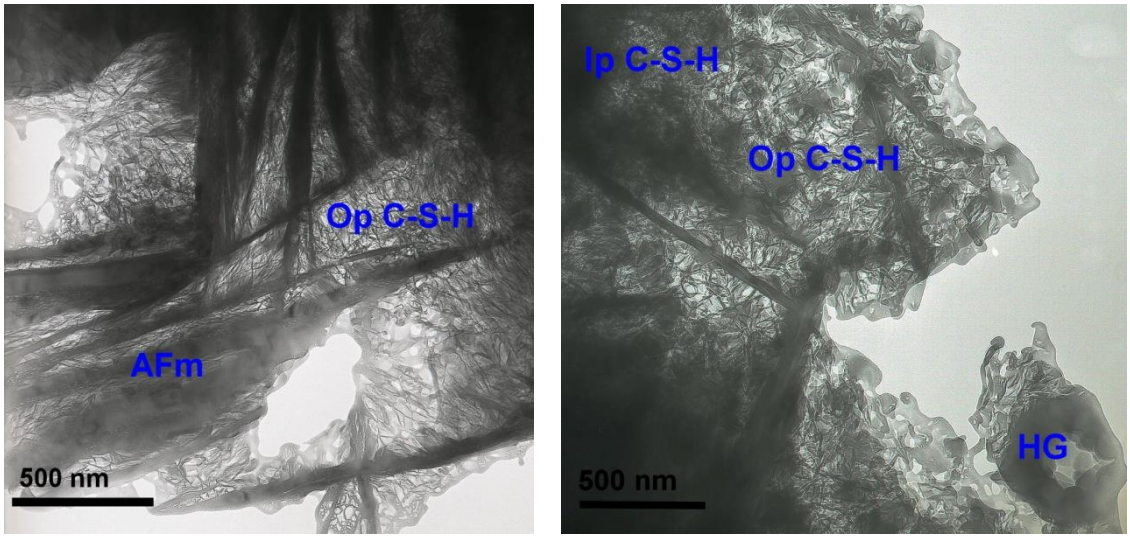


Figure 7.8 The left TEM image shows AFm phase; the right TEM image shows Hydrogarnt phase in Op C-S-H in the OPC:BFS blended cement paste cured at 80 ºC.

A distinctive nanostructure of the paste hydrated at 80 ºC is the presence of round and poorly crystalline particles which are rich in iron and aluminium, and it is hydrogarnet phase (Rodger and Groves, 1989). Figure 7.8 (right image) shows that the hydrogarnet phase is well mixed with the foil-like Op C-S-H and AFm phases.

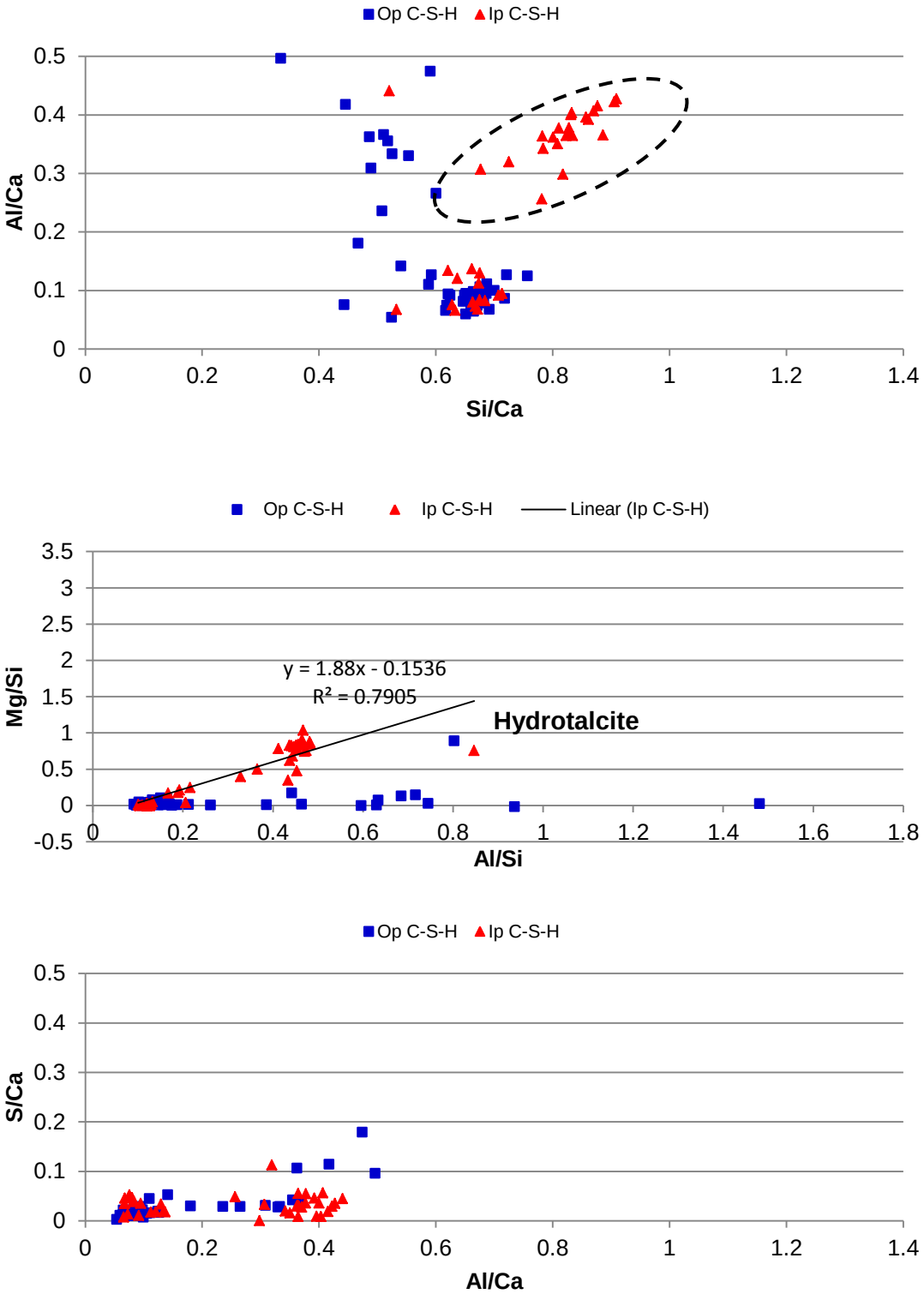


Figure 7.9 Atomic ratio plots from TEM-EDX analysis of Op and Ip C-S-H present in the OPC:BFS blended cement paste hydrated at 80 ºC: Al/Ca against Si/Ca (top), Mg/Si against Al/Si (middle) and S/Ca against Al/Ca (bottom).

The EDX data of Op and Ip C-S-H present in the OPC:BFS blended cement paste hydrated at 80 ºC, are plotted out as Al/Ca against Si/Ca, Mg/Si against Al/Si and S/Ca against Al/Ca, in Figure 7.9. The average Ca/Si ratio of the C-S-H is 1.48 ± 0.04 (n=18), which is statistically similar to that in the blended cement paste cured at lower temperature. But, under high curing temperature, Ip C-S-H produced from slag with low Ca/Si ratio is largely observed as shown in in the dashed circle in the Al/Ca *vs.* Si/Ca plot, confirming that the slag is further hydrated. From the Mg/Si vs. Al/Si plot, it is observed that the Al/Si ratio is 0.12 ± 0.02 (n=18), which is statistically lower than that in the cement paste hydrated at lower temperature. The S/Ca vs. Al/Ca graph demonstrates the presence of AFm phase as there is a clear trend line in the direction of AFm phase.

## 7.6 Atomic-scale structure studied by using Solid-state MAS NMR

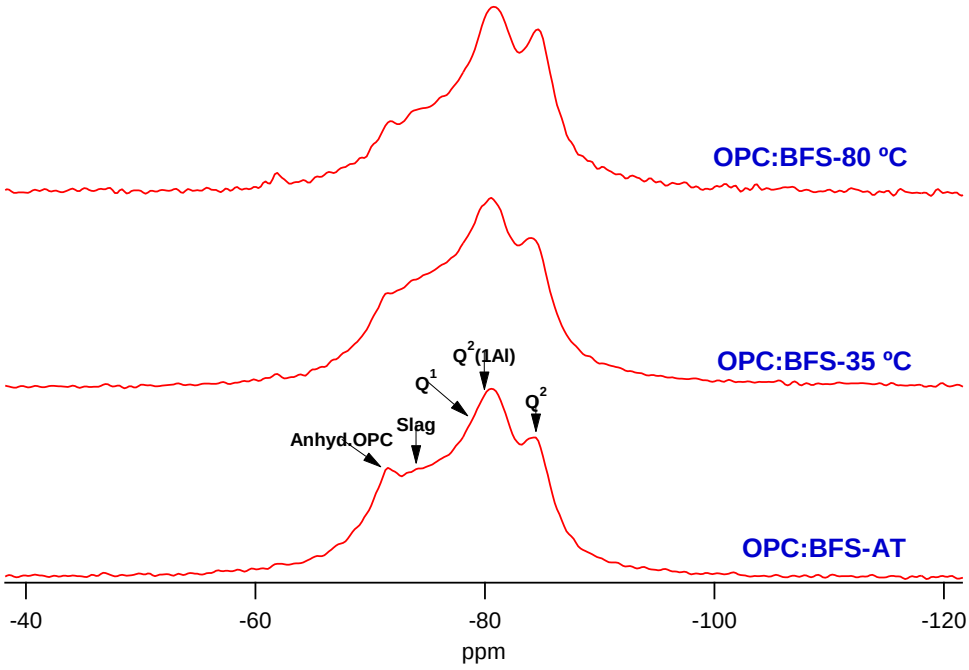


Figure 7.10 $^{29}$Si solid state MAS NMR spectra for the OPC:BFS blended cement paste hydrated at ambient temperature (OPC:BFS-AT), 35 ºC (OPC:BFS-35 ºC) and 80 ºC (OPC:BFS-80 ºC).

Figure 7.10 shows $^{29}$Si MAS NMR spectra for OPC:BFS blended cement paste hydrated at ambient temperature, 35 ºC and 80 ºC. Five main peaks, at -71.3 ppm for anhydrous OPC (in this study, it is β-belite), -73.5 ppm for anhydrous slag, -79.0 ppm for $Q^1$ site, -80.5 ppm for $Q^2$(1Al) site and -84.5 ppm for $Q^2$ site are detected, which is similar to the observation by Richardson using similar cement mixture (Richardson et al., 1993).

Unfortunately, it is difficult to quantitatively evaluate the relative amounts of each $Q^n$ species due to the complex overlap between the peaks. The complex overlap is partly due to the chemical shift dispersion resulted from the amorphous nature of the phases, *e.g*. C-S-H and BFS , and partly due to the broadening caused by the interactions with unpaired electrons from paramagnetic components in the slag (such as iron) (Wang and Scrivener, 2003). Generally, glass slags exhibit very broad $^{29}$Si SS MAS NMR peak, which may extend over the full chemical shift range for $SiO_4$ sites, *i.e*. -60 ppm to -120 ppm (Dyson et al., 2007, Skibsted and Hall, 2008).

Nevertheless, it is shown in Figure 7.10 that the height of the peak for anhydrous OPC decreases with increasing curing temperature. In the OPC: BFS-80 ºC, barely anhydrous OPC Is left, suggesting that the curing temperature could induce further hydration of OPC. In addition, the increasing height difference between the $Q^2$(1Al) peak and the $Q^1$ peak, and the rising of the $Q^2$ peak as increasing of curing temperature suggests that higher curing temperature induces the elongation of the MCL of the C-S-H chain.

## 7.7 Summary

The main phases in the blended cements OPC:BFS paste hydrated at ambient temperature and 35 °C, are C-S-H gel, CH, HT-type phase and AFm phase. However, the main phases in the paste hydrated at 80 °C, are C-S-H gel, CH, HT-type phase and HG phase. The CH content in the blended cements OPC:BFS paste hydrated at ambient temperature, 35 °C and 80 °C are 1.47%, 1.72% and 2.36%, respectively, as observed by thermal analysis. None of the blended cements paste has been carbonated.

Generally, Op C-S-H has a fine and fibrillar morphology, however some Op C-S-H has a foil-like morphology. Ip C-S-H has a compact and fine feature and it is intermixed with HT-type phase.

As curing temperature increases, the microstructure and nanostructure of the blended cement paste becomes more porous, and more hydrated slag is observed.

# Chapter 8 Nano- and atomic-scale structure of synthetic C-A-S-H

## 8.1 Introduction

This chapter presents the results and discussions of the synthetic C-A-S-H[1] with a low Ca/Si atomic ratio and C-A-S-H[2] with a high Ca/Si atomic ratio, respectively. A range of analytical techniques are used to characterize the synthetic C-A-S-H:

- Identification of the bulk oxide composition of C-A-S-H by using XRF;
- Identification of the phases in the C-A-S-H by using XRD;
- Study the nanostructure and chemical composition by using TEM-EDX;
- Study the structure at atomic-scale by using Solid-state MAS NMR.

## 8.2 Identification of the bulk oxide compositions studied by XRF

Table 8.1 Bulk oxide compositions of the C-A-S-H[1] and C-A-S-H[2] analysed by XRF.

| Compound | Unit (Weight) | C-A-S-H[1] | C-A-S-H[2] |
|---|---|---|---|
| **$Na_2O$** | % | 0.05 | 0.08 |
| **MgO** | % | 0.01 | 0.00 |
| **$Al_2O_3$** | % | 5.14 | 3.91 |
| **$SiO_2$** | % | 36.91 | 31.11 |
| **$P_2O_5$** | % | 0.04 | 0.04 |
| **$SO_3$** | % | 0.17 | 0.17 |
| **CaO** | % | 22.07 | 37.43 |
| **$Mn_3O_4$** | % | 0.01 | 0.01 |
| **$Fe_2O_3$** | % | 0.03 | 0.00 |
| **SrO** | % | 0.01 | 0.00 |
| **$Y_2O_3$** | % | 0.08 | 0.08 |
| **$ZrO_2$** | % | 0.06 | 0.06 |

The XRF is used to identify the bulk oxide compositions of the C-A-S-H$^1$ and C-A-S-H$^2$, with results shown in Table 8.1. The Bulk Ca/Si and Al/Si atomic ratios of C-A-S-H$^1$ and C-A-S-H$^2$ are calculated using the XRF results and shown in Table 8.2.

Table 8.2 The target and the bulk Ca/Si and Al/Si atomic ratios of C-A-S-H$^1$ and C-A-S-H$^2$ calculated using the XRF results.

| | C-A-S-H$^1$ | | C-A-S-H$^2$ | |
|---|---|---|---|---|
| | **Target** | **Bulk atomic ratio** | **Target** | **Bulk atomic ratio** |
| **Ca/Si** | 0.66 | 0.64 | 1.40 | 1.31 |
| **Al/Si** | 0.15 | 0.17 | 0.15 | 0.15 |

## 8.3 Qualitative analysis of the phases studied by XRD

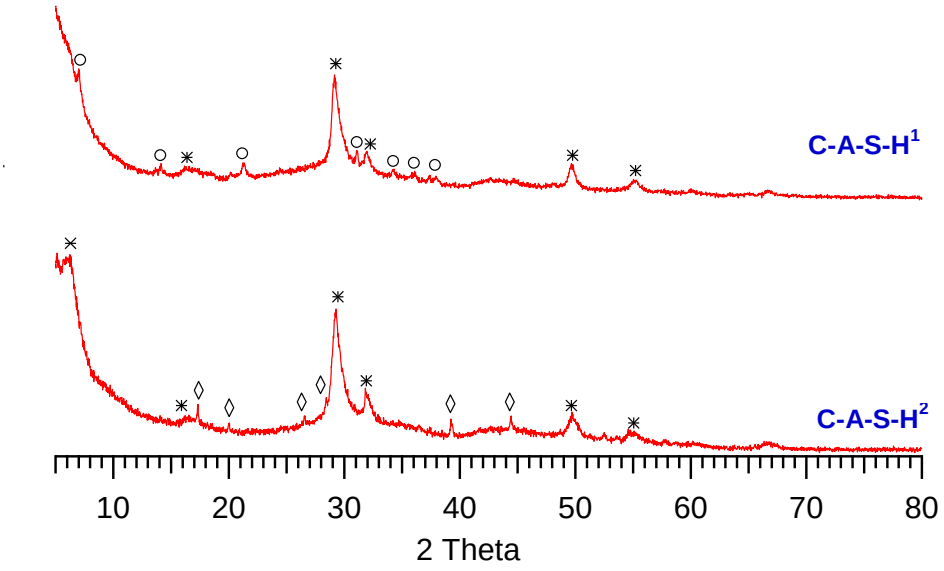


Figure 8.1 XRD patterns of the C-A-S-H$^1$ and C-A-S-H$^2$. The circle (○) labelled peaks, diamond (◊) labelled peaks and the star (*) labelled peaks correspond to the stratlingite, hydrogarnet and C-S-H gel phase, respectively.

Figure 8.1 shows the XRD patterns for the synthetic C-A-S-H$^1$ and C-A-S-H$^2$. The diffraction patterns indicate a fairly low degree of order in two samples, and the small sharp peaks correspond to stratlingite ($2CaO•Al_2O_3•SiO_2•8H_2O$) (Kwan et al., 1995) and hydrogarnet ($3CaO•Al_2O_3•XSiO_2•[16-2X]H_2O$) in the C-A-S-H$^1$ and C-A-S-H$^2$. It is

difficult to synthesize pure C-A-S-H phase which has high Al/Si, and generally they are intermixed with aluminium hydrate. The broad peaks at 29.5 2θ, 32 2θ and 49.5 2θ are observed in both C-A-S-H, and they are the reflection peaks for the C-S-H (Pardal et al., 2009). There is one more peak at 6.0 2θ corresponding to the C-A-S-H$^2$, which was also observed from synthetic C-S-H samples with high Ca/Si atomic ratio (Black et al., 2005, Garbev et al., 2008). This peak is absent in the C-S-H with low Ca/Si atomic ratio and its intensity increases with increasing of Ca/Si atomic ratio, thus it is absent in the C-A-S-H$^1$, which has low Ca/Si atomic ratio.

## 8.4 Nano-scale structure studied by TEM-EDX

TEM combined EDX is used to analyse the nanostructure and chemical composition of the synthetic C-A-S-H, and to verify the homogeneity of the sample. Other phases are also identified by TEM, like stratlingite which is high in Al content.

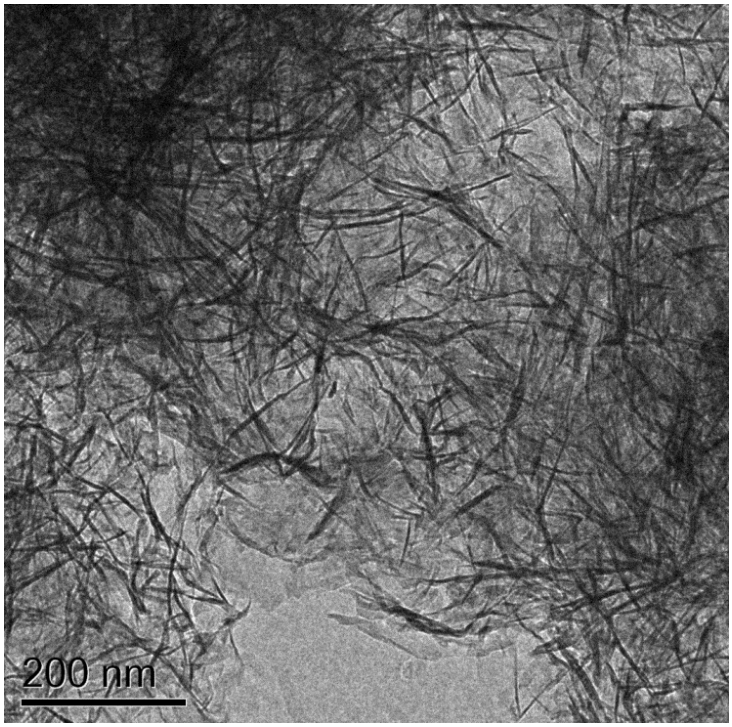


Figure 8.2 TEM image shows short fibrillar C-A-S-H with a Ca/Si atomic ratio of 0.45 and an Al/Si atomic ratio of 0.10 analysed by EDX.

In Figure 8.2 the C-A-S-H[1] has a short fibrillar morphology which is typical in the low Ca/Si ratio C-A-S-H. A similar morphology is also observed in the blended cement paste with low Ca/Si atomic ratio (Girao, 2007, Taylor, 2010). EDX analysis of the area in Figure 8.2 shows that the Ca/Si atomic ratio is 0.45 and the Al/Si atomic ratio is 0.10. In addition, a big rod stratlingite phase is identified by TEM, as shown in Figure 8.3. With the SAD analysis, the phase is identified to be crystalline, and it is large enough to be distinguished with the C-A-S-H.

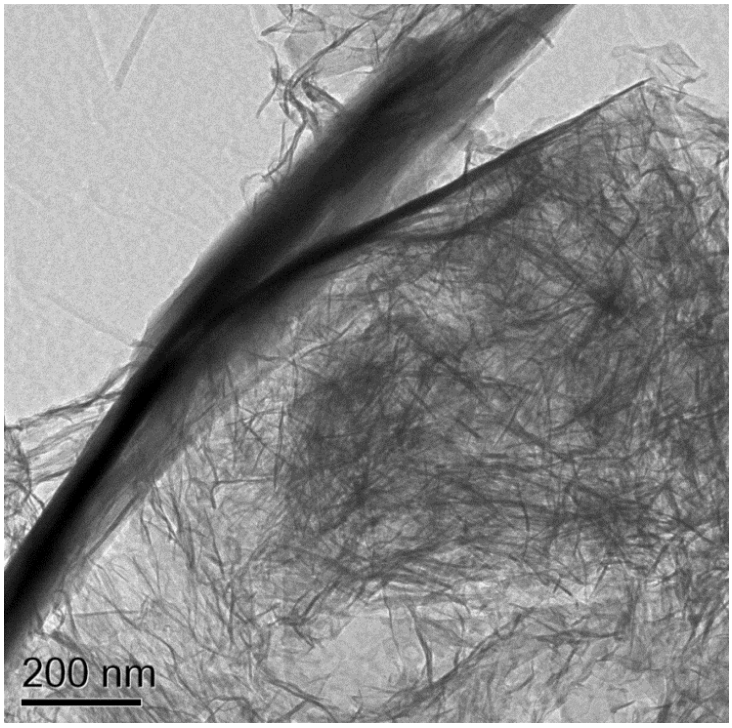


Figure 8.3 TEM image shows a short fibrillar featured C-A-S-H[1] and a big rod of straglingite on the left top.

Areas of the C-A-S-H and stratlingite are analysed by TEM-EDX, and the EDX results are plotted as the $CaO$-$Al_2O_3$-$SiO_2$ ternary diagram in Figure 8.4. It shows that the Ca/Si distribution is narrowly centred at 0.4~0.5, indicating that the sample is chemically homogeneous. The presence of Al content implies the incorporation of Al in the silicate anion structure, and the position of the Al will be analysed later with the assistance of the SS NMR. There is a clear trend line indicating the presence of stratlingite, and it is clear that this phase is higher in Al and Ca content than the C-A-S-H. The average Ca/Si atomic ratio of the C-A-S-H[1] is 0.46 ± 0.02 (n=17) which is lower

than that of the tobermorite, probably due to the C-A-S-H[1] intermixing with the amorphous silica. The Ca/Si observed by TEM-EDX is lower than those obtained by the bulk calculation of the XRF results, because of the presence of stratlingite which has a high Ca/Si atomic ratio.

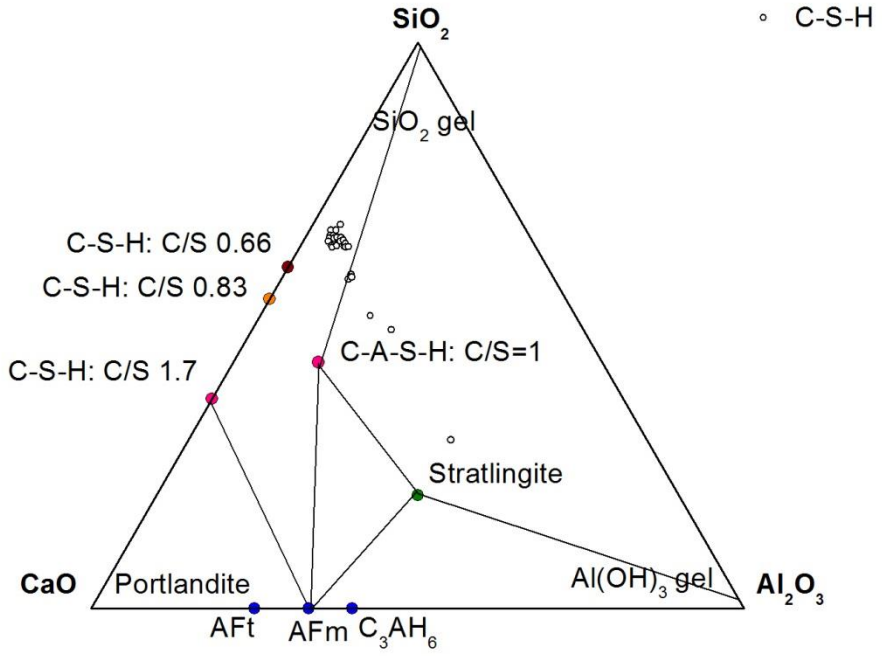


Figure 8.4 $CaO-Al_2O_3-SiO_2$ ternary diagram for TEM-EDX phase analysis of the C-A-S-H[1].

The top TEM image in Figure 8.5 shows that the C-A-S-H has a fine fibrillar feature, which is generally observed in the high Ca/Si atomic ratio C-A-S-H (Girao, 2007, Taylor, 2010). In addition, there is foil-like C-S-H in the C-A-S-H[2], as shown in the bottom TEM image in Figure 8.5. From EDX analysis, the Ca/Si and Al/Si atomic ratio of both fine fibrillar feature and foil-like feature are 0.90 and 0.10, respectively. Hydrogarnet is not observed by TEM, although it is observed by XRD, probably due to the TEM technique only analysing a small size sample. C-A-S-H[2] is analysed by TEM-EDX, and the EDX results are plotted as $CaO-Al_2O_3-SiO_2$ ternary diagram in Figure 8.6. It is clear that the Ca/Si atomic ratio is centred in 0.8~1.2, suggesting the C-A-S-H[2] is chemically homogenous. The Ca/Si atomic ratio is lower than that observed by the XRF bulk analysis, again, because of the presence of the impurity in the C-A-S-H[2].

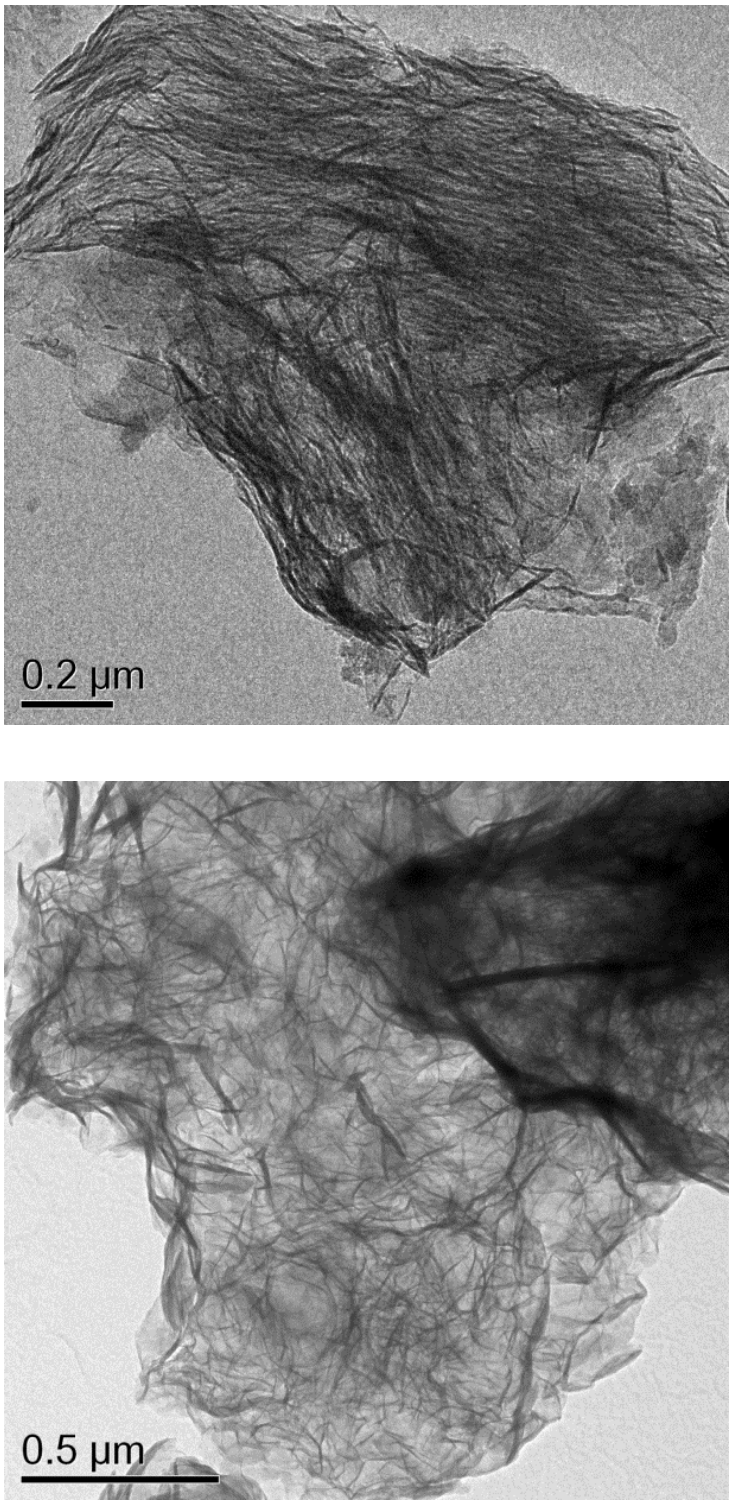


Figure 8.5 The top TEM image shows the long fibrillar C-A-S-H with a Ca/Si atomic ratio of 0.90 and a Al/Si atomic ratio of 0.10; the bottom TEM image shows the foil-like C-A-S-H[2] with a Ca/Si atomic ratio of 0.95 and a Al/Si atomic ratio of 0.12.

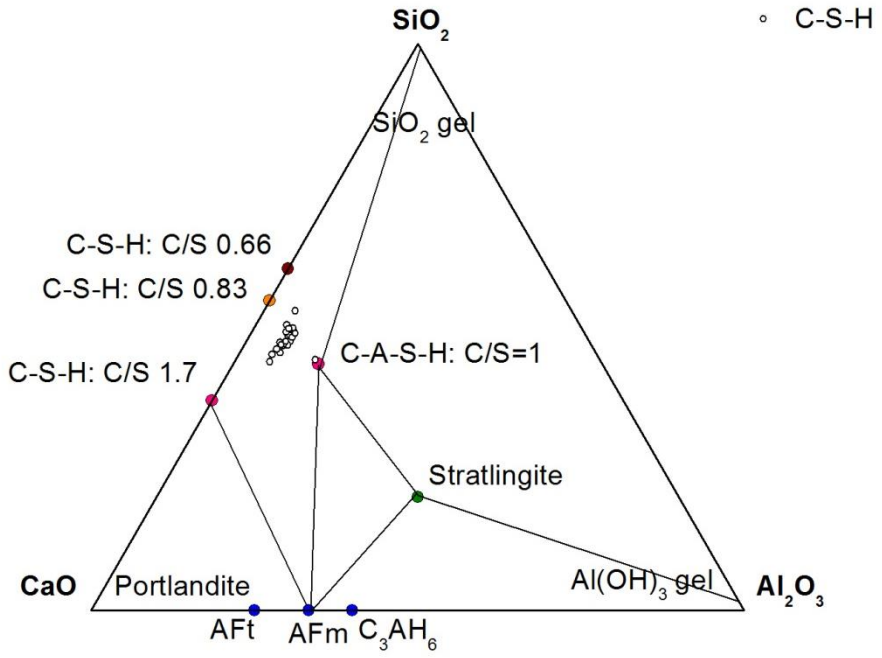


Figure 8.6 $CaO-Al_2O_3-SiO_2$ ternary diagram for TEM-EDX phase analysis of the C-A-S-H[2].

## 8.5 Atomic-scale structure studied by Solid-state MAS NMR

### 8.5.1 $^{29}$Si solid state MAS NMR spectra

Figure 8.7 presents the $^{29}$Si solid state MAS NMR spectra for C-A-S-H[1] and C-A-S-H[2]. The spectrum for the C-A-S-H[1] shows that it's similar to that of aluminium substituted tobermorite (Komarneni et al., 1985) and the cement paste after leaching, which are both low in Ca/Si atomic ratio of C-S-H. There are three main peaks, *i.e.* -79.4 ppm ($Q^1$), -81.9 ppm ($Q^2$(1Al)) and -85.3 ($Q^2$), and there is a broad peak around -95 ppm, which could be assigned to $Q^3$(1Al) and $Q^3$ at this chemical shift range (Komarneni et al., 1985, Cong and Kirkpatrick, 1996b). The large and sharp peak for $Q^2$ is the resonance from the C-S-H and stratlingite (Kwan et al., 1995). The presence of $Q^3$(1Al) and $Q^3$ indicates that the C-S-H chain is cross-linked, in addition, the height of $Q^2$ is much higher than that of $Q^1$, indicating the C-A-S-H[1] has long chain length (Wang and Scrivener, 2003).

There are three main peaks in the spectrum for the C-A-S-H$^2$, *i.e*. -79.5 ppm ($Q^1$), -81.8 ppm ($Q^2$(1Al)) and -85.2 ($Q^2$), and no $Q^3$ and $Q^4$ peaks are observed, suggesting the C-A-S-H$^1$ is not cross linked and the silica gel is absent. Comparing to the spectrum of the C-A-S-H$^1$, the relative height of the $Q^2$ peak to the $Q^1$ peak is obviously smaller, suggesting that the MCL is shorter. However, due to the presence of $Q^3$(1Al) and $Q^3$, and thus the aluminosilicate anion structure of the C-A-S-H is complex, it is difficult to calculate the MCL.

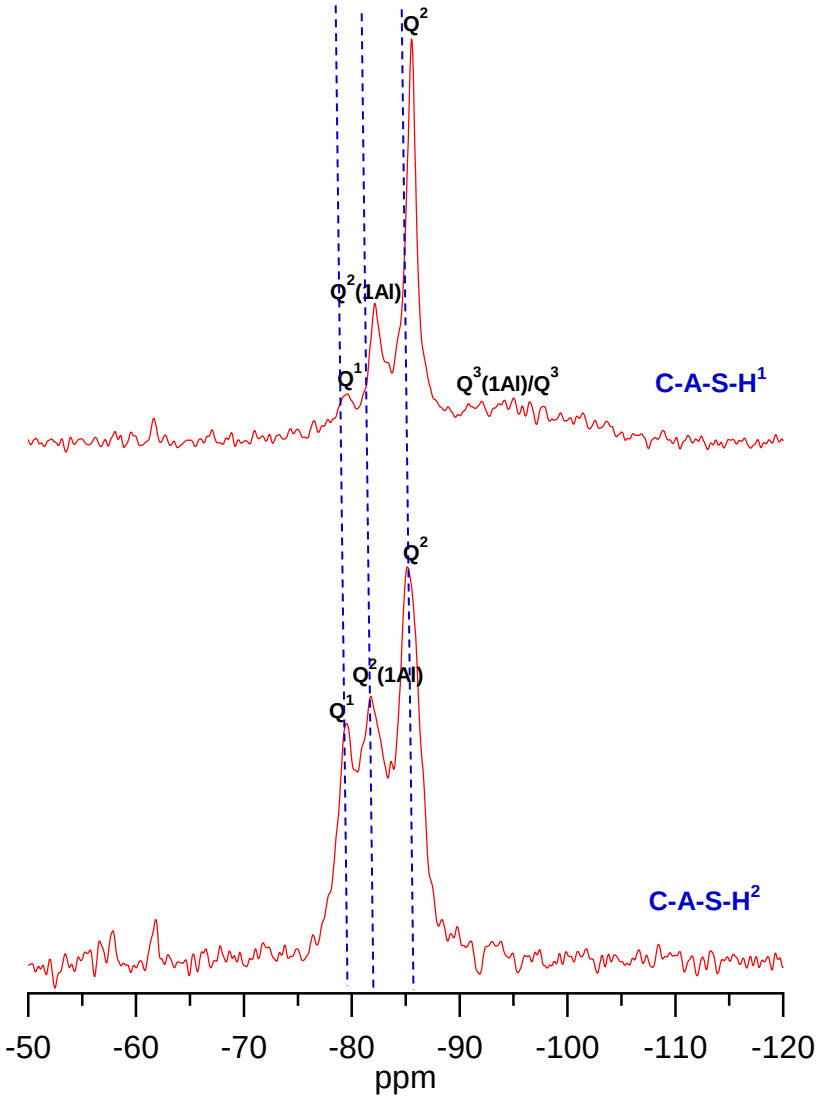


Figure 8.7 $^{29}$Si solid state MAS NMR specta for C-A-S-H$^1$ and C-A-S-H$^2$.

The spectra also show that the chemical shifts of $Q^1$, $Q^2$(1Al) and $Q^2$ of the C-A-S-H$^1$ with a lower Ca/Si atomic ratio are more negative than the those in the C-A-S-H$^2$ with a higher Ca/Si atomic ratio. It is shown in the leaching experiment in Chapter 4, 5 and 6 that as leaching proceeds, the chemical shifts of the $Q^1$, $Q^2$(1Al) and $Q^2$ move negatively. This phenomenon was also observed by Chen (2003) in the synthetic C-S-H. Probably because of the presence of the cross linked structure, which could largely influence the chemical environment of the $Q^1$, $Q^2$(1Al) and $Q^2$, and consequently influence their chemical shifts.

### 8.5.2 $^{27}$Al solid state MAS NMR spectra

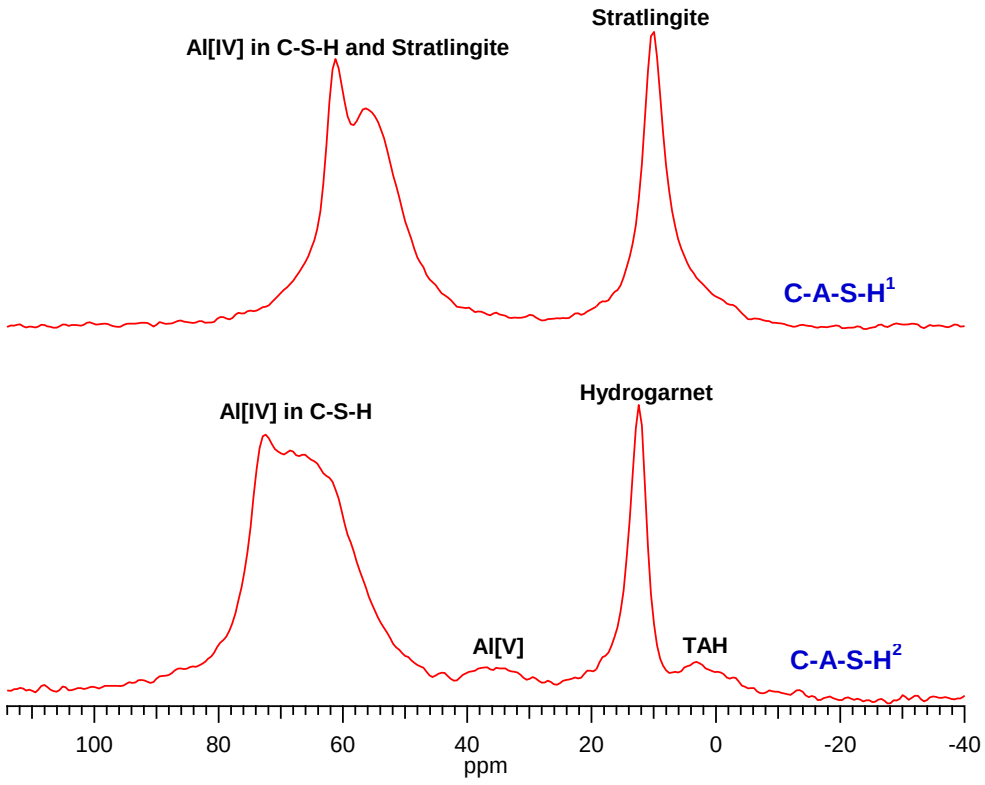


Figure 8.8 $^{27}$Al solid state MAS NMR spectra for C-A-S-H$^1$ and C-A-S-H$^2$.

The incorporation of Al in the C-S-H is characterized by $^{27}$Al solid state MAS NMR spectroscopy, and the collected spectra are shown in Figure 8.8. In the spectrum for C-A-S-H$^1$ which has a Ca/Si ratio of 0.45 observed by TEM-EDX, there are two types of

Al coordination, *i.e.* Al[IV] and Al[VI] coordination. In the Al[IV] coordinated region (50-70 ppm), two peaks are observed, a broad peak near 56.1 ppm and a narrow one near 60.9 ppm. It is generally agreed that the former broad peak corresponds to Al[IV] in the C-A-S-H structure with double chains, and the later peak is attributed to the aluminosilicate phase, stratlingite in which Al occurs in both Al[IV] and Al[VI] environments (Kwan et al., 1995, Sun et al., 2006, Pardal et al., 2012). The Al[VI] coordinated region (-10−20 ppm) exhibits one narrow peak at 9.7 ppm, which is assigned to stratlingite, and its presence has also been confirmed by XRD and TEM. Regarding the Al coordination in the C-S-H structure, the spectrum is similar to that observed in the cement paste after leaching (see Figure 4.18), which has low Ca/Si atomic ratio due to the decalcification.

The spectrum for C-A-S-H$^2$ which has a Ca/Si atomic ratio of 1.0 observed by TEM-EDX shows three Al coordinations, *i.e*. Al[IV], Al[V] and Al[VI]. In the Al[IV] coordinated region (50-70 ppm), a broad peak at 68.1 ppm and a narrow one at 72.2 ppm, where the first broad peak is unambiguously assigned to the Al[IV] in the bridging site in C-S-H and the second narrow peak is assigned to the Al[IV] in the C-S-H with high Ca/Si atomic ratio, particular in the C-S-H with Ca/Si ≥ 1.25 observed by Andersen and Sun (2003, 2004, 2006). At lower frequency, a broadened peak with low intensity is observed at around 36.6 ppm, which has been ascribed to a Al[V] coordination that originates from $Al^{3+}$ substituting for $Ca^{2+}$ ions situated in the interlayers of the C-S-H structure (Faucon et al., 1999). In the Al[VI] coordination, there are two peaks, *i.e*. 12.2 ppm for the hydrogarnet and 2.9 ppm for the TAH. The presence of the hydrogarnet is confirmed by XRD, but it is not observed by TEM. The TAH is absent in the spectrum for the C-A-S-H$^1$ with a low Ca/Si atomic ratio, and it is also absent in the cement paste after leaching which also has a low Ca/Si atomic ratio due to the decalcification, suggesting that the TAH tends to exist in the C-S-H with higher Ca/Si atomic ratio.

## 8.6 Summary

The synthetic C-A-S-H with different Ca/Si atomic ratio has been characterized. It's observed that the synthetic samples are impure, *i.e*. the C-A-S-$H^1$ is intermixed with stratlingite and the C-A-S-$H^2$ is intermixed with the hydrogarnet, as observed from the XRD analysis. TEM images show that the C-A-S-$H^1$ with Ca/Si atomic ratio of 0.46 has a short fibrillar feature and the presence of the stratlingite is confirmed; the C-A-S-$H^2$ which has Ca/Si atomic ratio of 1.0 has a long fibrillar and foil-like feature. The $^{29}$Si solid state MAS NMR spectra show that the presence of cross linking in the C-A-S-$H^1$. The MCL of the C-A-S-$H^1$ is longer than the C-A-S-$H^2$ as the relative intensity of the $Q^2$ peak to $Q^1$ peak of the C-A-S-$H^1$ is obviously larger than that of C-A-S-$H^2$. The $^{27}$Al solid state MAS NMR confirms the presence of the cross linking and the presence of stratlingite in the C-A-S-$H^1$, as well as the presence of hydrogarnet in the C-A-S-$H^2$.

# Chapter 9 Comparisons

## 9.1 Introduction

This Chapter presents detailed comparisons of chemical compositions between the WPC cement paste blended with two different percentages of PFA, *i.e*. 30% and 50%, at three different ages, *i.e*. one year, 9 years and 13 years. CH dissolution and C-S-H decalcification of the 1Y-WP30, 13Y-WP30 and 13Y-WP50 cement paste during the leaching process are also compared. Finally the atomic-scale structure of C-S-H formed in the 1Y-WP30 cement paste and the synthetic C-A-S-H is compared.

## 9.2 WPC cement paste blended with 30% PFA (WP30) and 50% PFA (WP50) at different ages

Table 9.1 summaries the CH as a percentage of ignited weight observed by STA, the Ca/Si and Al/Si atomic ratios observed by TEM-EDX, the Al/Si atomic ratio and MCL calculated from the deconvolution results of the $^{29}$Si SS NMR spectra of the WP30 and WP50 at one year old, 9 years old and 13 years old casted by Love, Girão (2002, 2007) and the author. The one year old samples were characterized by Love, Girão and the author, respectively; the 9 years old Love's samples were characterized by Taylor (2010); the 13 years old Love's samples were characterized by the author.

Table 9.1 shows that in Love's sample, as the age increases, the amount of the CH decreases, especially in the 9 year old sample. This indicates that as hydration time increases, more PFA hydrates and consumes the CH. In addition, over the ageing period, the CH is formed slowly than consumed.

Table 9.1 Results from thermal analysis, TEM-EDX and deconvolution of the SS $^{29}$Si NMR spectra for the WPC cement paste blended with 30% PFA (WP30) and 50% PFA (WP50) at one year old, nine years old and 13 years old analysed by Love, Girão, Taylor and the author (bold font).

| | | | WP30 | | | WP50 | | |
|---|---|---|---|---|---|---|---|---|
| | | | **1y** | **9y** | **13y** | **1y** | **9y** | **13y** |
| **%CH (STA)** | | **Love** | 23 | 11.4 | **10.6** | 15 | 5.9 | **6.3** |
| | | **Girão** | 18 | - | - | - | - | - |
| | | **The author** | **13.9** | - | - | - | - | - |
| **Ca/Si (TEM )** | | **Love** | - | 1.30 | **1.36** | - | 1.1 | **1.26** |
| **Al/Si** | **TEM** | **Love** | - | 0.20 | **0.18** | | 0.23 | **0.22** |
| | **NMR** | **Love** | 0.17 | 0.19 | **0.20** | 0.20 | 0.22 | **0.23** |
| | | **Girão** | 0.19 | - | - | - | - | - |
| | | **The author** | **0.19** | - | - | - | - | - |
| **MCL** | | **Love** | 8.7 | 12.4 | **13.8** | 9.6 | 16.2 | **23.5** |
| | | **Girão** | 11.5 | - | - | - | - | - |
| | | **The author** | **11.3** | - | - | - | - | - |

The Ca/Si atomic ratio in the C-S-H of the 13 years old Love's sample is slightly higher than the 9 years old sample, probably due to further hydration of WPC. The MCL of the C-S-H chain increases as the age increases, especially in the WP50 cement paste, indicating the longer the hydration takes, the longer the aluminosilicate anion chain becomes.

## 9.3 Leaching experiments on the 1Y-WP30, 13Y-WP30 and 13Y-WP50

As discussed in Chapters 4, 5, and 6 that, during the leaching process, the main changes in the cement paste are the CH dissolution and the C-S-H decalcification. Figure 9.1 shows the CH as a percentage of ignited weight observed by thermal analysis and the Ca/Si atomic ratio of the C-S-H on the degraded layer observed by SEM-EDX in the 1Y-WP30, 13Y-WP30 and 13Y-WP50 cement paste during the leaching process. It illustrates that during the leaching process, the CH is totally dissolved and the C-S-H is largely decalcified. Before leaching, the 1Y-WP30 cement paste has the most abundant content of CH, then the 13Y-WP30 cement paste and finally the 13Y-WP50 cement paste, because of the further consumption of pozzolanic reaction. After 45 days of leaching, 13.86, 10.57 and 6.34 of CH as % of ignited weight of 1Y-WP30, 13Y-WP30 and 13Y-WP50 cement paste has all totally been dissolved. The more CH dissolved, the more porous of cement paste will be (Haga et al., 2005). Before leaching, the Ca/Si atomic ratio in the 1Y-WP30 cement paste and 13Y-WP30 cement paste are similar, however, in the 13Y-WP50 cement paste, the Ca/Si atomic ratio is slightly lower, due to higher replacement of PFA which has low Ca content. During the first 5 days of leaching, the C-S-H in the cement paste is slightly decalcified, on the contrary, the CH has been significantly dissolved during this time, suggesting that the CH is dissolved before the C-S-H is decalcified. After 5 days of leaching, the C-S-H starts to be decalcified significantly in the 13Y-WP30 cement paste and 13Y-WP50

cement paste, however, it's not decalcified in the 1Y-WP30 cement paste, due to the larger content of the CH left at this stage as shown in top BSE image in Figure 4.5, which postpones the C-S-H decalcification. After 10 days of the leaching, the C-S-H in all the paste has been largely decalcified, as at this stage, the CH on the degraded zone has been thoroughly dissolved as shown in the BSE images of Figure 4.5, Figure 5.6 and Figure 6.5. After 15 days of leaching, the decalcification of C-S-H gel in the 13Y-WP30 cement paste and 13Y-WP50 cement paste becomes steady, however, the decalcification of C-S-H gel continues, probably due to the larger CH dissolution which produces larger pores in the cement paste and then induces the larger C-S-H decalcification. Unfortunately, due to lack of amount of the aged cement paste, the leaching experiments of the 13Y-WP30 cement paste and 13Y-WP50 cement paste are not performed as long as on the 1Y-WP30 cement paste, and it is difficult to evaluate whether it has already reached the C-S-H decalcification limit. The leaching experiment performed on the 1Y-WP30 cement paste lasts longer, and the Ca/Si atomic ratio in the cement paste is similar after 55 days, 65 days and 75 days leaching, suggesting that the decalcification of C-S-H probably reach its limit. The decalcification of C-S-H is different from the dissolution of CH, that after a certain time of leaching, there is still a great amount of Ca in the C-S-H, however, the CH has already been thoroughly dissolved.

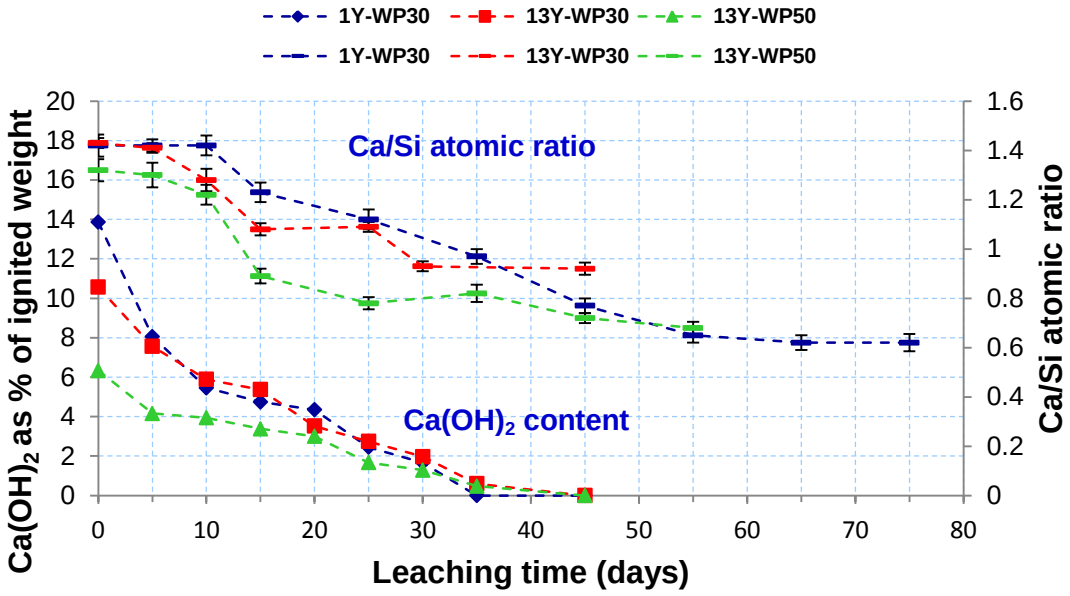


Figure 9.1 The CH as a percentage of ignited weight observed by bulk thermal analysis and Ca/Si atomic ratio of the C-S-H in the degraded zone observed by SEM-EDX at different leaching time in the 1Y-WP30, 13Y-WP30 and 13Y-WP50 cement paste.

## 9.4 The structure of the C-A-S-H in the cement paste and the synthetic C-A-S-H at atomic-scale

The $^{29}$Si SS MAS NMR spectra for the one year WPC cement paste blended with 30% PFA after 35 and 75 days of leaching with Ca/Si atomic ratio of 0.97 and 0.62, and the synthetic C-A-S-H with Ca/Si atomic ratio of 0.90 and 0.45 are presented in Figure 9.3. The Ca/Si atomic ratio of the C-A-S-H of the cement paste are analysed by SEM-EDX, and the Ca/Si atomic ratio of the C-A-S-H of the synthetic C-A-S-H are analysed by TEM-EDX. The bottom spectra in Figure 9.3 show that the spectrum shape of the cement paste with a Ca/Si atomic ratio 0.97 is similar to the synthetic C-A-S-H with a Ca/Si atomic ratio 0.90, except there are extra peaks of $Q^0$ and $Q^4$ for the anhydrous WPC cement and anhydrous PFA in the cement paste and the resonance peaks for the synthetic C-A-S-H are slightly sharper and more well defined than those in the cement paste, indicating that the atomic-structure of the synthetic C-A-S-H is similar to,

however more well-ordered than, that of the C-A-S-H in the cement paste. The top spectra in Figure 9.3 present that the spectrum shape of the cement paste with a Ca/Si atomic ratio of 0.62 is similar to the synthetic C-A-S-H with a Ca/Si atomic ratio of 0.45, both of which are similar to the spectrum observed from tobermorite (Wieker et al., 1982, Cong and Kirkpatrick, 1996b, Cong and Kirkpatrick, 1996a). There is a hump around the chemical shift of -95 ppm in both samples, which is assigned to the $Q^3$(1Al) and $Q^3$, indicating the presence of the cross-linking in the C-A-S-H structure. The $Q^2$ is dominant in both samples, indicating the MCL is long, which is generally observed in the C-S-H with a low Ca/Si atomic ratio. The NMR analysis illustrates that the atomic structure of the C-A-S-H formed in the cement paste is similar to, although less well-ordered, that of the synthetic C-A-S-H with similar chemical compositions.

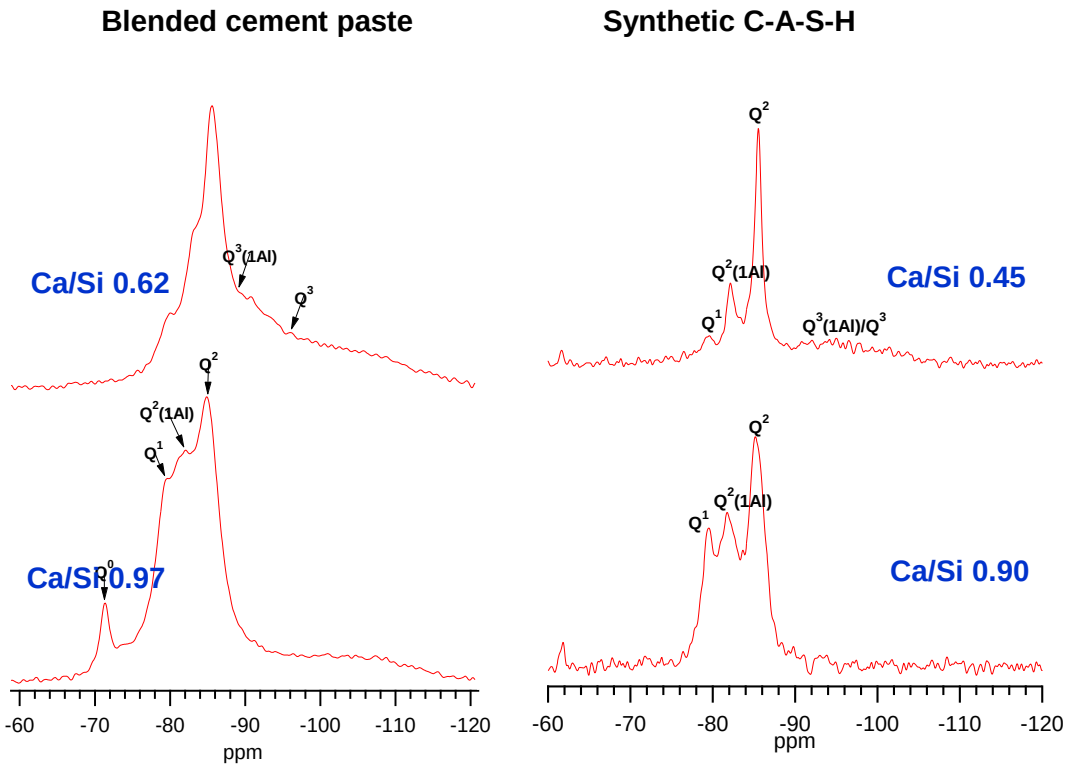


Figure 9.2 The left $^{29}$Si SS MAS NMR spectra for the 1Y-WP30 after 35 days of leaching with a Ca/Si atomic ratio of 0.97 (bottom) and 75 days of leaching (top) with a Ca/Si atomic ratio of 0.62; the right $^{29}$Si SS MAS NMR spectra for the synthetic C-A-S-H with a Ca/Si atomic ratio of 0.90 (bottom) and bulk Ca/Si atomic ratio of 0.45 (top).

# Chapter 10 Conclusions and recommendations for future work

## 10.1 Conclusions

This thesis has studied the leaching mechanism by using one year old white Portland cement paste blended with 30% pulverised fly ash and 13 years old white Portland cement paste blended with 30% and 50% pulverised fly ash. It is observed that the chemical compositions, the micro-, the nano- and the atomic-scale structure evolve during the leaching process in similar way in all three blended cement systems: (1) CH with $K_{SP}$ of $4.68\times10^{-6}$ at ambient temperature is first dissolved due to its easy dissolved nature, and the more CH content in the original cement paste, the faster the CH dissolution speed is; (2) the anhydrous cement left in the cement paste after a certain time of hydration is further hydrated due to the addition of water; initially, the ettringite further precipitated on the degraded layer of the cement paste, and then it is dissolved due to its dissolution nature; (3) the microstructure of the cement paste becomes more porous; the morphology of the C-S-H changes from one dimensional fine fibrillar and two dimensional foil-like feature to three dimensional net like feature; (4) the C-S-H is decalcified from 1.3~1.4 to 0.6~0.9, which is considered that the Ca ions is dissolved in the interlayer of the C-S-H chain; and (5) there are $Q^3$(1Al) and $Q^3$ precipitated in the cement paste, indicating the cross linking of two silicate chains through the interlayer of the C-S-H. However, after 45 days of leaching, the CH dissolved content has an order of the one year old white Portland cement paste blended with 30% pulverised fly ash, 13 years old white Portland cement paste blended with 30% pulverised fly ash and 13 years old white Portland cement paste blended with 50% pulverised fly ash, and there is a strong connection between the CH dissolved content and porosity of the cement paste.

This thesis has also investigated the micro-, nano- and atomic-scale structure of the white Portland cement paste blended with 30% and 50% pulverised fly ash. As the

amount of PFA replacement becomes 50 percentage instead of 30 percentage, it is found that the content of CH decreases due to further consumption by pozzolanic reaction; the microstructure of the cement paste becomes more porous as the PFA is less reactive than WPC; and the Ca/Si atomic ratio in the C-S-H is lower as the PFA has lower content of Ca.

Regarding the effects of ageing on the cement paste, it is concluded that the CH in the 13 years old sample has been further consumed due to the pozzolanic reaction compared to that in the 9 years old sample. In addition, the MCL have slightly increased indicating a further hydration of the cement paste.

This thesis also investigated the chemical compositions and micro/nano/atomic-scale structure of ordinary Portland cement paste blended with blast furnace slag cured at ambient temperature, 35 ºC and 80 ºC. It is observed that the main phases in the blended cements OPC:BFS paste hydrated at ambient temperature and 35 °C, are C-S-H gel, CH, HT-type phase and AFm phase. And, the main phases in the paste hydrated at 80 °C, are C-S-H gel, CH, HT-type phase and HG phase. It is also observed that as the curing temperature increases: (1) the content of CH and hydrated slag increase as the curing temperature accelerates the hydration process; (2) the microstructure becomes more porous and inhomogeneous; and (3) the MCL of the C-S-H increases.

The synthetic C-A-S-H is also studied in this thesis, and its structure is compared with the C-A-S-H formed in the cement paste. The experimental observations include: (1) the synthetic C-A-S-H is intermixed with other aluminate hydrate, *i.e.* stratlingite in the low Ca/Si atomic ratio C-A-S-H and hydrogarnet in the high Ca/Si atomic ratio C-A-S-H; (2) The C-A-S-H with a low Ca/Si atomic ratio has a foil-like feature, and the C-A-S-H with a high Ca/Si atomic ratio has a fibrillar feature under the observation of the TEM; (3) there are $Q^3$(1Al) and $Q^3$ observed in the C-A-S-H with low Ca/Si atomic ratio, which

are also observed in the cement paste after leaching; (4) the C-A-S-H with low Ca/Si atomic ratio has longer mean chain length of the aluminosilicate anion; and (5) there is Al in the interlayer for balancing in the C-A-S-H with a low Ca/Si atomic ratio.

## 10.2 Industrial benefits

The durability of cementitious materials is a big concern when they are applied in the GDF. This study provides some industrial guides:

The micro-, nano-, atomic-scale structural evolution of the cement paste has been understood. It provides the knowledge of the leaching mechanism to NDA when they perform the field experiments.

The elevated curing temperature leads to accelerate the cement hydration process, however, the porosity of cement paste also increases, and that means the transport properties of the cement paste increases. So, in practice, the surrounding temperature of the GDF should be controlled.

Regarding the influence of ageing on the cement paste, the microstructure of cement paste become more homogeneous with ageing, and it is a good sign for durability.

## 10.3 Recommendations for future work

This study has investigated the evolutions of chemical compositions and micro/nano/atomic-scale structure of the blended cement paste during the leaching process, and it will be useful to investigate the evolutions of the mechanical properties, *i.e.* the compressive strength and the porosity during the leaching process, although the investigation of compressive strength is of less important in the application of the ILW materials disposal.

It's difficult to predict the long term leaching phenomena, due to the limitations of the laboratory work, *e.g.* short-term duration, small sample size, *etc*., thus it is

recommended to develop a model based on the data from the laboratory experiments, and then to predict the long-term performance of cementitious materials.

## Reference


ADENOT, F. & BUIL, M. 1992. Modelling of the corrosion of the cement paste by deionized water. *Cement and Concrete Research,* 22**,** 489-496.

ALARCON-RUIZ, L., PLATRET, G., MASSIEU, E. & EHRLACHER, A. 2005. The use of thermal analysis in assessing the effect of temperature on a cement paste. *Cement and Concrete Research,* 35**,** 609-613.

ANDERSEN, M. D., JAKOBSEN, H. J. & SKIBSTED, J. 2003. Incorporation of aluminum in the calcium silicate hydrate (C-S-H) of hydrated Portland cements: A high-field Al-27 and Si-29 MAS NMR Investigation. *Inorganic Chemistry,* 42**,** 2280-2287.

ANDERSEN, M. D., JAKOBSEN, H. J. & SKIBSTED, J. 2004. Characterization of white Portland cement hydration and the C-S-H structure in the presence of sodium aluminate by 27Al and 29Si MAS NMR spectroscopy. *Cement and Concrete Research,* 34**,** 857-868.

ANDERSEN, M. D., JAKOBSEN, H. J. & SKIBSTED, J. 2006. A new aluminium-hydrate species in hydrated Portland cements characterized by 27Al and 29Si MAS NMR spectroscopy. *Cement and Concrete Research,* 36**,** 3-17.

ANGSTADT, R. & HURLEY, F. 1963. Hydration of the alite phase in Portland cement.

ATKINS, M. & GLASSER, F. 1992. Application of Portland cement-based materials to radioactive waste immobilization. *Waste Management,* 12**,** 105-131.

ATKINSON, A., GOULT, D. & HEARNE, J. An assessment of the long-term durability of concrete in radioactive waste repositories. MRS Proceedings, 1985. Cambridge Univ Press.

BARNES, J. R., CLAGUE, A. D. H., CLAYDEN, N. J., DOBSON, C. M., HAYES, C. J., GROVES, G. W. & RODGER, S. A. 1985. Hydration of Portland-cement followed by Si-29 solid-state NMR-spectroscopy. *Journal of Materials Science Letters,* 4**,** 1293-1295.

BENSTED, J. & BARNES, P. 2008. *Structure and Performance of Cements*.

BERNER, U. R. 1992. Evolution of pore water chemistry during degradation of cement in a radioactive waste repository environment. *Waste Management,* 12**,** 201-219.

BHATTY, J. I. 1991. A review of the application of thermal analysis to cement-admixture systems. *Thermochimica Acta,* 189**,** 313-350.

BI, Q. 2010. Investigation of the leaching behavior of mortar pipe lining in drinking water. *Journal of Wuhan University of Technology-Mater. Sci. Ed.,* 25**,** 893-896.

BLACK, L., BREEN, C., YARWOOD, J., DENG, C.-S., PHIPPS, J. & MAITLAND, G. 2006. Hydration of tricalcium aluminate (C3A) in the presence and absence of gypsum—studied by Raman spectroscopy and X-ray diffraction. *Journal of Materials Chemistry,* 16**,** 1263-1272.

BLACK, L., STUMM, A., GARBEV, K., STEMMERMANN, P., HALLAM, K. R. & ALLEN, G. C. 2005. X-ray photoelectron spectroscopy of aluminium-substituted tobermorite. *Cement and Concrete Research,* 35**,** 51-55.

BORGES, P. H. R., COSTA, J. O., MILESTONE, N. B., LYNSDALE, C. J. & STREATFIELD, R. E. 2010. Carbonation of CH and C–S–H in composite cement pastes containing high amounts of BFS. *Cement and Concrete Research,* 40**,** 284-292.

BRINDLEY, G. & KIKKAWA, S. 1979. A crystal-chemical study of Mg, Al and Ni, Al hydroxy-perchlorates and hydroxy-carbonates. *American Mineralogist,* 64**,** 836-843.

BROUGH, A. R., DOBSON, C. M., RICHARDSON, I. G. & GROVES, G. W. 1994. In-situ solid-state NMR-studies of $Ca_3SiO_5$-Hydration at room-temperature and at

elevated-temperatures using Si-29 enrichment. *Journal of Materials Science,* 29**,** 3926-3940.

BROWN, P. W. 1993. Kinetics of tricalcium aluminate and tetracalcium aluminoferrite hydration in the presence of calcium sulfate. *Journal of the American Ceramic Society,* 76**,** 2971-2976.

BRUNET, F., CHARPENTIER, T., CHAO, C. N., PEYCELON, H. & NONAT, A. 2010. Characterization by solid-state NMR and selective dissolution techniques of anhydrous and hydrated CEM V cement pastes. *Cement and Concrete Research,* 40**,** 208-219.

BULLARD, J. W., JENNINGS, H. M., LIVINGSTON, R. A., NONAT, A., SCHERER, G. W., SCHWEITZER, J. S., SCRIVENER, K. L. & THOMAS, J. J. 2011. Mechanisms of cement hydration. *Cement and Concrete Research,* 41**,** 1208-1223.

BYE, G. C. 1999. *Portland Cement: composition, production and properties.,* London, Thomas Telford.

CAO, Y. & DETWILER, R. J. 1995. Backscattered electron imaging of cement pastes cured at elevated temperatures. *Cement and Concrete Research,* 25**,** 627-638.

CARDE, C. & FRAN OIS, R. 1997. Effect of the leaching of calcium hydroxide from cement paste on mechanical and physical properties. *Cement and Concrete Research,* 27**,** 539-550.

CARDE, C., FRAN OIS, R. & TORRENTI, J.-M. 1996. Leaching of both calcium hydroxide and C-S-H from cement paste: Modeling the mechanical behavior. *Cement and Concrete Research,* 26**,** 1257-1268.

CHATTERJI, S. 1997. Mesostructure of calcium silicate hydrate (C-S-H) gels in portland cement paste: Short-range ordering, nanocrystallinity, and local compositional order - Comment. *Journal of the American Ceramic Society,* 80**,** 2959-2960.

CHATTERJI, S. & JEFFERY, J. 1962. Studies of Early Stages of Paste Hydration of Cement Compounds, I. *Journal of the American Ceramic Society,* 45**,** 536-543.

CHEN, J. J. 2003. *The nanostructure of Calcium Silicate Hydrate.* Ph.D, Northwestern University.

CHEN, J. J., THOMAS, J. J. & JENNINGS, H. M. 2006. Decalcification shrinkage of cement paste. *Cement and Concrete Research,* 36**,** 801-809.

CHEN, J. J., THOMAS, J. J., TAYLOR, H. F. W. & JENNINGS, H. M. 2004. Solubility and structure of calcium silicate hydrate. *Cement and Concrete Research,* 34**,** 1499-1519.

CHOI, Y. S. & YANG, E. I. 2013. Effect of calcium leaching on the pore structure, strength, and chloride penetration resistance in concrete specimens. *Nuclear Engineering and Design,* 259**,** 126-136.

CONG, X. & KIRKPATRICK, R. J. 1996a. 29Si and 17O NMR investigation of the structure of some crystalline calcium silicate hydrates. *Advanced Cement Based Materials,* 3**,** 133-143.

CONG, X. & KIRKPATRICK, R. J. 1996b. 29Si MAS NMR study of the structure of calcium silicate hydrate. *Advanced Cement Based Materials,* 3**,** 144-156.

CONG, X. D. & KIRKPATRICK, R. J. 1993. Hydration of calcium aluminate cements-A solid-state Al-27 NMR-study. *Journal of the American Ceramic Society,* 76**,** 409-416.

DWECK, J., BUCHLER, P. M., COELHO, A. C. V. & CARTLEDGE, F. K. 2000. Hydration of a Portland cement blended with calcium carbonate. *Thermochimica Acta,* 346**,** 105-113.

DYSON, H. M., RICHARDSON, I. G. & BROUGH, A. R. 2007. A combined Si-29 MAS NMR and selective dissolution technique for the quantitative evaluation of hydrated blast furnace slag cement blends. *Journal of the American Ceramic Society,* 90**,** 598-602.

ESCALANTE-GARC A, J. I. & SHARP, J. H. 1998. Effect of temperature on the hydration of the main clinker phases in portland cements: part ii, blended cements. *Cement and Concrete Research,* 28**,** 1259-1274.

ESCALANTE-GARC A, J. I. & SHARP, J. H. 2001. The microstructure and mechanical properties of blended cements hydrated at various temperatures. *Cement and Concrete Research,* 31**,** 695-702.

FAUCON, P., ADENOT, F., CABRILLAC, R. & JORDA, M. 1998a. Deterioration Mechanisms of a Cement Paste under Waste Attack. *Proceedings of second international conference on concrete under severe conditions.*

FAUCON, P., ADENOT, F., JACQUINOT, J. F., PETIT, J. C., CABRILLAC, R. & JORDA, M. 1998b. Long-term behaviour of cement pastes used for nuclear waste disposal: review of physico-chemical mechanisms of water degradation. *Cement and Concrete Research,* 28**,** 847-857.

FAUCON, P., ADENOT, F., JORDA, M. & CABRILLAC, R. 1997. Behaviour of crystallised phases of Portland cement upon water attack. *Materials and Structures,* 30**,** 480-485.

FAUCON, P., DELAGRAVE, A., PETIT, J. C., RICHET, C., MARCHAND, J. M. & ZANNI, H. 1999. Aluminum incorporation in calcium silicate hydrates (C-S-H) depending on their Ca/Si ratio. *Journal of Physical Chemistry B,* 103**,** 7796-7802.

FAUCON, P., LE BESCOP, P., ADENOT, F., BONVILLE, P., JACQUINOT, J. F., PINEAU, F. & FELIX, B. 1996. Leaching of cement: Study of the surface layer. *Cement and Concrete Research,* 26**,** 1707-1715.

FERNANDEZ-JIMENEZ, A. & PALOMO, A. 2003. Characterisation of fly ashes. Potential reactivity as alkaline cements. *Fuel,* 82**,** 2259-2265.

GAITERO, J. J., CAMPILLO, I. & GUERRERO, A. 2008. Reduction of the calcium leaching rate of cement paste by addition of silica nanoparticles. *Cement and Concrete Research,* 38**,** 1112-1118.

GARBEV, K., BEUCHLE, G., BORNEFELD, M., BLACK, L. & STEMMERMANN, P. 2008. Cell dimensions and composition of nanocrystalline calcium silicate hydrate solid solutions. Part 1: Synchrotron-based x-ray diffraction. *Journal of the American Ceramic Society,* 91**,** 3005-3014.

GARD, J. A. & TAYLOR, H. F. W. 1976. Calcium silicate hydrate (II) ("C-S-H(II)"). *Cement and Concrete Research,* 6**,** 667-677.

GARTNER, E. 2004. Industrially interesting approaches to "low-CO2" cements. *Cement and Concrete Research,* 34**,** 1489-1498.

GIRAO, A. V. 2007. *The nanostructure and degradation of C-S-H in Portland and Blended Cements.* PhD, Leeds University.

GIRAO, A. V., RICHARDSON, I. G., PORTENEUVE, C. B. & BRYDSON, R. M. D. 2007a. Composition, morphology and nanostructure of C-S-H in white Portland cement pastes hydrated at 55 °C. *Cement and Concrete Research,* 37**,** 1571-1582.

GIRAO, A. V., RICHARDSON, I. G., PORTENEUVE, C. B. & BRYDSON, R. M. D. 2007b. Composition, morphology and nanostructure of C–S–H in white Portland cement–fly ash blends hydrated at 85 °C. *Advances in Applied Ceramics,* 106**,** 10.

GIRAO, A. V., RICHARDSON, I. G., TAYLOR, R. & BRYDSON, R. M. D. 2010. Composition, morphology and nanostructure of C-S-H in 70% white Portland cement-30% fly ash blends hydrated at 55 °C. *Cement and Concrete Research,* 40**,** 1350-1359.

GLASSER, F. & ATKINS, M. 1994. Cements in radioactive waste disposal. *MRS Bulletin,* 19**,** 33-38.

GLASSER, F. P. 1992. Progress in the immobilization of radioactive wastes in cement. *Cement and Concrete Research,* 22**,** 201-216.

GOLLOP, R. S. & TAYLOR, H. F. W. 1994. Microstructural and microanalytical studies of sulfate attack. II. Sulfate-resisting Portland cement: Ferrite composition and hydration chemistry. *Cement and Concrete Research,* 24**,** 1347-1358.

GOMES, S. & FRAN OIS, M. 2000. Characterization of mullite in silicoaluminous fly ash by XRD, TEM, and< sup> 29</sup> Si MAS NMR. *Cement and concrete research,* 30**,** 175-181.

GOUGAR, M., SCHEETZ, B. & ROY, D. 1996. Ettringite and C S H Portland cement phases for waste ion immobilization: A review. *Waste Management,* 16**,** 295-303.

GROVES, G. W. TEM studies of cement hydration. Materials Research Society Proeedings, 1987. 3-12.

GROVES, G. W., BROUGH, A., RICHARDSON, I. G. & DOBSON, C. M. 1991. PROGRESSIVE CHANGES IN THE STRUCTURE OF HARDENED C3S CEMENT PASTES DUE TO CARBONATION. *Journal of the American Ceramic Society,* 74**,** 2891-2896.

GRUTZECK, M. W. 1999. A new model for the formation of calcium silicate hydrate (C-S-H). *Materials Research Innovations,* 3**,** 160-170.

HAGA, K., SHIBATA, M., HIRONAGA, M., TANAKA, S. & NAGASAKI, S. 2002. Silicate anion structural change in calcium silicate hydrate gel on dissolution of hydrated cement. *Journal of Nuclear Science and Technology,* 39**,** 540-547.

HAGA, K., SHIBATA, M., HIRONAGA, M., TANAKA, S. & NAGASAKI, S. 2005. Change in pore structure and composition of hardened cement paste during the process of dissolution. *Cement and Concrete Research,* 35**,** 943-950.

HAMMOND, G. P. & JONES, C. I. 2008. Embodied energy and carbon in construction materials. *Proceedings of the ICE-Energy,* 161**,** 87-98.

HARRISSON, A., TAYLOR, H. F. & WINTER, N. 1985. Electron-optical analyses of the phases in a Portland cement clinker, with some observations on the calculation of quantitative phase composition. *Cement and Concrete Research,* 15**,** 775-780.

HAWORTH, A., SHARLAND, S. & TWEED, C. Modelling of the degradation of cement in a nuclear waste repository. Material Research Society Symposium Proceedings, 1989. Cambridge Univ Press, 447-454.

HE, J.-Y., SCHEETZ, B. E. & ROY, D. M. 1984. Hydration of fly ash-portland cements. *Cement and Concrete Research,* 14**,** 505-512.

HEWLETT, P. 2003. *Lea's chemistry of cement and concrete*, Butterworth-Heinemann.

HJORTH, J., SKIBSTED, J. & JAKOBSEN, H. J. 1988. 29Si MAS NMR studies of portland cement components and effects of microsilica on the hydration reaction. *Cement and Concrete Research,* 18**,** 789-798.

HOUSTON, J. R., MAXWELL, R. S. & CARROLL, S. A. 2009. Transformation of meta-stable calcium silicate hydrates to tobermorite: reaction kinetics and molecular structure from XRD and NMR spectroscopy. *Geochemical Transactions,* 10.

JAIN, J. & NEITHALATH, N. 2009. Analysis of calcium leaching behavior of plain and modified cement pastes in pure water. *Cement and Concrete Composites,* 31**,** 176-185.

JANSEN, S. R., HINTZEN, H. T., METSELAAR, R., DE HAAN, J. W., VAN DE VEN, L. J. M., KENTGENS, A. P. M. & NACHTEGAAL, G. H. 1998. Multiple quantum Al-27 magic-angle-spinning nuclear magnetic resonance spectroscopic study of SrAl12O19: Identification of a Al-27 resonance from a well-defined AlO5 site. *Journal of Physical Chemistry B,* 102**,** 5969-5976.

JOST, K. H., ZIEMER, B. & SEYDEL, R. 1977. Redetermination of the structure of β-dicalcium silicate. *Acta Crystallographica section B,* 33**,** 1696-1700.

JUILLAND, P., GALLUCCI, E., FLATT, R. & SCRIVENER, K. 2010. Dissolution theory applied to the induction period in alite hydration. *Cement and Concrete Research,* 40**,** 831-844.

KAMALI, S., MORANVILLE, M. & LECLERCQ, S. 2008. Material and environmental parameter effects on the leaching of cement pastes: Experiments and modelling. *Cement and Concrete Research,* 38**,** 575-585.
KJELLSEN, K. O., DETWILER, R. J. & GJ RV, O. E. 1990. Backscattered electron imaging of cement pastes hydrated at different temperatures. *Cement and Concrete Research,* 20**,** 308-311.
KOLOVOS, K., TSIVILIS, S. & KAKALI, G. 2005. SEM examination of clinkers containing foreign elements. *Cement and Concrete Composites,* 27**,** 163-170.
KOMARNENI, S., ROY, R., ROY, D. M., FYFE, C. A., KENNEDY, G. J., BOTHNERBY, A. A., DADOK, J. & CHESNICK, A. S. 1985. Al-27 and Si-29 magic angle spinning nuclear magnetic resonance spectroscopy of Al-substituted tobermorites. *Journal of Materials Science,* 20**,** 4209-4214.
KUTCHKO, B. G. & KIM, A. G. 2006. Fly ash characterization by SEM–EDS. *Fuel,* 85**,** 2537-2544.
KWAN, S., LAROSA, J. & GRUTZECK, M. W. 1995. Si-29 and Al-27 MASNMR study of stratlingite. *Journal of the American Ceramic Society,* 78**,** 1921-1926.
LE SAOUT, G., KOCABA, V. & SCRIVENER, K. 2011. Application of the Rietveld method to the analysis of anhydrous cement. *Cement and Concrete Research,* 41**,** 133-148.
LERCH, W. 1946. *The influence of gypsum on the hydration and properties of Portland cement pastes*, Portland Cement Association.
LI, X. A. & YAN, P. Y. 2010. Microstructural variation of hardened cement-fly ash pastes leached by soft water. *Science China-Technological Sciences,* 53**,** 3033-3038.
LIANG, T. & NANRU, Y. 1994. Hydration products of calcium aluminoferrite in the presence of gypsum. *Cement and concrete research,* 24**,** 150-158.
LIPPMAA, E., MAGI, M., SAMOSON, A., ENGELHARDT, G. & GRIMMER, A. R. 1980. Structural studies of silicates by solid-state high-resolution Si-29 NMR. *Journal of the American Chemical Society,* 102**,** 4889-4893.
LOTHENBACH, B., SCRIVENER, K. & HOOTON, R. D. 2011. Supplementary cementitious materials. *Cement and Concrete Research,* 41**,** 1244-1256.
LOVE, C. A. 2002. *Mictrostructure and silicate anion structure of hardened blended cement pastes.* Ph.D, Leeds University.
LOVE, C. A., RICHARDSON, I. G. & BROUGH, A. R. 2007. Composition and structure of C-S-H in white Portland cement-20% metakaolin pastes hydrated at 25 °C. *Cement and Concrete Research,* 37**,** 109-117.
LUKE, K. & GLASSER, F. P. 1988. Internal chemical evolution of the constitution of blended cements. *Cement and Concrete Research,* 18**,** 495-502.
MACPHEE, D. E., LUKE, K., GLASSER, F. P. & LACHOWSKI, E. E. 1989. Solubility and aging of calcium silicate hydrates in alkaline solutions at 25 C. *Journal of the American Ceramic Society,* 72**,** 646-654.
MAKI, I., FUKUDA, K., SEKI, S. & TANIOKA, T. 1991. Impurity distribution during crystal growth of alite in Portland cement clinker. *Journal of the American Ceramic Society,* 74**,** 2082-2085.
MANZANO, H., DOLADO, J. S. & AYUELA, A. 2009. Aluminum Incorporation to Dreierketten Silicate Chains. *Journal of Physical Chemistry B,* 113**,** 2832-2839.
MARGESON, J. *Hydrated Cement Paste* [Online]. http://www.cementlab.com/cement-art.htm.
MEHTA, P. 1973. Mechanism of expansion associated with ettringite formation. *Cement and Concrete Research,* 3**,** 1-6.
MEHTA, P. K. 1985. Influence of fly ash characteristics on the strength of Portland-fly ash mixtures. *Cement and Concrete Research,* 15**,** 669-674.
MIDGLEY, H. 1979. The determination of calcium hydroxide in set Portland cements. *Cement and concrete research,* 9**,** 77-82.

MORANVILLE, M., KAMALI, S. & GUILLON, E. 2004. Physicochemical equilibria of cement-based materials in aggressive environments—experiment and modeling. *Cement and Concrete Research,* 34**,** 1569-1578.
MURGIER, S., ZANNI, H. & GOUVENOT, D. 2004. Blast furnace slag cement: a $^{29}$Si and $^{27}$Al NMR study. *Comptes Rendus Chimie,* 7**,** 389-394.
NDA 2010. An overview of the Generic Disposal System Safety Case. NDA Report NDA/RWMD/010.
ODLER, I. 2003. 6 - Hydration, Setting and Hardening of Portland Cement. *In:* HEWLETT, P. C. (ed.) *Lea's Chemistry of Cement and Concrete (Fourth Edition).* Oxford: Butterworth-Heinemann.
ODLER, I. & ABDUL-MAULA, S. 1984. Possibilities of quantitative determination of the AFt-(ettringite) and AFm-(monosulphate) phases in hydrated cement pastes. *Cement and Concrete Research,* 14**,** 133-141.
OGBONNA, J., AJAKA, E. O., SHAKER, S. A., FARINA, Y., MAHMMOD, S., ESKENDER, M., AGRAWAL, N., VENUGOPALAN, K., DHANAPANDIAN, S. & GNANAVEL, B. 2006. The secondary effects of lignosulfonate cement retarder on cement slurry properties.
PADE, C. & GUIMARAES, M. 2007. The CO2 uptake of concrete in a 100 year perspective. *Cement and Concrete Research,* 37**,** 1348-1356.
PALMER, J. D. & FAIRHALL, G. A. 1992. Properties of cement systems containing intermediate level wates. *Cement and Concrete Research,* 22**,** 325-330.
PALOMO, A., ALONSO, S. & FEMANDEZ-JIMENEZ, A. 2004. Alkaline activation of fly ashes: NMR study of the reaction products. *Journal of the American Ceramic Society,* 87**,** 1141-1145.
PANE, I. & HANSEN, W. 2005. Investigation of blended cement hydration by isothermal calorimetry and thermal analysis. *Cement and Concrete Research,* 35**,** 1155-1164.
PAPADAKIS, V. G. 1999. Effect of fly ash on Portland cement systems: Part I. Low-calcium fly ash. *Cement and Concrete Research,* 29**,** 1727-1736.
PARDAL, X., BRUNET, F., CHARPENTIER, T., POCHARD, I. & NONAT, A. 2012. Al-27 and Si-29 Solid-State NMR Characterization of Calcium-Aluminosilicate-Hydrate. *Inorganic Chemistry,* 51**,** 1827-1836.
PARDAL, X., POCHARD, I. & NONAT, A. 2009. Experimental study of Si–Al substitution in calcium-silicate-hydrate (C-S-H) prepared under equilibrium conditions. *Cement and Concrete Research,* 39**,** 637-643.
PENA, P., RIVAS MERCURY, J. M., DE AZA, A. H., TURRILLAS, X., SOBRADOS, I. & SANZ, J. 2008. Solid-state $^{27}$Al and $^{29}$Si NMR characterization of hydrates formed in calcium aluminate-silica fume mixtures. *Journal of Solid State Chemistry,* 181**,** 1744-1752.
PORTENEUVE, C., ZANNI, H., KORB, J.-P. & PETIT, D. 2001a. Water leaching of high and ultra high performance concrete: a nuclear magnetic resonance study. *Comptes Rendus de l'Académie des Sciences - Series IIC - Chemistry,* 4**,** 809-814.
PORTENEUVE, C., ZANNI, H., VERNET, C., KJELLSEN, K. O., KORB, J.-P. & PETIT, D. 2001b. Nuclear magnetic resonance characterization of high- and ultrahigh-performance concrete: Application to the study of water leaching. *Cement and Concrete Research,* 31**,** 1887-1893.
PUERTAS, F. & FERNANDEZ-JIMENEZ, A. 2003. Mineralogical and microstructural characterisation of alkali-activated fly ash/slag pastes. *Cement & Concrete Composites,* 25**,** 287-292.
PURNELL, P. 2009. *Novel uses for cement-brief review and outlook* [Online]. Available: http://www.engineering.leeds.ac.uk/resilience/partners/documents/sota1-outline-webdraft1.pdf [Accessed 26.10 2014].

PURNELL, P. & BLACK, L. 2012. Embodied carbon dioxide in concrete: Variation with common mix design parameters. *Cement and Concrete Research,* 42**,** 874-877.
RAMACHANDRAN, V. S. & BEAUDOIN, J. J. 2001. *Handbook of Analytical Techniques in Concrete Science and Technology 2001,* New Jersey, New York: Noyes Publications.
RAMACHANDRAN, V. S., PAROLI, R. M., BEAUDOIN, J. J. & DELGADO, A. H. 2002. *Handbook of thermal analysis of construction materials*, William Andrew.
REGOURD, M. Microstructure of cement blends containing fly ash, silica fume, slag and fillers. MRS Proceedings, 1986. Cambridge Univ Press, 187.
REHAN, R. & NEHDI, M. 2005. Carbon dioxide emissions and climate change: policy implications for the cement industry. *Environmental Science & Policy,* 8**,** 105-114.
RICHARDSON, I. G. 1999. The nature of C-S-H in hardened cements. *Cement and Concrete Research,* 29**,** 1131-1147.
RICHARDSON, I. G. 2000. The nature of the hydration products in hardened cement pastes. *Cement & Concrete Composites,* 22**,** 97-113.
RICHARDSON, I. G. 2004. Tobermorite/jennite- and tobermorite/calcium hydroxide-based models for the structure of C-S-H: applicability to hardened pastes of tricalcium silicate, [beta]-dicalcium silicate, Portland cement, and blends of Portland cement with blast-furnace slag, metakaolin, or silica fume. *Cement and Concrete Research,* 34**,** 1733-1777.
RICHARDSON, I. G., BROUGH, A. R., BRYDSON, R., GROVES, G. W. & DOBSON, C. M. 1993. Location of aluminium in substituted calcium silicate hydrate (C-S-H) gels as determined by Si-29 and Al-27 NMR and EELS. *Journal of the American Ceramic Society,* 76**,** 2285-2288.
RICHARDSON, I. G., BROUGH, A. R., GROVES, G. W. & DOBSON, C. M. 1994. The characterization of hardened alkali-activated blast-furnace slag pastes and the nature of the calcium silicate hydrate (C-S-H) phase. *Cement and Concrete Research,* 24**,** 813-829.
RICHARDSON, I. G. & GROVES, G. W. 1992a. Microstructure and microanalysis of hardened cement pastes involving ground granulated blast-furnace slag. *Journal of Materials Science,* 27**,** 6204-6212.
RICHARDSON, I. G. & GROVES, G. W. 1992b. Models for the composition and structure of calcium silicate hydrate (C-S-H) gel in hardened tricalcium silicate pastes. *Cement and Concrete Research,* 22**,** 1001-1010.
RICHARDSON, I. G. & GROVES, G. W. 1993. Microstructure and microanalysis of hardened ordinary Portland-cement pastes. *Journal of Materials Science,* 28**,** 265-277.
RICHARDSON, I. G. & GROVES, G. W. 1997. The structure of the calcium silicate hydrate phases present in hardened pastes of white Portland cement blast-furnace slag blends. *Journal of Materials Science,* 32**,** 4793-4802.
RODGER, S. A. & GROVES, G. W. 1989. Electron-microscopy study of ordinary Portland-cement and ordinary Portland cement-pulverized fuel ash blended pastes. *Journal of the American Ceramic Society,* 72**,** 1037-1039.
RODGER, S. A., GROVES, G. W., CLAYDEN, N. J. & DOBSON, C. M. 1988. Hydration of tricalcium silicate followed by Si-NMR with cross-polarization. *Journal of the American Ceramic Society,* 71**,** 91-96.
SAKAI, E., MIYAHARA, S., OHSAWA, S., LEE, S. H. & DAIMON, M. 2005. Hydration of fly ash cement. *Cement and Concrete Research,* 35**,** 1135-1140.
SCRIVENER, K. & SKALNY, J. 1989. Materials science of concrete I. *ed. JP Skalny, American Ceramic Society, Westerville, OH, USA*.
SCRIVENER, K. L. 2004. Backscattered electron imaging of cementitious microstructures: understanding and quantification. *Cement and Concrete Composites,* 26**,** 935-945.

SCRIVENER, K. L., F LLMANN, T., GALLUCCI, E., WALENTA, G. & BERMEJO, E. 2004. Quantitative study of Portland cement hydration by X-ray diffraction/Rietveld analysis and independent methods. *Cement and Concrete Research,* 34**,** 1541-1547.

SCRIVENER, K. L. & KIRKPATRICK, R. J. 2008. Innovation in use and research on cementitious material. *Cement and Concrete Research,* 38**,** 128-136.

SCRIVENER, K. L. & PRATT, P. Backscattered electron images of polished cement sections in the scanning electron microscope. Proceedings of the International Conference on Cement Microscopy, 1984. 145-155.

SERCO 2012. Cement materials for use as backfill, sealing and structural materials in geological disposal concepts. SERCO/005125/001Issue 3.

SHARP, J., HILL, J., MILESTONE, N. & MILLER, E. Cementitious Systems for Encapsualation of Intermediate Level Waste. ASME 2003 9th International Conference on Radioactive Waste Management and Environmental Remediation, 2003. American Society of Mechanical Engineers, 1425-1433.

SKIBSTED, J., ANDERSEN, M. D. & JAKOBSEN, H. J. 2007. Applications of solid-state Nuclear Magnetic Resonance (NMR) in studies of Portland cement-based materials. *Zkg International,* 60**,** 70-83.

SKIBSTED, J. & HALL, C. 2008. Characterization of cement minerals, cements and their reaction products at the atomic and nano scale. *Cement and Concrete Research,* 38**,** 205-225.

SKIBSTED, J., JENSEN, O. M. & JAKOBSEN, H. J. Hydration kinetics for the alite, belite, and calcium aluminate phase in Portland cements from 27Al and 29Si MAS NMR spectroscopy. 10th International congress on the chemistry of cement, 1997.

SKINNER, L. B., CHAE, S. R., BENMORE, C. J., WENK, H. R. & MONTEIRO, P. J. M. 2010. Nanostructure of Calcium Silicate Hydrates in Cements. *Physical Review Letters,* 104.

SNELLINGS, R., MERTENS, G. & ELSEN, J. 2012. Supplementary cementitious materials. *Reviews in Mineralogy and Geochemistry,* 74**,** 211-278.

STARK, J. 2011. Recent advances in the field of cement hydration and microstructure analysis. *Cement and Concrete Research,* 41**,** 666-678.

STUTZMAN, P. 2004. Scanning electron microscopy imaging of hydraulic cement microstructure. *Cement and Concrete Composites,* 26**,** 957-966.

SUGIYAMA, D. & FUJITA, T. 2006. A thermodynamic model of dissolution and precipitation of calcium silicate hydrates. *Cement and Concrete Research,* 36**,** 227-237.

SUN, G. K., YOUNG, J. F. & KIRKPATRICK, R. J. 2006. The role of Al in C-S-H: NMR, XRD, and compositional results for precipitated samples. *Cement and Concrete Research,* 36**,** 18-29.

TAYLOR, H. F. W. 1950. Hydrated calcium silicates. Part I. Compound formation at ordinary temperatures *Journal of the Chemical Society (Resumed)***,** 3682-3690.

TAYLOR, H. F. W. 1993. Nanostructure of C-S-H: Current status. *Advanced Cement Based Materials,* 1**,** 38-46.

TAYLOR, H. F. W. 1997. *Cement Chemistry,* London, Academic Press.

TAYLOR, H. F. W., MOHAN, K. & MOIR, G. K. 1985a. Analytical study of pure and extended Portland-cement pastes. 1. Pure Portland-cement pastes. *Journal of the American Ceramic Society,* 68**,** 680-685.

TAYLOR, H. F. W., MOHAN, K. & MOIR, G. K. 1985b. Analytical study of pure and extended Portland-cement pastes. 2. Fly ash-cement and slag-cement pastes. *Journal of the American Ceramic Society,* 68**,** 685-690.

TAYLOR, R. 2010. *Characterizatin of C-S-H in early and late age systems containing admixtures.* Ph.D, Leeds University.

TAYLOR, R., RICHARDSON, I. G. & BRYDSON, R. M. D. 2007. Nature of C-S-H in 20 year old neat ordinary Portland cement and 10% Portland cement-90% ground granulated blast furnace slag pastes. *Advances in Applied Ceramics,* 106**,** 294-301.

TAYLOR, R., RICHARDSON, I. G. & BRYDSON, R. M. D. 2010. Composition and microstructure of 20-year-old ordinary Portland cement-ground granulated blast-furnace slag blends containing 0 to 100% slag. *Cement and Concrete Research,* 40**,** 971-983.

THOMAS, J. J., CHEN, J. J., ALLEN, A. J. & JENNINGS, H. M. 2004. Effects of decalcification on the microstructure and surface area of cement and tricalcium silicate pastes. *Cement and Concrete Research,* 34**,** 2297-2307.

TOUTANJI, H., DELATTE, N., AGGOUN, S., DUVAL, R. & DANSON, A. 2004. Effect of supplementary cementitious materials on the compressive strength and durability of short-term cured concrete. *Cement and Concrete Research,* 34**,** 311-319.

VILLAIN, G., THIERY, M. & PLATRET, G. 2007. Measurement methods of carbonation profiles in concrete: thermogravimetry, chemical analysis and gammadensimetry. *Cement and Concrete Research,* 37**,** 1182-1192.

WANG, S.-D. & SCRIVENER, K. L. 1995. Hydration products of alkali activated slag cement. *Cement and Concrete Research,* 25**,** 561-571.

WANG, S.-D. & SCRIVENER, K. L. 2003. $^{29}$Si and $^{27}$Al NMR study of alkali-activated slag. *Cement and Concrete Research,* 33**,** 769-774.

WIEKER, W., GRIMMER, A. R., WINKLER, A., M GI, M., TARMAK, M. & LIPPMAA, E. 1982. Solid-state high-resolution 29Si NMR spectroscopy of synthetic 14 Å, 11 Å and 9 Å tobermorites. *Cement and Concrete Research,* 12**,** 333-339.

WILDING, C. R. 1992. The performance of cement based systems. *Cement and Concrete Research,* 22**,** 299-310.

WORRELL, E., PRICE, L., MARTIN, N., HENDRIKS, C. & MEIDA, L. O. 2001. Carbon dioxide emissions from the global cement industry. *Annual Review of Energy and the Environment,* 26**,** 303-329.

WU, X., JIANG, W. & ROY, D. M. 1990. Early activation and properties of slag cement. *Cement and Concrete Research,* 20**,** 961-974.

XU, Z. K. & VIEHLAND, D. 1997. Mesostructure of calcium silicate hydrate (C-S-H) gels in portland cement paste: Short-range ordering, nanocrystallinity, and local compositional order - Reply. *Journal of the American Ceramic Society,* 80**,** 2961-2962.

# Appendix

## Conference presentations

S. Jia, L. Black, and I.G. Richardson. *Microanalysis of ordinary Portland cement/ blast-furnace slag blended cement paste hydrated at different temperatures*, 31st Cement and Concrete Science Conference, Sep. 2011, Imperial College, London, UK.

S. Jia, L. Black, and I.G. Richardson. *Water leaching of 13-year-old hardened white Portland cement-fly ash blended cement paste*, 32nd Cement and Concrete Science Conference, Sep. 2012, Queen's university Belfast, Belfast, UK.

S. Jia, L. Black, and I.G. Richardson. *Micro/nano-structural evolutions in aged blended cement paste due to progressive deionized water leaching*, 1st research postgraduate students conference, Oct. 2012, School of Civil Engineering, University of Leeds, Leeds, UK.